POLITECNICO DI MILANO

DEPARTMENT OF CHEMISTRY, MATERIALS
AND CHEMICAL ENGINEERING "GIULIO NATTA"

DOCTORAL PROGRAMME IN INDUSTRIAL CHEMISTRY
AND CHEMICAL ENGINEERING

FLUORINATED SYSTEMS FOR BIOMEDICAL APPLICATIONS:

FROM IMAGING TO DRUG DELIVERY

Doctoral dissertation of:
Eleonora Veronese
971701

Supervisor: Prof. Pierangelo Metrangolo
Co-Supervisor: Prof. Valentina Dichiarante
Tutor: Prof. Maria Elisabetta Brenna
The Chair of the Doctoral Program: Prof. Carlo Alessandro Cavallotti

2020-2023, Cycle 36

Table of contents

Table of contents ..... **I**
Abstract ..... **III**
Chapter 1 ..... **1**
Introduction **1**
1.1 Properties of the fluorine atom and effect of fluorination on organic molecules 2
1.2 The role of fluorine in biomedicine and life sciences 4
1.2.1 Fluorine-based biomedical imaging 5
1.2.1.1 Fluorinated Magnetic Resonance Imaging contrast agents 8
1.2.1.2 PERFECTA 9
1.2.2 Fluorine in proteins, peptides and amino acids 11
1.2.2.1 Interactions between proteins and fluorinated materials 16
1.3 Fluorinated supramolecular architectures: from vesicles to fibers 18
1.3.1 Amphiphiles and their supramolecular assemblies 19
1.3.1.1 Dendrimers and dendritic architectures 23
1.3.1.2 Fluorinated dendrimers 25
1.3.2 Amino acidic hydrogels and their fibrillar network 28
1.3.2.1 Fluorination as a strategy to influence hydrogelation on the nanoscale 31
1.4 Aim and outline of the thesis 36
Chapter 2 ..... **37**
Fluorinated Dendrimers and Proteins as Supramolecular Hosts for PERFECTA **37**
2.1 Oligoglycerol-based dendrimers and model proteins 38
Results and discussion 41
2.2 PERFECTA@dendrimers as ^{19}F MRI contrast agents 41
2.2.1 Optimization of formulation protocols 41
2.2.2 Characterization and formulation of sulphated Janus dendrimer 49
2.2.3 Morphological characterization 53
2.2.4 ^{19}F-MRI performance 56
2.2.5 Cellular compatibility and uptake 59
2.2.6 Fluorinated *versus* hydrogenated dendrimers 62
2.3 PERFECTA@protein complexes: interaction study 64
2.3.1 Characterization of the formulations 64
2.3.2 Structural and morphological characterization 70

2.4 Conclusion 81
2.5 Materials and methods 82
Chapter 3 96
Amino Acid-Based Hydrogels with Tuned Properties: a Molecular Understanding 96
3.1 Crystal engineering principles to design low molecular weight hydrogelators 97
Results and discussion 100
3.2 Acid⋯Amide heterosynthon design 100
3.2.1 Solid-state study: co-crystallization 100
3.2.2 Hydrogel state study 106
3.2.3 Approach validation 109
3.2.4 Tunable performance: delayed release of substances 110
3.3 Halogen bond-based design 113
3.3.1 Crystallization trials 113
3.3.2 The influence of XB on hydrogelation 120
3.3.3 Validation of the crystallographic approach 124
3.3.4 Halogen bonding investigation 126
3.4 Conclusion 131
3.5 Materials and methods 132
Conclusions 142
Appendix – Advanced Characterization Techniques 144
List of abbreviations 150
Bibliography 152
List of publications 169

Abstract

Fluorination represents a powerful tool to tailor the properties of organic molecules, and biomedical research gets big advantages from the resulting systems in the fields of bioimaging and drug delivery, which are both relevant to the present thesis. The multiple benefits provided by fluorine are mainly related to its unique properties, such as high electronegativity, hydrophobicity, low polarizability, small steric demand, and very good magnetic response. In particular, Magnetic Resonance Imaging (MRI) based on ^{19}F provides an effective platform for diagnosis and selectively guided therapies. Due to the low amount of endogenous organic ^{19}F atoms in the human body, this nucleus provides good contrast, and furnishes useful anatomical information, if coupled with ^{1}H-MRI. However, fluorinated tracers have limited solubility in biological media. For this reason, proper formulations are a main target for their clinical use.

In my thesis work, I focused on the study of amphiphilic fluorinated dendrimers that self-assemble in aqueous environments into supramolecular structures, *e.g.*, micelles and vesicles, creating fluorophilic regions able to host fluorinated tracers. In this context, two synthesized amphiphilic dendrimers, BFTG2-OH and BFTG2-S, were demonstrated to efficiently host the popular ^{19}F-MRI tracer PERFECTA, allowing its efficient dispersion in water. An optimized formulation *via* nanoprecipitation was developed, which led to more than 50% of solubilized PERFECTA. Preliminary ^{19}F-MRI experiments on PERFECTA@BFTG2-OH and PERFECTA@BFTG2-S demonstrated the validity of the approach, producing bright images. In particular, BFTG2-S dendrimer was designed with the aim to confer selectivity for cells involved in the inflammatory response, and preliminary data confirmed the targetability of the system.

Another strategy I exploited to disperse PERFECTA in biological solutions was the use of two natural proteins, *i.e.*, bovine serum albumin (BSA) and lysozyme (LYS). PERFECTA@protein formulations were prepared, exploring different stoichiometry ratios, achieving a good loading of PERFECTA. An interesting structural transition observed in LYS upon interacting with PERFECTA prompted us to study in more detail the supramolecular chemistry behind the formation of PERFECTA@LYS complexes. A detailed structural characterization along with computational modelling highlighted the formation of unprecedented rod-like oligomers.

Finally, fluorination was also demonstrated to have a key role in driving, enhancing, and modifying the self-assembly of *N*-Fmoc protected amino acids yielding hydrogels, which were used for drug delivery. In particular, we focused on *N*-Fmoc-pentafluorophenylalanine, an effective low molecular weight hydrogelator (LMWH), and tuned its properties by involving it in hydrogen-bonded co-crystals with biologically relevant molecules. Importantly, a supramolecular acid⋯amide synthon formation between the -COOH group of the gelator and the -$CONH_2$ group of the drug-like molecule was exploited to drive their co-crystallization in a two-component system. Importantly, the co-crystal structure was demonstrated to survive in the gel state, where efficient Fmoc group packing was frustrated resulting in gel rheology weakening. Delayed release of the co-crystal former from the gel was demonstrated also when involving Vitamin B_3 as a biologically relevant co-crystal former.

Finally, the strategy to modify gelation properties of Fmoc-based LMWHs by interfering with the fibre packing of Fmoc groups was also demonstrated by using a halogen bond (XB)-donor hydrogelator, namely *N*-Fmoc-2,3,5,6-tetrafluoro-4-iodophenylalanine. Involvement of the XB-donor in interactions with solvents and salts resulted in weakening of the gel as a result of the perturbation of the Fmoc packing in the gel fibres, as demonstrated by solid-state X-ray structures.

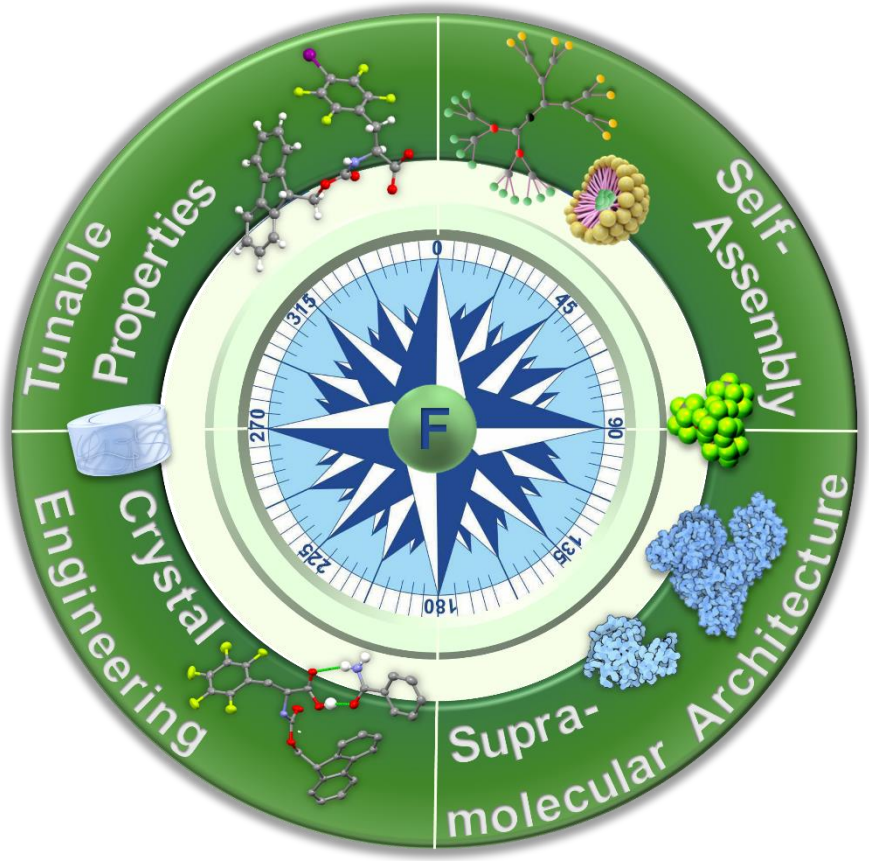

Chapter 1

Introduction

1.1 Properties of the fluorine atom and effect of fluorination on organic molecules

Fluorine is the most electronegative element of the periodic table, and the most reactive among the halogen atoms. Its configuration $1s^2 2s^2 sp^5$ describes two electrons in the first energetic level and seven in the second one: this incomplete configuration of the external shell makes the fluorine atom highly chemically reactive. Consequently, to reach electronic stability it binds other elements, hydrogen, carbon, oxygen and metals to name a few. In particular, fluorine atom is known for its capacity in binding carbon. In opposition to the high reactivity of fluorine, the C-F bond is extremely stable, making it fundamental in many fluorinated organic compounds. This remarkable stability is due to the interaction between the polarized $C^{\delta+}$ and $F^{\delta-}$ atoms, conferring a more electrostatic than covalent nature to this bond.[1]

Despite the larger size of fluorine (**Table 1.1**) and the partial charge inversion in comparison with hydrogen atom, the substitution of C-H with C-F (fluorine-scanning[2]) is considered isosteric. Isomerism is primarily defined by the similarity of the volumes and shapes of two isosteric molecules, but in medicinal chemistry this definition must be taken in its broadest sense. This is because isosteres are often much more alike in their biological than in their physical and chemical properties. Consequently, the relationship between shape and/or aspects of physicochemical properties of an isostere can be oblique.[3] Thus, huge changes in the physico-chemical properties of organic materials are observable after this substitution: *e.g.,* pKa of the nearby functional groups, solubility, hydro-/lipophilicity, reactivity and stability.[1]

Table 1.1*: Comparison between the chemical properties of hydrogen and fluorine atoms and their bonds with carbon.*[1]

Electronegativity (Pauling)	H (2.1)	F (4)
Van der Waals radii (Å)	H (1.2)	F (1.47)
Bond length (Å)	C–H (1.09)	C–F (1.35)
Bond dissociation energy (kcal/mol^{-1})	C–H (98.8)	C–F (105.4)

To name an example, 1,2-difluoroethane (**Figure 1.1**) displays the stereoelectronic consequences of the introduction of polarized C-F bonds. In fact, the conformational study of the rotational isomers of the molecule revealed that they were not in perfect equilibrium, but the *gauche*-form was preferred to the *anti*-form.[4] The so-called *gauche effect* is observed in presence of a fluorinated organic molecule containing vicinal electron-withdrawing groups (σ-bonds, nonbonding electron pairs, and π-systems), favouring discrete conformations (**Figure 1.1**).[5] Different halogen atoms do not bear the

same effect, because of steric reasons, advantaging the equilibrium towards the *anti*-conformation. The low steric demand in combination with the electronic arrangement and stability of the C-F bond are direct consequences of the unicity of the fluorine atom, opening a series of other observations and subsequently applications.[4,6]

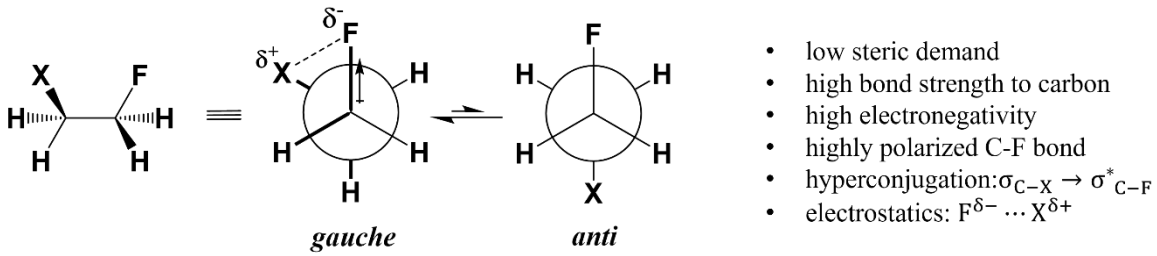

Figure 1.1 *The fluorine gauche effect. X = F (1,2-difluoroethane), OCOR, NHCOR, etc.*

This attitude was useful to pre-organise molecules, finding application in i) catalysis, conferring a predictable topology and avoiding undesired side products;[7,8] ii) pharmaceutics, to probe a specific active conformation;[9,10] iii) in peptides for folding regulation;[11] iv) synthesis of a new class of fluorinated alkanes (Teflon®).[12,13]

Thus, engineering materials containing fluorinated moieties found a wide range of applications, animating a multibillion dollar industry.[14] Oilfield industry took advantage of perfluorinated polyethers (PFPE) for their high chemical inertness, non-flammability and low interfacial energy for high-quality lubrification.[15,16] Fluorosurfactants originated a new class of cleaning agents since their accidental discovery in 1953[17] and for the same principle they were subsequently applied on textiles and papers.[14,18,19] Repellent surfaces derived from fluorosurfactants' ability in creating low-surface-energy coatings, and provided resistance to water, oils and stainings.[20] Consequently, they resulted in anti-icing, antifouling, antiadhesive, and corrosion-resistant surfaces.[14,21]

More generally, fluorinated substances are lipo- and hydro-phobic at the same time and show weak affinity for both polar and non-polar environments.[22] This behaviour is triggered by the so-called *fluorous effect*, which is the propensity to favour fluorine-fluorine interactions over those with other elements.[23]

Apart from the low wettability of fluorinated surfaces, fluorine scanning was shown to affect also boiling and melting points of a molecule. In many cases, they are higher in comparison with non-fluorinated compounds with similar molecular weight. This is due to the interactions between C-F units which provide additional stabilization. This behaviour makes these materials useful for the

development of thermal fluids resistant to high temperatures, but also to harsh conditions of pH and salinity.[15,24]

All these beneficial properties, which are typical of molecules bearing a high number of fluorine atoms, come with a main drawback represented by the fact that per- and polyfluoroalkyl substances (PFAS), especially those bearing more than six $-CF_2$ units, suffer from long-lasting persistence in the environment.[25] Thus, persistent organic pollutants are those that cannot be decomposed by natural physical agents in the environment (atmospheric conditions) or biological processes (microorganisms).[25]

The persistence in the environment is associated to the absorption of PFAS on mineral soil, which cause their detection also in fresh water and oceans, the easiest vehicle to cause bioaccumulation and toxicity.[25,26] Nowadays, this problematic has a huge impact on the environmental safety and urged researchers to find greener alternatives or make fluorinated compounds more degradable and better tolerated. This means paying attention in the design of new fluorinated molecules, reducing the number of $-CF_2$, introducing degradable functional groups and preferring branched systems against linear ones to promote metabolism.[27]

1.2 The role of fluorine in biomedicine and life sciences

Aside from the industrial aspects of PFAS, fluorine atom has important applications in life sciences. Fluorination has been used as a tool for fashioning pharmaceuticals and agrochemicals in the last 50 years.[28,29] Therefore, many interesting advantages regarding the ADME system (Administration, Distribution, Metabolism and Excretion) and drug discovery are associated:[29–33]

- enhanced oral and nervous system absorption because of the higher hydrophobicity;
- empowered selectivity of drugs for their pharmacological target and binding affinity, reducing off-target interactions and consequently lowering toxicity and dosage;
- delayed metabolic inactivation;
- bio-isosteric substitution of many other functional groups to alter metabolism and interaction with the target (**Figure 1.2a**);
- alteration of pK_a of vicinal functional groups
- production of crop-protecting agents for the agrochemical field (insecticides, fungicides and herbicides).

Nowadays, the batch of drugs containing at least one fluorine atom counts more than 300 pharmaceuticals with various effects and targets (**Figure 1.2b**), and it is not surprising that more than 50% of blockbusters pharmaceuticals approved by FDA are fluorinated.[34]
5-Fluorouracil for cancer treatment, fluoroquinolones (*i.e.,* Ciprofloxacin) as antibiotics, Celecoxib for inflammatory diseases, Ezetimibe and Atorvastatin for heart failure prevention are just few famous examples.[35] Close to these therapeutic purposes, there are also pharmaceuticals approved for imaging techniques, as better explained in the following section.

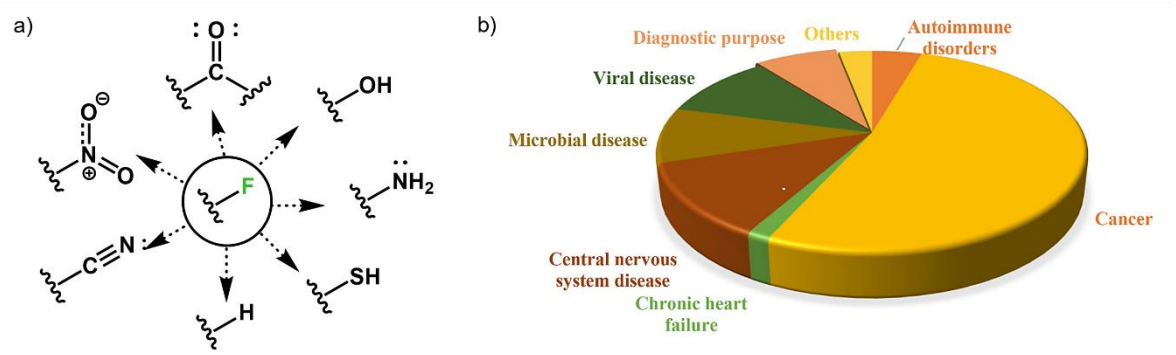

Figure 1.2 *a) Chemical functionalities which can be mimicked by fluorine atom.*[36] *b) Diseases targeted by FDA-approved fluorinated drugs between 2015 and 2022.*[35]

1.2.1 Fluorine-based biomedical imaging

In the scenario of personalized medicine, the development of effective imaging platforms for diagnosis and selectively guided therapies is nowadays a clinical demand.[37] Fluorinated materials can answer to this need thanks to ^{19}F-MRI (Magnetic Resonance Imaging) and ^{18}F-PET (Positron Emission Tomography), whose combination can provide accurate anatomical and metabolic information.

In the case of PET, ^{18}F results to be particularly advantageous because of i) its relatively long half-life (109.8 min), which admits the preparation and distribution to the hospitals, while other radionuclides have to be prepared on site.[38] ii) The high percentage of positrons emitted and iii) the low positron energy, admitting a high resolution imaging.[32] ^{18}F-labeled carbohydrates are currently used in PET imaging, and in particular 2-deoxy-2-[^{18}F]fluoro-D-glucose ([^{18}F]FDG) was the first approved and widely exploited in oncology.[32,38] In fact, a 3D-mapping of tumor tissues can be evaluated after administration of [^{18}F]FDG by following its pathway in the body. As all the carbohydrates, it follows the glucose metabolism *in vivo*. It is then uptaken by cells for energy production through glycolysis: the higher is the energy demand of the cell, the more is the uptake of

glucose. Cancer cells are high glucose-using cells because of their fast reproduction, so [^{18}F]FDG is massively uptaken and it can be traced by ^{18}F-PET returning a precise map of distribution in tissues.[38] After this first approval by FDA, the same approach was pursued with other radiolabelled-molecules, to explore other diseases and understand their molecular mechanisms.[38,39]

Concerning the former imaging technique, a strong research effort is focused on ^{19}F-MRI, coupled with ^{1}H-MRI. The ability of a nucleus to generate a magnetic resonance (MR) signal is mainly related to the presence of a non-zero magnetic moment associated to the nuclear spin.[40]
^{1}H nucleus resonance is already established in clinical anatomical imaging, but its main limitation is due to the high water content of the human body (>60%), which disturbs the signal with a strong background noise, affecting sensitivity and resolution.[41] For this reason, considering the high value of the technique, urged the necessity to develop contrast agents (CA) with the ability to increase sensitivity.[42,43] There are two ways to enhance imaging contrast: mitigate the signal produced by the molecules surrounding the objective tissue (water in most cases) is the first method. As a result, it is possible to distinguish in a clearer way the anatomical features of the subject. These CAs are named ^{1}H relaxation agents, and they are not MRI active. It is the case of Gd^{3+}-chelates, commonly used in clinics. Because gadolinium can bioaccumulate causing toxicity, new MRI techniques were developed, involving other magnetically active nuclei.[44,45] The development of heteronuclear imaging probes represents the second way to produce contrast, exploiting the generation of a second MRI signal.[43]

Table 1.2 *Properties of some elements capable of generating a MR signal.*[40]

nucleus	$\gamma/2\pi$ (MHz/T)	natural abundance (%)	relative sensitivity (constant number of nuclei)	shift parameter range (ppm)
^{1}H	42.576	99.98	1.0	13
^{3}He	−32.434	0.000134	0.442	
^{7}Li	16.546	92.41	0.294	
^{13}C	10.705	1.108	0.0159	250
^{14}N	3.0766	99.636	0.001	
^{15}N	−4.3156	0.364	0.001	
^{17}O	−5.7716	0.038	0.0291	
^{19}F	40.076	100	0.83	400
^{23}Na	11.262	100	0.0927	
^{31}P	17.235	100	0.066	530
^{129}Xe	−11.777	26.4	0.0216	200

Among the nuclei able to generate MR (**Table 1.2**), ^{19}F took particular interest for its remarkable characteristics:[46]

- 100% abundance of the stable isotope (nuclear spin ½)
- Wide range of chemical shift (>350ppm). Thus, even a tiny change in the microenvironment has a detectable effect in the chemical shift of the fluorine atoms, unlocking the possibility to make precision studies.
- High MR sensitivity (83% compared to ^{1}H) and high signal to noise ratio (SNR=89%), meaning high signal intensity.
- Gyromagnetic ratio very close to hydrogen (40.08 vs 42.58 MHz/T of ^{1}H, **Table 1.2**). This allows to perform ^{19}F-MRI with the same hardware used for ^{1}H, just with the addition of a coil suitable for ^{19}F.

^{19}F-MRI is indeed an emerging technique, powerful and non-invasive, and it can be combined with ^{1}H-MRI standard protocols.

Furthermore, the presence of endogenous ^{19}F atoms in the human body is strictly limited to bones and teeth (< 10^{-6}M), where they are immobilized in the solid phase preventing interferences in the MRI. Consequently, the lack of endogenous ^{19}F background admits the selective visualization of exogenous ^{19}F as "hot spots", over ^{1}H-MRI anatomical maps of the same subject (**Figure 1.3**).[41,46,47]

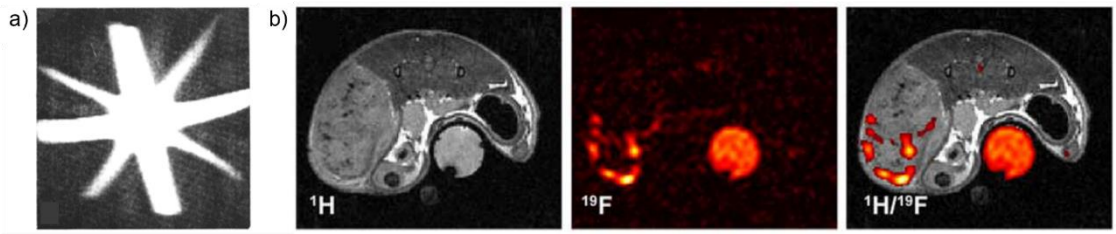

Figure 1.3 *a) Image of the first ^{19}F-MRI of perfluorotributylamine acquired from Holland and co-workers.*[48] *b) representative image of a modern ^{1}H and ^{19}F, and overlayed $^{1}H/^{19}F$ in vivo images of a mock-infected tumor-bearing mouse.*[49]

The principle behind MRI technique is the same of Nuclear Magnetic Resonance (NMR): the presence of a magnetic field causes the alignment of ^{19}F atoms. The application of a transverse radiofrequency (RF) pulse disturbs the nuclei from their equilibrium state, and their relaxation while returning to the ground state can be recorded (as changes in the magnetic field), and processed to generate the signal.[41] The term "relaxometry" is used to indicate the process of measuring the signal decay (relaxation) after excitation of the nuclei by RF pulses. The speed of signal decay is described by two main parameters: longitudinal or spin-lattice relaxation time (T_1) and transverse or spin-spin

relaxation time (T_2). Although occurring simultaneously, these two relaxation paths are mainly independent the one from the other. Deepening further, T_1 describes the energy dissipation of the nuclei to the surrounding molecular lattice. T_2 is not associated with a loss of energy, but is related to the loose of coherence in the oscillation of the nuclei after the RF pulse. The faster the coherence is lost, the faster the MR signal decays (short T_2).[43] A short T_1 can make MRI signal bright, improving SNR (between 10^2-10^3 msec[50]), while a short T_2 can blur the image (<10^2 msec[50]), also causing a signal quenching, like in the case of ^{19}F in bones and tooth aforementioned.[41]

1.2.1.1 Fluorinated Magnetic Resonance Imaging contrast agents

There are many types of CAs available in literature and the features which distinguish a good ^{19}F CA are:[46]

- High fluorine content. This can improve SNR, obtaining bright signals with low concentration of administration.
- Optimised synthesis, easy formulation, scalable and cost-effective on industrial level
- Chemical and biological stability over time in order to guarantee a long shelf life.
- Low biological toxicity
- Clear and simple ^{19}F-NMR spectrum: CAs with more than one signal are ambiguous, so the presence of one single sharp peak is preferred.
- Short T_1 and long T_2

^{19}F-MRI CAs can be classified in three main groups according to their chemical structure [41,46]: organic fluorides, metal-organic complexes, and inorganic fluorides. Just to name few examples for category, CaF_2 nanoparticles were synthesised by Ashur *et al.* as inorganic tracers: in this case, the main drawback is represented by the short T_2 typical of these nanoparticles. Consequently, specific ^{19}F-MRI sequences of magnetization for short T_2 had to be developed before using CaF_2 as CA.[51]

Later, metal-organic complexes were reported to be very interesting because of the combination of a paramagnetic metal ion, like Gd(III) or other lanthanide tracers, with a fluorinated molecule. The necessity of this combination was dictated by the poor relaxivity of the fluorinated ligand. The coordination of the metal ion gave place to the so-called paramagnetic relaxation enhancement (known as PRE effect), which was described in the pioneering work of Parker and co-workers to improve the relaxation properties of the fluorinated moiety, overcoming this issue.[52–54] The drawback associated with lanthanide-based CAs is the risk of unbound metal-ions in blood circulation, which can cause toxicity.

The class of organic fluorides constitutes a huge and varied source of CAs, and can be further divided in two subgroups[55]: i) perfluorocarbons (PFCs) stabilized and encapsulated in nanoemulsions, (*i.e.,* perfluoro-*n*-crown-*n*-ethers – PFCEs – and FDA-approved perfluorooctyl bromide – PFOB, **Figure 1.4**)[56,57] ii) partially fluorinated polymers. The latter ones derived generally from a copolymerization process between a fluorinated monomer and a hydrophilic part, which could be linear, (hyper)-branched or dendritic (one example is reported in **Figure 1.4**).[46,55]

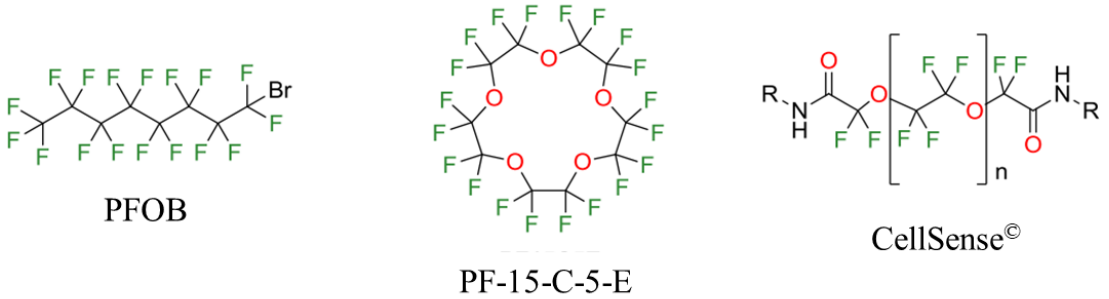

Figure 1.4 *Chemical structures of perfluorooctyl bromide (PFOB), perfluoro-15-crown-5-ether (PF-15-C-5-E – PFCE) and the perfluoropolyether portion of the commercial (PFPE – CellSense©).*[58]

FCs need to be formulated because their high fluorine content hampers their solubility in aqueous media, and consequently limits their administration. On the other hand, the high content of C-F bonds makes these materials biologically inert and non-toxic *in vivo*.[46] Their stability against enzymes and physiological pH requires a different clearance process from the body, exploiting in many cases the reticuloendothelial system and exhalation through lungs.[59]

1.2.1.2 PERFECTA

One of the main issues about the application in clinics of ^{19}F-MRI is related to sensitivity problems. Despite ^{19}F signal is detected like a *hot spot* when overlapped with ^{1}H imaging map, it is difficult to reach the proper amount of ^{19}F for the detection, and sometimes there is the need of long incubation times, affecting cell viability.[60,61] Increasing the number of ^{19}F atoms per molecule, although improving sensitivity, can cause the possibility to have not magnetically equivalent fluorine atoms, producing another drawback. This issue regards most of all linear PFCs, like PFOB (**Figure 1.4**), that generate more than one resonance frequency, and can induce chemical shift artefacts. On the other hand, PFCE (**Figure 1.4**) originates only one signal, but its high symmetry prevents the possibility to chemically alter its structure without losing the equivalence of fluorine atoms. Not less important is the absence of functional groups that could be hydrolysed by enzymes. This could be advantageous in terms of stability, but requires organ functions for clearance from the body. Researchers focused their attention on these molecules in order to overcome these cons. Among the possible alternatives,

they preferred branched molecules to linear ones, and introduced functional groups that could be processed by endogenous enzymes, instead of PFCs containing only C-F bonds. Starting from these studies, a new ^{19}F-MRI probe was synthesised, called PERFECTA (suPERFluorinatEd ContrasT Agent, **Figure 1.5**).[62]

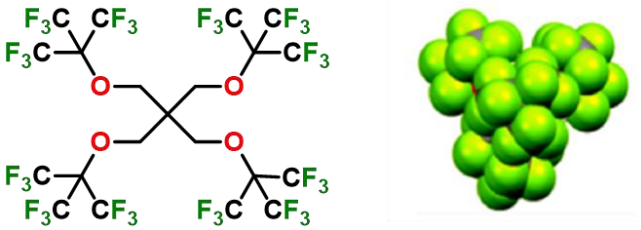

Figure 1.5 *Chemical structure of PERFECTA (left) and its single crystal X-ray structure (right).*[62]

PERFECTA bears all the good features required by a ^{19}F-MRI contrast agent. Its 36 equivalent fluorine atoms originate only one resonance frequency with a good SNR. The ^{19}F-NMR signal is a sharp singlet peak in the region of -73 ppm, making easy the interpretation, quantification and setting of a proper RF pulse for magnetic resonance. Moreover, both its relaxation times are suitable to guarantee a bright signal, and to be detected without the need of special pulse sequences. The one-step synthesis of PERFECTA has been optimized for gram-scale production. Starting from pentaerythritol and perfluoro-*tert*-butanol, through a Mitsunobu reaction, the compound is obtained as a crystalline colourless solid, in good yield (>50%).[62,63] Regarding biological stability and compatibility, the only partial fluorination degree of PERFECTA prevents its bioaccumulation. When administered *in vivo,* the presence of four ether bonds adds degradability to the molecule through enzymatic digestion.[64]

More recently, PERFECTA was also proved to be an interesting probe for Raman spectroscopy.[65] This non-invasive technique relies on the specific recognition of chemical bonds present in the analysed molecule. Even if Raman microscopy is widely used as label-free technique, the application of a specific probe can enhance the difference between healthy and pathological tissues, extending sensitivity and specificity.[66–68] Indeed, Raman probes enable the optical imaging of cells and subcellular units with nanometric precision, which are not detectable through other techniques, as MRI.[69] Among chemical groups which can originate a diagnostic vibrational signal there are triple bonds (*i.e.*, alkyne[67]) and C-F bond. Comparing PFCE, PFOB (Figure 1.4) and PERFECTA, the latter was demonstrated to be the most performant as bimodal agent, joining ^{19}F-MRI for *in vivo* full body/organs imaging and *ex vivo* Raman microscopy of tissues and cellular imaging.[65]

Despite all the promising features of PERFECTA, its X-ray crystal structure (**Figure 1.5**) clearly shows that the polar core constituted by ether bonds is completely shielded by the 36 fluorine atoms. This structure explains its insolubility in water and in most organic solvents, except for ethyl acetate and fluorinated solvents (*i.e.,* hexafluoroisopropanol). Consequently, many efforts were made in studying appropriate formulations for its administration in aqueous media. Until now, all the reported formulation strategies required amphiphilic polymers or surfactants for the stabilization of nanoemulsions, demonstrating that all the promising features of PERFECTA are effectively working for *in vivo* imaging.[62,65] Thus, it pushes the research towards further improvements.

1.2.2 Fluorine in proteins, peptides and amino acids

Among the interesting variety of fluorinated building blocks already mentioned, biomacromolecules play a central role in the related research context. Apart from nucleic acids,[70] carbohydrates,[71] and lipids,[72] several research efforts are focused on proteins, peptides and amino acids. In particular, fluorinated amino acids (FAAs) are emerging as fundamental ingredients in fashioning materials for biomedical applications. Because of their chemical versatility and bio-reactivity, they attracted particular interest, and their consequent incorporation in peptides and proteins endowed the production of novel biopolymers employed as biosensors, molecular probes, and enzyme inhibitors.[73–76] The key role of fluorine is basically related to its ability to induce conformational changes in molecules. In addition, the inextricable correlation between the conformation of amino acids, peptides and proteins and their function makes this approach particularly relevant. Moreover, this conformation control starts from the single amino acid, and passes through the secondary structure of peptides, reaching the tertiary and quaternary structure of proteins.[77] This long-range intermolecular interaction is potentiated by fluorine-fluorine interactions, and it is the direct result of the incorporation of electron-withdrawing fluorinated substituents (**Figure 1.6**).[78]

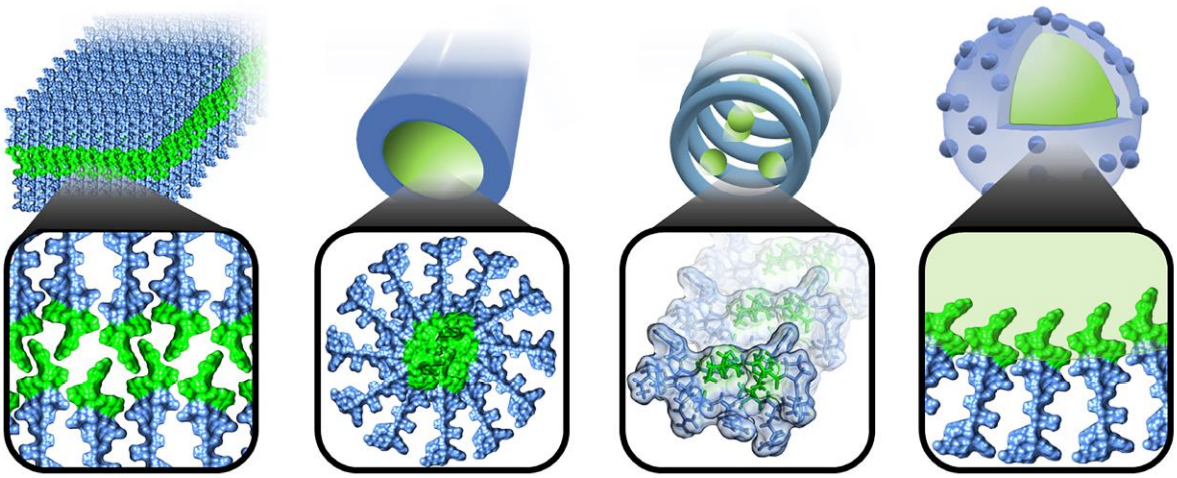

Figure 1.6 *Representative examples of different supramolecular morphologies driven by incorporation of fluorinated amino acids (green spots) within peptides structures (blue features). From the left ribbons, cylindrical nanofibers, coiled coils and nanoparticles are reported.*[79]

Life sciences take inspiration from these templates, their folding and unfolding processes mainly due to their involvement in pathologies, *i.e.* Alzheimer's disease.[80] Furthermore, the biomedical field finds in these substrates a source for new-generation pharmaceuticals.[77] Indeed, some FAAs and fluorinated peptide-based drugs reached the clinics, with approval from FDA (*i.e.* Sitagliptin for diabetic disease, Eflornithine as antiprotozoal drug used in case of sleeping sickness, and Fluciclovine as diagnostic agent for ^{18}F-PET).[81]

Although the impact of fluorination is somehow predictable and well-known when talking about small molecules, a robust understanding of how it contributes to the structural integrity of peptides and proteins remains still missing. These are the reasons why many efforts are spent nowadays to understand the role and the effect of amino acids' fluorination, trying to find rational rules. The discovery of discrete trends could unlock the possibility to tune specific conformations and properties.

Koksch and co-workers systematically described the consequences of fluorine introduction into the majority of amino acids, finding some common aspects: i) despite fluorine is described as hydrophobic, the introduction of a small number of fluorine atoms brings a polar character into hydrophobic amino acids. ii) Fluorination severely changes the secondary structure of aliphatic amino acids, and of the subsequently derived peptides and proteins. iii) The presence of fluorine can improve proteolytic stability. iv) The final outcome depends on the kind of fluorinated side chain, but at the same extent it relies on its interactions with the surrounding environment.[77,78]

Recently, because of the increasing multiple choice of applications in life science and the lack of fluorination predictability, many synthetic strategies were fine tuned to obtain a huge library of

FAAs.[81–84] Moreover, there are two main approaches to incorporate fluorine atoms into peptide and proteins: (i) top-down, which involve post-modification of the final peptidic/proteic product; (ii) bottom-up, where FAAs are directly introduced in the sequence. Both of them can be supported by chemistry (solid phase peptide synthesis and fluorinating agents) and biology (incorporation of non-canonical amino acids during transcription and post-transcriptional enzymatic modification).[36] Despite top-down strategies tend to be more efficient and economic, they are also more complicated to perform and required very specific conditions in comparison with bottom-up ones.[36]

As already mentioned in **Section 1.2**, fluorinated compounds, in particular amino acids and peptides are advantageous for pharmacokinetic and physicochemical properties: absorption and distribution are enhanced by the general higher hydrophobicity which improves the membrane permeability. A highlighting example is offered by anticancer drug Mephalan (**Figure 1.7**). It represents a nitrogen mustard, used in chemotherapy as alkylating agent; it is administered as peptide-conjugate prodrug, with the incorporation of a 4-fluoro-phenylalanine. The presence of the fluorine atom enhances the membrane permeability imparting higher efficiency.[77,85,86]

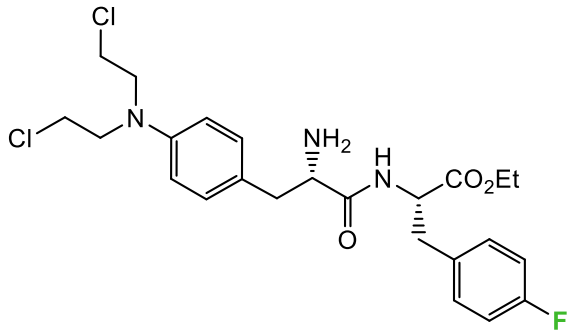

Figure 1.7 *Chemical structure of Melphalan flufenamide (Pepaxto®), FDA approved drug against multiple myeloma.*

The introduction of FAAs into peptide sequences can also reduce *in vivo* metabolism thanks to the escape from circular proteases. The mechanism is quite unspecific, but mainly related to the steric demand of fluorine atoms. The presence of a proper number of fluorine can cause incompatibility with the binding pocket of the proteolytic enzyme, advantaging bioavailability of the molecule.[87,88]

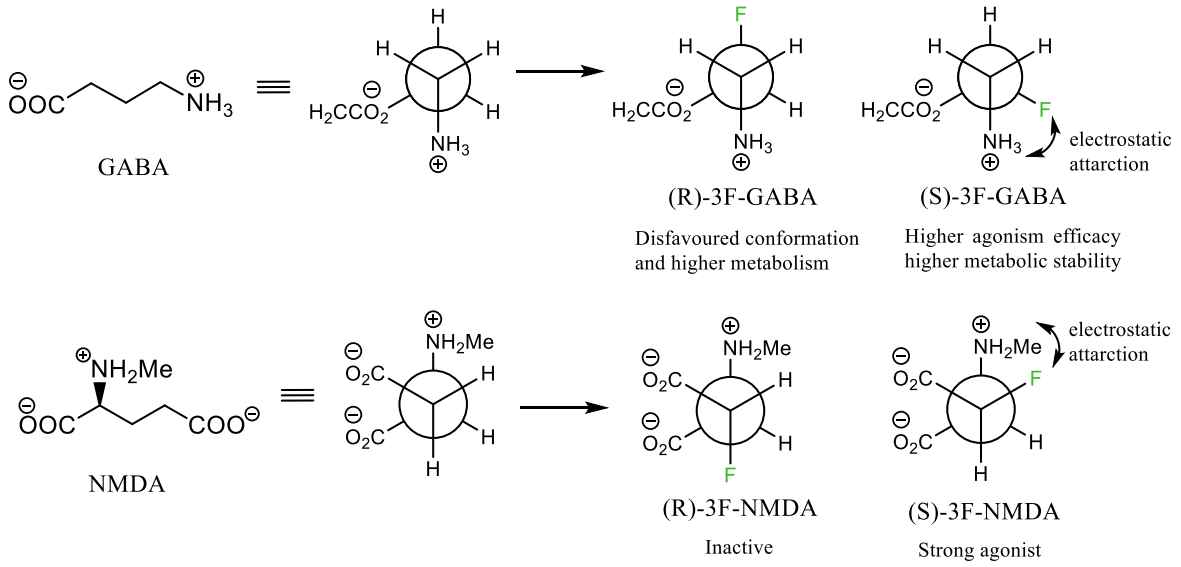

Figure 1.8 *Chemical representation of the conformational control originated by fluorination with the respective biological activities obtained.*

Indeed, amino acid and peptide design can pursue increased affinity for the target binding, reinforcing specific protein-protein interactions, advantaging both efficacy and selectivity.[36,77] Aiming to give a practical example of the *gauche effect* described in **Section 1.1**, O'Hagan and co-workers demonstrated that the fluorination of *N*-methyl-D-aspartate (NMDA) and γ-aminobutyric acid (GABA) originates isomers with very different agonism activity toward NMDA and GABA receptors respectively. These receptors are involved in many nervous system disorders and their modulation is extremely useful to treat these pathologies. Such modulation occurs thanks to the possibility to interact with the receptors through specific lead compounds, whose discovery becomes particularly relevant. O'Hagan's group proved that there is only one conformation which leads to agonism, while the other defines dramatic changes (**Figure 1.8**).[89,90]

The molecular pre-organization offered by fluorine atom can also reduce the entropic cost needed for the interaction with specific targets, obtaining higher binding affinity. This situation can be found not only for single FAAs, but also in peptides containing FAAs in the modulation of the secondary structure.[77] Further details about the conformational contribution of fluorine atoms to supramolecular assemblies will be examined in **Section 1.3**.

Furthermore, efficacy can be enhanced by fluorination also for the different non-covalent interactions towards the biological target. **Figure 1.9** reports some examples: a CF_3 moiety can stabilize the interaction by hydrophobic bonds.

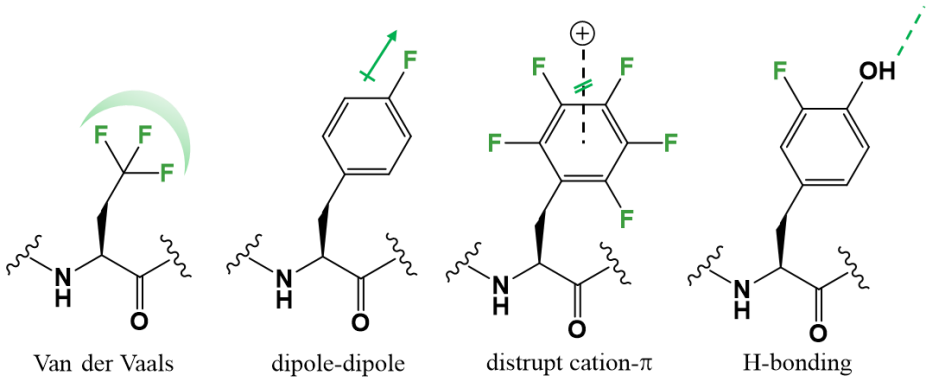

Figure 1.9 *Amino acid side chain fluorination and their contribute to binding interactions with the target.*

Phenylalanine, with the presence of only one fluorine atom, can define a dipole interaction as already mentioned by Koksch et al.[78,91]. On the other side, the perfluorination of the phenyl ring leads to a quadrupolar inversion of the aromatic, as a consequence, if the natural amino acid would instore a cation-π interaction, the fluorine scanning disrupts the latter, obtaining a different outcome in the binding affinity[92]. Then, fluorine has a contribution to the pK_a of the nearby chemical functionalities, improving their hydrogen bonding character.[77,93]

Near to pharmacokinetic influence, FAAs can also improve antimicrobial activity if they are included in antimicrobial peptides (AMPs), a new class of therapeutics for bacterial infections.[88,94,95] Moreover, fluorination of low molecular weight hydrogelators (LMWHs) exert an important role among biomedicine: small peptides and amino acids can originate hydrogels by their particular self-assembly when suspended in water. In particular, Nilsson *et al*. widely described hydrogels obtained by pentafluoro-phenylalanine, as scaffolds for mimic extracellular matrix and drug delivery of anti-inflammatory agents.[96–99] The same amino acid was incorporated in a dental resin by Schnaider and co-workers to prevent bacterial growth.[100] Yuran *et al.* synthesised anti-fouling fluoropeptides, containing two 4F-phenylalanine for implant coatings. These innovative materials can avoid bacterial biofilm deposition and integrate into the local tissue, preventing the implant rejection and support cell adhesion.[101]

In conclusion, the presence of fluorine atoms can be useful as a "*spy*" in ^{19}F-NMR/MRI and ^{18}F-PET. In this case, the FAA can act as a label for deciphering the destiny of the peptide agent after administration. Binding events can be monitored and studied by NMR, as well as conformational

changes in proteins. ^{19}F-MRI can be also pursued with properly fluorinated peptides, as Stupp *et al.* reported,[73] and also ^{18}F-modified tyrosine represents one of the study objects as radiotracer for brain imaging.[102]

FAAs offer a world of possibilities, and the potency of the approach can be further implemented for interesting new research lines in the biomedical field.

1.2.2.1 Interactions between proteins and fluorinated materials

Despite fluorination of proteins is highly widespread and studied in the scientific community, less information is available about the interactions between native proteins and fluorinated molecules. The bioaccumulation mechanism of perfluorocarbons highlights the importance of this topic. Indeed, the toxicity of perfluorooctanoic acid (PFOA), one of the most popular water contaminants, derive mainly by its interaction in the human body with human serum albumin (HSA). In fact, despite its hydrophobicity, PFOA does not accumulate in fatty tissues, but in those organs with a high protein content, like liver, kidneys and brain.[103,104] The presence of more than 6 binding sites makes the binding affinity of HSA for PFOA very high. Wei and co-workers recently published a proof of concept about the disruption of this interaction by competition with cyclodextrins, in order to study the protein interaction, still quite unknown, and a mechanism of detoxification from this perfluorocarbon.[103] Thus, this example defines the possibility to consider proteins as carriers of fluorinated molecules, ennobling the usage of their binding sites for biomedical purposes, as long as protein-based therapeutics gained increasing attention because of their high biological activity and specificity. Deepening, two major mechanisms are known for proteins' interactions with hydrophobic guests: host-guest mechanism and protein corona formation.[105]

In the first case, proteins are perfectly suitable for the Trojan horse approach. In fact, (i) they can recognise different materials as guests, distinguishing one another depending on the amino acids that compose the available cavity/-ies. (ii) The recognition process is based on complementarity; (iii) the 3D structure of the protein favour the pre-organization needed to lower the entropic cost for the guest binding.[106] Indeed, there are many interactions possible between hydrophobic guests and the amino acidic binding pockets: Van der Waals forces are the most frequent, followed by hydrogen bonding and electrostatic interactions.[105] Despite the big chance offered by proteins, there is poor literature about highly fluorinated organic molecules encapsulated in proteins. On the other side, many other hydrophobic molecules encourage the possibility to follow this approach proving its efficacy. It is the case of fullerenes, carboranes and gold nanoclusters complexes, used to originate theranostic tools.[105]

More information is available about the interaction between fluorosurfactants and proteins. In particular, it was demonstrated that in comparison with hydrogenated surfactants, fluorinated ones interact stronger with proteins, and the length of the hydrophobic chain has an outcome in altering the protein structure. The challenge of understanding the nature of these interactions was faced investigating many proteins, i.e., bovine serum albumin (BSA), lysozyme (LYS, **Figure 1.10**), β-lactoglobulin and ubiquitin.[107–109] Recently, Scanavachi *et al*. explored the interaction between BSA and sodium perfluorooctanoate (SPFO), finding an increased aggregation propensity of this protein in the presence of this fluoro-surfactant. Moreover, the comparison with sodium dodecyl sulphate (SDS) revealed that the aggregation process can be also modulate by changing the geometry and the stiffness of the ligand/guest. This study highlighted another important biomedical application, since the comprehension of fluorosurfactant-protein interactions can be useful to understand the early stages of protein-aggregation-based diseases (Alzheimer, Parkinson, Huntington, bovine spongiform encephalopathy, dementia with Lewy bodies, among others).[110] Nevertheless, there is still no sound of complete understanding of the interactions between fluorinated surfactants and proteins.

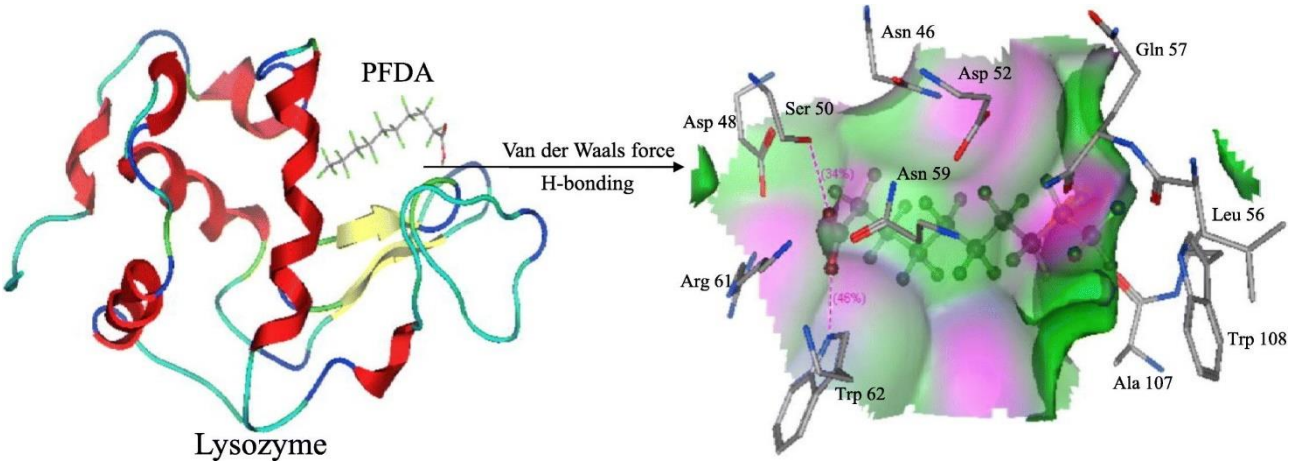

Figure 1.10 *Docking profiles of perfluorodecanoic acid (PFDA) and lysozyme.*[108]

The latter mechanism of interactions between proteins and fluorinated agents is less specific and leads to the formation of a protein coating, which could be exploited for imaging purposes. In this case, proteins act as surfactants, which help to maintain in solution fluorinated liquids, otherwise insoluble in water. Optison® is an FDA approved contrast agent for echocardiography, and consists of a colloidal suspension of octafluoropropane microdroplets coated by BSA.[27] Similarly, another example of surfactant proteins is represented by hydrophobins (HFB), a class of small fungal amphiphilic proteins. Among them, HFBII – produced by *Trichoderma reseei* – is characterized by a remarkable surface activity. Its ability to organize in monolayers at interfaces was exploited to

formulate in water gaseous perfluorohexane microbubbles, as well as solid fluorinated nanoparticles for ^{19}F-MRI.[111,112] It is evident that protein-fluorine interactions constitute a huge resource for biomedicine and the lack of their full understanding boosts further studies in the field.

1.3 Fluorinated supramolecular architectures: from vesicles to fibers

The presence of C-F bonds has an influence on the chemical properties, as described in previous sections, and it plays a special role also in directing the supramolecular assemblies of molecules. Proteins, peptides and amino acids are strongly perturbed by the presence of fluorine atoms, and it was already mentioned that their conformation is intimately connected with their function. Interpreting the concept with another view, modifying their 3D architecture opens the possibility to tune specific properties. Indeed, the study of such interesting 3D structures and how to manipulate them has a high research value, and this is why the scientific community focuses wide attention on this topic. The term self-assembly refers to the ability of discrete molecules under thermodynamic equilibrium to spontaneously aggregate, generating hierarchical and well-defined structures, by virtue of the noncovalent interactions occurring among single units.[113] The interactions involved are typically hydrogen bonding, ionic bonds, and Van der Waals interactions. Despite each single force is considered *weak*, the collective interactions can originate structures of high stability. Complementarity, compatibility, size and correct orientation are key elements to boost the self-assembly.[113] Indeed, self-assembly is considered a "*bottom-up*" approach, meaning an autonomous organization of molecular components build up into more complex and structurally well-defined nanoaggregates. On the contrary, it differs from "*top-down"* approach, which corresponds to the usage of nanofabrication tools, to create nanoscaled structures with the desired shapes and features, starting from larger dimensions and reducing them to the required values.[114] In this case, the objective is reached through the control of external parameters, while in case of *bottom-up* the process is mainly spontaneous.[114] Indeed, the latter has many benefits: it is cost-effective, versatile, easy to perform and it is highly selective and specific, avoiding defects (less energetically stable) and therefore guarantees high degree of perfection.[115] It is evident that the fluorine scanning can alter completely this balance, resulting in a powerful tool to change the direction of the self-assembly. Amphiphiles, lipids, polymers, surfactants etc. has been central for colloidal and material scientists and continue to be attractive for their wide field of applications: pharmaceutical, food and cosmetic formulations,

catalysis and controlled synthesis of nanostructured materials.[116] In particular, I will focus on the outcome regarding two different materials: amphiphiles and amino acids.

1.3.1 Amphiphiles and their supramolecular assemblies

Amphiphiles are molecules bearing two distinct portions: a hydrophilic and polar head, covalently bound to a lipophilic nonpolar tail. The polar head can be neutral or ionic (cationic, anionic or zwitterionic), while the hydrophobic tail is generally constituted by a hydrocarbon or fluorocarbon chain. The opposite nature of these two functions defines an intrinsic reciprocal incompatibility, and causes a special organization into ordered nanostructures, when suspended in particular solvents (mainly water) or at the solvent-air interface.[117] Thus, aggregation occurs in the presence of a medium, and it is contemporarily driven and limited by solubility: the different solvophilicity of the two components makes the entire molecule more comfortable in a situation where each part is located in an appropriate environment, driving discrete orientations. This means that self-assembly is the outcome of the amphiphile's attempt to reduce the enthalpic and entropic costs of its dispersion in the medium, considering the contribute of all the noncovalent interactions involved (solvent-solute, solvent-solvent and solute-solute).[118,119] The soft nature of these interactions makes possible to manipulate the amphiphile's aggregation by modifying temperature, pH (if the media is aqueous), ionic strength and nature of the electrolytes, polarity of the solvent, presence of other organic molecules in the media and concentration.[120,121]

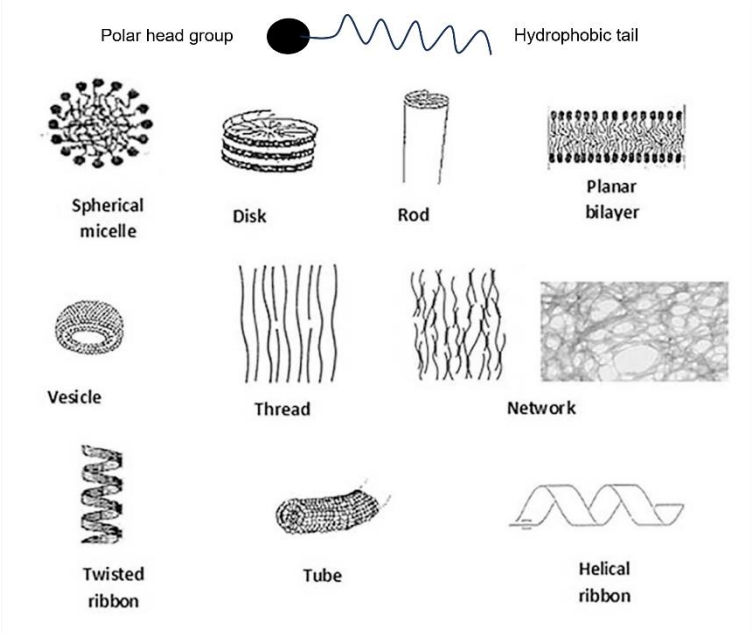

Figure 1.11 *Basic amphiphile structure on the top, then, examples of self-assembly shapes adopted by amphiphiles in water.*[118]

The high interest gained by amphiphiles is due to their solubility in water, generating superstructures which maintain a hydrophobic core. Thus, many of the architectures observable are referred to aqueous media, and consequently acquire importance for the biological environment. (**Figure 1.11**).[118]

The most familiar aggregate in water is micelle, consisting in a hydrophobic core, shielded from water by a surrounding corona formed by the hydrophilic heads of the amphiphile itself. Interestingly, amphiphiles can organise in micelles only above a discrete concentration, called critical micelle concentration (CMC). The self-assembly induced by exceeding this threshold causes dramatic changes in the physico-chemical properties of the resulting suspension (**Figure 1.12**).[116] It is quite evident that those parameters which were already mentioned to tune the amphiphile's aggregation are the same that influence also the CMC.

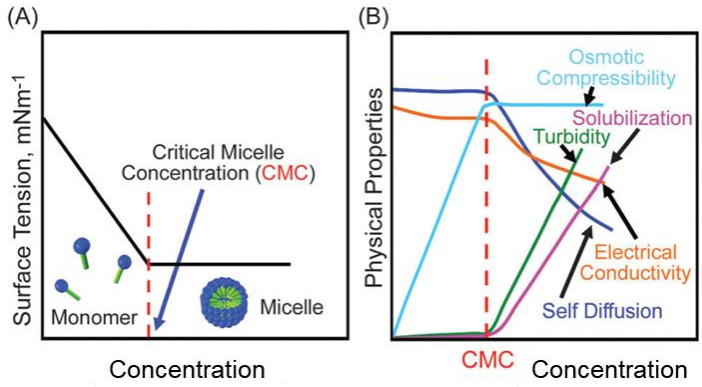

Figure 1.12 *Changes in physical properties at critical micelle concentration (CMC): (A)surface tension; (B) various other parameters.*[116]

Apart from micelles, amphiphiles are reported to aggregate in various supramolecular shapes, e.g., membranes, films, vesicles, tubules etc. (**Figure 1.11**).[118] The resulting aggregate types depend on the different size and shape of both the hydrophilic head and the lipophilic tail. There are two important parameters which allow to predict the morphology of the nanoarchitectures and their behaviour after suspension:

1. The molecular packing parameter (CPP) was introduced for the first time by Israelachvili, Mitchell, and Ninham in 1976. According to geometrical considerations about the amphiphile, there is a correlation between the value of the CPP parameter and the shape of the aggregate (**Figure 1.13a**).[122]
2. The so-called hydrophilic-lipophilic balance (HLB), defined for the first time by the pioneer work of William C. Griffin in 1949.[123,124] It correlates the size and the strength of the two

opposite groups of the amphiphile with the behaviour of the amphiphile dissolved. It admits to predict if it would work as emulsifier, wetting agent or other type of agents (**Figure 1.13b**).[123,124]

a)

Critical Packing Parameter ($v/a_0 l_c$)	Critical Packing Shape	Structures Formed
<1/3	Cone	Spherical micelles
1/3 – 1/2	Truncated cone	Cylindrical micelles
1/2 - 1	Truncated cone	Flexible bilayers, vesicles
~1	Cylinder	Planar bilayers
>1	Inverted Truncated cone or wedge	Inverted micelles

b)

Surfactant solubility / Behaviour in water	HLB number		Application
No dispersibility in water	0, 2		–
Poor dispersibility	4, 6		W/O emulsifier
Milky dispersion, unstable	8		Wetting agent
Milky dispersion, stable	10		Wetting agent
Translucent-to-clear-solution	12, 14	Detergent	O/W emulsifier
Clear solution	16, 18	Solubilizer	O/W emulsifier

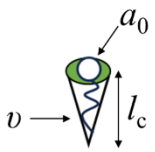

$$CPP = \frac{v}{a_0 \cdot l_c}$$

$$HLB = 20 \times \frac{MW_h}{MW_{tot}}$$

Figure 1.13 *a) Molecular shapes and critical packing parameter (CPP) of surfactants and the structures formed (here, v=volume of hydrophobic tail, a_0=effective head group area, l_c=hydrophobic tail length).*[125] *b) The hydrophobic-lipophilic balance (HLB) scale (MW_h=molecular weight of the hydrophilic head and MW_{tot}=total molecular weight of the amphiphile).*[126]

Another supramolecular morphology which gained the attention of researchers is constituted by vesicles. The reason is due to the natural involvement of vesicles in daily cell communication and biological processes, for instance membrane fusion, such as in fertilization process, synapses release, intercellular traffic, viral infection *etc.*.[127] Consequently, they result to be crucial for understanding biological processes, and for their mimicking for therapeutic necessities (drug delivery, pharmaceutical formulations) and more (cosmetic, material architectonic).[116] From a supramolecular point of view, vesicles originate when CPP value is between 0.5 and 1, thus, when the head group surface area (a_0) is similar to the hydrophobic tail cross section (influencing the parameters v and l_c,

Figure 1.13a), coming up with 10-100 nm nanoparticles. When this situation occurs, micelles are disfavoured, making way for the formation of bilayers with a curvature smaller than in micelles. Furthermore, the number of bilayers defines a form of classification of vesicles, that can be unilamellar, but can also originate more complicated multilamellar architectures (**Figure 1.14**).[116]

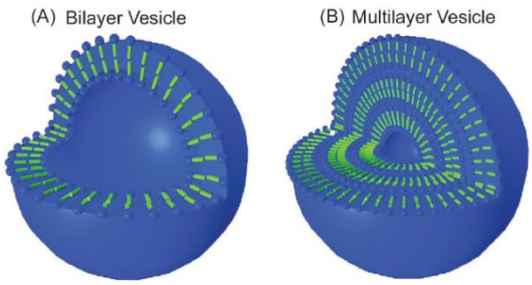

Figure 1.14 *Bilayer vesicles originating a classic unilamellar system (A) and a multilamellar one (B).*[116]

Typically, the bilayer pattern is obtained thanks to the interactions between kindred parts of the amphiphile, involving polar interactions between heads (exposed to the aqueous solvent), and two monolayers of tails facing each other, stabilized by dispersion forces. Besides these interactions, vesicles are thermodynamically considered as non-equilibrium systems, but they are kinetically stable for quite a long period (over 1 year in some cases), confirming their applicability in pharmaceutical/cosmetic formulations.[116]

The huge number of possible amphiphilic structures, their correlated nano-architectures and applications remark a strong interest in the continuous development of bigger amphiphiles, which nowadays can be classified into 4 different classes of macromolecules:[128]

I. Linear amphiphiles, mainly constituted by polymers, with generally two end-groups and organising basically in random shapes.
II. Cross-liked macromolecules, which are constituted by an insoluble network which swells in water due to penetration of the solvent. They can exhibit rubber-like elasticity, with susceptibility to diffusion and semi-permeability.
III. Branched macromolecules, which differentiated from classical linear polymers by possessing more than two end-groups per molecule. They generally occupy a smaller volume, causing a lower viscosity increase after suspension in the medium, compared to linear macromolecules of similar molecular weight.
IV. Dendrons and dendrimers, better described in the following section.

1.3.1.1 Dendrimers and dendritic architectures

Dendrimers are classified as polymeric structures with many branching monomers originating from a central core. Each dendrimer is made up of branched subunits known as dendrons. Thus, in all dendrons, three main regions can be recognized: the core, the branches and the peripherical end groups. The number of branches identify the number of generation of the dendrimer (G_1, G_2,.. G_n).[129]

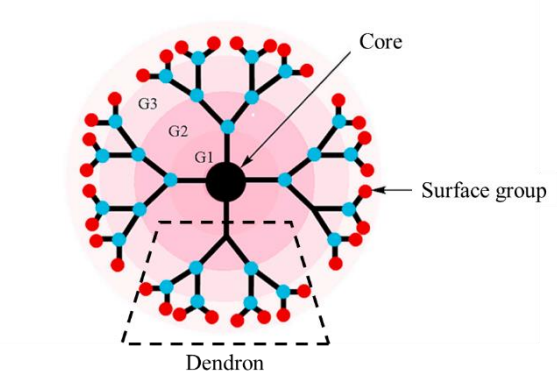

Figure 1.15 *Anatomy of a dendrimer.*[130]

Dendrimers can be synthesised following two different routes: convergent or divergent synthesis. The latter indicates the exponential growth of the dendrimer from the core from one generation to the next, while in the convergent approach dendrons are synthesised separately, and then attached to the central core in the final step. Synthesis of dendrimers is in any case stepwise, close to solid-phase peptide synthesis and oligonucleotide one. Differently from polymerization, which follows a chain growth mechanism originating statistical and polydisperse products, the advantage of a stepwise synthesis is the theoretical obtainment of a monodisperse product, which is highly desirable for experimental reproducibility and applicability. Monodisperse dendrimeric products are normally quite easy to be obtained up to G_3.[129]

The most exploited feature of dendrimers is probably their multivalency, due to the fact that the generation growth comes with the increase of the amount of end groups. Consequently, if the end group bears the functional activity of the dendrimer, such activity is sharpened. In addition, water solubility can be improved by the rising number of hydrophilic end groups, whereas hydrophobic peripheral moieties can make a dendrimer with hydrophilic core soluble in oils.[129]

Nowadays, the dendrimer field is in continue expansion and, in particular, for biological applications there is a big variety of examples reported, based on polyamidoamines (PAMAM, commercially available), polyamines, polyamides (polypeptides), poly(aryl ethers), polyesters, Percec-type dendrimers. All these macromolecules, with all their different functionalities, can be designed in

different ways, and may originate very diverse architectures such as hyperbranched structures, linear-branched polymers combinations and others (**Figure 1.16**).[129,131] Moreover, they can cover a wide range of biological necessities, spanning from drug delivery (with various administration ways *i.e.* ocular, oral, intravenous, intranasal, pulmonary, transdermal and across central nervous system), gene delivery, bioimaging (magnetic resonance imaging, O_2 sensing), drug/vaccine (prion-clearing agents, multivalent binding inhibitors), scaffold for tissue engineering.[129,130]

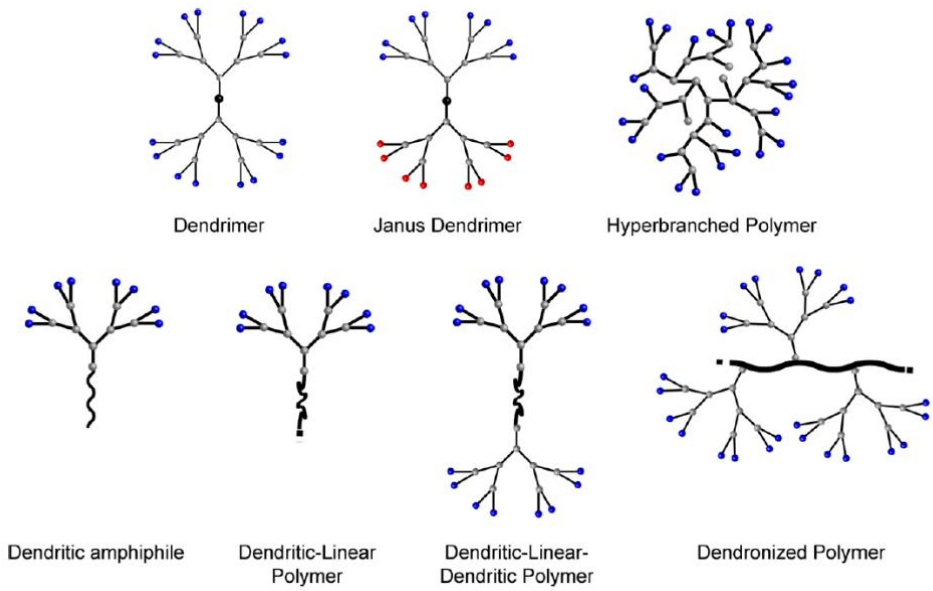

Figure 1.16 *Schematic representation of different dendritic architectures.*[132]

The strength of dendritic systems is their general high biocompatibility, including a proper elimination from biological organisms that avoids accumulation and toxicity against living cells and tissues. In fact, dendrimers of low molecular weight, generally below 30-40 kDa, are eliminated through renal filtration, whereas bigger substrates are designed to contain hydrolysable moieties, in order to be degraded. The low toxicity regards neutral or anionic dendrimers, while cationic ones, such as PAMAM, generally display a toxicity concentration-dependant and hemolysis.[129] In other cases, pharmacokinetics can be tuned controlling dendrimer size and conformation.

To name a practical example of the dendrimer power, recently, Filippi and co-workers proposed a new Janus dendrimer for bioimaging purposes. Janus dendrimers (JDs), schematically displayed in **Figure 1.16**, derived this name from their double-faced nature. In particular, JDs have two opposite peripheries, one hydrophilic and one hydrophobic, similarly to the bifunctional character of phospholipids. This dual nature facilitates the self-assembly in water in supramolecular aggregates of different morphologies, including nanosized bilayers vesicles called dendrimersomes, describer for

the first time by Percec *et al.* in 2010.[133] In particular, Filippi's group synthesised a JD, called JDG0G1(3,5), which bears a G_0 generation on the hydrophobic periphery and a G1 derivative of Bis-MPA (2,2-Bis(hydroxymethyl)propionic acid), ending with four -OH hydrophilic groups, linked together by an ethylene glycol residue (**Figure 1.17a**). The hydrophilic periphery makes it soluble in water environment, while the hydrophobic portion drives the self-assembly in nanosized dendrimersomes, as shown in the cryo-TEM image of **Figure 1.17b**. The presence of this bilayer vesicles delimitates an aqueous core which was exploited for the loading of the clinically approved MRI Gd-based contrast agent Gadoteridol (**Figure 1.17a**).[134,135]

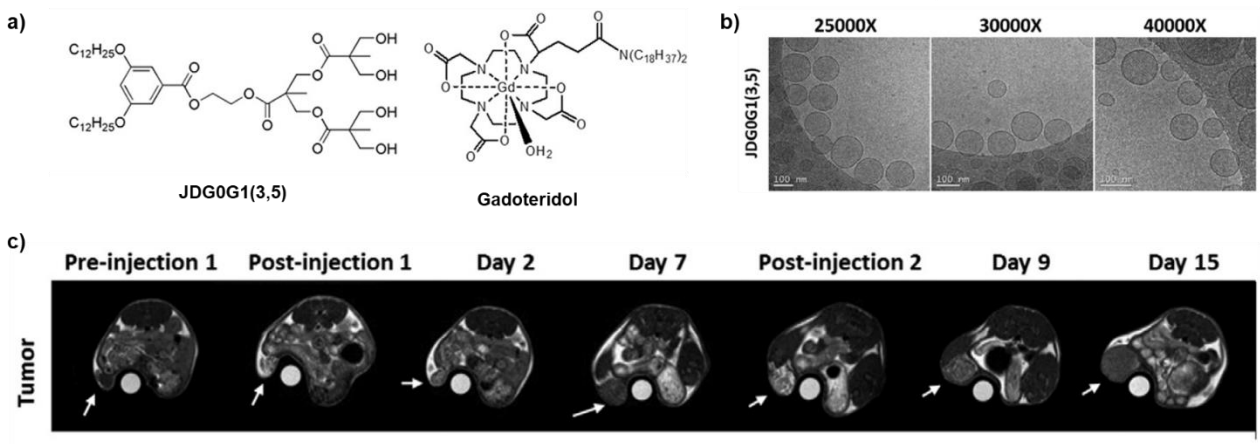

Figure 1.17 *a) Chemical structures of JDG0G1(3,5) and the MRI contrast agent Gadoteridol. b) Cryo-TEM images of vesicles originated from JDG0G1(3,5) formulation in water. c) Representative MR images. Representative axial T_1w-images showing the evolution of T_1 contrast over 15 days of MRI monitoring on murine melanoma model.*

This formulation resulted to be highly biocompatible among three different cell lines (fibroblasts and two populations of murine macrophages) with optimum results in cell viability and proliferation. Indeed, the proof of the goodness of this new candidate for MRI was given by *in vivo* tests performed on a melanoma murine model.[134,135] The authors then used a theranostic approach, implementing also an antitumor drug in the aqueous core of the vesicles, in order to have a real time imaging (**Figure 1.17c**), coupled with cancer treatment. These results are in line with those obtained with already known liposomes for similar applications, but the great potential of these dendrimersomes is highlighted by their easier synthesis and lower costs of production.[134,135]

1.3.1.2 Fluorinated dendrimers

With the assessment of the powerful world of dendrimers, and obviously the well described potential of fluorine scanning, it is of special interest to explore the consequences of dendrimer fluorination. It

is clear that any little change in the amphiphile' structure may lead to dramatic consequences in the nano-architectonics derived. Decorating dendrimers and amphiphiles with fluorine moieties affects considerably the HLB, CPP and CMC and this may cause changes in their assembly, and applications as well. By virtue of the higher size of fluorine atoms in comparison with hydrogens, perfluoroalkyl chains result to be bulkier and stiffer than their hydrogenated counterparts. This affects the conformational freedom, and it is followed by a more rigid, but ordered packing into more stable aggregates.[117,136] Indeed, fluorinated dendrimers have a considerably higher surface activity, compared to hydrogenated analogues, and their CMC is commonly two order of magnitude lower than hydrogenated surfactants of similar length. Then, CPP and HLB are significantly altered because of the different size and weight of fluorine atoms, causing a decrease of both values.[14,136]

Thanks to this high tendency to aggregate and sometimes very pronounced micro-segregation, a low concentration is needed to obtain equal performances to those obtained from non-fluorinated amphiphiles. This favours the efficacy/toxicity ratio, and reduces also the costs of production.[136] In summary, the properties of fluorinated dendrimers can be different from those of the analogous hydrogenated counterparts, and in particular they are deeply connected to the fluorophobic effect which drives the self-assembly.

Fluorinated dendrimers are widely exploited in many areas, including chemistry (catalysis and molecules' extraction from water), development of novel materials with improved mechanical properties, biology (drug delivery and gene vectors), in addition to the already mentioned ^{19}F-MRI technique.[136–143]

Most fluorinated dendrimers contain fluorinated end groups, but this is not the only way. There are mainly four synthetic approaches, as presented in **Figure 1.18**. Fluorine can be grafted to the surface of the dendrimers (case A), or to the surface of the dendron (B); it can be covalently bound to the core of the dendrons (C), or even throughout the structure of the dendrimer (case D). [140]

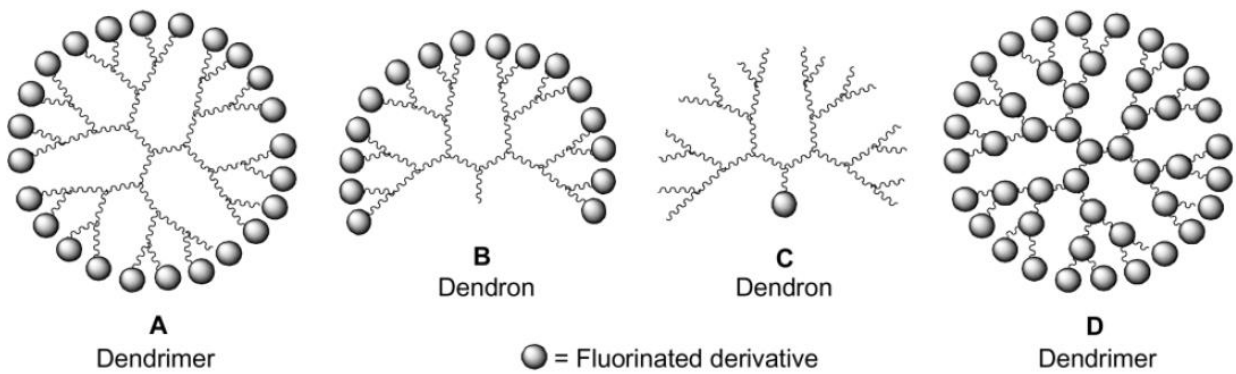

Figure 1.18 *Various types of fluorinated dendrimeric structures.*[140]

Comparing hydrogenated dendrimers with fluorinated ones denoted the superiority of the latter in terms of bioavailability, with a higher cellular uptake and reduced cytotoxicity thanks to their low reactivity. [59,112] Furthermore, the highly stable aggregates originated in water can guarantee the delivery of hydrophobic and fluorinated molecules thanks to fluorine-fluorine interactions. [64,117,144,145] In conclusion, to highlight the power of fluorine in making the difference from a supramolecular point of view, Percec-type dendrimers furnish a key example.[146] The replacement of some hydrogen atoms with fluorines at the tail end of a dendron afforded an unexpected change in the structural motif and self-assembly behaviour (**Figure 1.19**).[146] In more detail, the fluorine scanning at the tail portion of the dendron transforms the spatial conformation of the molecule from an elongated conical shape to a flatter crown-like shape.[146]

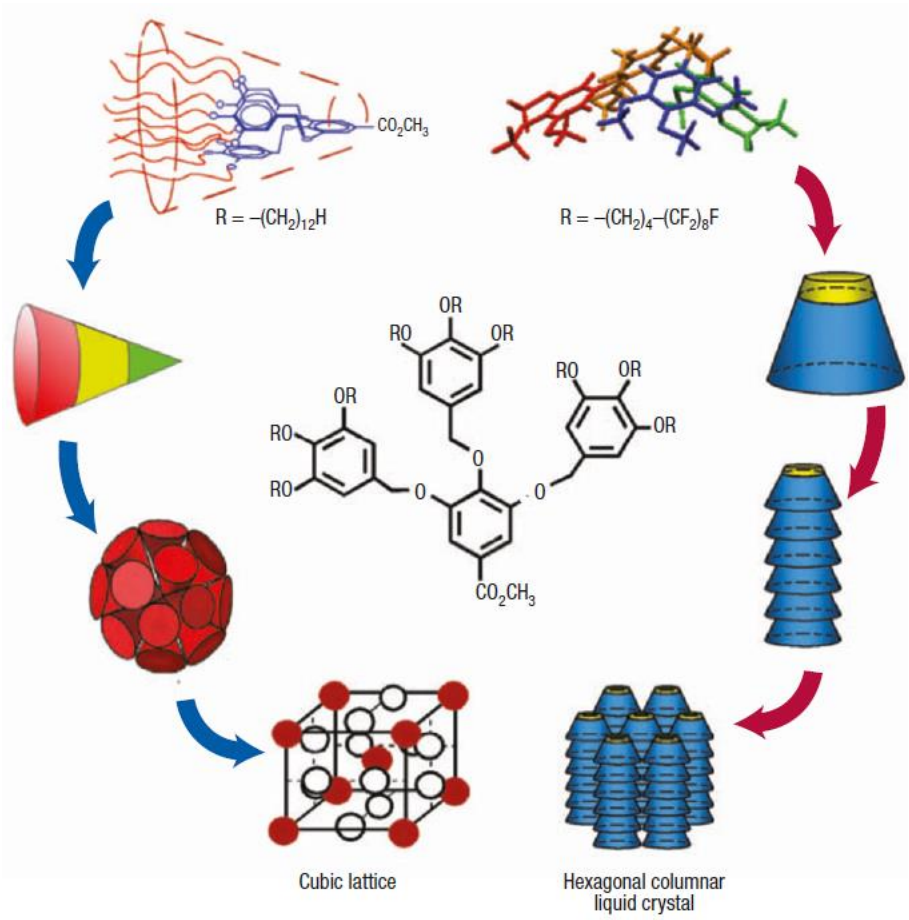

Figure 1.19 *The structure of the Percec-type dendron is represented in the middle. On the left, the non-fluorinated dendron its conical shape self-assembled to lead to spherical assemblies which self-organise in a cubic lattice. On the right the crown-like shape of the partially fluorinated dendron gives rise to columnar assemblies which self-organise in hexagonal liquid crystalline lattice.*[147]

The crown shape reported by Percec *et al.* prevented the formation of the usual supramolecular spheroids, and provided access to an unprecedented pyramidal stack that formed a columnar

supramolecular structure mediated by fluorophobic effect. In all previous examples, fluorination of a self-assembling dendron enhanced its ability to aggregate into the same structure of its hydrogenated homologue.[148] So, the total change in self-assembly and self-organization patterns observed in this case comes as a surprise. Additionally, with the selection of this new architecture a liquid crystalline behaviour of the material appeared as new consequent property.[146]
It is clear that fluorinated dendrimers have a huge potential, not only regarding biomedicine, and it is not surprising that researchers are spending lot of efforts in the continuous development and study of such fascinating macromolecules.

1.3.2 Amino acidic hydrogels and their fibrillar network

In **Section 1.2.1** the concept of low-molecular-weight hydrogelators (LMWHs) was introduced as important feature of peptide and amino acids. The ability to self-assemble in supramolecular hydrogels arises from the organisation in anisotropic structures, most commonly fibers, thanks to noncovalent interactions.[149,150] At a sufficiently high concentration (called minimum concentration of gelation, MCG), these fibers entangle immobilising the solvent through surface tension and capillary forces. Furthermore, the resulting porous soft materials show similarities with biological tissues for mechanical properties and high water content.[149,150]

Traditionally, hydrogels originate from chemical cross-links between polymer chains *via* covalent bonds, but there are many advantages offered by supramolecular hydrogels, obtained *via* noncovalent interactions. In fact, the dynamic nature of the connections offers considerable flexibility, overcoming rigidity of the permanent bonds, which prevents injectability of these materials and generally precludes responsiveness.[149] Processability of supramolecular gels often depends on the possibility of breakage and reformation of nonconvalent bonds. As a result, materials with reversible multi-site bonding structural motifs are expected to have exceptional processability.[149]

Obviously, the typical noncovalent interactions involved are the same of the supramolecular architectures already described: hydrogen bonding, hydrophobic and Van der Waals interactions, π-π stacking, metal-ligand coordination and host-guest interactions (**Figure 1.20**).[149]

Among the interactions, those affected by the presence of water are the most impacting on the swelling behaviour of the material. Giving an example, the presence of water molecules decreases the strength of hydrogen bonding connections. Therefore, engineering materials with excellent mechanical characteristics in the swollen state remains difficult.[149,151]

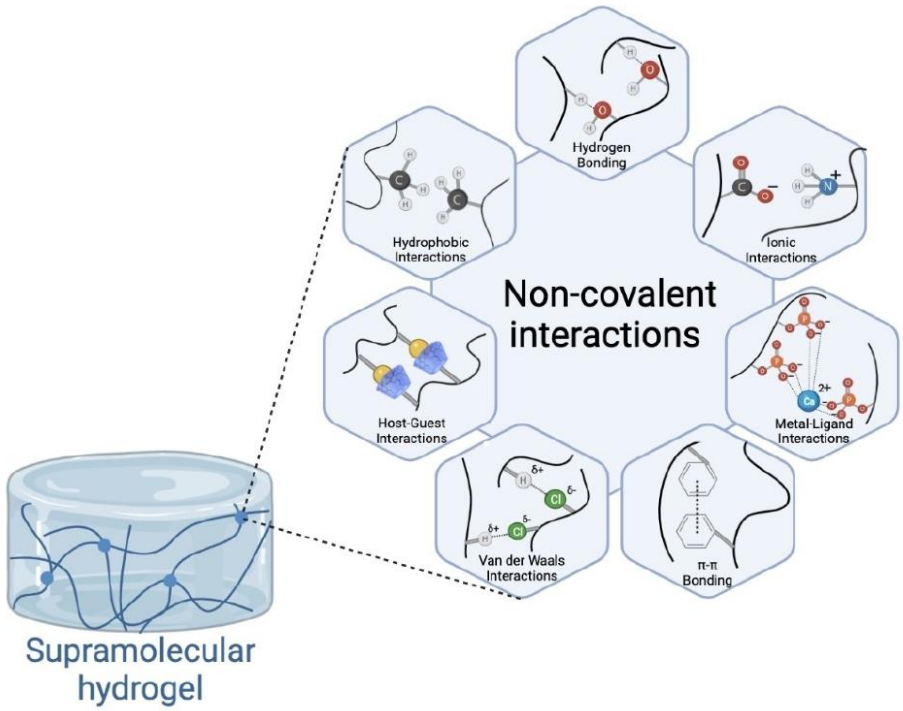

Figure 1.20 *Non-covalent interactions used to form supramolecular hydrogels.*[149]

Nevertheless, such materials are gaining increasing relevance in a wide range of applications, which span from tissue engineering and cell culturing to sustained drug delivery, including wound healing, catalysis, and 3D bioprinting.[149,150,152–154] Consequently, the main challenge of scientists is to ensure that supramolecular hydrogels possess both the desired biomedical properties and the required mechanical characteristics.[149]

Deepening in supramolecular hydrogelation of amino acids and peptides, the hydrophilic-lipophilic balance is fundamental. Interactions involving hydrophobic amino acidic side chains give an important contribution to the self-assembly. In fact, hydrophobic interactions and hydrogen bonds often result to cooperate synergistically.

The association between hydrophobic domains, such as phenylalanine-phenylalanine (Phe-Phe), excludes water molecules from those domains, preventing the competition for hydrogen bonding. Consequently, the self-assembly stabilisation is maximised by hydrophobic interactions and, on the other side, by polar groups interacting with water through hydrogen bonding.[149,155,156] The key role of the hydrophobic contribution during fibrils' formation is shown by Phe-Phe dipeptide (**Figure 1.21**).

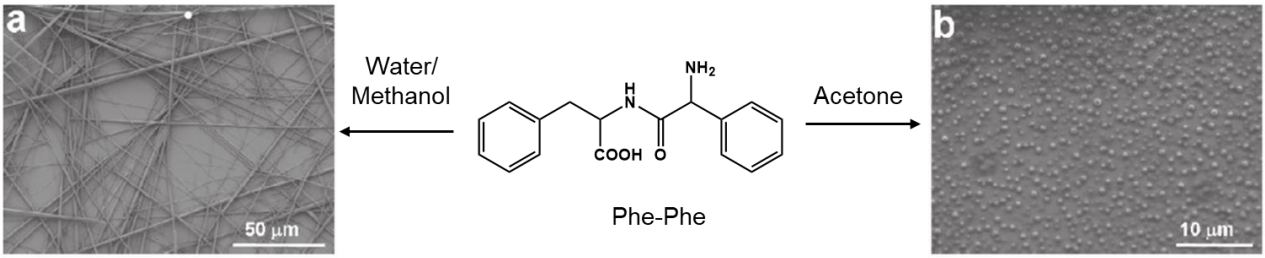

Figure 1.21 *On the top Phe-Phe dipeptide chemical structure. SEM analyses of its supramolecular self-assembly upon dissolution in high and low dielectric solvents is shown: nanotubes (a) and vesicular shape (b) respectively.*[157]

Phe-Phe has been widely studied for its properties in solution, and was one of the earliest dipeptides shown to self-assemble in supramolecular architectures like vesicles and nanotubes, although not into gels, according to Gazit *et al*.[158] Demirel and co-workers supported Gazit's data, studying deeply the behaviour of Phe-Phe in different solvents, explaining that increasing the dielectric constant of the solvent (water, methanol, ethanol) led to the solvation of the hydrophilic head groups in the medium, allowing self-assembly into nanotubes (**Figure 1.21a**). On the contrary, the choice of low dielectric constant solvents (e.g., acetone) led to the prevalence of hydrophobic interactions, and favoured the formation of vesicles-like aggregates (**Figure 1.21b**), in order to reduce the concentration of hydrophilic groups in the medium. Furthermore, using non-polar solvents, like toluene, chloroform or benzene, defined an extreme condition in which no peptide architecture was observed.[157] This example shed a light on the delicate balance between hydrophobic and hydrophilic interactions.

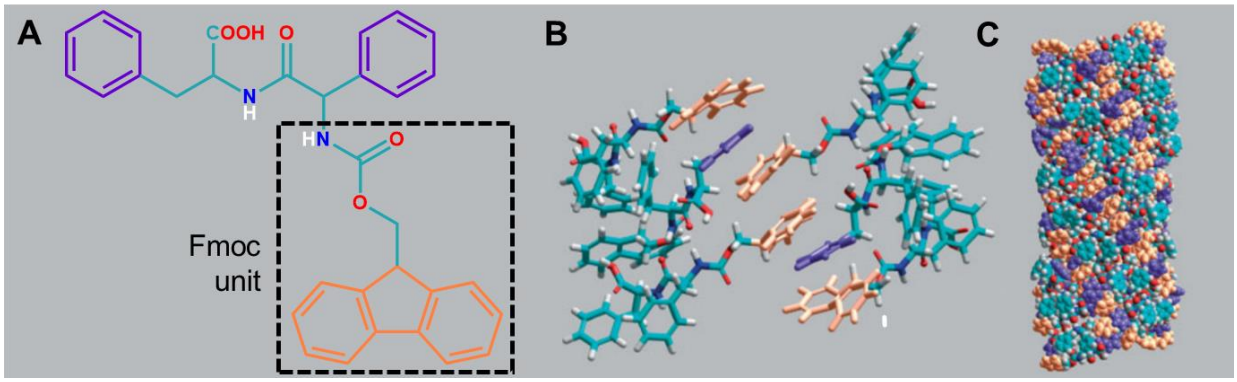

Figure 1.22 *A) chemical structure of Fmoc-Phe-Phe. B) Model structures representing the molecular arrangements during Fmoc-Phe-Phe self-assembly. Note that the fluorenyl and phenyl groups are separately coloured orange and purple to illustrate the paired π-stacking nature of the aromatic moieties during self-assembly .*[159]

Gazit's research went further with the addition of an aromatic protecting group upon the *N*-terminus of the same dipeptide (**Figure 1.22**).[160] 9-fluorenylmethoxycarbonyl-diphenylalanine (Fmoc-Phe-Phe) formed fibrillar suprastructures very similar to amyloid fibrils obtained by much longer

polypeptides. Studies have confirmed that during self-assembly, Fmoc-Phe-Phe molecules form cylindrical nanofibrils by interlocking four twisted antiparallel β-sheets through lateral antiparallel π–π interactions (**Figure 1.22**).[159]

The Fmoc protecting group, commonly used in peptide synthesis, is undoubtedly crucial for the self-assembly, and it gave inspiration for several research lines involving single amino acids as gelators. Among the latter ones, those with aromatic side chains are the favoured, and include for instance tyrosine and tryptophan. The high aromaticity of these Fmoc-protected systems induces a great self-assembly, higher thermal stability and elasticity of the hydrogel derived.[154,161] In fact, the synergistic π-π interactions between aromatic side chains and Fmoc-groups distinctly promotes self-association.[154,162]

Considering the strong fibrillation tendency, it remains a big challenge the prediction and tuning of the hydrogelation process.[149] Aiming to deeply elucidate the mechanism and fine-tune hydrogel properties, various chemical modifications were perpetrated as co-assembly strategies. In particular, the pioneering work of Nilsson *et al.* on *N*-Fmoc-phenylalanine (Fmoc-Phe) is a clear evidence of the wide number of available strategies: protection at the *C*-terminus,[97] halogenation of the phenyl-side chain - exploring both different halogen types and positions[163,164] - co-assembly,[97,165] functionalization with poly(ethylene glycol) (PEG) chains,[166] and synthesis of cationic derivatives.[96,98,167] Among these, it is important to notice that fluorination of the aromatic side chain is a trend which appears in most of the approaches, and special attention will be reserved for fluorinated amino acids in the next section.

1.3.2.1 Fluorination as a strategy to influence hydrogelation on the nanoscale

The principal advantages and applications of amino acids' fluorination were already described in **Section 1.2.2**. This section aims to provide an overview of the specific supramolecular properties originated by FAAs as LMWHs and how this chemical functionalization can affect gelation properties. In particular, the attention is focused on phenylalanine, because of its practical and widespread usage as LMWH. In 2010 Nilsson *et al.* studied the physico-chemical properties of Fmoc-Phe upon fluorination in the three available positions on the phenyl ring, *ortho-meta-para (***Figure 1.23***)*.[164]

The authors observed stronger gels after fluorination in comparison with Fmoc-Phe, and they identified also a different mechanical response, depending on the position of the fluorine atom.[164]

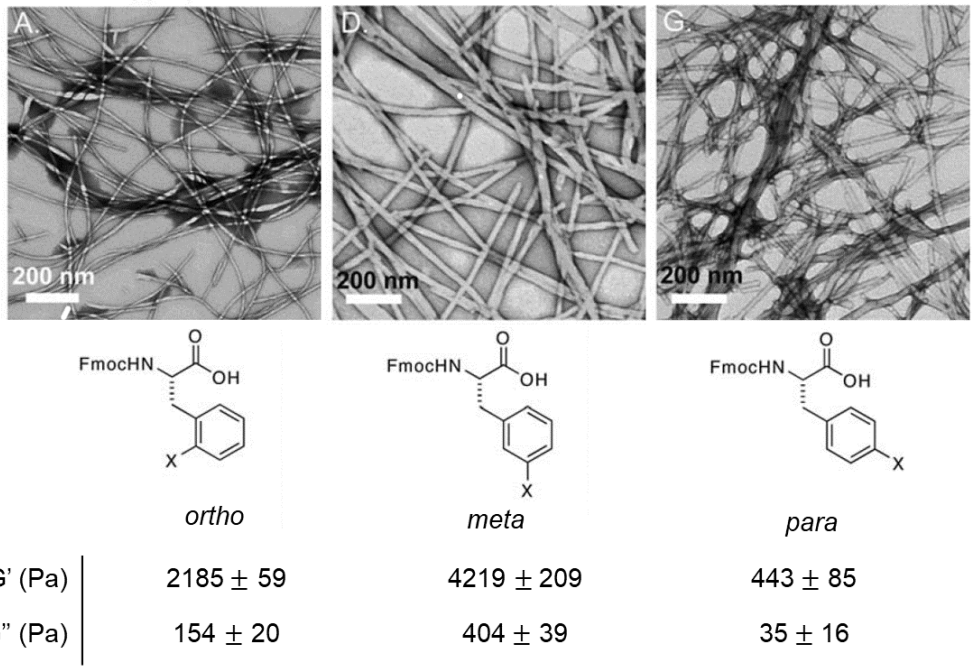

Figure 1.23 *TEM images of fibril network of hydrogels derived by Fmoc-ortho-F-Phe (left), Fmoc-meta-F-Phe (centre) and Fmoc-para-F-Phe (right), the relative chemical structure and rheological parameters of hydrogel strength, G'-G".*[164]

Although fibrils were formed in all cases, and their morphology was not significantly different, there were different kinetics of formation, with the *meta* and *para* positions being faster in self-assembling than the *ortho* substituted one. There was also a big discrepancy in the strength of the relative hydrogels (quantified by the rheological parameter G'), identifying one order of magnitude of difference between G' of the *para*-fluorinated Phe and those of the other isomers (**Figure 1.23**). To explain these observations, both electronic and steric factors were claimed to be involved, influencing the geometry and conformation of the monomer and subsequently the assembly (helicity) of fibers, and the ultimate character of the hydrogel network. They also hypothesised that addition of the fluorine atom and its position can perturb the energy of aromatic π–π interactions that mediate self-assembly.[164]

Recently, Lu and co-workers demonstrated such hypothesis. They synthesised C_2-symmetric benzene-paradicarboxamide-based phenylalanine derivatives (L-phe) and three monofluorinated variants (L-2F-phe, L-3F-phe and L-4F-phe), showed in **Figure 1.24**. Experimental results, coherently with theoretical simulations, confirmed that the type and strength of fluorous interactions have a role in dictating the helical orientation and morphology of the supramolecular assemblies.[168]

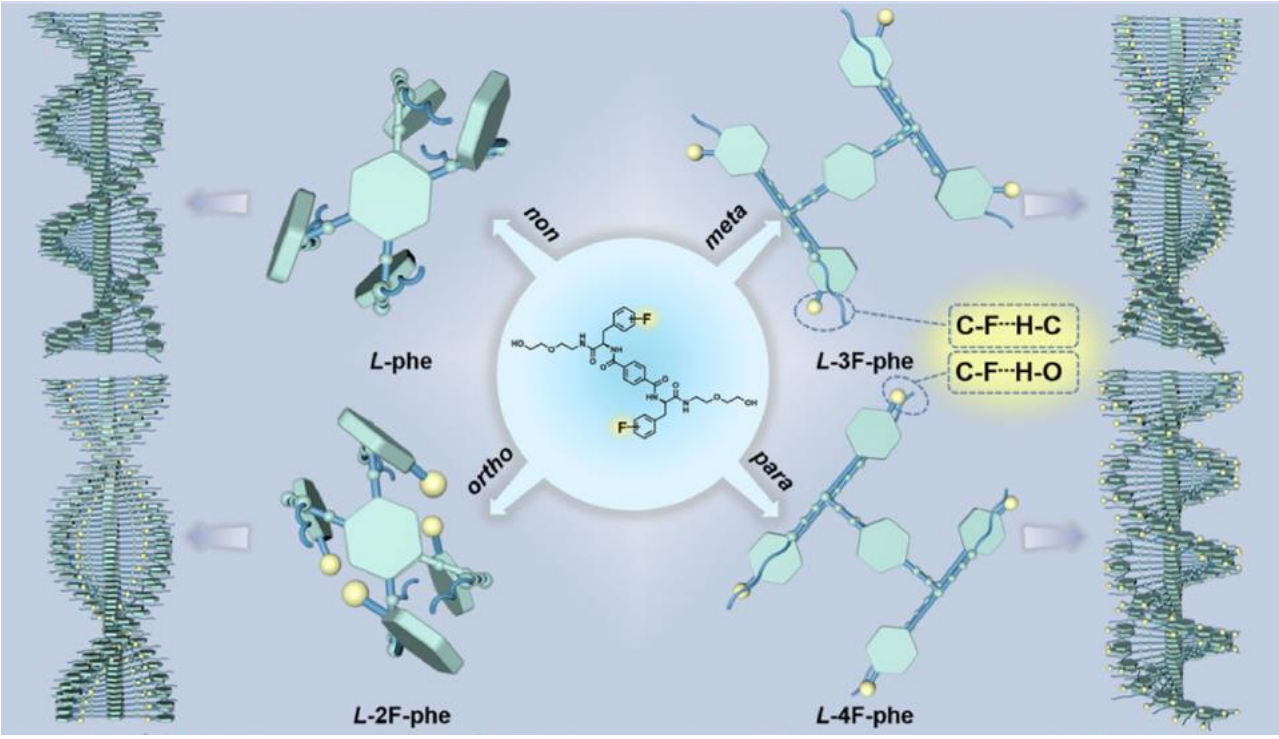

Figure 1.24 *Schematic illustration of helix inversion tuned by C_{Ar}–F···H–O/C interactions.*[168]

Furthermore, the influence on the nanoscale architecture of bis-fluorinated Fmoc-Phe was also studied by Adler-Abramovich's group.[169] Fmoc-3,4F-Phe and Fmoc-3,5F-Phe presented macroscopic differences in behaviour and hydrogelation performances. While Fmoc-3,5F-Phe organised in a transparent hydrogel and remains clear and stable over time, Fmoc-3,4F-Phe disintegrated and underwent phase separation after one month from gel preparation. Furthermore, the high stability of Fmoc-3,5F-Phe hydrogel is justified by a more ordered and aligned microstructure of the nanofibrils, with a consequent higher strength and density of the gel. On the contrary, an additional assembly into crystals is reached for Fmoc-3,4F-Phe, not obtained for the other compound where fibrillation is prevalent.[169]

Further fluorination in Fmoc-pentafluoro-phenylalanine (Phe(F_5)), where fluorine scanning involves all the positions of the aromatic phenyl ring, leads to quadrupolar inversion due to the different electronegativity between H and F. As shown in **Figure 1.25**, the electrostatic potential and the partial charges of the pentafluorophenyl ring are completely different from the wild type.

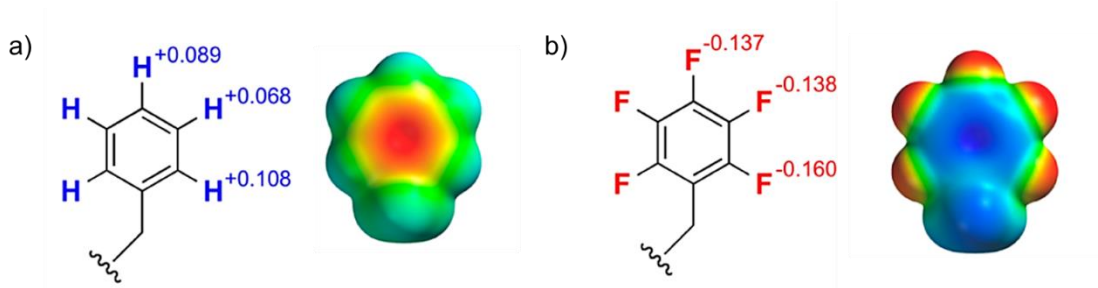

Figure 1.25 *Electrostatic potential maps showing the reversed electron distribution of phenyl ring (a) upon perfluorination (b) and their calculated partial charges. Colour code: negative potential, red; positive potential, blu.*[170]

The term quadrupole refers to the negative potential of the π-face and positive potential around the periphery of a benzene/phenyl ring. This electron distribution allows aromatic moieties to engage in electrostatic interactions with a charge (*i.e.*, cation-π interaction), a partial charge, a dipole or another quadrupole.[170] Perfluorination of the ring causes an inversion of this distribution, creating a positive potential on the aromatic face and a negative charge on the periphery. Theoretical studies have suggested that the shift of electron density upon fluorination is more localized to the carbon skeleton than the π-clouds.[171] Nevertheless, charge distributions of phenyl and perfluorophenyl groups complement each other. The consequence is that the self-assembly of Phe(F_5) is highly reinforced by fluorination in comparison with its hydrogenated counterpart.

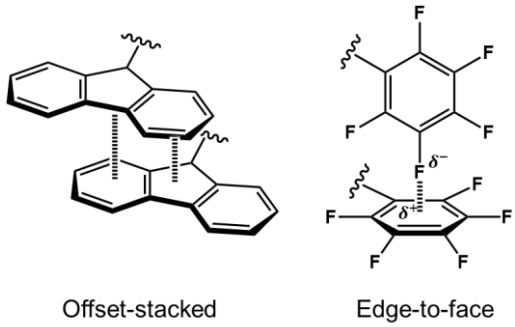

Figure 1.26 *π-π interactions between Fmoc-moieties of Phe(F_5) and edge-to-face interactions involving the partial charged fluorine atom and partial charged π-aromatic system thanks to quadrupolar effect.*

In 2009 Nilsson proposed a model of interaction, supported by experimental data, which displayed a crucial role of quadrupolar charge distribution of the perfluoro-ring. [163] In fact, the lowest energy model aligned Fmoc moieties in an offset, face-to-face stacking mode, and pentafluorophenyl rings

in an edge-to-face packing mode (**Figure 1.26**). In this alignment, it was fundamental the quadrupolar effect which allowed the interaction between fluorinated rings.
Thus, hydrogelation occurred in a few minutes, while Fmoc-Phe did not produce hydrogels in the same conditions.[163] Furthermore, the incorporation of Phe(F_5) as a strategy to promote polar-π interactions, regulate self-assembly, and dictate the organization pattern, was used also in dipeptide hydrogels and in their co-assembly with not fluorinated phenylalanines.[172–174]

These examples underline efficiently how amino acids' fluorination can face the challenge of hydrogels rational design. Fluorination is undoubtedly a technique for influencing supramolecular organization at the nanoscale, and understanding the self-assembly process may provide the key insight to facilitate the development of ideal amino-acid-based LMWHs, with tailored features and applications.

1.4 Aim and outline of the thesis

Given the scientific importance of PERFECTA as CA for ^{19}F-MRI, the first objective was the investigation of proper formulations for its administration in biological environments (**Chapter 2.2**). In particular, the carrier was designed in collaboration with the Freie Universität of Berlin, and it was chosen to exploit the promising potential of fluorinated Janus dendrimers. The novelty of this approach consisted in the presence of several equivalent ^{19}F atoms both in the host (dendrimer) and in the guest (PERFECTA). The interest was focused first on the characterization of the self-assembling mode of the system, and then on its performance in terms of ^{19}F-MRI response and cellular biocompatibility and targetability.

In **Chapter 2.3**, a second approach for solubilising PERFECTA in water was tested, exploiting biocompatible natural proteins. In collaboration with the University of Bologna, formulations of PERFECTA@lysozyme and PERFECTA@BSA (Bovine Serum Albumin) were studied and characterized, aiming to evaluate the applicability of this strategy, and also to elucidate the consequences of the interaction between proteins and fluorinated molecules, still quite unexplored.

In **Chapter 3.2** amino acidic hydrogels obtained from Phe(F_5) were studied in order to tailor the release of small molecules, like benzamide and nicotinamide (Vitamin B_3). The big challenge about LMWHs is the tuning of their properties in order to reach a specific performance. Aiming to face this challenge, a crystallographic approach was investigated as a new tool to engineer hydrogels. The objective was the study of the supramolecular system and the mechanical properties of the composite hydrogels, aiming to tune the release of pharmaceuticals exploiting noncovalent interactions. Then, the effect of fluorination upon the same amino acid has been further investigated in presence of a different halogen atom (**Chapter 3.3**). For this purpose, *N*-Fmoc-2,3,5,6-tetrafluoro-4-iodophenylalanine (Phe(F_4I)) was synthesised and investigated from a supramolecular point of view, as a potential tool to enable additional noncovalent forces.

Chapter 2

Fluorinated Dendrimers and Proteins as Supramolecular Hosts for PERFECTA

2.1 Oligoglycerol-based dendrimers and model proteins

During my research stay at Freie Universität Berlin (Germany), in the research group led by Prof. R. Haag, three different oligoglycerol Janus dendrimers (**Figure 2.1**) were tested for their ability to solubilize the ^{19}F MRI contrast agent PERFECTA, with the objective to provide a new supramolecular tracer for magnetic resonance imaging.

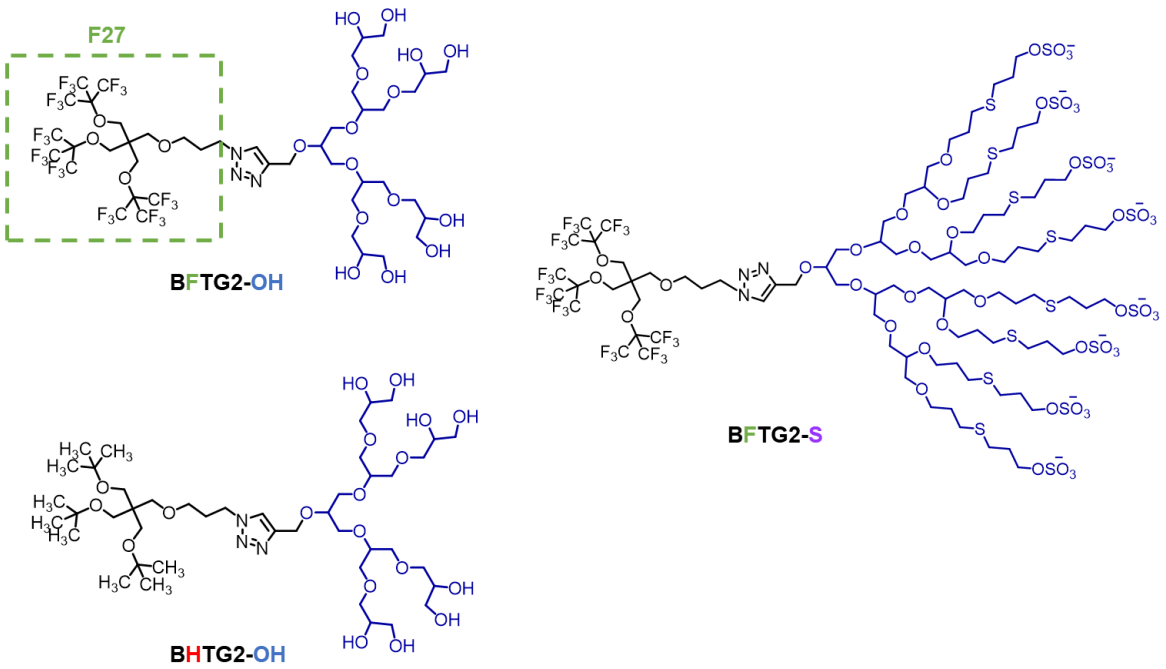

Figure 2.1 *Molecular structure of the three Janus-dendrimers tested for the encapsulation of PERFECTA.*

Literature examples of supramolecular assemblies and potential applications of different generations of oligoglycerol-based dendrimers (from generation 1 to generation 3, G1-G3) bearing linear fluoroalkyl chains were reported, and compared with their hydrogenated counterparts.[175–179] Recently, linear fluoroalkyl chains were substituted by a multibranched one, containing perfluoro-*t*-butoxyl groups (F27, **Figure 2.1**, green dotted square). Indeed, fluorinated branched groups with ether bonds showed enhanced biodegradability and lower bioaccumulation in comparison with linear ones.[27,63,180] Based on this background, the second-generation oligoglycerol dendron (G2) was linked to the branched (B) fluorinated F27 (F) unit through a triazole core (T), leading to BFTG2-OH (**Figure 2.1**).[181] This compound was dispersible in water, thanks to its eight -OH end-groups. In order to prevent the contact between the lipophilic fluorinated part and the aqueous solvent, it self-assembled into unilamellar vesicles.[181] Moreover, this supramolecular assembly displayed good biocompatibility, holding potential as special carrier for biomedical applications.

The structural similarity between the F27 group and PERFECTA made BFTG2-OH a promising carrier for hosting this MRI tracer, exploiting fluorine-fluorine interactions. In this chapter, the first focus pointed on the design and optimization of PERFECTA formulations using the Janus dendrimer BFTG2-OH, which was provided by the collaborators at Freie Universität Berlin. In a second instance, its hydrogenated counterpart BHTG2-OH was synthesised, and tested as a carrier as well (**Figure 2.1**). In this second case the investigation pointed to the possibility to exploit hydrophobic interactions – different from F-F – to encapsulate PERFECTA.

BFTG2-S was the last dendrimer tested with the aim to impart targetability to the system. In fact, the substitution of -OH end-groups with sulphates $-OSO_3^-$ was demonstrated to confer particular affinity for inflammatory cells.[182–186] Generally, polyglycerol sulphate dendrimers (dPGS) showed a heparin-like structure,[187] which defined a strong binding affinity to cellular targets involved in the inflammatory process *e.g.* cell adhesion molecules consisting of L-selectin and P-selectin expressed on leukocytes, platelets, and vascular endothelium.[187,188] The positive charge at the ligand interface of such molecules addressed the negatively charged dPGS towards inflammatory cells, ending with an anticoagulant and anti-inflammatory activity. [187]

The totally new dendrimer BFTG2-S was characterised in terms of self-assembly properties and capacity to encapsulate PERFECTA. BFTG2-OH was compared with BFTG2-S for hosting efficiency, cellular uptake and ^{19}F-MRI performance (in collaboration with IRCCS San Raffaele Hospital and Istituto Neurologico "Carlo Besta" in Milan).

In the second section of this chapter, another interesting tool to solubilise PERFECTA was investigated in collaboration with Prof. M. Calvaresi and Prof. F. Zerbetto (University of Bologna, Italy). In particular, two proteins were studied as surfactants, Bovine Serum Albumin (BSA, **Figure 2.2**) and hen egg white lysozyme (LYS, **Figure 2.2**). Cow-derived BSA shares 76% identity with Human Serum Albumin, including the three-domain structure (583 amino acids and ~ 66 kDa molecular weight *versus* 585 amino acids and ~ 66.5 kDa) and the distribution of its 17 disulfide bridges. Additionally, the physiological role of all serum albumins is crucial for maintaining plasma osmotic pressure, as free radical scavengers, regulating immune responses and transporting endogenous compounds. Thus, this globular protein represents the transport protein *par excellence* in the blood stream.[189–191] On the other hand, LYS is a smaller protein of only 129 amino acids (14.3 kDa), known by the scientific community as a model protein among the most studied so far.[192] LYS is the abbreviation for peptidoglycan *N*-acetylmuramoylhydrolase, from which it can be deduced its physiologic activity. In fact, it is an antimicrobial enzyme belonging to the innate immune system.

By virtue of its catalytic activity, LYS can hydrolyse glycosidic bridges contained in peptidoglycans, basic constituents of gram-positive bacterial cell walls.

BSA and LYS were already present in studies about host-guest interactions.[105,106,193] BSA presents at least 6 nonpolar cavities, able to interact with other molecules for their transport.[194] On the contrary, the presence of only one catalytic channel along LYS sequence could admit the interaction with mainly one molecule at a time.[192]

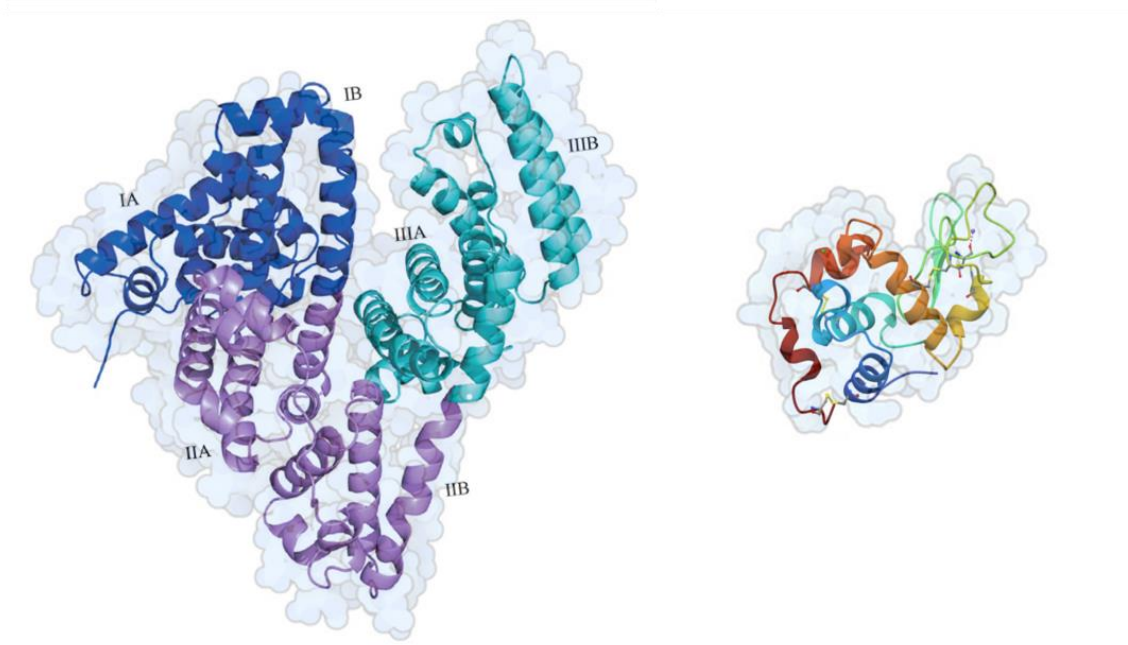

Figure 2.2 *Left) Domain division of BSA structure (PDB reference 4F5S). Right) LYS structure (PDB reference 193L).*

Considering these premises, BSA and LYS were selected as potential hosts for PERFECTA with two main purposes: i) the possibility of using proteins as Trojan horses for the probe transport and ii) investigate the interactions between proteins and fully fluorinated molecules. In fact, apart from few information about the effect of fluorinated molecules on proteins,[108,109] this topic was still quite unexplored.

Results and discussion

2.2 PERFECTA@dendrimers as ^{19}F MRI contrast agents

2.2.1 Optimization of formulation protocols

The first aim of the project was to design a formulation to incorporate PERFECTA within BFTG2-OH vesicles and/or BFTG2-S to admit stabilization of the probe in water environment. Indeed, the high amount of fluorine atoms of PERFECTA prevents its solubility in water, rather hampers also the solubility in most organic solvents, except for hexafluoroisopropanol and ethyl acetate. On the other hand, by virtue of its hydrophilic end groups, BFTG2-OH and BFTG2-S displayed good solubility in protic solvents, such as alcohols and water, but they were not soluble in ethyl acetate. Three different formulation methods were tested, considering the necessity to solubilise both components. The method and parameters' optimization started from the study of the BFTG2-OH, which was available in a bigger amount. In particular, the optimization regarded: i) temperature, ii) sonication time, iii) ratio between guest and host, iv) purification method.

All formulations were prepared in 1 mL amount, in order to have a 5 mg/mL theoretical concentration of dendrimer, as previously reported.[181] Starting from three different approaches, a preliminary investigation was conducted in order to determine the real possibility to encapsulate PERFECTA:

1. **Solvent-dry method**: it consisted in the solubilization of PERFECTA (1 mg) and BFTG2-OH (5 mg) in the minimum amount of organic solvent (ethyl acetate and methanol, respectively). The two solutions were mixed and vacuum-dried in order to get a homogeneous film. One mL of pure water was then added, and stirred at room temperature overnight. The formulation was filtered on a 0.45-µm filter, to remove non-encapsulated PERFECTA.
2. **Melting method**: 1 mg of PERFECTA was melted at 80°C. A water solution of BFTG2-OH (5 mg/mL) was directly added. The mixture was stirred overnight and then purified by filtration (0.45-µm filter).
3. **Thin film method**: 1 mg of PERFECTA was solubilized in 250 µL of ethyl acetate and air-dried overnight in a glass vial. To the remaining thin film, a water solution of BFTG2-OH (5 mg/mL) was added. The mixture was stirred overnight and then purified by filtration (0.45-µm filter).

All the formulations were analysed by DLS and ^{19}F-NMR to determine size of the self-assembled supramolecular systems, polydispersity and encapsulation amount. Preliminary NMR analyses

showed the presence of PERFECTA in at least two samples, confirming the success of the proposed approach. The thin film method gave the best results (**Table 2.1**), while the absence of PERFECTA ^{19}F-NMR signal when using the solvent-dry method excluded it from further optimization (**Figure 2.3a**).

Table 2.1 *DLS data and ^{19}F-NMR quantification about preliminary formulations using three different method of preparation. Legend: S = Solvent dry method; M = melting method; T = thin film method. The control formulation 0 was obtained by dissolving BFTG2-OH in water.*

	Method	**DLS**		**^{19}F NMR quantification**				
				PERFECTA		BFTG2OH		F/mL total
		Diameter (nm)	PDI	Theor. mg/mL	Experim. mg/mL (%)	Theor. mg/mL	Experim. mg/mL (%)	
0	-	442	0.2	-	-	5	1.8 (35%)	2 x 10^{19}
1	S	150	0.3	1	x	5	3.5 (69%)	4 x 10^{19}
2	M	144	0.2	1	0.24 (24%)	5	2.2 (44%)	3 x 10^{19}
3	T	120	0.2	1	0.4 (40%)	5	2.5 (50%)	4.2 x 10^{19}

This initial screening underlined three main issues:

i) Beside the similar chemical structure of PERFECTA and F27 building block, their ^{19}F-NMR resonance frequencies were slightly different. The latter allowed to quantify both compounds. Additionally, for future MRI performance, the short distance constituted an advantage, because the two peaks would be detected as a unique and more intense signal improving signal to noise ratio (SNR) and reducing the acquisition time.

ii) The experimental concentration of BFTG2-OH was always lower than the theoretical one. This fact could derive from two factors: self-assembly in water reduced the $-CF_3$ mobility, or filtration caused a loss of material.

iii) All the formulation protocols reduced the size of the aggregates and, apart from solvent-dry method, this might be a good parameter to evaluate the success of the encapsulation.

The attempt to improve the melting and thin film formulation methods proceeded with the introduction of tempering and sonication steps, taking inspiration from already known protocols of PERFECTA formulation with other polymers.[57,65]

In more detail, 3 cycles of bath sonication (1 min, 40 kHz) alternated with heating at 70°C for 15 min were added to the previously described melting and thin film protocols, finishing with a heating step at 70°C. Then, formulations were left to cool down to room temperature and stirred overnight. Filtration was maintained as final purification step.

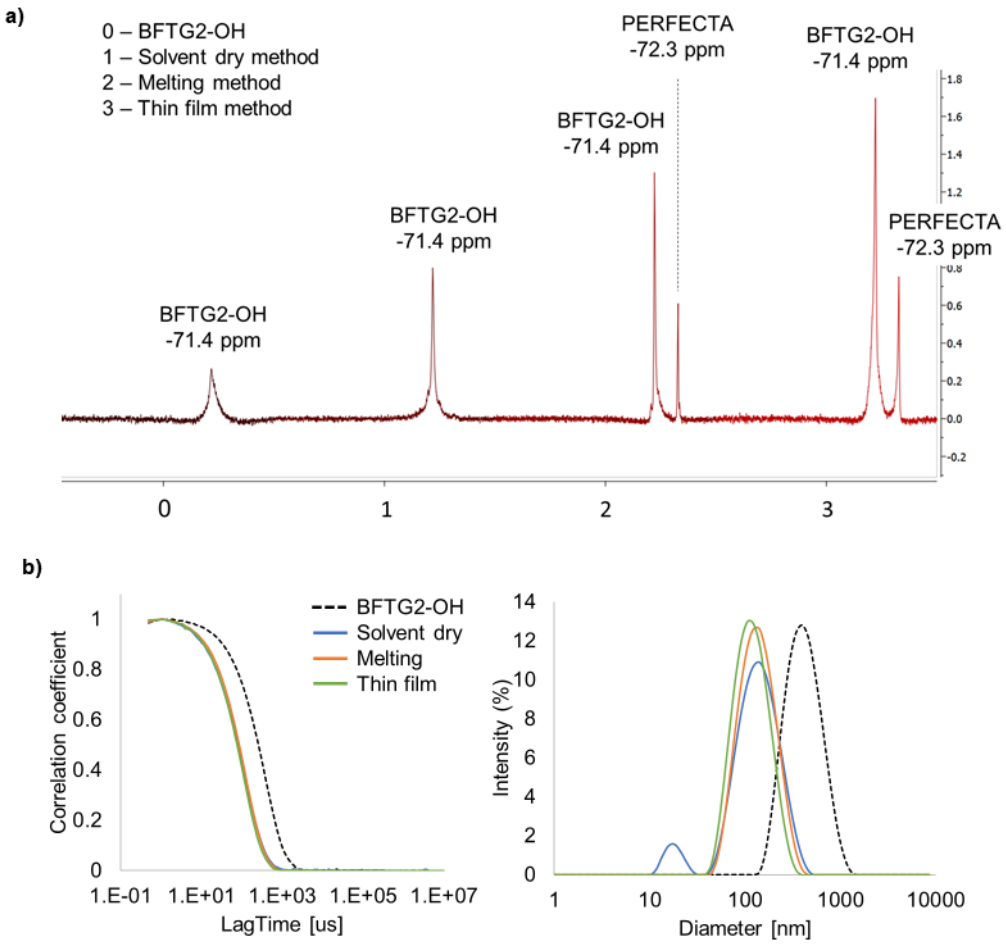

Figure 2.3 *a) ^{19}F-NMR spectra of the three preliminary formulations compared to a solution of BFTG2-OH in water. Chemical shifts are referred to an external reference of TFA in D_2O set at -75.5 ppm. b) DLS autocorrelation function (left) and size distribution vs intensity (right) of preliminary formulations in comparison with BFTG2-OH solution in pure water.*

The comparison between melting and thin film (conditions 4 and 5, **Table 2.3**) gave no significant difference, while a good improvement in term of polydispersity was obtained if compared with the same protocols without temperature control and sonication (conditions 2 and 3, **Table 2.1**). Since the same loss of BFTG2-OH was observed also in case of 4 and 5, a different final purification step was tested. Additionally, given the small difference between melting and thin film methods, it was decided to proceed with the optimization of the thin film protocol only, which gave better results comparing conditions 3 and 2 (**Table 2.1**). The removal of unloaded PERFECTA was pursued by centrifugation (2 x 2 min, 3000 rpm), which gave a good improvement, as shown by the comparison between 5 and 6 (Table 2.2). The loss of 40% of BFTG2-OH still recorded by NMR seemed to support the hypothesis of reduced ^{19}F-NMR signal because of the self-assembly.

The weight ratio of 1:5 between PERFECTA and BFTG2-OH, which was kept so far, was then changed for further optimization.

Table 2.2 *DLS data and ^{19}F-NMR quantification about formulations during parameter optimization. Different method of preparation. Legend: M Δ+s = melting method with heat and sonication cycles; T = thin film method with heat and sonication cycles.*

	Method	**Purification**	**DLS**		**^{19}F NMR quantification**				F/mL total
					PERFECTA		BFTG2OH		
			Diameter (nm)	PDI	Theor. mg/mL	Experim. mg/mL (%)	Theor. mg/mL	Experim. mg/mL (%)	
4	M	Filtration	107	0.13	1	0.14 (14%)	5	2.0 (40%)	2.5×10^{19}
5	T	Filtration	125	0.14	1	0.1 (10%)	5	1.9 (38%)	2.3×10^{19}
6	T	Centrifuge	115	0.16	1	0.32 (32%)	5	2.7 (54%)	3.5×10^{19}
7	T	Centrifuge	114	0.15	2.5	0.36 (15%)	5	3.5 (70%)	4.6×10^{19}
8	T	Centrifuge	126	0.16	5	0.33 (6.5%)	5	2.4 (48%)	3.4×10^{19}
9	T	Centrifuge	161	0.21	10	0.22 (2%)	5	1.9 (38%)	3.7×10^{19}
10	T	Centrifuge	158	0.17	0.5	0.19 (38%)	5	3.1 (62%)	3.9×10^{19}

Four different ratios PERFECTA/BFTG2-OH were explored (1:2, 1:1, 2:1; 1:10, respectively case 7, case 8, 9 and 10 in **Table 2.2**). The best result was obtained with formulation 7, with a ratio 1:2, dissolving 2.5 mg/mL of PERFECTA for the thin film, while maintaining 5 mg/mL the concentration of BFTG2-OH. The optimized final protocol is reported in **Figure 2.4a**.

Interestingly, the simple dissolution of BFTG2-OH in water (formulation 0, **Table 2.1**) produced vesicles of ~ 440 nm. On the other hand, formulation of the same dendrimer following the optimized thin film method in the absence of PERFECTA gave vesicles of ~ 500 nm (**Figure 2.4b**).

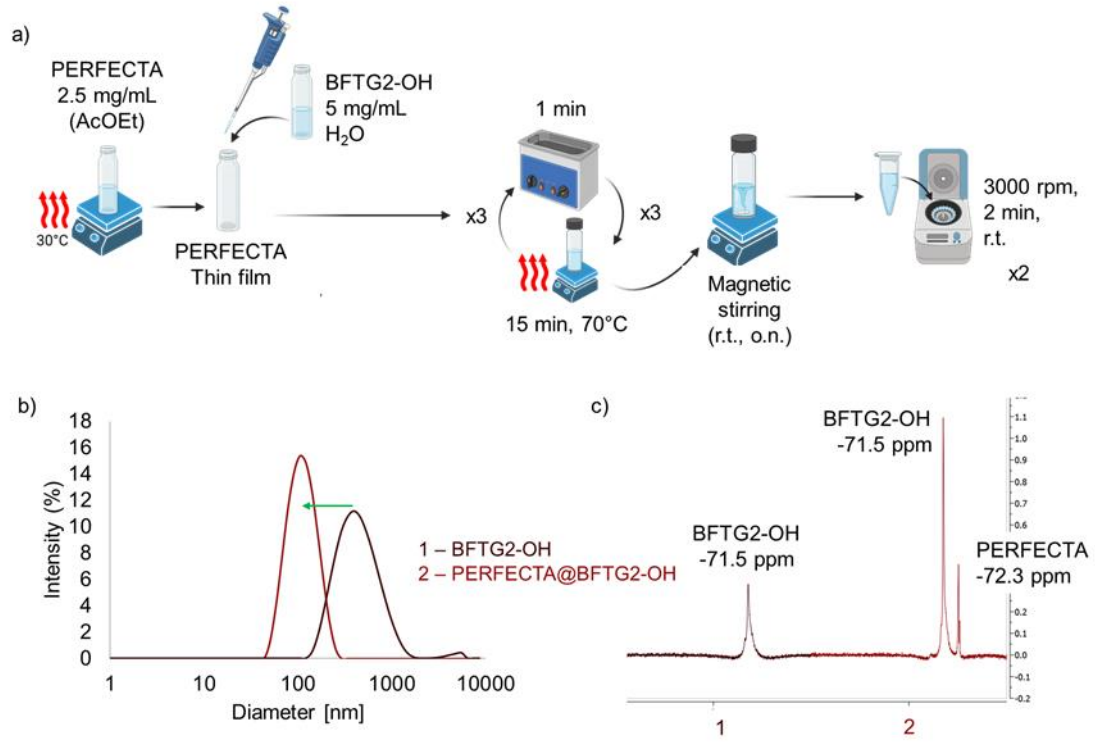

Hydrodynamic diameter distribution	1	2
Size by intensity	500 ± 3 nm	109 ± 3 nm
Size by volume	646 ± 17 nm	94 ± 7 nm
PDI	0.35 ± 0.01	0.15 ± 0.01

Sample	[PERFECTA] mg/mL	[BFTG2-OH] mg/mL	F/mL total
1	-	3.6 ± 0.08 mg/mL	4.0×10^{19}
2	0.36 ± 0.07 mg/mL	3.5 ± 0.07 mg/mL	4.6×10^{19}

Figure 2.4 *a) Scheme of the optimized formulation protocol. b) DLS chart of size distribution vs intensity; on the bottom PDI, diameter distribution by intensity and volume are reported for formulation 1 (BFTG2-OH) and 2 (PERFECTA@BFTG2-OH). c)* ^{19}*F-NMR spectra of 1 and 2 in water. Chemical shifts are referred to an external reference of TFA in* D_2O *set at -75.5 ppm. Standard deviations were reported considering n=3.*

The size reduction observed upon addition of PERFECTA was attributed to additional fluorine-fluorine interactions, which had a consistent effect on self-assembly (**Figure 2.4b**). Additionally, the optimized protocol afforded good polydispersity and reproducibility, and a satisfactory number of F atoms/mL (4.6 x 10^{19} F/mL) considering the sum of both PERFECTA and BFTG2-OH (**Figure 2.4c**). On the other side, the issue regarding the reduced amount of resonant fluorine atoms of BFTG2-OH was still present, and it was confirmed when an organic co-solvent was added. In fact, with the addition of 25%$_{v/v}$ of methanol, the amount of BFTG2-OH which could be quantified by ^{19}F-NMR reached 89% (4.4 mg/mL). On the opposite, the detected concentration of PERFECTA remained the same observed in pure water (**Figure 2.5**). For comparison, the 25%$_{v/v}$ of pure water was then added to another aliquot of stock formulation: the amount of BFTG2-OH and PERFECTA quantified upon dilution was the same of the stock.

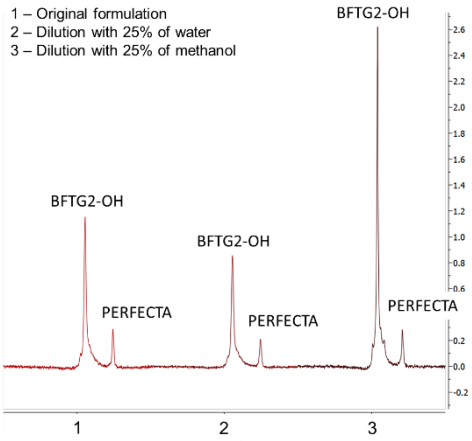

Figure 2.5 *^{19}F-NMR comparison between the original optimized formulation (1), after the addition of 25% of water (2) and 25% of methanol (3). The peak intensity of BFTG2-OH had a consistent increase upon dilution with the organic solvent.*

This experiment confirmed that the reduction of resonant -CF_3 of BFTG2-OH was due to the self-assembly, which was not altered upon the addition of water. On the opposite, the addition of methanol disrupted the aggregates, causing the solubilisation of the dendrimer and increasing the mobility of the fluorine atom during the magnetization.

Furthermore, the presence of the triazole group, which absorbs in the UV-visible spectral region, allowed to crosscheck the total amount of BFTG2-OH in the final formulation with this technique. The comparison between UV-vis spectroscopy and NMR quantifications (**Figure 2.6**) was consistent with the hypothesis proposed. The self-assembly in water hampered the magnetic response of the F27 building block, and this was something to be considered for MRI performance. Indeed, formulation

7 was confirmed to be the best candidate, thanks to the highest amount of BFTG2-OH detectable by NMR (**Figure 2.6**).

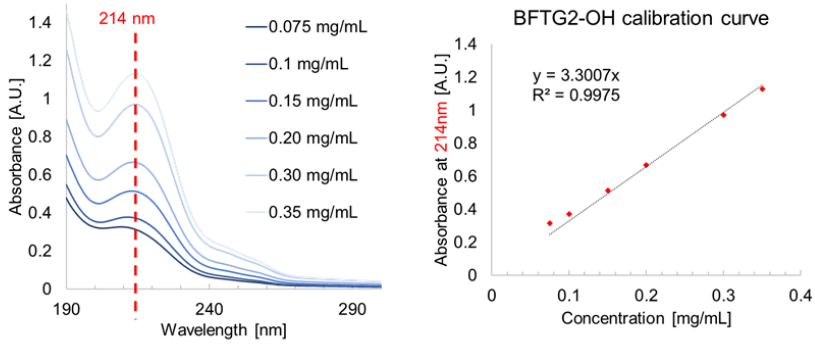

	2	3	4	5	6	7	8	9	10	BFTG2-OH CTRL
NMR concentration exp. [mg/mL]	2.2 44%	2.5 50%	2.0 40%	1.9 38%	2.7 54%	3.5 70%	2.4 48%	1.9 38%	3.1 62%	3.0 (60%)
UV concentration exp. [mg/mL]	4.1 82%	4.0 80%	3.5 70%	3.8 76%	5.0 100%	4.7 94%	4.1 82%	4.9 98%	5.1 100%	5.1 100%

Figure 2.6 *Top) UV-vis absorption spectra of different concentrations of BFTG2-OH. The wavelength of the absorbance maximum was used to define the calibration curve. Bottom) Comparison between the experimental concentrations of BFTG2-OH in the formulation reported in Table 2.1 and Table 2.2, quantified by ^{19}F-NMR and the amount quantified by UV-vis spectroscopy.*

Beside the good colloidal properties and reproducibility of the formulations, the amount of PERFECTA which could be loaded was still small. Considering that its limit of detection by ^{19}F-MRI was 0.3 mg/mL,[65] the optimized formulation loaded a concentration of PERFECTA too close to this threshold. For this reason, a fourth method of formulation was tested. Inspired by a previously published protocol,[195] a nanoprecipitation process was followed for formulating PERFECTA in presence of BFTG2-OH (**Figure 2.7a**).

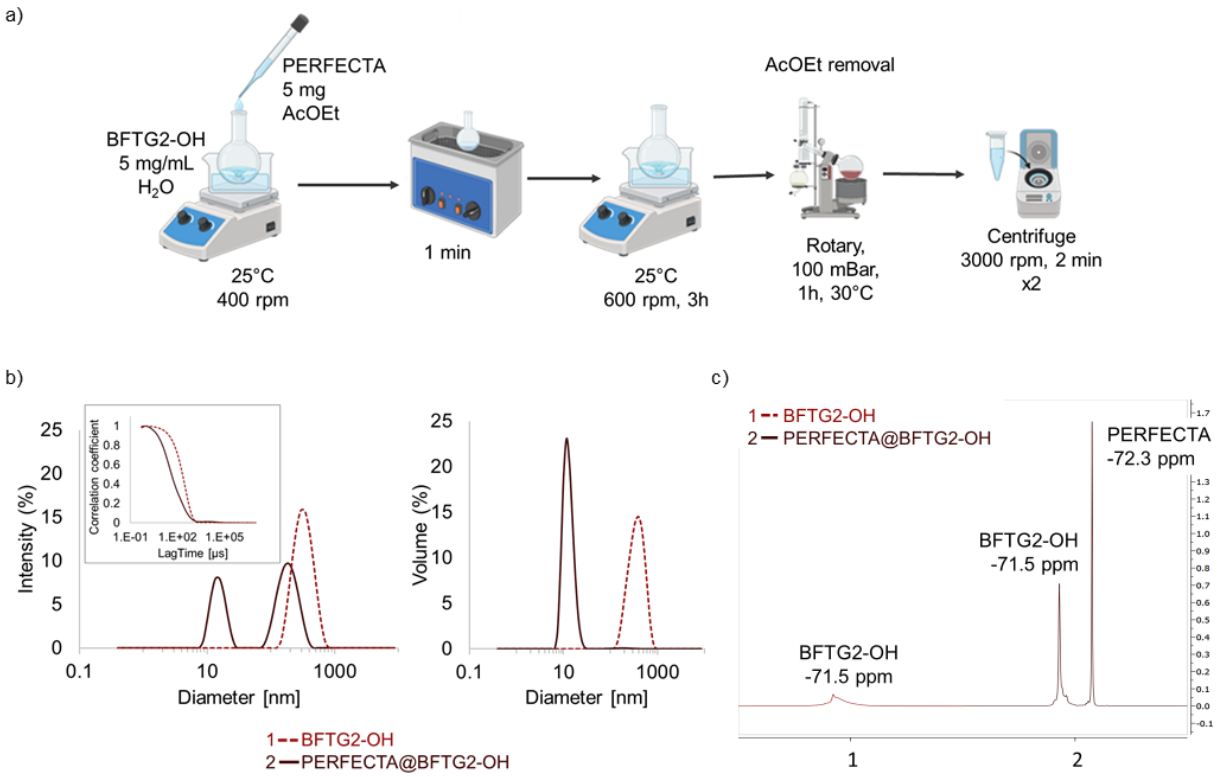

Hydrodynamic diameter distribution	1	2
Size by intensity [nm]	326 ± 17	190 ± 8 14 ± 1
Size by volume [nm]	367 ± 17	13 ± 1 nm
PDI	0.19 ± 0.02	0.37 ± 0.02

Concentration	1	2
[PERFECTA] mg/mL	-	2.7 ± 0.4
[BFTG2-OH] mg/mL	3.9 ± 1.3	4.6 ± 0.5
F/mL total	4.3 x 10^{19}	10.9 x 10^{19}

Figure 2.7 *a) Scheme of the optimized nanoprecipitation protocol. b) DLS chart of size distribution vs intensity (left) and size distribution vs volume (right); at the bottom PDI, diameter distribution by intensity and volume are reported for formulation 1 (BFTG2-OH) and 2 (PERFECTA@BFTG2-OH). c) ^{19}F-NMR spectra of 1 and 2 in water. Chemical shifts are referred to an external reference of TFA in D_2O set at -75.5 ppm. Standard deviations were reported considering n=3.*

The new protocol involved a bi-phase, constituted by the aqueous solution of BFTG2-OH (5 mg/mL) to which was added a PERFECTA (5 mg) solution in ethyl acetate (0.4 mL). Dropwise addition was followed by sonication (1 min, 40 kHz) to create a white emulsion, and then magnetic stirring for 3 hours at controlled temperature (25°C). After this stirring time, the formulation appeared transparent and it was vacuum dried to remove the organic solvent. Centrifugation was maintained as purification method to exclude unloaded PERFECTA.

The first difference between the two formulation methods regarded diameter distributions in the presence of PERFECTA. Good polydispersity properties reached with the optimized thin film method, gave vesicles of 109 ± 3 nm (**Figure 2.4b**). In the case of nanoprecipitation two main peaks

were observable in the distribution: 190 ± 8 nm and 14 ± 1 nm (**Figure 2.7b**, left), indicating presence of aggregation. Due to the presence of two species, the latter measured a much higher PDI. Interestingly, the double peak situation was fixed analysing the diameter distribution in term of volume (**Figure 2.7b**, right), where only the smaller population could be identified. The dramatic decrease of diameter as a consequence of the introduction of PERFECTA was much more pronounced in the nanoprecipitation than in the thin film method and a huge change in self-assembly could be hypothesised. Indeed, it is difficult to imagine vesicles of such a small diameter. Furthermore, the reduced size was followed by a significant increase in PERFECTA loading (**Figure 2.7c**). In fact, the intensity of its peak in the NMR spectrum exceeded that of BFTG2-OH signal, defining an opposite situation than in the thin film method (**Figure 2.4c**). Thus, the F/mL count reached the threshold of 1 x 10^{20} atoms/mL, more than two times higher than in the case of formulation 7.

The nanoprecipitation data reported were referred to the already optimized protocol. Different weight ratios were tested (1:1, 1:2 and 2:1), proving that the formulation with 5 mg of PERFECTA and 5 mg of BFTG2-OH gave the best loading (54 % of encapsulation, against 15 % achieved with the thin film method). In conclusion, the fourth protocol of formulation seemed to be more promising than the others, and was then used with the second dendrimer BFTG2-S.

2.2.2 Characterization and formulation of sulphated Janus dendrimer

BFTG2-S (**Figure 2.1**) was synthesized in collaboration with Prof. Haag's research group, at the Freie Universität Berlin (FUB) through a multistep pathway, using the F27 building block I synthesised at Politecnico of Milano. More details about the synthesis are provided in the **Experimental section 2.4**.

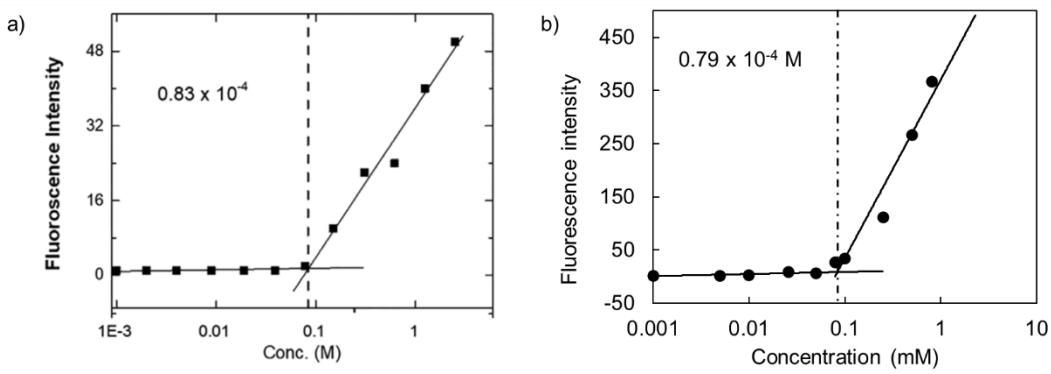

Figure 2.8 *Critical micelle concentration (CMC) profile for BFTG2-OH (a, published)*[181] *and BFTG2-S (b).*

First, the critical micelle concentration (CMC) of BFTG2-S was determined using Nile Red as a fluorescent probe. Indeed, this dye has a solvatochromic behaviour, meaning that the intensity of its fluorescence emission increases when micelles and vesicles are formed.[196] The comparison between CMC of BFTG2-OH and BFTG2-S is reported in **Figure 2.8**. Although water solubility of BFTG2-S was expected to be higher than BFTG2-OH, thanks to the presence of eight negative charges, its CMC was very close to that of BFTG2-OH, indicating a similar aggregation propensity.

After CMC, the dendrimer was characterized for its hydrophilic-lipophilic balance (HLB) in order to predict its self-assembly behaviour in water and its capacity to solubilize PERFECTA.

a)

$$HLB_{BFTG2-OH} = 20 \cdot \frac{616\frac{g}{mol}}{1447\frac{g}{mol}} = 8.5$$

b)

$$HLB_{BFTG2-S} = 20 \cdot \frac{2240\frac{g}{mol}}{3138\frac{g}{mol}} = 14.3$$

c)

Surfactant solubility / Behaviour in water	HLB number		Application
No dispersibility in water	0, 2		–
Poor dispersibility	4, 6		W/O emulsifier
Milky dispersion, unstable	8		Wetting agent
Milky dispersion, stable	10		Wetting agent
Translucent-to-clear-solution	12, 14	Detergent	O/W emulsifier
Clear solution	16, 18	Solubilizer	O/W emulsifier

Figure 2.9 *a) Picture of BFTG2-OH suspension in water. b) Picture of BFTG2-S suspension in water. On the bottom HLB determination of BFTG2-OH vs BFTG2-S are reported. Equation of Griffin was used.* [123] c) *The hydrophobic-lipophilic balance (HLB) scale – "Griffin scale".*[126]

According to the HLB scale proposed by Griffin (**Figure 2.9c** and **Section 1.3.1**)[123,124], BFTG2-S (HLB = 14.3) has a much higher capacity of solubilizing in water than BFTG2-OH (HLB = 8.5). These HLB values determined also which type of suspension should be obtained after the dispersion of the dendrimer. Specifically, BFTG2-S should result in a translucent-to-clear solution, whereas BFTG2-OH should produce a milky dispersion. Experimentally, the prediction was perfectly verified as shown in **Figure 2.9a** and **2.9b**, confirming the lower solubility of the BFTG2-OH in the medium than the sulphated dendrimer. Following the same estimation, BFTG2-S should be applied as O/W

emulsifier (**Figure 2.9c**), and it should behave as a detergent/solubilizer. On the contrary, 8.5 obtained from BFTG2-OH classified the dendrimer as a wetting agent, with a lower ability to dissolve and to be dissolved in water than BFTG2-S. Therefore, in line with the HLB scale, the sulphated dendrimer was expected to solubilise PERFECTA better then BFTG2-OH.

Then, BFTG2-S was tested to dissolve PERFECTA in water, following the nanoprecipitation protocol. An ethyl acetate solution containing 5 mg of PERFECTA was added dropwise to a 5 mg/mL solution of BFTG2-S. Similarly to BFTG2-OH, the size distribution of the aggregates was evaluated both in terms of intensity and volume. Interestingly, the self-assembly of bare BFTG2-S produced aggregates of different sizes, a small one with a diameter of 8 nm, a medium of ~ 280 nm and a bigger one of a micrometric size which could not be removed by centrifugation. However, the DLS volume distribution individuated only one predominant population of few nanometre dimension (**Figure 2.10**).

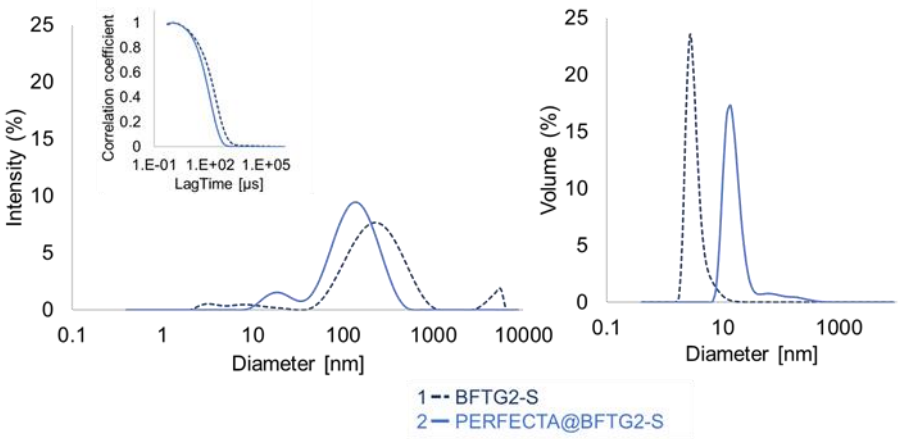

Hydrodynamic diameter distribution	1	2
Size by intensity [nm]	4643 ± 34 281 ± 28 8 ± 1	148 ± 6 12 ± 3
Size by volume [nm]	6 ± 0.1	14 ± 2 nm
PDI	0.55 ± 0.03	0.43 ± 0.02

Figure 2.10 *DLS charts of size distribution vs intensity (left) and size distribution vs volume (right); on the bottom PDI, diameter distribution by intensity and volume are reported for formulation 1 (BFTG2-S) and 2 (PERFECTA@BFTG2-S). Standard deviations were reported considering n=3.*

This result was consistent with the theoretical considerations about HLB values and the corresponding different types of architectures expected for BFTG2-S and BFTG2-OH.

On the other hand, it was curious that the supramolecular aggregates found in PERFECTA@BFTG2-S and PERFECTA@BFTG2-OH solutions had identical dimensions: 14 ± 2 nm vs 13 ± 1 nm, respectively.

The difference between the formulations was definitively shown by NMR (**Figure 2.11**). The encapsulation of PERFECTA was much higher with BFTG2-S, which gave a loading of ~ 3.9 mg/mL (78% of the starting 5 mg, **Figure 2.11**), while only 2.7 mg/mL were achieved with BFTG2-OH (54%, **Figure 2.7c**).

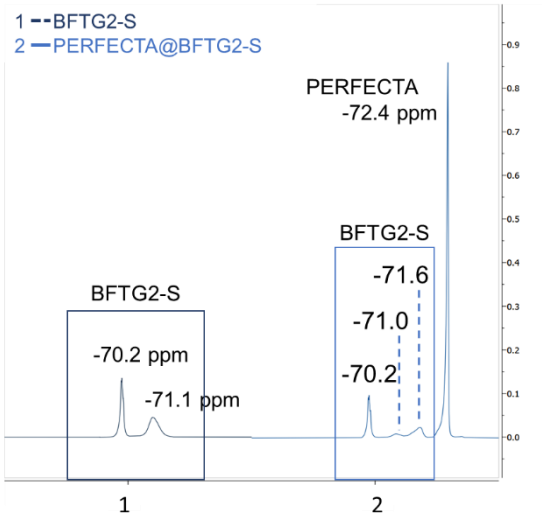

Concentration	1	2
[PERFECTA] mg/mL	-	3.9 ± 0.7
[BFTG2-S] mg/mL	2.9 ± 1.7	4.3 ± 0.9
F/mL total	1.5×10^{19}	10.5×10^{19}

Figure 2.11 *^{19}F-NMR spectra of 1 and 2 in water. Chemical shifts are referred to an external reference of TFA in D_2O set at -75.5 ppm. Standard deviations were reported considering n=3.*

Interestingly, BFTG2-S originated more than one resonance peak in water, both in the presence and in the absence of PERFECTA. This behaviour was already reported for anionic dendrimers.[197–200] The downfield signal (-70.2 ppm) in the spectrum of BFTG2-S probably belonged to the monomer state of the dendrimer, while the peak at -71.1 ppm was related to the self-assembled architecture, probably micelles.[195,198] The presence of one more peak (-71.6 ppm) in PERFECTA@BFTG2-S, closer to PERFECTA signal, could be related to those micelles involved in F-F interactions with PERFECTA. The complexity of the system and the exchange between different populations of aggregates would be interesting to be studied in detail. Because of the poor amount of BFTG2-S available, this study will be carried on in the future, after synthesizing a new batch of dendrimer. By the way, NMR results

confirmed that PERFECTA@BFTG2-S system was polydisperse, probably containing not only mixed aggregates, but also monocomponent of only BFTG2-S.

2.2.3 Morphological characterization

The diversity of the supramolecular assemblies afforded by the different methods of preparation, the presence of PERFECTA, and the different type of dendrimer was investigated by cryogenic transmission electron microscopy (cryo-TEM). Pictures were acquired by Dr. Boris Shade (FUB).

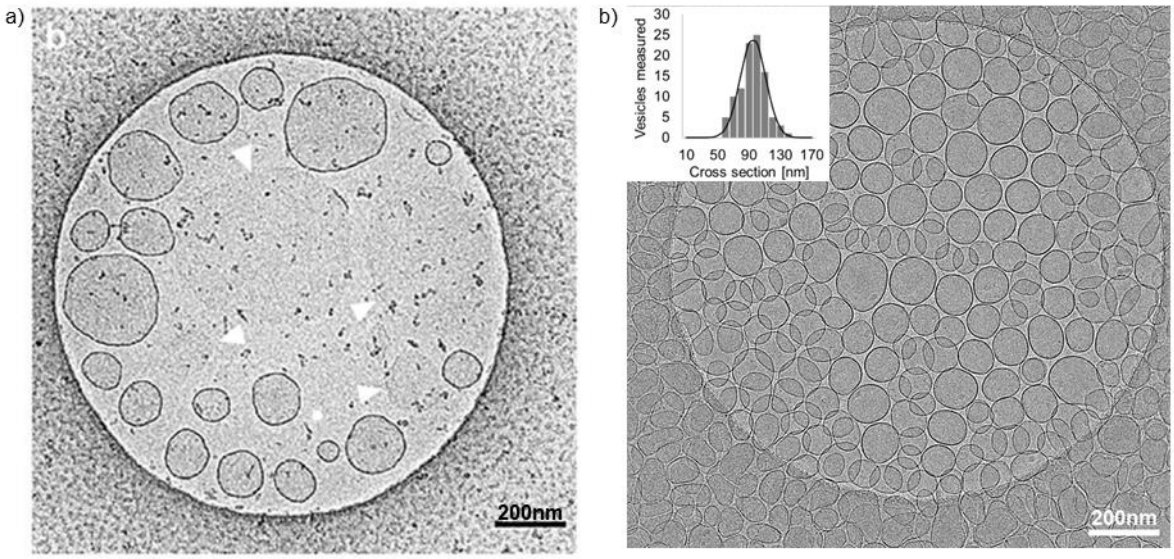

Figure 2.12 *a) Cryo-TEM analysis of BFTG2-OH in water.*[181] *b) Cryo-TEM analysis of PERFECTA@BFTG2-OH formulation through thin film method. The insert shows the cross section distribution calculated upon measurement of 100 vesicles.*

The thin film method gave supramolecular architectures similar to those reported in the literature for the same dendrimer.[181] Vesicles were clearly well defined in both cases (**Figure 2.12**), and the presence of PERFECTA did not alter the overall morphology, but conferred a strong reproducibility to the vesicles size. This result was consistent with DLS data (**Section 2.2.1**, **Figure 2.4a**), confirming both the low polydispersity and the reduction of vesicles diameter. The average cross section was measured to be 97 ± 17 nm and matched perfectly the 109 ± 3 nm value measured by DLS. The low encapsulation yield of PERFECTA could be due to the fact that PERFECTA might be positioned in between the bilayer formed by BFTG2-OH, where its polar head with eight -OH groups was exposed to the water environment, while the F27 building block was confined inside. If PERFECTA and F27 could come into contact only in this latter region, only a reduced amount of PERFECTA might fit in.

Cryo-TEM analysis of BFTG2-OH in water, obtained through nanoprecipitation (**Figure 2.13a**) evidenced vesicles similar to the previous ones (**Figure 2.12a**). Surprisingly, a complete change of self-assembly was observed after addition of PERFECTA (**Figure 2.13b-c**), when vesicles were mostly replaced by micelles.

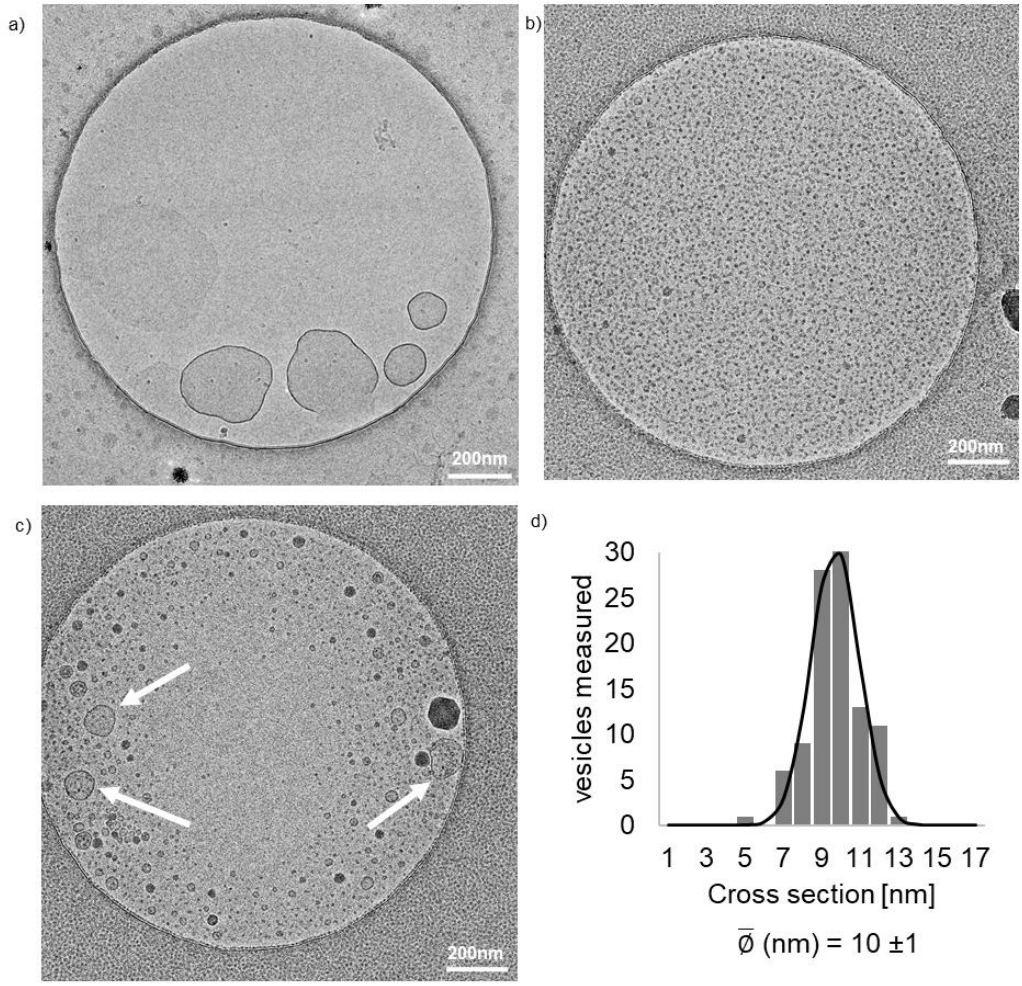

Figure 2.13 *a) Cryo-TEM analysis of BFTG2-OH formulated by nanoprecipitation in water. b-c) Cryo-TEM analysis of PERFECTA@BFTG2-OH formulation through nanoprecipitation method. White arrows indicate vesicles observed. d) Cross section distribution calculated upon measurement of 100 micelles.*

Dynamic light scattering investigation confirmed these morphological observations. The diameter obtained fitting DLS data showed ~ 14 nm of cross section, and the medium diameter calculated upon the measure of 100 micelles was around 10 nm. The difficulty of manual measuring such small architectures could justify the little discrepancy between the two techniques. This impressive change of self-assembly between thin film and nanoprecipitation methods determined also the different loading of ^{19}F MRI probe. The amount of PERFECTA which could be stably loaded in the micelles

was considerably higher than in the vesicles. It was probably easier to prevent the contact of PERFECTA with the aqueous solvent within micelles, than in the vesicles' bilayer.

The cryo-TEM analysis of BFTG2-S confirmed the expectations, according to HLB considerations. The higher solubility of the dendrimer and the obtainment of a clear solution was supported by the presence of small micelles in the cryo-TEM picture reported (**Figure 2.13a**).

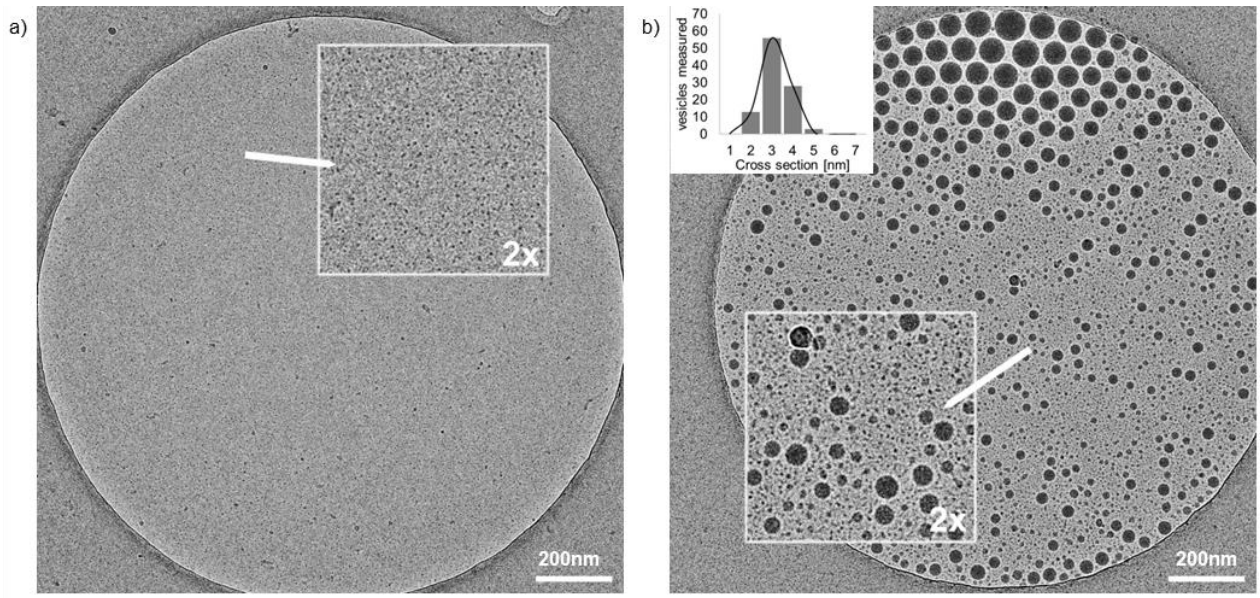

Figure 2.13 *a) Cryo-TEM analysis of BFTG2-S formulated by nanoprecipitation in water. b) Cryo-TEM analysis of PERFECTA@BFTG2-S formulation through nanoprecipitation method. The insert shows the cross section distribution calculated upon measurement of 100 micelles.*

Due to low contrast and small size, it was not possible to accurately measure the size of the micelles given by BFTG2-S, and so they were supposed to be smaller than those obtained by PERFECTA@BFTG2-S (average diameter of 3 nm). Considering the experimental error due to manual measurement, this result was not significantly different from what found by DLS, and it confirmed that the presence of PERFECTA increases the dimension of aggregates. A resume of the data was furnished in the following **Table 2.3**.

Table 2.3 *Comparison between size of the aggregates measured by DLS versus cryo-TEM for all the formulation tested.*

Formulation	Formulation method	DLS size ($\bar{\emptyset}$ nm)	Cryo-TEM size ($\bar{\emptyset}$ nm)
BFTG2-OH	Thin film	500 ± 3 nm	~ 280*
PERFECTA@BFTG2-OH	Thin film	109 ± 3	97 ± 17
BFTG2-OH	Nanoprecipitation	326 ± 17	~ 265*
PERFECTA@BFTG2-OH	Nanoprecipitation	14 ± 1	10 ± 1
BFTG2-S	Nanoprecipitation	8 ± 1	< 3**
PERFECTA@BFTG2-S	Nanoprecipitation	12 ± 3	3 ± 1

** Amount of aggregates observed was too low to determine a statistical standard deviation*
*** Aggregates size was too small to be measured manually*

2.2.4 ^{19}F-MRI performance

The suitability of these formulations for magnetic resonance imaging was assessed through the initial evaluation of the relaxation properties of their components. In particular, three samples were tested:

1. PERFECTA@BFTG2-OH formulated *via* thin film method
2. PERFECTA@BFTG2-OH formulated *via* nanoprecipitation
3. PERFECTA@BFTG2-S formulated *via* nanoprecipitation

T_1 – spin-lattice relaxation – and T_2 – spin-spin relaxation – were determined through specific experiments by ^{19}F-NMR. It was already mentioned that a good MRI probe should have a sufficiently short T_1, in order to improve signal brightness and SNR, and a long T_2 to guarantee signal detection. Information about PERFECTA relaxation properties were already available in the literature,[62] with T_1 ranging from 350 to 700 msec and T_2 = ~ 200 msec, depending on the carrier (protein, polymer or surfactant).[62,65,195,201]

Table 2.4 *Experimental T_1 and T_2 relaxation times*

Method	Formulation code		T_1 [msec]	T_2 [msec]
Thin film	**1** PERFECTA@BFTG2-OH	BFTG2-OH	381	25
		PERFECTA	420	60
Nanopre-cipitation	**2** PERFECTA@BFTG2-OH	BFTG2-OH	400	35
		PERFECTA	460	101
Nanopre-cipitation	**3** PERFECTA@BFTG2-S	BFTG2-S	497	44
		PERFECTA	489	110

Since the peak of PERFECTA was not overlapped to ^{19}F-NMR signals of the dendrimers, it was possible to separately evaluate T_1 and T_2 of each component of the formulations. From **Table 2.4** PERFECTA and dendrimers always displayed similar spin-lattice relaxation times, shorter than what reported for PERFECTA in the literature. Similarly, T_2 was always shorter. In detail, the MRI probe showed quite good T_2 in the case of formulations **2** and **3**. In formulation **1** the rigidity of the vesicles affected the -CF_3 mobility and its spin-spin relaxation was the shorter recorded among all the formulations. Formation of micelles might improve the mobility of fluorine atoms, and resulted in T_2 > 100 msec, which could be considered effective for MRI. Regarding the dendrimers, without any doubt BFTG2-OH was more rigid than BFTG2-S, and gave a very short T_2 which could blur the MRI signal.

Given the promising results of PERFECTA encapsulation and the acceptable relaxation properties, ^{19}F-MRI measurements were performed by Dr. Cristina Chirizzi, thanks to the collaboration with San Raffaele Hospital and Istituto Neurologico "Carlo Besta".

^{19}F-MRI was performed on phantoms containing undiluted PERFECTA formulations (**Figure 2.14a-b**) using a 7T instrument. The low amount of PERFECTA loaded in the vesicles of formulation **1** gave a MRI signal with a very low contrast. Additionally, the short T_2 worsened the analysis. In the images of formulations **2** and **3**, the brightness of the two signals was immediately verified, visible as a red spots over a black background. The resonance signals were recorded setting the pulse radiofrequency for the experiment in between the ^{19}F chemical shift frequencies of the dendrimer – BFTG2-OH or BFTG2-S – and PERFECTA. SNR was measured on a slice corresponding to a sample volume ranging from 24.5 to 31.6 µL for all formulations.

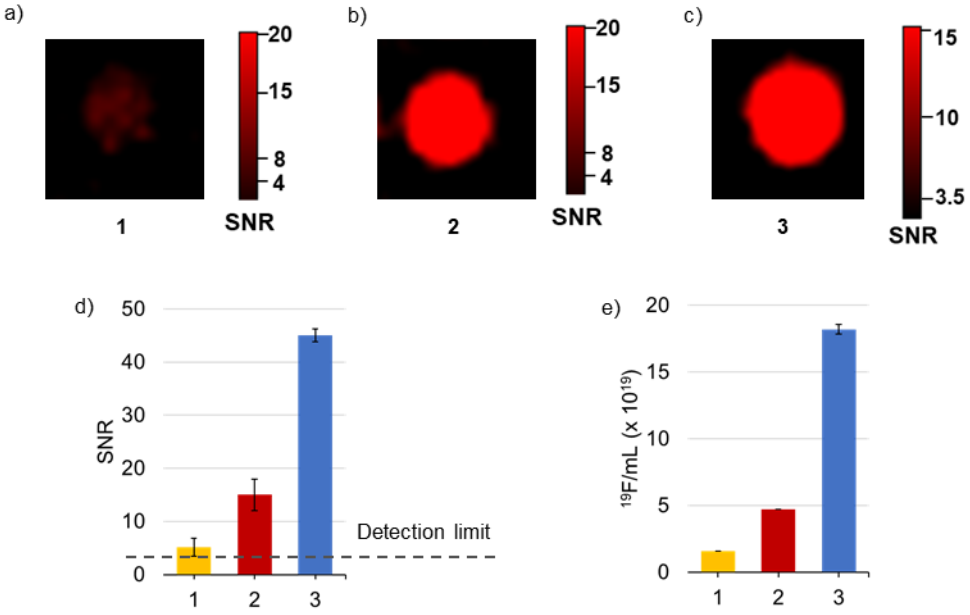

Figure 2.14 *a-c) ^{19}F-MRI of PERFECTA formulations 1, 2, 3 with their respective SNR scale. d) quantification of the SNR for each sample. e) ^{19}F/mL quantification obtained with the usage of proper references. Standard deviation were calculated upon 3 replicates.*

The evaluation of SNR made possible to identify the detection limit, which was very close to the signal originated by formulation **1** (**Figure 2.14d**). On the other side, **2** and **3** were distant from the limit and this justified the good spot visualized. Then, experiments were conducted in the presence of external references, to quantify the MRI active F/mL in each sample. More details are provided in the **Experimental section 2.4**.

Table 2.5 *F/mL quantification for formulation **1**, **2** and **3**. Quantification by NMR was reported as contribute in F/mL from PERFECTA and the respective dendrimer. Then, the total amount was compared with the MRI quantification.*

	^{19}F NMR (F/mL x 10^{19})			^{19}F MRI (F/mL x 10^{19})
	PERFECTA	Dendrimer	Total	Total
1	0.75	BFTG2-OH 4.23	4.98	1.6 ± 0.94
2	4.76	BFTG2-OH 5.23	9.99	4.7 ± 0.94
3	15.1	BFTG2-S 1.9	17.0	18.2 ± 2.41

The number of ^{19}F atoms/mL obtained by MRI was compared with the quantification acquired by NMR (**Table 2.5**). As expected, the amount of resonant fluorine atoms for formulation **1** and **2** mainly derived from PERFECTA. This could be due to the too short T_2 of BFTG2-OH, which caused signal

decay before the end of the acquisition. On the contrary, formulation **3**, surprisingly, showed the amount of F/mL corresponding to the summary contribution of PERFECTA and BFTG2-S.

In summary, BFTG2-S demonstrated to be strongly interesting not only as emulsifying agent for PERFECTA, but also for MRI. Its T_2 resulted to be long enough to be detected, improving the overall signal quality. The results of this preliminary MRI screening seemed to identify formulation **3** as the best candidate for imaging purposes.

2.2.5 Cellular compatibility and uptake

In order to evaluate the potential of these formulations for in vivo administration, cytotoxicity was an important aspect to be addressed. Two different cellular lines were tested, namely HeLa cells and monocyte macrophages U937. The former was chosen to have a direct comparison with the reference article,[181] while U937 are known to be main actors in inflammatory response, and consequently they could be actively targeted by the sulphated dendrimer.[182]

Cells were incubated with diluted formulations in order to reach a final dendrimer concentration of 0.5, 0.25, 0.125 mg/mL, respectively, and viability was assessed after 24 h using the CCK8 assay (**Figure 2.15**).

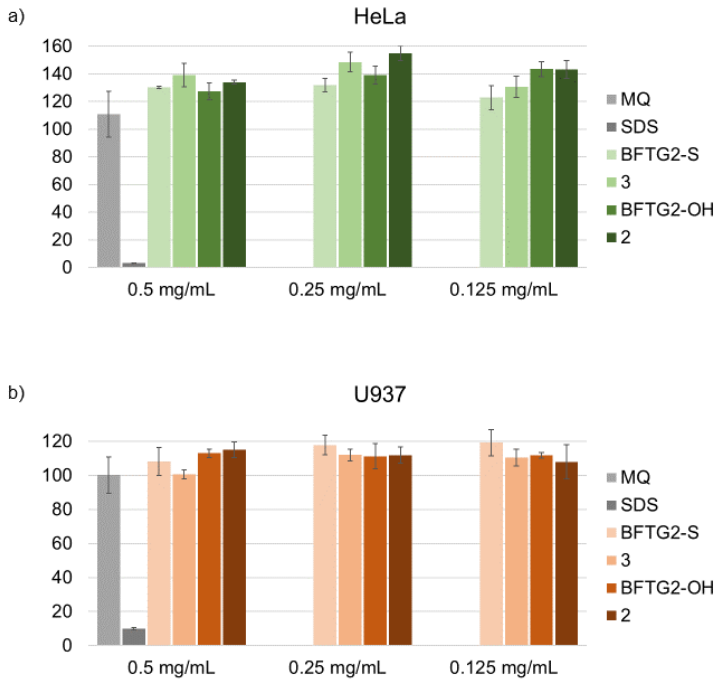

Figure 2.15 *Cell viability of HeLa cells and U937 incubated with BFTG2-S, formulation 3, BFTG2-OH and formulation 2 for 24 h. Cell viability was determined using a CCK8 assay (Sigma–Aldrich). Each bar represents the mean value of three experiments. Sodium dodecyl sulphate (SDS) (1%) and Milli-Q water (MQ) treated cells served as a control.*

Only formulations **2** and **3** were tested, according to the preliminary ^{19}F-MRI performance, and compared to formulations of BFTG2-OH and BFTG2-S as controls. All the developed systems exhibited no cytotoxicity, and could be potentially appropriate for use in biological applications.

A preliminary uptake experiment was also performed, using fluorescent formulations analogous to **2** and **3**, prepared encapsulating both PERFECTA and the dye Nile Red in the same step. A stock solution of Nile Red (1 mg/mL) in ethyl acetate was prepared, and 100 µL of it were added to PERFECTA solution in ethyl acetate. The mixture was added dropwise to the stirred water solution of dendrimer, and then treated according to the optimized nanoprecipitation protocol described in **Section 2.2.1**. HeLa and U937 cells were then treated with Nile Red loaded formulations. After 9 h of incubation, confocal microscopy images were acquired thanks to the collaboration with SupraFAB (FUB). As positive control, a Nile Red solution in DMSO was used and cell nuclei were stained with Hoechst, becoming visible as blue spots (**Figure 2.16**).

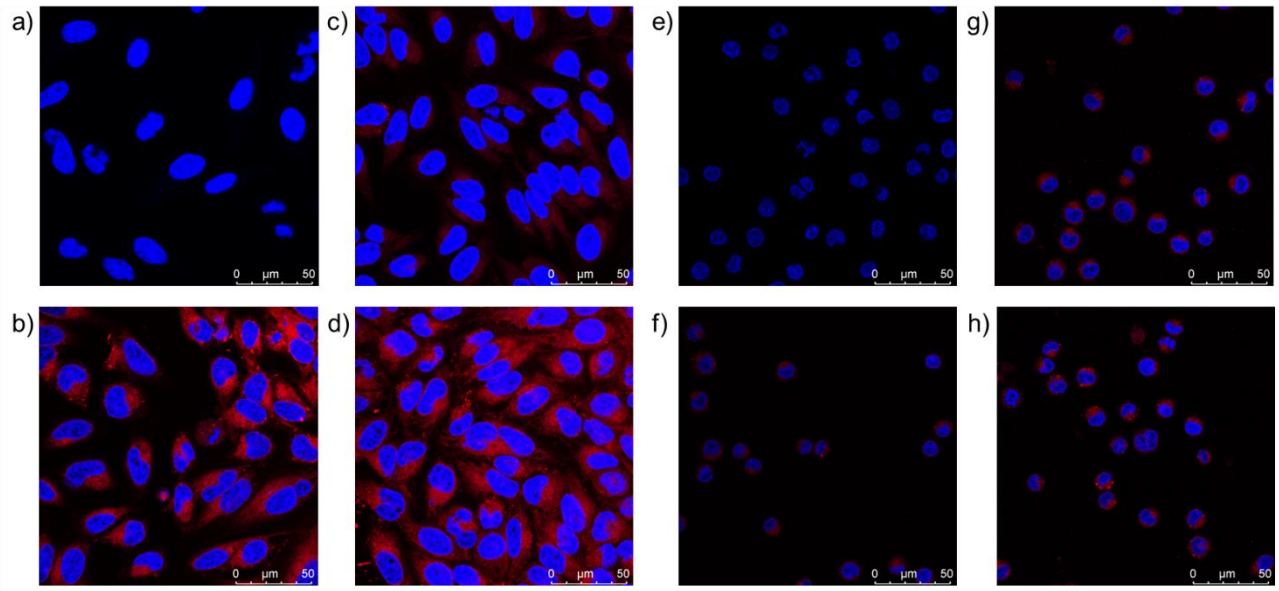

Figure 2.16 *Fluorescence microscopy images of stained nuclei (negative control) of HeLa cells (a) and U937 cells (e). Positive control of Hela cells (b) and U937 (f) treated with a solution 0.0002 mg/mL of Nile Red in DMSO. Cellular uptake images of formulation **2**' Nile Red internalized by Hela cells (c) and U937 (g). Cellular uptake images of formulation **3**' Nile Red internalized by in Hela cells (d) and U937 (h).*

The experiments showed that the Nile Red (visible as red spots) loaded by formulation **2** and **3** was uptaken from both cell lines. In particular, HeLa cells seemed to display a higher intensity of fluorescence after the treatment with formulation **3** than with formulation **2**, suggesting a higher uptake of the former (**Figure 2.16 c-d**). On the other hand, no particular difference could be observed

for U937. From this experiment it could be concluded that formulations were uptaken from both cell lines and the uptake did not affect cellular viability, consistently with cytotoxicity tests.
The internalization of Nile Red was not the proof that PERFECTA was effectively internalized. In order to proceed with further MRI experiments on cells, there was the necessity to demonstrate the carrier efficacy of dendrimers. Thus, after incubation of HeLa and U937 cells with formulation **2** and **3** (0.5 mg/mL of dendrimer) for 24 h, cells were washed, counted and lysate using TRITON X detergent. The cellular lysate was analysed by ^{19}F-NMR to evaluate the success of uptake and the amount of ^{19}F/cell. For the quantification, an external reference of trifluoroacetic acid (TFA) in D_2O was used. Preliminary data obtained for one single sample will be replicated in the future.

Table 2.6 *Quantification of ^{19}F/mL uptaken in comparison with the F/mL administered to HeLa cells uptake. Values are referred to the sum of both contributes of dendrimer and PERFECTA. Total amount of F/cell and percentage of uptake are also reported. The uptake refers to the F/mL uptaken vs administered.*

HeLa				
Sample	^{19}F/mL (x 10^{19}) administered	^{19}F/mL (x 10^{19}) uptaken	^{19}F/cell (x 10^{13})	% uptaken
Formulation **3**	2.73	0.096	1.63	**3.5**
BFTG2-**S**	0.25	0.031	0.35	**12.5**
Formulation **2**	2.96	0.11	0.69	**3.7**
BFTG2-**OH**	1.61	0.06	0.58	**3.7**

Data exposed in **Table 2.6** did not evidence a significantly different uptake between the two formulations, with a percentage around 4 % in both cases. A curious increase in internalisation was found for the control BFTG2-S. As these data have to be repeated, it is not safe to make considerations about the possible reasons of this phenomenon. Anyway, a further increase was obtained with the administration of BFTG2-S to U937 macrophages (12.5% for Hela *versus* 23.7% for U937) (**Table 2.6** and **2.7**), which could be due to the selectivity of the sulphated dendrimer for targeting inflammatory cells.

Table 2.7 *Quantification of ^{19}F/mL uptaken in comparison with the F/mL administered to U937 cellar uptake. Values are referred to the sum of both contributes of dendrimer and PERFECTA. Total amount of F/cell and percentage of uptake are also reported. The uptake refers to the F/mL uptaken vs administered.*

U937				
Sample	^{19}F/mL (x 10^{19}) administered	^{19}F/mL (x 10^{19}) uptaken	^{19}F/cell (x 10^{13})	% uptaken
Formulation **3**	2.73	0.17	1.34	**6.3**
BFTG2-**S**	0.25	0.06	0.52	**23.7**
Formulation **2**	2.96	0.11	1.03	**3.7**
BFTG2-**OH**	1.61	-	-	**-**

Moreover, the comparison between the uptake of formulations **2** and **3** displayed a significant difference, 3.7 % *vs* 6.3 %. This result enhanced the initial hypothesis and pushed the conclusion that BFTG2-S could be the best candidate for further optimization and in vivo ^{19}F-MRI tests. The absence of internalization of BFTG2-OH could be due to handling problems during the experiment, thus it will be necessary to replicate the experiment.

2.2.6 Fluorinated *versus* hydrogenated dendrimers

As a final proof of the intense F-F interactions between PERFECTA and F27 moiety of BFTG2-OH and BFTG2-S, the hydrogenated counterpart of BFTG2-OH was synthesised for the first time. This dendrimer, called BHTG2-OH (**Figure 2.1**) was used for comparison to test the superiority of the fluorinated one, as well as to verify the possibility to encapsulate PERFECTA through hydrophobic interactions instead of *fluorous effect*.

Again, the hydrophilic part of the dendrimer was provided by FUB, while I synthesised the hydrophobic part. The procedure for this synthesis has never been reported before, and was carried out through 4 steps, starting from pentaerythritol and *t*-butyl acrylate. Details about the synthesis of BHTG2-OH are reported in the **Experimental section 2.4**.

The estimated HLB of 12.8 defined BHTG2-OH as dendrimer with detergent behaviour, that could act as O/W emulsifier similarly to BFTG2-S. The solubilization of this hydrogenated derivative formed one main population of aggregates, observed by volume distribution through DLS (**Figure**

2.17). These self-assembled architectures had an approximate diameter of 8 nm, comparable with the micelles of the sulphate dendrimer and consistent with HLB. The high PDI was justified by the presence of bigger aggregates, which appeared in the intensity distribution of size (**Figure 2.17**).

The nanoprecipitation protocol was used to encapsulate PERFECTA also in this case, starting from a 5 mg/mL solution of BHTG2-OH. The outcome was a high polydisperse formulation, which displayed two main populations, a bigger one of 250 nm and a smaller of 49 nm, very different from what obtained with the bare dendrimer (**Figure 2.17**).

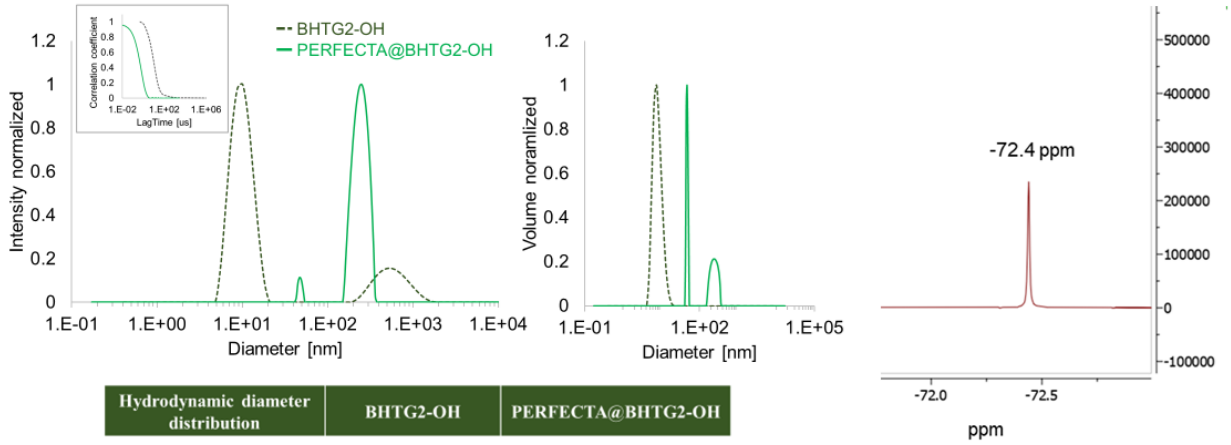

Hydrodynamic diameter distribution	BHTG2-OH	PERFECTA@BHTG2-OH
Size by intensity [nm]	493 10	250 49
Size by volume [nm]	8	287 47
PDI	0.32	0.55

Figure 2.17 *left) DLS chart of size distribution vs intensity and size distribution vs volume; on the bottom PDI, diameter distribution by intensity and volume are reported for BHTG2-OH and PERFECTA@BHTG2-OH. Right)* ^{19}*F-NMR spectra of PERFECTA@BHTG2-OH in water. Chemical shifts are referred to an external reference of TFA in* D_2O *settled at -75.5 ppm.*

Unfortunately, ^{19}F-NMR analyses were not much encouraging (**Figure 2.17**). The quantified amount of PERFECTA was 0.07 mg/mL, equivalent to 1 % of total encapsulation. The amount of 0.15 x 10^{19} F/mL was too low for any further application in ^{19}F-MRI.

This last result confirmed that fluorine-fluorine interactions are necessary to stabilize PERFECTA in water, determining the straightforward superiority of the fluorinated dendrimer for this purpose.

2.3 PERFECTA@protein complexes: interaction study

In collaboration with the University of Bologna, PERFECTA was encapsulated within BSA and LYS, originating two new systems PERFECTA@BSA and PERFECTA@LYS. In particular, the calculated volume of BSA was ~ 120 nm^3 (ellipsoid with dimensions: 14.0 x 4.0 x 4.0 nm)[202] while for LYS was ~ 21 nm^3 (ellipsoid with dimensions: 4.5 x 3.0 x 3.0 nm)[203]. Thus, considering that PERFECTA has an estimated volume of ~ 3 nm^3,[62] more than one molecule of PERFECTA could be hosted by both proteins. Additionally, BSA has more than one hydrophobic cavity which could possibly interact with PERFECTA. For this reasons, different stoichiometric ratios between PERFECTA and proteins were analysed.

2.3.1 Characterization of the formulations

Formulations were prepared by Dr. M. Di Giosia, research assistant at Prof. Calvaresi group (University of Bologna) by ultrasonication of the protein aqueous solution in the presence of solid PERFECTA. The procedure was previously developed by the same group to formulate fullerenes C60 and C70 with the same proteins.[106,193] Samples were analysed here at Politecnico of Milano.

The loading of PERFECTA was quantified through ^{19}F-NMR, by means of an external reference of TFA in D_2O. Additionally, characterization of the hydrodynamic size of the protein particles was performed by multiangle dynamic light scattering.

PERFECTA@BSA (in this chapter PERFECTA will be abbreviated as “P”, consequently the protein complexes will be named P@BSA and P@LYS) were prepared in different molar ratios in order to investigate the presence of discrete cavities able to host PERFECTA. Two conditions with an excess of PERFECTA were studied (6:1 and 2:1 molar ratio between PERFECTA and BSA), two samples with an excess of BSA (1:2 and 1:4), and one in equimolar ratio 1:1. As shown in **Table 2.8**, a fixed amount of PERFECTA was used for all the samples, while the amount of BSA was changed according to the different molar ratios. It is worth to mention that increasing the protein concentration determined a rise in viscosity of the final solution. For this reason, sample P@BSA 6:1 was prepared by halving the concentration of PERFECTA from 1 mM to 0.5 mM and maintaining a 2 mM concentration of BSA, the highest which could be reached without hampering its handling.

Table 2.8 *Samples analysed with the theoretical concentrations of BSA and PERFECTA used for the formulation.*

Sample code	Molar ratio PERFECTA:BSA	[BSA] mM (mg/mL)	[PERFECTA] mM (mg/mL)
P@BSA	6:1	0.17 (11.0)	1.0 (1.0)
	2:1	0.5 (33.0)	1.0 (1.0)
	1:1	1.0 (66.0)	1.0 (1.0)
	1:2	2.0 (132.0)	1.0 (1.0)
	1:4	2.0 (132.0)	0.5 (0.5)
BSA	-	1.0 (66.0)	-

^{19}F-NMR spectra acquired from aqueous samples showed the presence of a signal (**Figure 2.19a**), that could derive only from PERFECTA. Interestingly, the shape of this signal was far away from the classical sharp peak of this ^{19}F-MRI probe. Indeed, the typical peak at 72.4 ppm observed also with the dendrimers in **Chapter 2.2**, was accompanied by another broad peak with a close chemical shift. Furthermore, the latter did not disappear when increasing the acquisition temperature from 32°C to 40°C (**Figure 2.19b**). This result could be due to the presence of different binding sites for PERFECTA. Thus, molecules in the different pockets might generate diverse ^{19}F signals by virtue of changed environment. This observation could confirm that there were more than one nonpolar cavity in BSA which could play a hosting role. Additionally, if this hypothesis was correct, there seemed to be no specific priority in binding PERFECTA among the available sites. An excess of protein, such as in case of P@BSA 1:4, should originate a predominant peak, corresponding to the binding site with the highest affinity for PERFECTA. On the other hand, the increase of the guest concentration should originate a second peak because of the saturation of the first site. This was not the case, and both the peaks appeared in all cases, suggesting an equal affinity of the sites.

Moreover, the quantification of encapsulated PERFECTA revealed always an amount between 65-70%. Even an excess of probe, as in P@BSA 6:1, did not induce an increased loading. In addition, a 0.7 mM concentration of PERFECTA (corresponding to 70% of encapsulation) corresponded to the presence of ~ 1.5 x 10^{19} F/mL, very close to ^{19}F-MRI detection limit observed in Section 2.2.4. This

makes these samples scarcely suitable for MRI purposes. The situation could be improved by concentrating the samples to consequently increase F/mL, but this would affect their viscosity, making this solution not practicable.

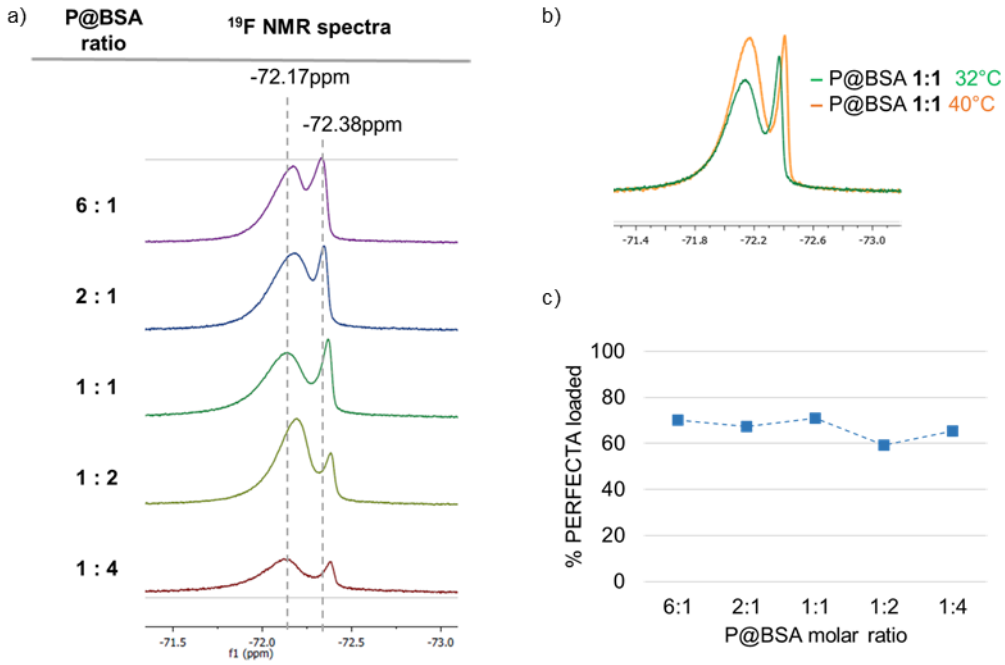

Figure 2.19 *a) ^{19}F-NMR spectra of P@BSA samples described in* ***Table 2.8****. Chemical shifts and quantification were referred to an external reference of TFA in D_2O, settled at -75.5 ppm. b) Comparison between ^{19}F-NMR spectra of sample P@BSA 1:1 acquired at different temperatures. c) Amount of PERFECTA loaded were reported as percentage for each sample.*

Samples were then characterized by multiangle DLS (**Figure 2.20**). All formulations had a high polydispersity index (0.3 < PDI < 0.5), and in all cases more than one population were identified. Excessive polydispersity prevented the determination of the size for sample P@BSA 1:2 and for BSA alone, proving that the presence of high amounts of BSA afforded worse results. Additionally, a big difference in size was appreciated with increasing amounts of guest. Particle size decreased of near 40% with an excess of PERFECTA (~ 120 nm), compared to the 1:1 ratio (~ 190 nm).

Considering that the best results were obtained with P@BSA 1:1 and 2:1 and 6:1, T_1 and T_2 experiments were conducted on these samples. The following relaxation times were found:

- P@BSA 1:1 → T_1 = 646 msec; T_2 = 31 msec
- P@BSA 6:1 → T_1 = 663 msec; T_2 = 33 msec

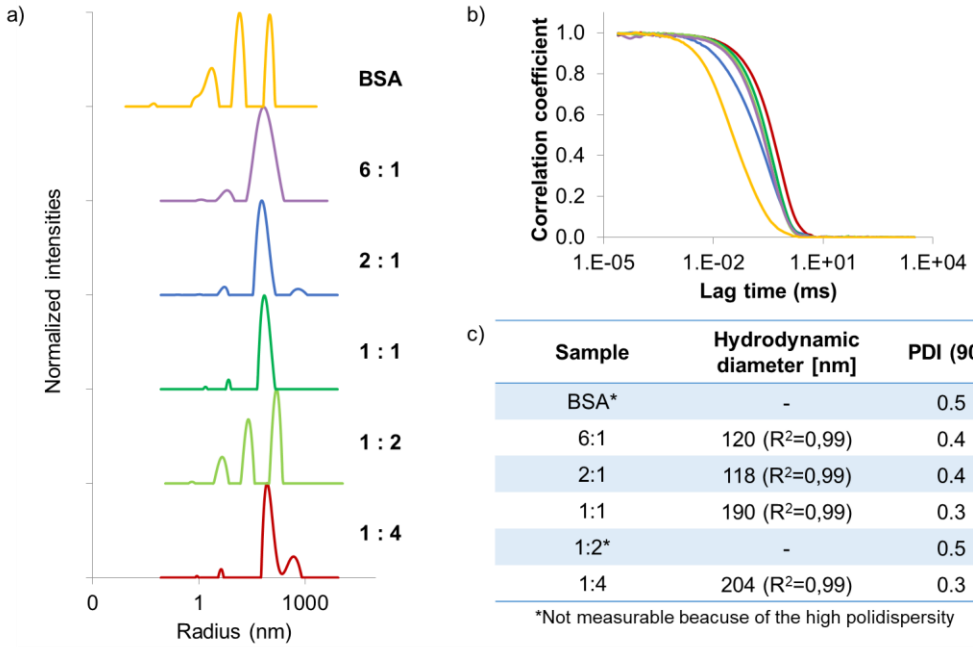

c)

Sample	Hydrodynamic diameter [nm]	PDI (90°)
BSA*	-	0.5
6:1	120 (R^2=0,99)	0.4
2:1	118 (R^2=0,99)	0.4
1:1	190 (R^2=0,99)	0.3
1:2*	-	0.5
1:4	204 (R^2=0,99)	0.3

*Not measurable beacuse of the high polidispersity

Figure 2.20 *a) Comparison between DLS profiles of size distribution of samples described in* ***Table 2.8*** *measured at θ = 90°. Samples were diluted with Milli-Q water in order to reach a protein concentration of 0.2 mM. b) Auto-correlation functions of the same samples at θ = 90°. c) Hydrodynamic diameters were determined by a cumulant fitting of the auto-correlation function obtained through DLS measurements at θ = 70°, 90°, 110° and 130°.*

Even if the long T_1 and too short T_2 values were not encouraging for MRI purposes, it was still interesting to study the interactions involved between BSA and PERFECTA.

The same preliminary investigations were conducted for lysozyme. In this case, in all formulations the concentration of LYS was maintained constant (1 mM), while modifying the amount of PERFECTA to reach the desired ratio (**Table 2.9**).

Table 2.9 *Samples analysed with the theoretical concentrations of LYS and PERFECTA used for the formulation.*

Sample code	Molar ratio PERFECTA : LYS	[LYS] mM (mg/mL)	[PERFECTA] mM (mg/mL)
P@LYS	5:1	1.0 (14.0)	5.0 (5.0)
	2:1	1.0 (14.0)	2.0 (2.0)
	1:1	1.0 (14.0)	1.0 (1.0)
	1:2	1.0 (14.0)	0.5 (0.5)
LYS	-	1.0 (14.0)	-

The choice to limit the protein's concentration avoided an enhancement of solution viscosity. The presence of one single catalytic channel might assume the possibility to host one molecule at a time, potentially a 1:1 molar ratio. On the contrary, preliminary NMR quantification results obtained from screening different PERFECTA:LYS ratios displayed that a higher amount of probe could be hosted. Indeed, P@LYS 5:1 showed a higher amount that the supposed equimolar one, quantifying a PERFECTA concentration of 3.1 ± 0.3 mM (**Figure 2.21b**).

On the other side, the percentage of successful loading was around 60% in almost all cases. An exception was constituted by P@LYS 1:2, where all the 0.5 mg/mL of starting PERFECTA were detected.

Looking at the ^{19}F NMR signal, a situation similar to that observed with BSA was identified also in LYS formulations (**Figure 2.21a**). The typical peak of PERFECTA was accompanied by a second shoulder, which reached the same intensity in 1:1 molar ratio. A possible explanation of this behaviour could be the presence of a second nonpolar site able to interact with PERFECTA, different from the catalytic channel. This scenario could justify both the two different frequencies of resonance, and the loaded amount of PERFECTA higher than the expected one.

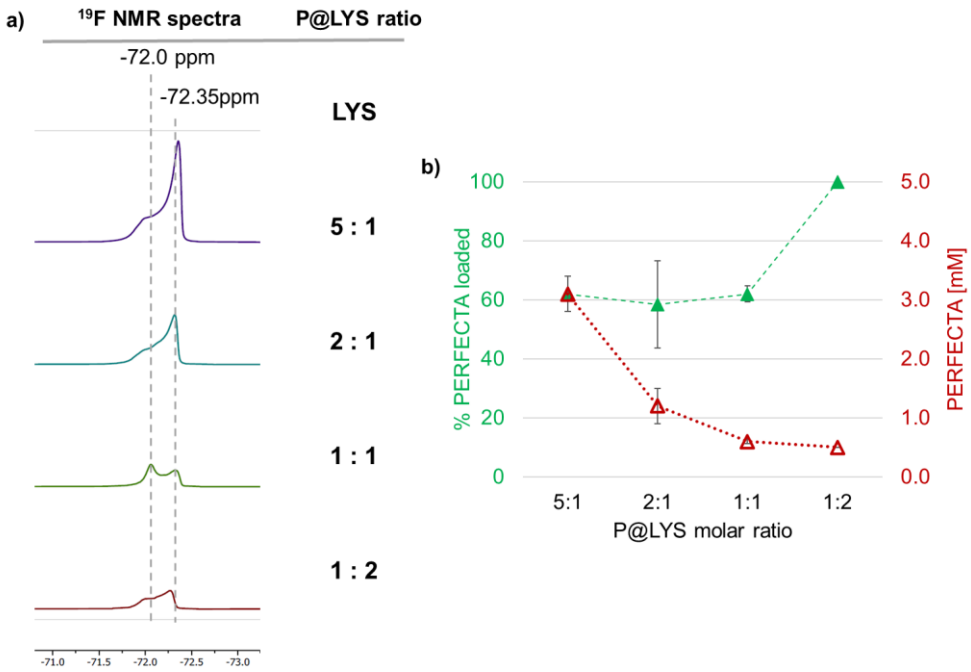

Figure 2.21 *a) ^{19}F-NMR spectra of P@LYS samples described in* ***Table 2.9****. Chemical shifts and quantification were referred to an external reference of TFA in D_2O, settled at -75.5 ppm. b) Amount of PERFECTA loaded for each sample were reported as percentage and molar concentration. Standard deviation was calculated upon analyses of 2 independent samples.*

The colloidal properties of LYS complexes were analysed through multiangle DLS (**Figure 2.22**). Although polydispersity was still high (> 0.2), a predominant scattering peak was always identified of about 40 nm of diameter. Interestingly, the presence of PERFECTA denoted a net improvement of the auto-correlation function in comparison with bare LYS. Considering the low dimension of monomeric LYS, DLS was not the ideal technique to identify such small particles. The interaction with PERFECTA increased the particle size (**Figure 2.22b**).

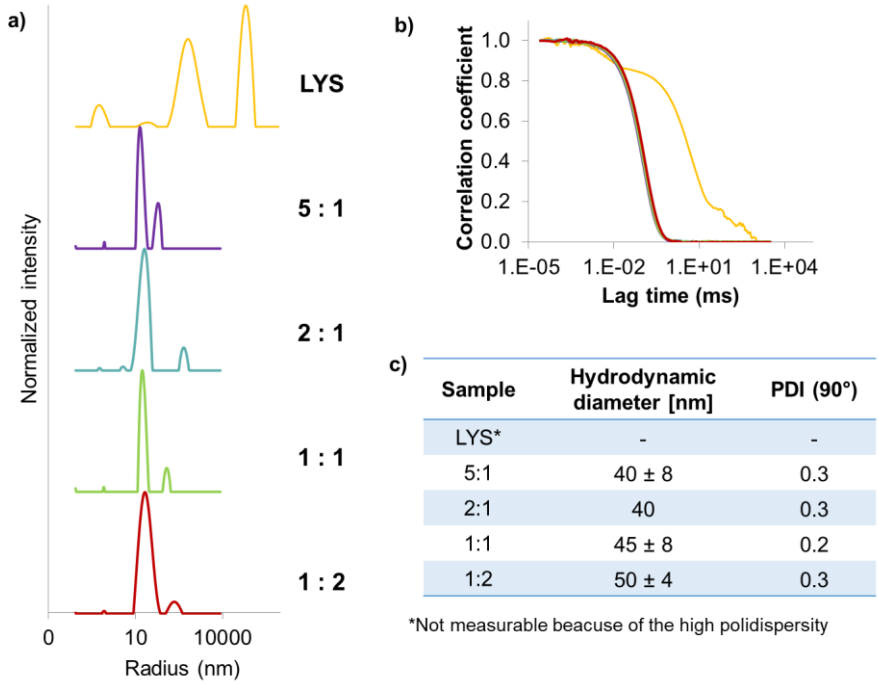

Sample	Hydrodynamic diameter [nm]	PDI (90°)
LYS*	-	-
5:1	40 ± 8	0.3
2:1	40	0.3
1:1	45 ± 8	0.2
1:2	50 ± 4	0.3

*Not measurable beacuse of the high polidispersity

Figure 2.21 *a) Comparison between DLS profiles of size distribution of samples described in* ***Table 2.9*** *measured at θ = 90°. Samples were diluted with Milli-Q water in order to reach a protein concentration of 0.5 mM. b) Auto-correlation functions of the same samples at θ = 90°. c) Hydrodynamic diameters were determined by a cumulant fitting of the auto-correlation function obtained through DLS measurements at θ = 70°, 90°, 110° and 130°. Standard deviation was calculated upon analyses of 2 independent samples (apart from P@LYS 2:1 where n=1) and fitting error was always* R^2*>0.95.*

Relaxation properties were determined for P@LYS 1:1. In particular, a T_1 of 485 msec and a very short T_2 of 35 msec were measured. Although spin-lattice relaxation was better than in BSA situation, T_2 was still too short to determine a good MRI signal. Anyway, the intriguing effect of PERFECTA upon the self-assembly of LYS, and the fact that LYS is often used as a model protein, unveiling its interactions with a high fluorinated molecule represents a hot research topic. For this reason, a structural characterization of these complexes was carried out, with a particular focus on lysozyme.

2.3.2 Structural and morphological characterization

In order to provide an insight into the structural modification occurred upon addition of PERFECTA, the spectroscopic properties of the complexes were further characterized by Attenuated Total Reflectance-Fourier Transform Infrared spectroscopy (ATR-FTIR) and circular dichroism (CD).

The latter was performed on all the samples to identify a possible effect of changes in stoichiometry (**Figure 2.22**).

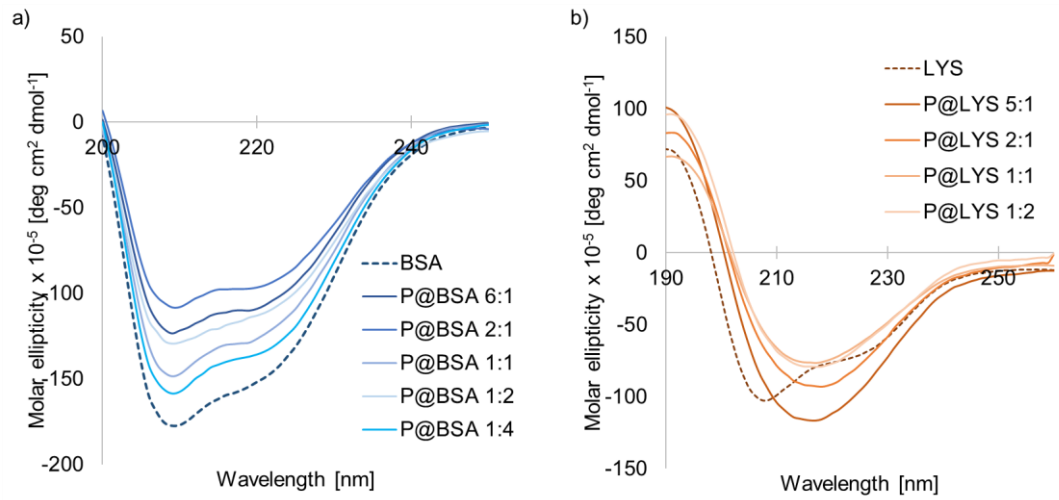

Figure 2.23 *a) CD spectra of BSA and its complexes with PERFECTA. All samples were diluted with Milli-Q water to reach a protein concentration of 0.1 mg/mL. b) CD spectra of LYS and its complexes with PERFECTA. All samples were diluted with Milli-Q water to reach a protein concentration of 0.2 mg/mL.*

Concerning BSA, no particular change was observed. All spectra presented two minima, at 209 and 220 nm, typical of a protein rich in α-helices (**Figure 2.23a**).[204] On the contrary, LYS displayed a huge change after the encapsulation of PERFECTA. In fact, the two minima at 209 and 222 nm were substituted by one minimum at 218 nm, which was typical of a β-sheet.[205] The amyloidogenic nature of lysozyme was not a novelty, but in our case the formation of fibrils occurred in unprecedented conditions. Generally, it occurred in denaturating conditions, such as in the presence of co-solvents (e.g. ethanol), strongly alkaline or acidic pH, detergents or heating.[192,206,207] Some studies assessed a change in conformation upon addition of fluorinated molecules, such as lithium perfluorononanoate (PFN)[109] and perfluorooctyl sulfonate (PFOS).[108] These conformational alterations had a totally different outcome in the CD spectrum, and were attributed to protein unfolding, causing toxicity. In our case, the transition from α-helix to β-sheet was particularly net, and the clear CD spectrum let us think of a structural transition, not an unfolding or denaturation process. This phenomenon constitutes something new for fluorinated compounds like PERFECTA.

CD data were supported by FTIR analyses. In particular, samples containing the higher amount of PERFECTA were compared with the formulation of the respective protein alone. Both complexes spectra (P@BSA 6:1 and P@LYS 5:1) showed clearly the presence of PERFECTA , with its two typical C-F signals at 736 and 726 cm^{-1} (**Figure 2.23**, red square) and the signals at 1017 and 971 cm^{-1} (blue square).

The regions of interest for structural information about the protein are located between 1700-1600 cm^{-1} – corresponding to the amide I region – and 1600-1500 cm^{-1} – amide II region.[208] The position and shifts of peaks in these sites could give useful indication about changes in the secondary structure of proteins.

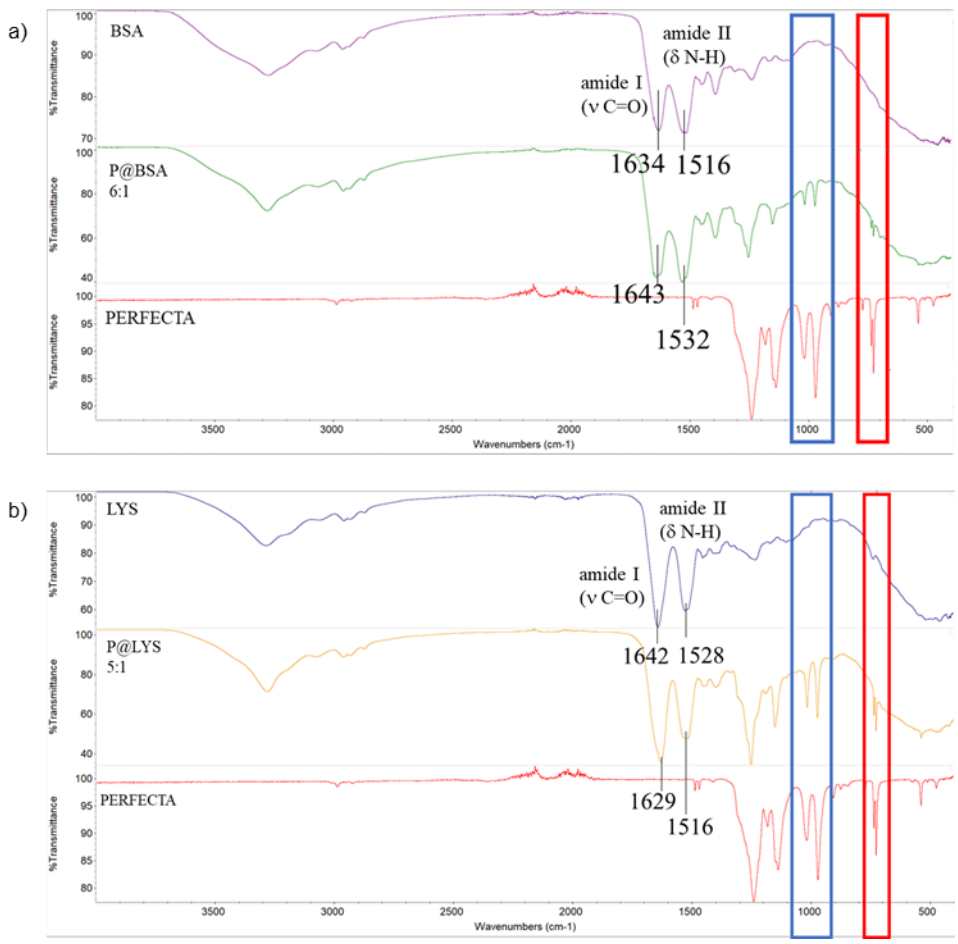

Figure 2.23 *a) ATR-FTIR spectra of BSA (violet line), P@BSA 6:1 (green line), PERFECTA (red line). b) ATR-FTIR spectra of LYS (blue line), P@BSA 6:1 (yellow line), PERFECTA (red line). Blue square and red square highlight the signals belonged to PERFECTA.*

Interestingly, both these signals underwent a consistent shift, but with an opposite shift direction between BSA and LYS complexes.

Amide II blue-shifted of +16 cm^{-1} when PERFECTA was present in the BSA complex, while a red-shift occurred in LYS situation, bearing a difference of -12 cm^{-1}. This result demonstrated that both protein structures were affected by the presence of the guest. Despite BSA did not display any difference in the CD spectra, FTIR open up a new scenario.

The amide I peak, relative to C=O stretching had a consistent movement of position (+9 cm^{-1} for BSA and -13 cm^{-1} for LYS in presence of PERFECTA). Although the position of the amide I signal of P@BSA 6:1 still fell into the α-helix position, the shift of P@LYS 5:1 at 1629 cm^{-1} can be attributed to the presence of a β-sheet intermolecular constrain.[208] Moreover, deconvolution analyses of amide I peaks gave an insight into the secondary structure composition of the proteins and their respective complexes (**Figure 2.24**).

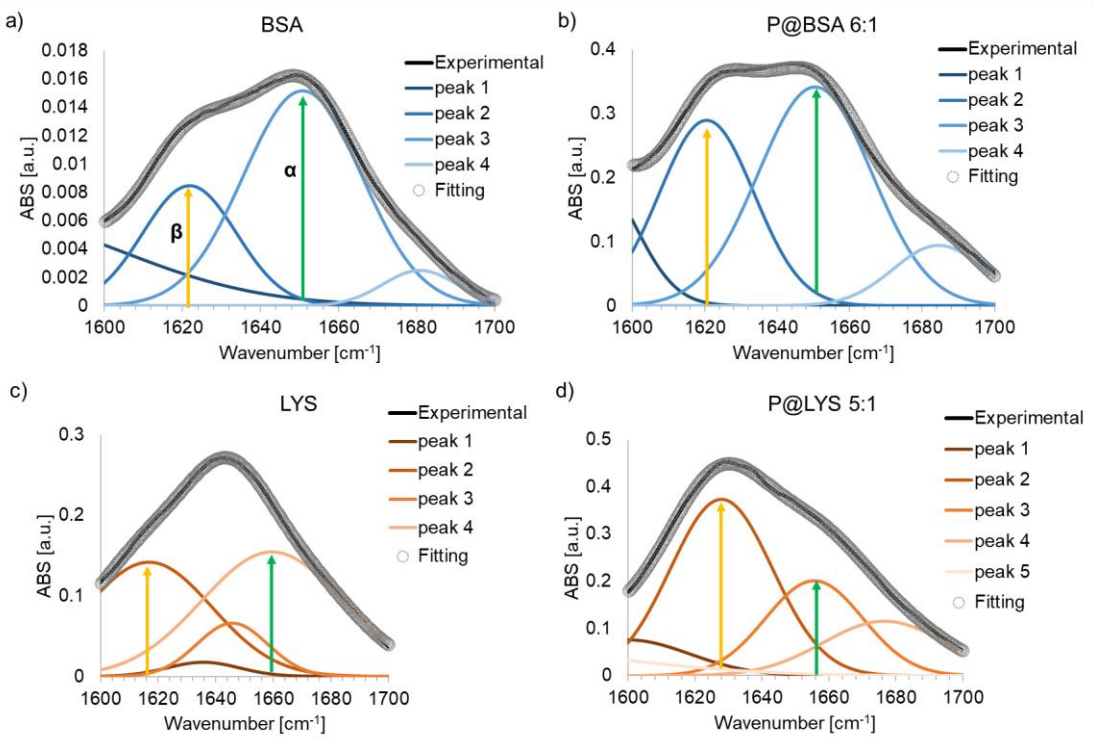

Figure 2.24 *Gaussian fitting of amide I region (1600-1700 cm^{-1}) of the ATR-FTIR spectrum (black curve) of BSA (a), P@BSA 6:1 (b), LYS (c) and P@LYS 5:1 (d). Fitting error was always $R^2 > 0.99$. Yellow arrow indicates the peak of the β-sheet contribute and the green one indicates the peak of mainly the α-helix contribute.*

The fitting of BSA spectrum underlined a strong α-helix contribute, with the peak positioned at 1650 cm^{-1}.[209] The same peak was conserved also in the pattern of P@BSA 6:1, confirming CD observations. Additionally, in the latter chart (**Figure 2.24b**), the peak at 1620 cm^{-1} indicated the contribution of a β-sheet component,[209,210] which was present also before the addition of PERFECTA. Overall, this analysis suggested a predominance of α-helix, with the presence of a less pronounced β-

sheet component. On the other hand, the presence of PERFECTA in P@LYS 5:1 determined a big increase of the β-sheet peak at 1627 cm^{-1}, while the occurrence of an α-helix signal (1655 cm^{-1}) was still maintained, but with reduced intensity. Thus, the overall red shift observed in **Figure 2.23b** was the result of the net increase of β-sheet content, consistent with CD observations.

The β-sheet presence was furtherly shown upon treatment of the samples with Congo Red assay. The brightness obtained from the sample exposed to polarized light was the ultimate proof of the amyloid nature of the sample (**Figure 2.25**). The treatment of LYS formulation did not gave any visible spot under the polarized microscope (data not shown).

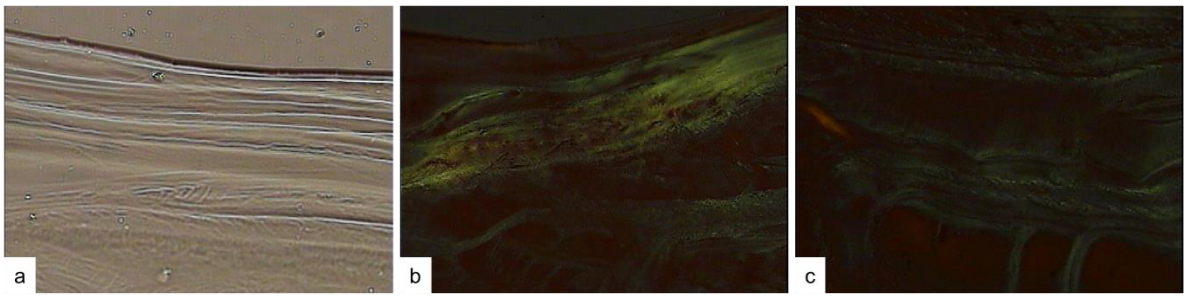

Figure 2.25 *Congo Red assay. Picture of dried P@LYS 1:1 exposed to white light (a) and polarized light (b-c).*

All the reported data pointed towards the same direction, and were further confirmed by morphological analysis by cryo-TEM.

Pictures obtained from a five-fold dilution of 1 mM sample of BSA (**Figure 2.26a**) showed the presence of small particles with average cross section diameter of 2.8 ± 2 nm, much different from the aggregates observed by DLS. This phenomenon might indicate the formation of transient aggregates, whose dynamicity could give explanation of the high PDI observed.

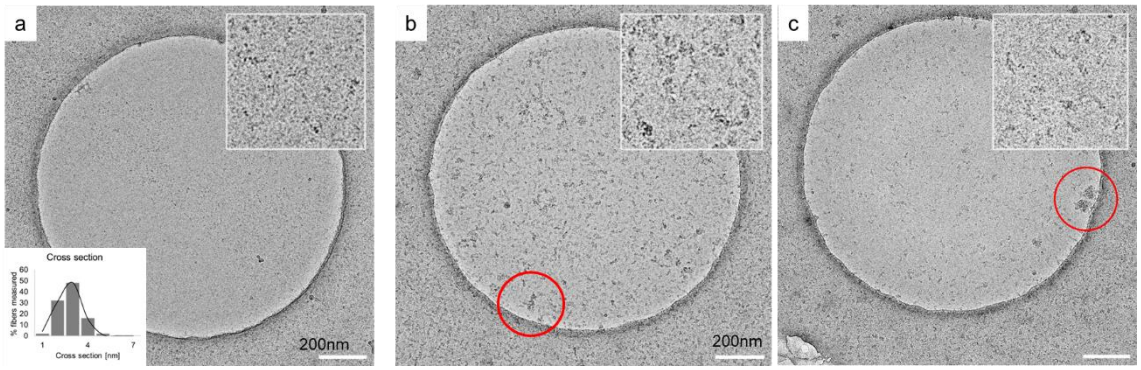

Figure 2.26 *a) Cryo-TEM image from BSA solution 13 mg/mL. Zoom square represents a threefold magnification of a small area of the ice film. Chart insert shows the Gaussian distribution of the cross section calculated with imaJ software upon the measurement of 50 particles. b-c) Cryo-TEM images of P@BSA 1:1 (dilution up to 13 mg/mL of protein). Red circle indicates the presence of larger aggregates.*

Some changes were displayed after the addition of equimolar amount of PERFECTA. P@BSA 1:1 sample was diluted five times to determine the presence of different populations (**Figure 2.26b-c**). Although no highly ordered assemblies or crystals occurred, BSA entities became obviously bigger, and sometimes even larger lumps formed (Figure 2.26 b-c, red circles). The close-ups suggested a distinct super structuring reminiscent of other single protein particles in vitreous ice. A preliminary test with a small number of automatically acquired micrographs analysed by standard Single Particle Acquisition (SPA) revealed no hints of uniformly ordered assemblies. The low contrast of the aggregates made too harsh to define a size distribution, but confirmed the consideration of structural change of BSA obtained from FTIR analysis.

Remarkable results were obtained through the analyses of LYS complex. Images of pure LYS formulation revealed the presence of small particles (Figure 2.27a), with an approximate averaged cross section of ~ 2 nm. Differently from BSA, DLS and morphological examination were totally consistent. Indeed, the impossibility to have a good auto-correlation function from DLS measurement of LYS could be attributed to such a small dimension of the particles. Using PERFECTA as a guest clearly altered the structure of LYS in water (**Figure 2.27c-e**). P@LYS 1:1 showed elongated aggregates, probably short needle-like crystals, that formed next to quite uniform small and round aggregates (red circle). Such crystals remained stable even upon dilution, that was necessary to achieve an appropriate concentration for observing the aggregates.

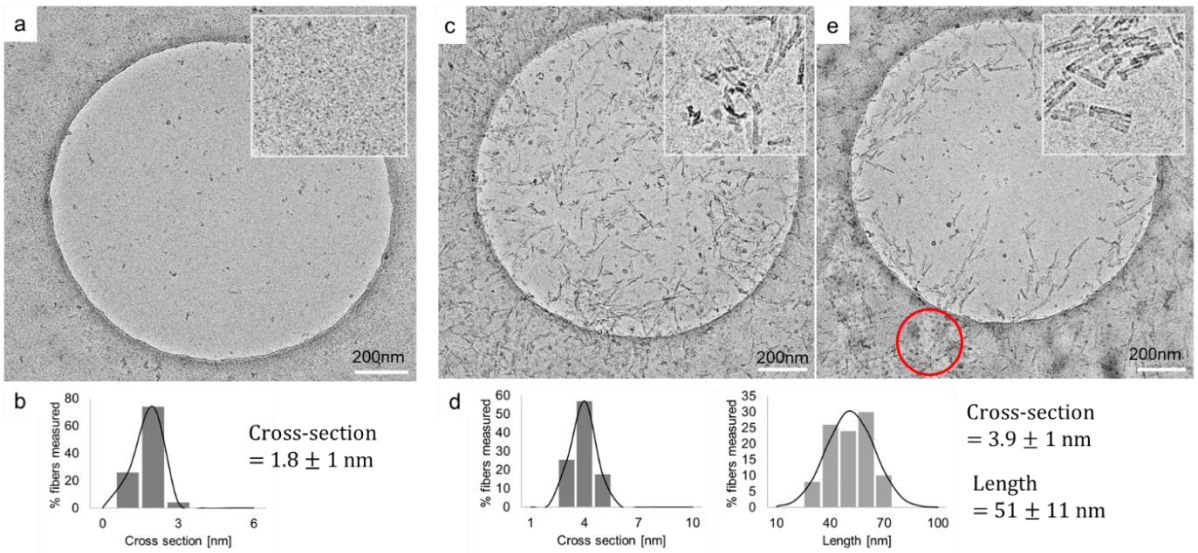

Figure 2.27 *a) Cryo-TEM image from lysozyme solution 2.8 mg/mL. Zoom square represents a threefold magnification of a small area of the ice film. b) Gaussian distribution of the cross section calculated with imaJ software upon the measurement of 50 particles. c, e) Cryo-TEM images of P@LYS 1:1 (dilution up to 2.8 mg/mL of protein). Red circle indicates the presence of small spherical aggregates. Zoom square represents a threefold magnification of a small area of the ice film. d) Gaussian distribution of the cross section and length of the rods calculated with imaJ software upon the measurement of 50 particles.*

The rod-like shapes had ~ 4 nm of cross section and ~ 50 nm of length. The fitting of multiangle DLS analysis of this specific sample, before cryo-TEM acquisition, gave an average diameter of 54 nm (R^2 = 0.99, PDI: 0.25, graph not shown), perfectly in line with the previous investigation (**Figure 2.21**).

The interesting and discrete morphology seen by cryo-TEM was confirmed by a Small Angle X-ray Scattering (SAXS) analysis (**Figure 2.28**).

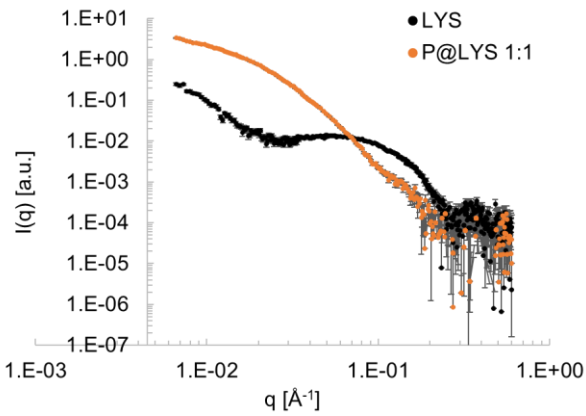

Figure 2.28 *Experimental SAXS profiles, reporting scattered intensity versus scattering vector q, of the LYS and P@LYS samples. The protein concentration in both samples is 14 mg/mL.*

From the comparison of experimental data, it was immediately noticeable the profile change upon addition of PERFECTA. A model-independent data analyses allowed to infer information about the nature of the samples. The presence of a flat region at low q values (q^0 slope, **Figure 2.29a**) in the SAXS profile of the LYS sample indicates the presence of globular particles.[211] Then, in the limit of small q values (qR_g <1, where R_g is the radius of gyration) scattering objects exhibit a universal shape-independent geometry that could be approximated by the so-called Guinier law:

$$I(q) = I(0)\exp\left(\frac{q^2 R_g^2}{-3}\right)$$

A linear trend in the Guinier plot (*I(q) versus* q^2, **Figure 2.29b**) indicates a monodisperse system and from the slope of the linear fitting R_g can be obtained. R_g gives an estimation of the overall size of the scattered particles in solution. We obtained from the fitting R_g = 14.4 Å , which is a value comparable to previous ones reported in literature for the same system.[212] Of note, the radius of the particle can be obtained from R_g, considering that for a sphere $R_g = \sqrt{\frac{3}{5}}R$.[213] Thus, from the Guinier

approximation the radius of the particles in the LYS sample is about 18 Å. Consequently, the diameter measures ~ 3.6 nm, in agreement with the cryo-TEM measurement. As mentioned, the Guinier regime guarantees a long range order that dominates in the low q region. As the scattering vector increases the scattering curves could be described by a power law:[213] $I(q) \propto q^{-\alpha}$

In this case, the curve slope followed a q^{-4} regime (Porod law), which further confirmed the globular nature of the particles in suspension. (**Figure 2.29a**).[213]

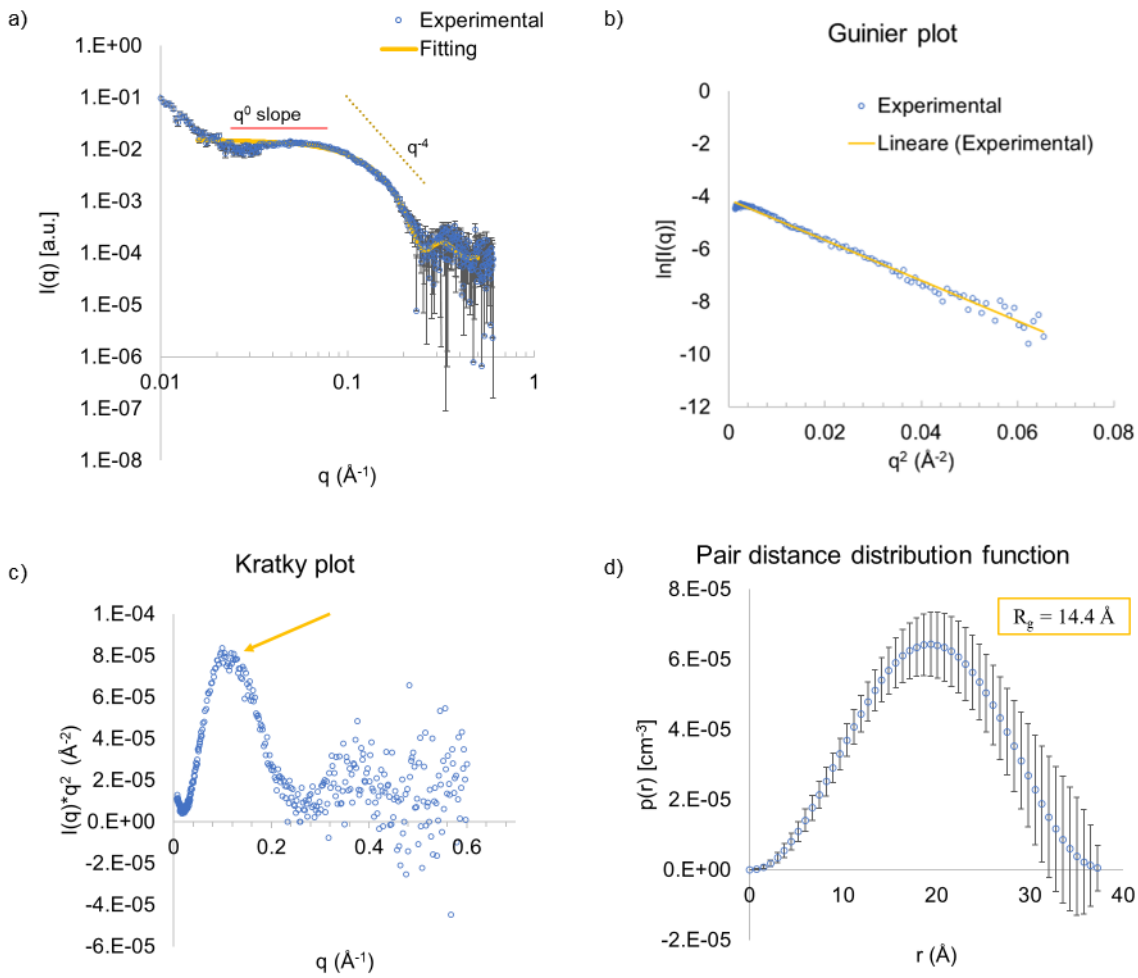

Figure 2.29 *SAXS analyses of LYS sample. a) Experimental SAXS profile and fitting curve according to the model reported in* ***Table 2.4.3*** *obtained by SASview analysis. b) Guinier plot and linear fitting. c) Kratky plot that indicates the presence of a folded protein in solution. d) P(r) distribution obtained with automatic derivation of the experimental data through SASview software.*

The Kratky plot – *I(q)*q² versus q* – (**Figure 2.29c**) is useful to appraise whether the protein of interest was properly folded in solution. The observation of a bell-shaped curve for the LYS sample confirmed the presence of a folded globular protein.[211] Thus, all the preliminary observations pointed toward a globular protein, which could be fitted with a spherical-type model. Before fitting the curve, we

extracted the pair-wise distance distribution function *P(r)* (**Figure 2.29d**), which describes the probability of finding an electron in the system separated by a distance *r* from another electron. The *P*(*r*) function can be directly obtained via Fourier transformation of the scattering intensity as a function of *q* following the equation:

$$p(r) = \frac{1}{2\pi^2}\int_0^\infty I(q)qr\sin qr dq$$

In this case, the *P(r)* distribution was obtained using SASview software.[214] From this analysis it was possible to extract another estimation of R_g (using SASview software), which resulted to be 14.4 Å, indicating the consistency of the analyses. At this point, taking inspiration from the literature, an ellipsoid form factor was tried. The presence of the initial slope at q < 0.0066 Å, could indicate the presence of aggregation, and for this reason it was excluded from the fitting analyses.[203,215] The fitting curve is reported in **Figure 2.29a** and the data extracted from the fitting in **Table 2.4.3** (**Experimental section 2.4**). A polar radius of 14.7 Å and an equatorial radius of 19.5 Å were obtained. The similarity of the axis sizes justifies an approximation to a sphere, in good agreement with the cryo-TEM observations (**Table 2.10**). Indeed, the calculation of the diameter according to this model fitting, determined elliptical particles of ~ 3 x 4 nm.

Table 2.10 *Comparison between the particle size obtained by SAXS data elaboration and cryo-TEM measurement of LYS. A schematic representation of the ellipsoid model is reported on the bottom.*

	SAXS data		**Cryo-TEM data**
$\bar{\emptyset}$ - Avarage dimension (nm)	Guinier/P(r): $\bar{\emptyset}$ = 3.6	Fitting: 3.4 (D_{eq} 3.9 ± 0.04 x D_p 2.94 ± 0.07)	$\bar{\emptyset}$ =1.8 ± 1

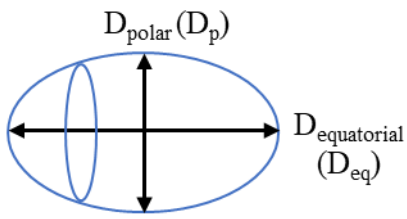

The SAXS curve of P@LYS 1:1 sample (**Figure 2.30a**) shows a different scattering pattern, the lack of the flat region at low *q* values suggests a different shape of the particles. In particular, the q^{-1} power law at low-*q* value indicates the presence of elongated model.[211] The q^{-1} trend was better evidenced

by the Holtzer plot (*q*I(q)* versus *q,* **Figure 2.30c**)[216], in which the q^{-1} region is represented by a plateau. This behaviour is typically attributed to cylindrical shape, like a rod.[216]

The Guinier plot was also analysed for this sample, obtaining a linear trend, from which a R_g = 150 Å was obtained (**Figure 2.30b, insert**). However, for elongated particles is often used a modified Guinier plot *ln(q*(I(q)) versus* q^2 (**Figure 2.30b**).[213,217] From this elaboration the cylinder/rod cross section can be determined as it follows:

$$qI(q) = I(0)\exp\left(\frac{q^2 R_c^2}{-2}\right)$$

The presence of a linear trend furtherly confirmed the elongated shape of the scattering material and according to the slope obtained from the linear fitting, the gyration radius of the cross section is 28 Å.

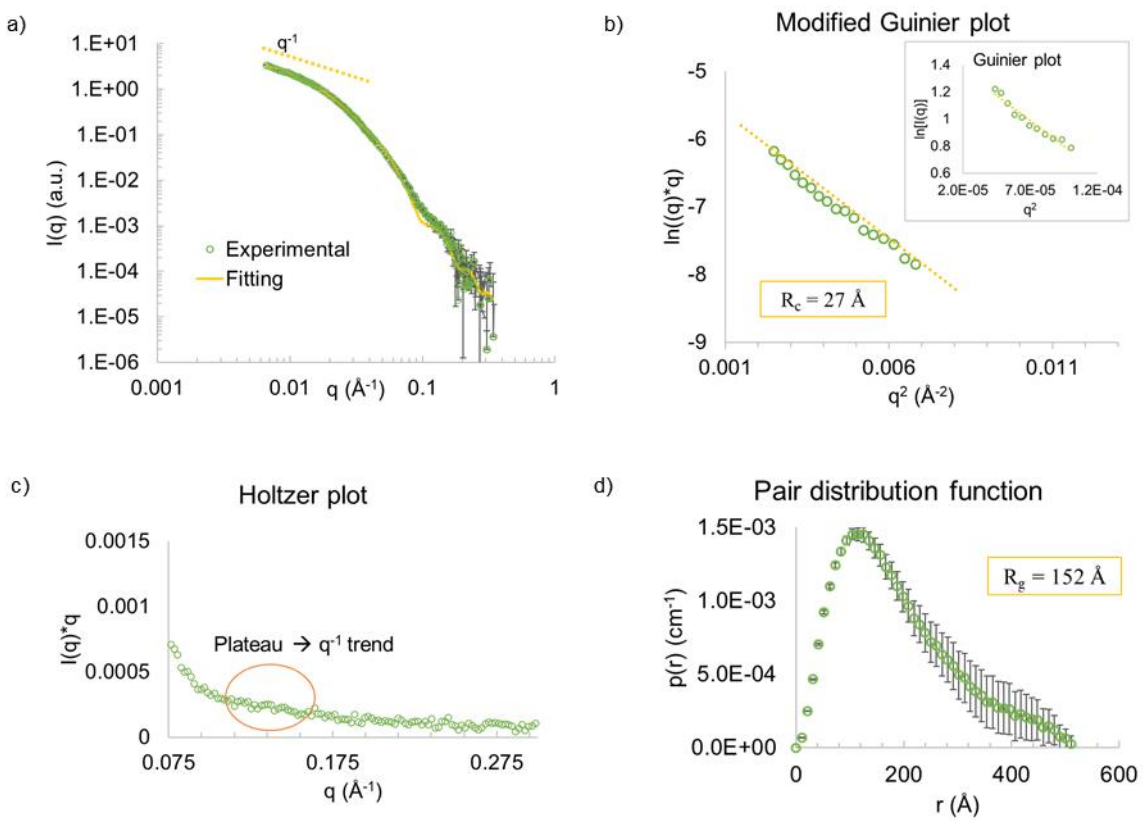

Figure 2.30 *SAXS analysis of the P@LYS 1:1 sample. a) Experimental SAXS profile with the fitting curve from the model reported in* ***Table 2.4.3*** *obtained by SASview analysis. b) Modified Guinier plot from which the cross section radius of gyration was extracted. The insert represented the Guinier plot. c) Holtzer plot highlighting the presence of a power law of* q^{-1}*1 in the plateau region, confirming the presence of a rod shape of the particles. d) P(r) distribution obtained with automatic derivation of the experimental data through SASview software.*

Additionally, considering that for uniform rod-like particles $R_c = R/\sqrt{2}$, the cross section of the hypothetic rod can be calculated. Thus, the calculated cross-section radius was equal to 4 nm, which was in line with the morphological analysis.

The pair distribution function *P(r)* gave a further confirmation of the elongated shape of the aggregates (**Figure 2.30d**). In fact, an asymmetric distribution with a maximum at small distances and a tail at longer distances was obtained, which is typical for elongated particles.[218] Importantly, the obtained gyration radius is equal to that calculated by Guinier plot (150 Å *versus* 152 Å, respectively). Additionally, the R_g obtained by the *P(r)* function was also considered more reliable due to the amount of data used. In fact, all the data were used for the Pair distribution, whereas only low q values contributed to the Guinier analysis.[218] From the value of R_g is it possible to calculate the contour length of the rod according to the following relation: $R_g = L/\sqrt{12}$.[213] Thus, considering R_g obtained from the *P(r)* inversion, the length of the rod results about 527 Å, which is very close to the data obtained by cryo-TEM measurements (**Table 2.11**).

In conclusion, the analysis suggests the presence of rod-like particles and for this reason an elliptical cylinder model was used for the fitting of the experimental data with SASview software. Interestingly, the fitting model identified a cross section radius of 35.7 Å and a length of 531.7 Å. The result was consistent with cryo-TEM: the length fitted perfectly (53 nm vs 51 ± 11 nm respectively), while a 7 nm cross section bared a very little excess in comparison with the ~ 4 nm measured from the images analysed. **Table 2.11** provided a summary comparison of the fitting a measurement data, giving an overview of the consistence of all the study.

Table 2.11 *Comparison between the particle size obtained by SAXS data elaboration and cryo-TEM measurement of P@LYS 1:1. A schematic representation of the elliptical cylinder model is reported on the bottom.*

	SAXS data		**Cryo-TEM data**
Length – L (nm)	Guinier/P(r): L = 52.7	Fitting: L = 53.2 ± 0.5	L = 51 ± 11
Cross section – C (nm)	Modified Guinier: C = 7.6	Fitting: C = 7.1 ± 0.01	C = 3.9 ± 1

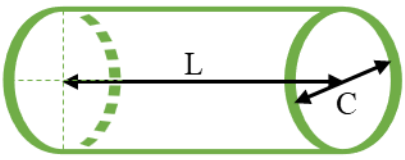

SAXS measurements of P@BSA complexes will be performed in the future, to clarify the structure alteration due to the interaction of the protein with PERFECTA. P@LYS results are particularly interesting for the capacity of PERFECTA to induce a peculiar oligomerization of the protein. The latter was intriguingly limited without the formation of longer aggregates, as those of micrometric dimensions reported in the literature.[192,207,219,220] Thus, the novelty of this interaction with C-F units could drive the structural transition of the protein in a very controlled manner.

2.4 Conclusion

The contrast agent PERFECTA was central focus of the chapter. Particularly, the solubilization of this probe in biological environment was the first goal. Two different approaches were developed: the first one involved fluorinated Janus dendrimers (BFTG2-OH and BFTG2-S) aiming to design proper formulations suitable for the *in vivo* ^{19}F-MRI. Subsequenlty, hydrophobic cavities of the two proteins lysozyme and BSA were exploited as hosts for PERFECTA.

Formulations PERFECTA@dendrimer were achieved with different methods, reaching good amount of solubilized probe in the aqueous medium. Starting from the dendrimer bearing eight -OH end groups, the variation of the formulation method highlighted differences in the probe loading. The latter event was then followed by a significant morphology change of the supramolecular architecture of PERFECTA@BFTG2-OH. Passing from thin film method to nanoprecipitation an increase of PERFECTA encapsulation was reached, followed by an evolution from vesicles to micelles. This observed transition may be attributed to differences in the amount of F-F interactions between the dendrimer and PERFECTA. Formulation *via* nanoprecipitation was then identified as the optimal method in terms of ^{19}F-MRI performance, producing bright signals against a dark background. Particularly, PERFECTA@BFTG2-S demonstrated superior results compared to PERFECTA@BFTG2-OH. While the T_2 relaxation time of BFTG2-OH was too short to contribute significantly to the MRI signal of PERFECTA, BFTG2-S exhibited a longer T_2, enhancing the MRI response. Encouraging cytotoxicity tests confirmed the safety of the formulations towards two cell lines, Hela cells, and macrophages U937. These cells were also assessed for preliminary uptake experiments, validating the initial hypothesis of BFTG2-S' ability to target inflammatory cells. Indeed, ^{19}F-NMR analysis confirmed that macrophages selectively uptake a higher amount of PERFECTA@BFTG2-S compared to PERFECTA@BFTG2-OH, providing promising results for future in vivo studies.

The same contrast agent was also studied with lysozyme (LYS) and bovine serum albumin (BSA), inducing interesting structural changes in both proteins, particularly notable in LYS. The controlled β-transition obtained after the addition of PERFECTA in LYS amyloid fibrillation presented a unique mechanism for further exploration, particularly in understanding the interaction between C-F units and proteins.

2.5 Materials and methods

Organic solvents were purchased from Sigma-Aldrich. All commercially available compounds were purchased from Sigma Aldrich, TCI, and abcr Chemicals. Milli-Q water was obtained from a Simplicity® water purification system (MerckMillipore). PERFECTA was synthesised according to the published procedure.[62]

Synthesis of BFTG2-OH

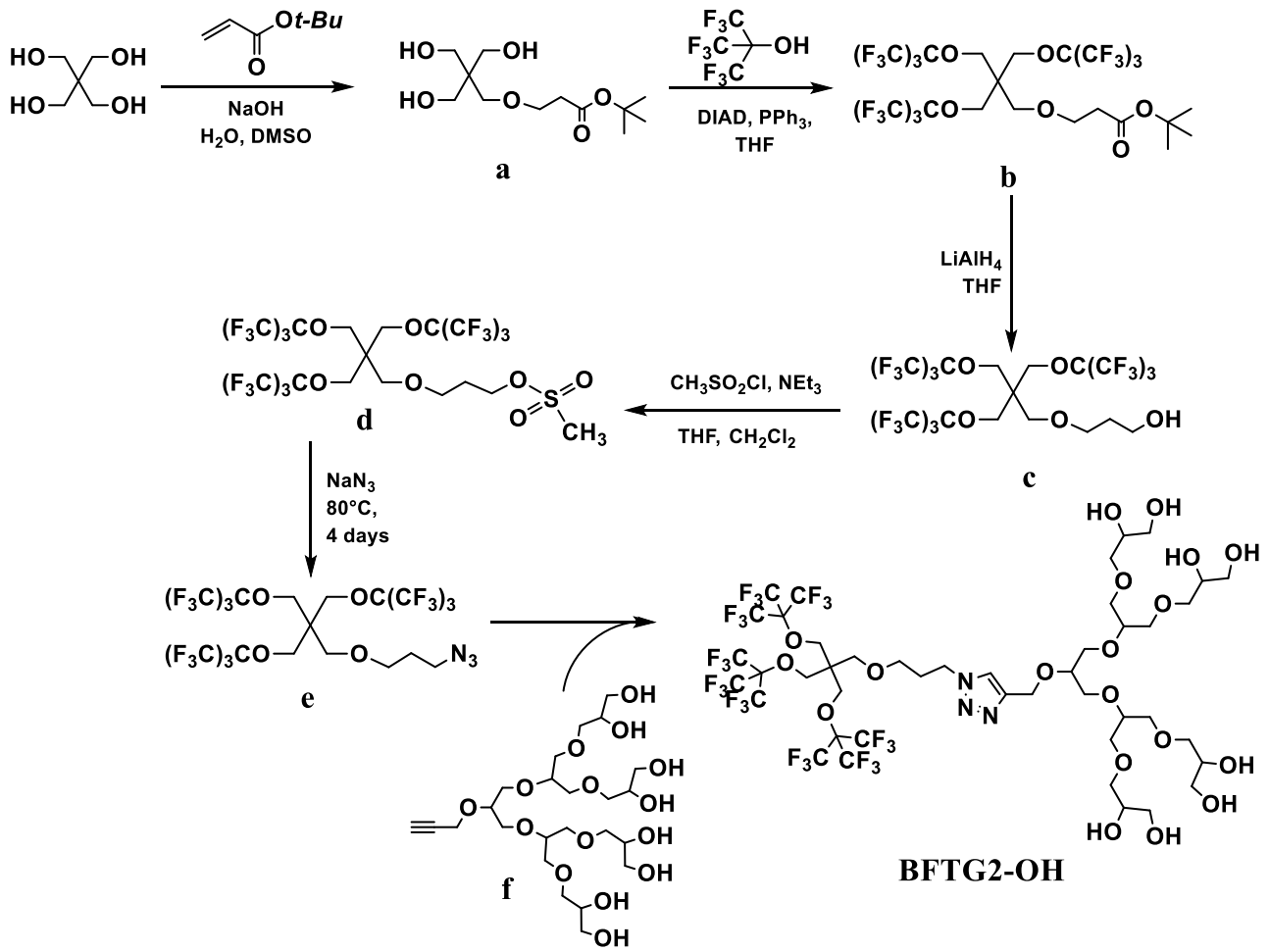

Synthesis of compound **d** was inspired by a published procedure.[137] G2-Oligoglycerol alkyne (intermediate **f**) was synthesized by Dr. Abhishek Kumar Singh (Freie Universität Berlin).

Synthesis of **compound a**

Following the same procedure described by Yue,[63] **compound a** was obtained in 38% yield as a colourless oil, eluting with Et_2O/Acetone (from 100% to 9:1, R_f = 0.1 in Et2O, permanganate staining).

^{1}H NMR (400 MHz, $CDCl_3$) δ: 3.69 (m, 2H), 3.67 (s, 6H), 3.56 (s, 2H), 2.57 (s, 3H) 2.48 (t, 2H, J = 5.8 Hz), 1.46 (s, 9H) ppm.

Synthesis of **compound b**

Triphenylphosphine (26 g, 100 mmol) were placed in an oven-dried round bottom flask, under nitrogen flow. Compound **a** (4.36 g, 16.5 mmol) and anhydrous THF (100 mL) were added and the solution was cooled to 0 °C. Diisopropylazodicarboxylate (DIAD, 19.5 mL, 100 mmol) was added dropwise under stirring. The resulting foamy mixture was warmed up to r.t. and stirred for additional 20 minutes, before adding perfluoro-*tert*-butyl alcohol (12 mL, 100 mmol) in one portion. The finally clear solution was stirred at 45 °C for 4 days. After cooling down to r.t., the mixture was dried and extracted with dichloromethane/water (3 x 80 mL). The collected organic layers were washed with brine, dried over Na_2SO_4 and concentrated under vacuum. The pure product was obtained as a white crystalline powder through recrystallization from methanol. 73 % yield.

^{1}H NMR (400 MHz, $CDCl_3$): δ 4.05 (s, 6H), 3.64 (t, J = 6.5 Hz, 2H), 3.43 (s, 2H), 2.45 (t, J = 6.5 Hz, 2H), 1.44 (s, 9H) ppm. ^{19}F NMR (376 MHz, $CDCl_3$): δ -71.41 (s) ppm.

Synthesis of **compound c**

To a THF suspension (100 mL) of $LiAlH_4$ (1 g, 26 mmol) compound **b** (6 g, 6.5 mmol) was added at 0°C. The reaction was stirred overnight under nitrogen flow. Then, the reaction was added with HCl 1 M until the disappearance of effervescence and then filtered by gravity. The mixture was evaporated and then extracted with dichloromethane (3 x 60 mL), washed with brine and dried over Na_2SO_4 and concentrated under vacuum. 4.73 g of crude (colourless oil) were directly used for the next step without any further purification.

^{1}H NMR (400 MHz, $CDCl_3$): δ 4.05 (s, 6H), 3.71 (t, J = 6.2 Hz, 2H), 3.53 (t, J = 6.1 Hz, 2H), 3.40 (s, 2H), 1.83 (qui, J = 6.2 2H) ppm. ^{19}F NMR (376 MHz, $CDCl_3$): δ -71.44 (s) ppm.

Synthesis of **compound d**

A anhydrous dichloromethane solution (40 mL) of crude **c** (3 g, 3.5 mmol) was added with triethylamine (1.4 mL, 10.6 mmol) and stirred for 10 minutes at 0°C. The mixture was then added with methanesulfonyl chloride (0.82 mL, 10.6 mmol) and stirred at room temperature for 3 days under nitrogen flux. The mixture was quenched with water (20 mL) and extracted with dichloromethane. The organic layer was then washed with brine, dried over Na_2SO_4 and concentrated under vacuum. The crude obtained as a colourless oil (3.7 g) was directly used for the next step.

^{1}H NMR (400 MHz, $CDCl_3$) δ 4.27 (t, J = 6.3 Hz, 2H), 4.05 (s, 6H), 3.52 (t, J = 6.1 Hz, 2H), 3.41 (s, 2H), 2.99 (s, 3H), 2.00 (qui, J = 6.2 Hz, 2H) ppm. ^{19}F NMR (376 MHz, $CDCl_3$): δ -70.41 (s) ppm.

Synthesis of **compound e**

In a dry round bottom flask a solution of the crude **d** (3.7g, 4 mmol) was prepared in anhydrous DMF (40 mL). To the stirring solution sodium azide (0.5 g, 8mmol) was added at 0°C. The mixture was heated at 80°C and stirred for 4 days under nitrogen flux. The reaction was then cooled until room temperature and added with ice-cooled water, then extracted with hexane. 2.4 g of product were purified with column chromatography (AcOEt/Hex 8:2) to obtained the desired product in 87% yield.

^{1}H NMR (400 MHz, Acetone): δ 4.06 (s, 6H), 3.39 (t, *J* = 6.1 Hz, 2H), 3.35 (s, 2H), 3.27 (t, *J* = 6.8 Hz, 2H), 1.70 (m, 2H) ppm. ^{19}F NMR (376 MHz, Acetone): δ -71.01 (s) ppm.

Synthesis of **BFTG2-OH**, published[181]

Compound **e** (0.2 g, 1 eq) and the G2-alkyne (**f**) (0.14 g, 1.1 eq), each dissolved in 20 mL of dry DMF were placed in a round bottom flask. Then, copper acetate (0.004 g, 0.1 eq) was added as a click chemistry catalyst. After the completion of the reaction, the solvent was removed under reduced pressure. The crude residue was purified with column chromatography using methanol and DCM as eluent. The desired compound was obtained as viscous solid in 81 % yield.

^{1}H NMR (700 MHz, MeOD-D_3): δ 8.10 (s, 1H), 4.81 (s, 2H), 4.49 (t, J = 6Hz, 2H), 4.13 (s, 8H), 3.76-3.68 (m, 7H), 3.56-3.45 (m, 30H), 2.19-2.15 (m, 2H) ppm. ^{13}C NMR (151 MHz, MeOD-D_4): δ 143.68, 124.28, 123.14, 121.21, 119.15, 99.98, 78.59, 72.67, 71.00, 69.97, 67.82, 65.66, 63.13, 46.17, 29.94 ppm; ^{19}FNMR (565 MHz, MeOD-D_4): δ -71.41ppm; MS (ESI) m/z = 1447.3390 $[M+Na]^+$ (calcd. for $C_{44}H_{60}F_{27}N_3NaO19$: 1470.3357, IR = 3350, 2919, 2862 cm^{-1}.

Synthesis of BFTG2-S was made by Dr. Abhishek Kumar Singh (Freie Universität Berlin) using the same compound **e** and following the procedure:

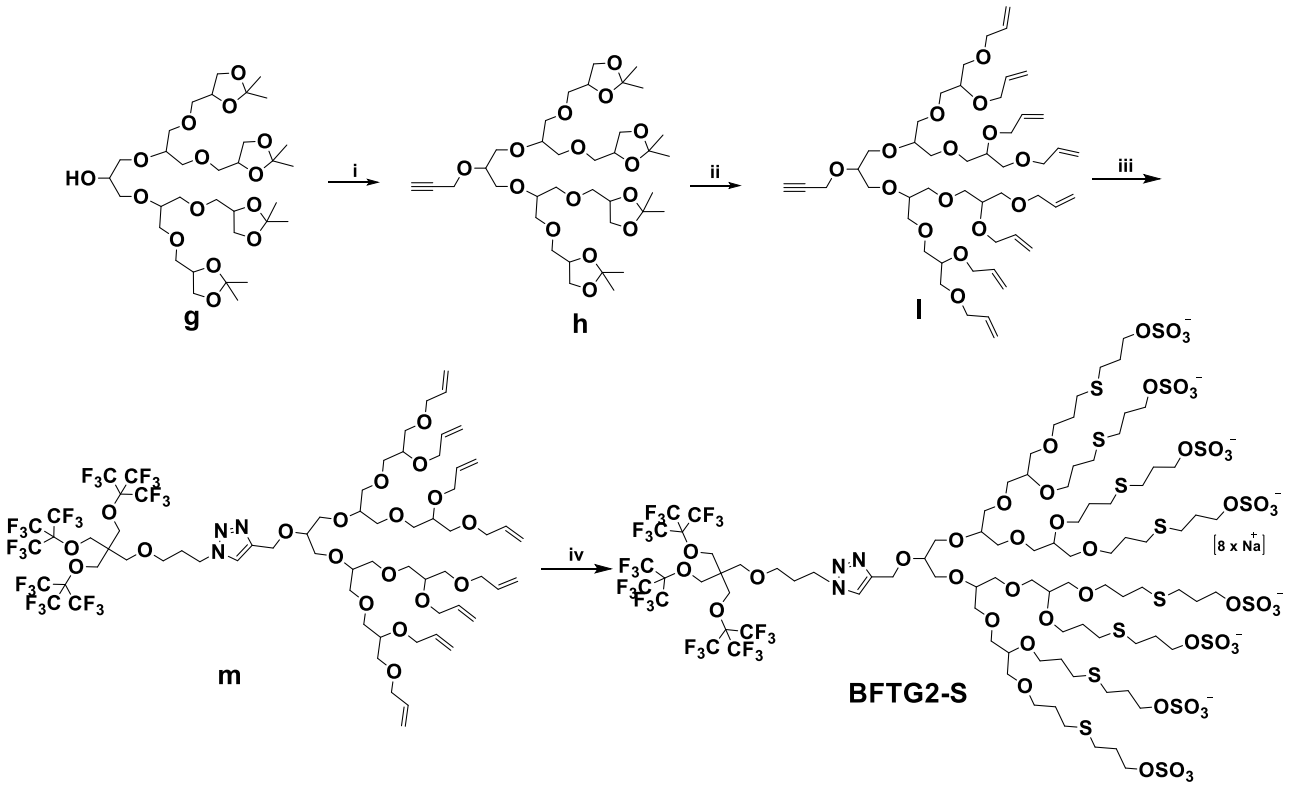

(i) NaH, Propargyl Bromide, THF, 50ºC, 24h, 75%. (ii) a. Dowex-50, Methanol, 50 ºC, 24 h, 95%. (ii) b. NaH, Allyl Bromide, 50ºC, 24 h, 85%. (iii) Compound **e**, Copper acetate, DMF, 60 ºC, 24 h, 85ºC. (iv) Sodium 3-mercapto-1-propanesulfonate, DMPA, MeOH, LED-370nm, 6h, 92 %.

^{1}H NMR (400 MHz, METHANOL-D_3) δ 7.98 (s, 1H), 5.97-5.88 (m, 11H), 5.30-5.07 (m, 27), 4.46 4.00 (m, 33H), 3.74-3.40 (m, 47H), 3.15-2.90 (m, 27), 2.32-2.16 (m, 2H) ppm.

^{19}F NMR (376 MHz, METHANOL-D_3) δ -71.34.

Synthesis of BHTG2-OH

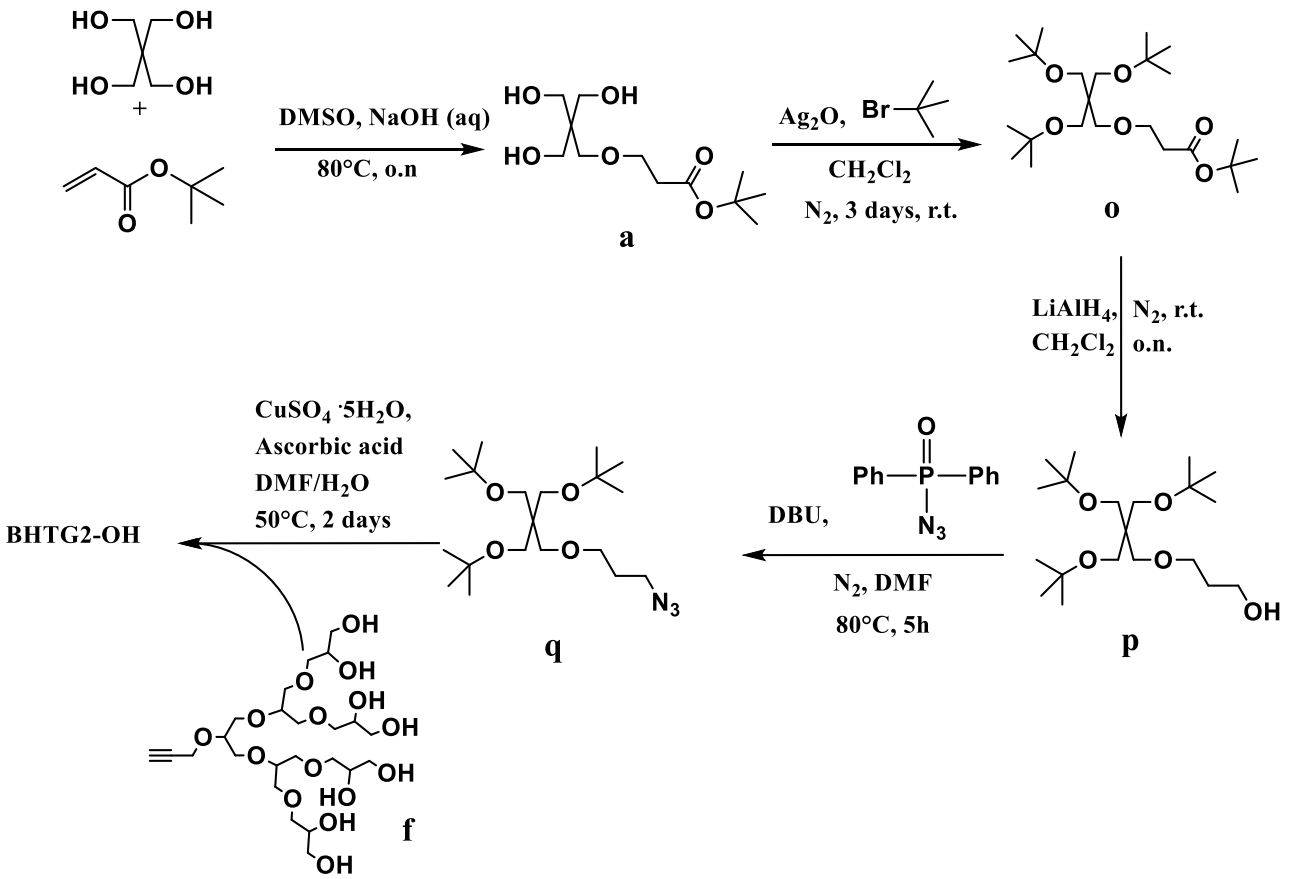

Synthesis of **compound o**

In a dry round bottom flask compound **a** (2 g, 7.6 mmol) was suspended in anhydrous DCM (20 mL). Ag_2O (5.8 g, 25 mmol) and t-butyl-bromide (2.8 mL, 25 mmol) were added. The mixture was stirred overnight in inert atmosphere of Argon. For the two next days, Ag_2O (2.9 mg, 12.5 mmol) and t-butyl-bromide (1.5 mL, 12.5 mmol) were added each day. After three total days, the reaction was stopped, vacuum filtered on celite and vacuum dried. The crude (3.3 g) was purified by flash column with Heaxane/AcOEt (from 100% hexane to 100% AcOEt). 78 % yield, $R_f = 0.5$ in Hex/AcOEt (97:3) permanganate staining.

^{1}H NMR (400 MHz, Acetone-D_6): δ 4.21 (td, J = 6.3, 0.9 Hz, 2H), 3.96 (d, J = 0.9 Hz, 2H), 3.87 (d, J = 0.9 Hz, 7H), 3.02 (td, J = 6.3, 0.8 Hz, 2H), 2.05 (d, J = 0.9 Hz, 9H), 1.74 (s, 27H) ppm.

Synthesis of **compound p**

To a THF suspension (30 mL) of $LiAlH_4$ (4.3 g, 10 mmol) compound **o** (1.3 g, 3 mmol) was added at 0°C. The reaction was stirred overnight under nitrogen flow. Then, the reaction was added with NaOH 0.1 M (4 mL) and then filtered by gravity. The mixture was evaporated and then extracted

with ethyl acetate (3 x 20 mL), washed with brine and dried over Na_2SO_4 and concentrated under vacuum. The crude (colourless oil) was directly used for the next step without any further purification.

^{1}H NMR (400 MHz, MeOD): δ 3.65 (t, *J* = 6.4 Hz, 2H), 3.49 (t, *J* = 6.1 Hz, 2H), 3.34 (s, 2H), 3.27 (s, 6H), 1.77 (qui, *J* = 6.3 Hz, 2H), 1.15 (s, 27H) ppm.

Synthesis of **compound q**

In a dry round bottom flask compound **p** (1.1 g, 3 mmol) was dissolved in dry DMF (20 mL). Diphenyl-phophoryl-azide (1.12 mL, 5.2 mmol) was added dropwise to the stirring solution at 0°C. 1,5-diazabiciclo(5.4.0)undec-7-ene (DBU, 0.78 mL, 5.2 mmol) was then added to the mixture. The reaction was heated to room temperature and then transferred in a pre-heated oil bath at 80°C. The reaction was stirred for 4h and the quenched adding 20 mL of cold water. The mixture was vacuum dried and extracted AcOEt/water (3 x 10 mL). The organic layers were washed with brine, dried over Na_2SO_4 and concentrated under vacuum. The crude was then purified by flash column chromatography Hexne/AcOEt (from 97 : 3 to 95 : 5) obtaining 950 mg of product as pale yellow oil. R_f 0.2 in 95 : 5 Hex/AcOEt, permanganate staining. 82% yield.

^{1}H NMR (600 MHz, Acetone-D6): δ 3.45 (dt, J = 16.3, 6.4 Hz, 4H), 3.33 (s, 2H), 3.27 (s, 6H), 1.82 (m, 2H), 1.14 (s, 27H) ppm. MS (ESI+) m/z = 410 $[M+Na]^+$, 426 $[M+K]^+$. IR = 2873, 2096, 1361, 1198, 1078 cm^{-1}.

Synthesis of **BHTG2-OH**

Compound **f** (477 mg, 0.83 mmol) and **p** (350 mg, 0.91 mmol) were dissolved in DMF (10 mL). Copper sulphate penta-hydrated (42.4 mg, 0.17 mmol) and sodium ascorbate (65.4 mg, 0.33 mmol) were dissolved separately in 0.5 mL of water each, then added to the mixture. The reaction was stirred for 2 days at 50°C. The reaction mixture was cooled to room temperature and then vacuum dried. The crude product (1.2 g) was dialysed with water/methanol mixture (7 : 3) overnight. The dialysed was then filtered and vacuum dried.

^{1}H NMR (400 MHz, MeOD-D3): δ 8.03 (s, 2H), 4.88 (s, 20H), 4.78 (s, 2H), 4.51 (t, J = 7.1 Hz, 2H), 3.84 – 3.33 (m, 38H), 3.34 – 3.23 (m, 14H), 2.22 – 2.08 (m, 2H), 1.15 (d, J = 2.7 Hz, 27H). MS (ESI+) m/z = 984 $[M+Na]^+$. IR = 3418, 2932, 1654, 1387, 1255, 1095, 1029, 660 cm^{-1}.

Optimized protocols for PERFECTA@dendrimer formulation

- **Thin film method**

2.5 mg of PERFECTA were solubilized in 250 µL of ethyl acetate and heated at 30°C until the major amount of solvent was evaporated. Then, the residue was air-dried overnight in a glass vial. To the remaining thin film, a Milli-Q water suspension of BFTG2-OH (5 mg/mL) was added. 3 cycles of bath sonication (1 min, 40 kHz) alternated with heating at 70°C for 15 min, finishing with a heating step at 70°C. Then, formulations were left to cool down to room temperature and stirred overnight. The removal of unloaded PERFECTA was pursued by centrifugation (2 x 2 min, 3000 rpm).

- **Nanoprecipitation**

5 mg of PERFECTA were solubilized in 400 µL of ethyl acetate. Separately, BFTG2-OH/BFTG2-S was suspended in Milli-Q water in a round bottom flask. Solution of PERFECTA was added dropwise to the stirring suspension of dendrimer (400 rpm) at 25°C. The mixture was bath sonicated for 1 minute (40 kHz) until the formation of a proper white emulsion. The emulsion was the stirred at 600 rpm for 3 hours at controlled temperature of 25°C. After this stirring time, the formulation appeared transparent and the excess of organic solvent was removed by rotary evaporation setting an initial pressure of 250 mbar and lowering by 10 mbar step until 100 mbar pressure at which it remains for 1 hour. The removal of unloaded PERFECTA was pursued by centrifugation (2 x 2 min, 3000 rpm).
For fluorescent formulations the same protocol was adopted, but for the initial solubilization of PERFECTA 300 µL of ethyl acetate were used, then added with 100 µL of Nile Red solution in ethyl acetate 1 mg/mL. The mixture was then used for the dropwise addition.

Dynamic light scattering (DLS)

DLS measurements were performed in a Malvern Zetasizer Nano ZS analyzer with temperature-controlled sample chamber and 4 mW He-Ne laser (λ = 633 nm) using backscattering detection (scattering angle θ = 173o) with an avalanche photodiode as a detector. Disposable micro‑BRAND UV-Cuvettes were used for the measurements. All measurements were repeated three times with 10 runs per measurement For fluorescent formulations DLS measurements were performed on an ALV apparatus equipped with ALV-5000/EPP Correlator, special optical fiber detector and ALV/CGS-3 Compact goniometer. The light source was He-Ne laser (λ = 633 nm), 22 mW output power. The z-averaged hydrodynamic diameter was extrapolated from the values obtained by a cumulant fitting of the auto-correlation functions measured at 70°, 90°, 110° and 130° scattering angles (θ). For all the samples at θ = 90° the intensity-weighted size distribution was obtained by CONTIN analysis of the relative auto-correlation function. DLS was performed without dilution of the samples.

Nuclear Magnetic Resonance (NMR)

NMR spectra in solution were recorded on a Bruker Avance III 400 MHz spectrometer, or spectrometers ECX 400 (400 MHz) or ECP500 and JEOL-Eclipse (500 MHz) or Avance 700 (700 MHz) from Bruker.

To evaluate the PERFECTA content into the formulations, ^{19}F NMR spectra were obtained adding an external co-axial capillary containing 0.04 M trifluoroacetic acid (TFA) in D_2O into the NMR tube containing 450 µL of formulation. All NMR spectra acquisitions were performed on a Bruker Avance III HD 400 MHz or ECX 400 spectrometer. All chemical shifts were compared to TFA (-75.5 ppm). All ^{19}F NMR spectra were automatically phased and baseline corrected for accurate quantitative analysis through MestReNova software. Each formulation was analysed by ^{19}F NMR for the fluorine content quantification. In detail, ^{19}F NMR spectra were performed on the formulation stocks using TFA reference as previously described. From the ratio of integrals from each peak, the fluorine content was calculated. The encapsulation efficiency (EE%) of PERFECTA and dendrimers into the micelles/vesicles was evaluated using the following formula:

$$EE\ (\%) = W_q / W_i * 100$$

where W_q is the total amount of PERFECTA quantified by ^{19}F NMR and W_i is the quantity of the fluorinated tracer added initially during preparation.

For protein complexes the same set-up was used. All NMR spectra in solution were recorded on a Bruker Avance III 400 MHz spectrometer and same external reference system was used.

T_1 and T_2 experiments were conducted on undiluted formulation in MilliQ water. The fitting of the data was performed by a single exponential fit and raw data were analysed by the Bruker TopSpin software and the MestReNova software.

Fourier transform infrared spectroscopy (FT-IR)

IR spectra were recorded on a *JASCO* FT/IR 4100 spectrometer for the synthetic product obtained at FUB. Infrared spectra at Politecnico of Milano were recorded at room temperature using a Nicolet iS50 FT-IR spectrometer equipped with a DTGS detector. Measurements were always performed on dried samples. Spectra represented an average of 64 scans recorded in a single beam mode. The units for wave numbers were cm^{-1} and values rounded to 1 cm^{-1} upon automatic assignment.

ATR-FTIR spectra fitting was performed by using 4 or 5 gaussian curves according to the following equation:

$$ABS = ABSmax \cdot \exp\left(-\frac{(\lambda-\lambda_0)^2}{2\cdot\sigma^2}\right)$$

Eq. 1

where $ABSmax$ is the maximum absorbance peak, $\lambda 0$ is the wavenumber corresponding to the absorbance peak and σ is the width at half height. Fitting parameters were calculated by minimizing the sum of the squared errors between the experimental data and the sum of the fitting curves.

Table 2.5.1 Fitting parameters for curves reported in Figure 2.24.

	BSA			P@BSA 6:1		
Fitting curve	ABSmax	λ_0	σ	ABSmax	λ_0	σ
Peak 1	0.0062	1569.04	0.027	0.2036	1589.64	0.088
Peak 2	0.0085	1621.92	0.083	0.2899	1620.51	0.076
Peak 3	0.0152	1650.87	0.066	0.3421	1650.46	0.064
Peak 4	0.0025	1680.94	0.105	0.0946	1684.57	0.079

	LYS			P@LYS 5:1		
Fitting curve	ABSmax	λ_0	σ	ABSmax	λ_0	σ
Peak 1	0.017	1635.65	0.080	0.076	1599.88	0.053
Peak 2	0.142	1616.77	0.045	0.373	1627.90	0.065
Peak 3	0.066	1645.74	0.081	0.200	1655.56	0.069
Peak 4	0.154	1659.56	0.041	0.115	1676.52	0.054
Peak 5	-	-	-	0.054	1555.39	0.023

ESI-MS analyses

Mass spectra were measured on a 6210 ESITOF or 6230 ESI-TOF from Agilent.

UV-vis measurements

UV/Vis measurements were conducted on an Agilent Cary 8454 UV-visible spectrophotometer using half-micro quartz cuvettes. Calibration curve of BFTG2-OH was obtained measuring the absorbance at 214 nm of 6 different concentrations of BFTG2-OH in water using serial dilutions (0.075, 0.1, 0.15, 0.20, 0.30, 0.35 mg/mL).

Determination of CMC Using Fluorescence Method

The CMC of BFTG2-S was determined by the fluorescence technique using Nile red as a model dye. A stock solution of the dye in methanol (1 mg mL^{-1}) was prepared. Each 20 µL of this stock solution was added to 10 sample vials were the methanol was allowed to evaporate to leave a thin-film of the dye. Note that, 5mg/mL stock solutions of the amphiphiles in Milli-Q water were stirred at least for 1 h before their serial dilutions to the final sample concentrations. The sample solutions were then transferred to the dye-loaded vials and kept stirring overnight, before nonencapsulated dye was removed by filtration through 0.45 µm polytetrafluoroethylene filter. Fluorescence measurements were performed using a Cary Eclipse fluorescence spectrophotometer. To graphically determine the CMC, the fluorescence intensity at λ = 635 nm was plotted against the logarithm of the amphiphile concentration. Fluorescence intensities were measured (excitation λ = 552 nm) using a fluorimeter Jasco FP-8500.

Cryo-Transmission Electron Microscopy (cryo-TEM)

All cryo-TEM for both study lines were performed by Dr. Boris Shade (FUB). Perforated carbon film covered microscopical 200 mesh grids (R1/4 batch of Quantifoil, MicroTools GmbH, Jena, Germany) were cleaned with chloroform and hydrophilized by 60 s glow discharging at 10 µA in a EMSCOPE SC500 before 4 µl aliquots of the amphiphile solution were applied to the grids. The samples were vitrified by automatic blotting and plunge freezing with an FEI Vitrobot Mark IV (Thermo Fisher Scientific Inc.,Waltham, Massachusetts, USA) using liquid ethane as cryogen and then transferred to the autoloader of a FEI TALOS ARCTICA electron microscope (Thermo Fisher Scientific Inc., Waltham, Massachusetts, USA). The microscope is equipped with a high-brightness field-emission gun operated at an acceleration voltage of 200 kV. Micrographs were acquired on an FEI Falcon three direct electron detector (Thermo Fisher Scientific Inc., Waltham, Massachusetts, USA) at a nominal magnification of 28 000, corresponding to a calibrated pixel size of 3.75 A/pixel.

MRI Protocol

Magnetic Resonance Imaging MRI was performed on a 7T MR system (Biospec; Bruker Biospin) equipped with a horizontal bore magnet (ultra-shielded). A dual-transmit-receive $^{19}F/^{1}H$ volume coil (35 x 59 mm) was used for both proton and fluorine MRI. ^{19}F-images were acquired with the resonance frequency centred halfway between PERFECTA and the dendrimer (BFTG2-OH or BFTG2-S) determined on ^{19}F-NMR spectrum obtained with a single pulse sequence (TR = 8s, average = 32, spectral width = 56818 kHz). For both 1H and ^{19}F MRI, a 3D turbo-spin echo sequence was

used with the same FOV (50 × 27.7 × 21.6 mm^3) but different parameters were optimized for fast imaging and high sensitivity MRI:

Table 2.5.2 *MRI parameters for in vitro experiments*

	TR/TE (ms)	Echo train	Matrix	Averages	Acquisition time
^{1}H	1000/24	10	256 x 128 x 16	2	4min 48s
^{19}F	1350/40	20	64 x 32 x 16	100	36min

^{19}F-MRI sensitivity experiments on optimized formulations were performed at a concentration ranging from 7 to 12 × 10^{18} ^{19}F atoms in 150 µL of Milli-Q water. The mean signal intensity was measured in the area of each sample on the ^{19}F image and divided by the standard deviation of the noise taken in an area of the image outside of the samples. The total amount of ^{19}F atoms was estimated in relation to the SNR of a PERFECTA reference standard (lecithin emulsion containing 5.5 × 10^{19} ^{19}F atoms).

Cytotoxicity Studies

The cytotoxicity of the formulation was studied at the concentration of 0.5, 0.25, and 0.125 mg/mL using cell viability assay by Cell Counting Kit-8 (CCK-8) from sigma conferring to the manufacturer's instructions. For the studies, HeLa and U-937 cells were cultivated in RPMI-Medium. For cell viability measurements both cell lines were seeded in a 96-well plate at a density of 5x10^4 cells/mL in RPMI-Medium (90.0 µL/well). The seeded cells were incubated over night at 37°C and 5% CO_2. A 1:1 dilution series of each compound was prepared starting with a stock concentration of 5.00 mg/mL. 10.0 µL/well of each compound was applied to the plate including positive (1% SDS) and negative (Medium, 10% DPBS) controls. The cells with compound were incubated for another 24h at 37°C and 5% CO_2. After 24h of incubation 10.0 µL/well of CCK-8 solution was added. After 3h of incubation at 37°C and 5% CO_2 the absorbance was measured (450nm/650nm) using a Tecan SPARK Plate Reader. All measurement were performed in triplicate. The cell viability was calculated by setting the negative control to 100% using the Excel software.

Cell lysis protocol

Cells from cytotoxicity test treated with 0.5 mg/mL formulation were collected and counted. Cells were then centrifugated to remove all the not uptaken formulation and the dead cells. The cell pellet was resuspended in 0.4 mL of lysis buffer (PBS+2.5% v/v Triton

X-100), mixed vigorously and incubate for at least 15min. The clear solution was analysed by NMR and the quantification was made using an external reference of TFA (4 x 10^{-4} M). Quantification of ^{19}F/cell was made dividing the total ^{19}F quantified by NMR for the number of cells counted. The % of uptake was obtained dividing the ^{19}F quantified for the starting ^{19}F administered.

Cellular uptake

The Cellular uptake of BFTG2-OH and BFTG2-S loaded with Nile red in HeLa cancer cell line and U937 pro-monocytic cell line was monitored using confocal laser scanning microscopy (cLSM). The cells were routinely cultivated. For cLSM, 270 µL of cells in RPMI with a cell density of 5 x10^4 cells/mL were seeded in each well of an 8-well µ-slide. After 9 h of incubation at 37°C and 5.00 % CO_2 30.0 µL of Nile red loaded compound were added at a final test concentration of 0.50 mg/. As a positive control 30.0 µL of Nile red in DMSO at a final test concentration of 0.0002 mg/mL was added. After incubation over night the cell nuclei was stained with 1.00 µg/mL Hoechst 33342 (Life Technologies GmbH, Darmstadt, Germany). The confocal images were taken by using an inverted confocal laser scanning microscope Leica DMI6000CSB SP8 (Leica, Wetzlar, Germany) with an 63x/1.4 HC PL APO CS2 oil immersion objective using the manufacture given LAS X software.

Circular dichroism (CD)

CD spectra were recorded in Milli-Q water (18.2 MΩ·cm) in a 0.1 cm quartz cuvette, using a JASCO J-815 CD spectrometer. Acquisitions were performed in the range 200−300 nm for BSA complexes and 190-300 for LYS complexes using 1.0 nm data pitch, 1.0 nm bandwidth, 100 nm/min scanning speed, and 1 s response time. All the spectra are an average of 3 scans. Samples were prepared by diluting with Milli-Q water in order to reach a final concentration in protein 0.1 (BSA) and 0.2 mg/mL. Raw data (θ, in millidegree) were subsequently converted to molar ellipticity (Mol. Ellip., in deg·cm^2·$dmol^{-1}$) for the sake of comparison, in accordance with the following formula:

$$Mol.Ellip. = \frac{\theta}{10 \cdot l \cdot C}$$

Eq. 2

where θ is the observed ellipticity in millidegrees, C is the concentration of the sample in mol·L^{-1}, and l is the path length of the cuvette in cm.

Congo Red staining

P@LYS and LYS solutions used for staining experiments were placed on a glass microscope, allowed to air dry and then stained with a Congo Red solution. An 80% ethanol solution saturated with NaCl and Congo Red was freshly prepared before each measurement. Samples were analysed using polarised light and monitored for green birefringence using an Olympus BX50 polarising microscope with a SensiCam PCO camera, which was used to display and enhance images.

Small Angle X-ray Scattering (SAXS)

SAXS measurement were performed with a Xeuss 3.0 UHR SAXS/WAXS system (Xenocs SAS, Grenoble, France) equipped with a GeniX 3D CuK α radiation source (λ ≈ 1.54 Å) and with in-vacuum motorized 3-axis Q-Xoom Eiger2 R 1M detector (Dectris Ltd., Switzerland) for 2D SAXS/WAXS data collection. The explored q range was 0.00017 $Å^{-1} < q < 1.7$ $Å^{-1}$ were q is the absolute value of the scattering vector and is defined as: $q = \frac{4\pi \sin(\theta/2)}{\lambda}$ and 2θ is the scattering angle. Measurements were performed under vacuum (< 0.1 mbar). 100 µL of protein aqueous solution was placed in 1 mm quartz capillary and sealed before measuring. Each sample was measured at three distances from the detector (90 cm, 35 cm, 15 cm) for 7200 sec, 3600 sec and 900 sec, respectively, at high-resolution collimation mode. Experimental data were subsequently corrected for capillary and solvent (Milli-Q water). Data were fitted in the SasView software package.[214] Polydispersity was not considered during the fitting analyses.

Scattering length density (sld) and volume of lysozyme were known from the literature.[215] PERFECTA sld and volume were calculated from the crystal structure (CCDC code 993466).[62] Scale was then calculated and fixed as well.

Table 2.5.3 *Fitting parameters obtained from the fit of the SAXS data. Scale, sld and sld solvent were calculated and fixed.*

LYS		**P@LYS**	
Fitting model	Ellipsoid	Fitting model	Elliptical cylinder
q range (Å)	$0.00662 < q < 0.6$	q range (Å)	$0.00662 < q < 0.6$
Chi^2/Npts	3.5031	Chi^2/Npts	8.5763
Scale	0.00012	Scale	0.006622
Background (cm^{-1})	$6.851 \times 10^{-5} \pm 6.8 \times 10^{-6}$	Background (cm^{-1})	$8.635 \times 10^{-5} \pm 9 \times 10^{-6}$
Radius polar (Å)	14.675 ± 0.363	Radius minor (Å)	35.66 ± 0.067
Radius equatorial (Å)	19.489 ± 0.22	Axis ratio	3.18 ± 0.016
		Length (Å)	531.71 ± 4.99
Sld ($x10^{-6}$/Å^2)	2.17	Sld ($x10^{-6}$/Å^2)	6.47
Sld solvent ($x10^{-6}$/Å^2)	9.4	Sld solvent ($x10^{-6}$/Å^2)	9.4

Chapter 3

Amino Acid-Based Hydrogels with Tuned Properties: a Molecular Understanding

3.1 Crystal engineering principles to design low molecular weight hydrogelators

In the field of supramolecular hydrogels, as introduced in **Section 1.3.2**, the tailoring of specific properties is a major challenge. This is due to the lack of molecular insights on the self-assembly process which drives gelation. Such limitation hampers scientists in the choice of effective gelators and in the design of supramolecular hydrogels. Recently, it was proposed to study the noncovalent interactions involved in the crystal packing of supramolecular synthons as a tool to predict and control the macroscopic characteristics of related hydrogels.[221–223] Despite the ongoing debate concerning the relationship between self-assembly in the solid state and in gel phase,[224] the design of low molecular weight hydrogelators (LMWHs) through crystal engineering has led to concrete results,[225–228] mainly in organic salts[229–232] and metallogels,[233,234] to name a few.

Fmoc-amino acids, particularly aromatic ones (*i.e.,* Fmoc-phenylalanine) and those bearing halogen atoms, are reported to rapidly associate into fibrillar structures in water, resulting in efficient gelation.[162,163,235] It was widely treated in **Section 1.3.2.1** the effect of fluorination upon *N*-Fmoc-phenylalanine, and in particular *N*-Fmoc-L-pentafluorophenylalanine - Phe(F_5), **Figure 3.1** was the focus of many studies. In fact, its capacity to afford stable hydrogels at low concentrations (0.1 wt.%) is due to the strong self-association tendency of perfluorinated phenyl ring.[163] The tailoring of its properties was tested through several strategies, spanning from chemical modifications (to enhance stability and promote self-association) to co-assembly with other Fmoc-amino acids or peptides, in order to interfere with the π-π stacking originated by the protecting moiety.[96–98,166,167,236]

In this chapter of the thesis, the crystal engineering-based strategy mentioned above has been tested for the first time to modulate the gelling properties of Phe(F_5) using a non-gelator partner able to form strong hydrogen bond (HB) interactions with its carboxylic moiety, instead of just interfering with the stacking of aromatic moieties. Thus, the co-crystal former BZ (**Figure 3.1**) was chosen for two reasons: i) the supramolecular synthon acid···amide between the -COOH of compound Phe(F_5) and -$CONH_2$ of BZ could drive the co-crystallization. ii) The structure similarity of BZ with some APIs. In fact, in the creation of ordered supramolecular crystalline systems, the acid···amide heterodimeric synthon (**Figure 3.3**, zoom) has been reported to be a robust and highly directional structural module.[237] Similarly, C=O···H-N interactions have been demonstrated to be important in hydrogel formation.[238] In this study, the self-assembly of Phe(F_5) and BZ (**Figure 3.1**) has been thoroughly investigated both in the solid state and in aqueous gel phase, and compared to the behaviour of Phe(F_5)

alone in the same conditions. The correspondence between crystalline and hydrogel Phe(F_5)+BZ mixed systems was proven through structural, spectroscopic, and thermal characterizations, which confirmed that the acid···amide supramolecular synthon was also occurring in the gel. I also performed preliminary release studies, replacing BZ with a bioactive compound with a similar molecular structure, namely nicotinamide or vitamin B_3 (NC, **Figure 3.1**), to assess the potential use of this design approach in drug release applications.

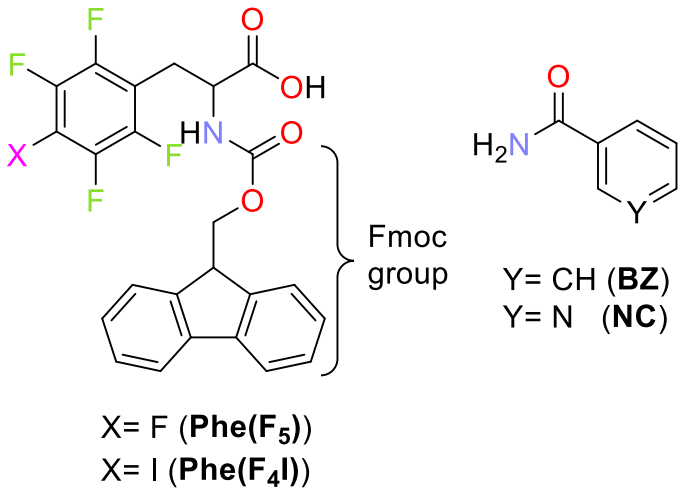

Figure 3.1 *Molecular structures of N-Fmoc-L-pentafluoro-phenylalanine (Phe(F_5)), N-Fmoc-L-2,3,5,6-tetrafluoro-4-iodo-phenylalanine (Phe(F_4I)) benzamide (BZ) and vitamin B_3 (NC).*

Subsequently, the same crystallographic approach was applied to another system, where the HB-based supramolecular synthon was replaced by a halogen bond- (XB-) forming one. According to the IUPAC definition, the 'halogen bond' is a highly directional noncovalent interaction between a covalently bound halogen atom X (usually Cl, Br, or I) in a molecule R-X and the negative site of a nucleophile (e.g., a lone pair of a Lewis base or π-electrons of an unsaturated system).[239,240] The ability of halogen atoms to act as electrophiles relies on the anisotropic distribution of electron density around the halogen involved in the covalent bond (**Figure 3.2a**). Along the extension of the covalent bond R-X, the halogen's electrostatic potential displays an electron-poor region, labelled as σ-hole, which is responsible of attracting nucleophiles. Conversely, the surrounding perpendicular region of X shows an enhanced electron density.[241,242]

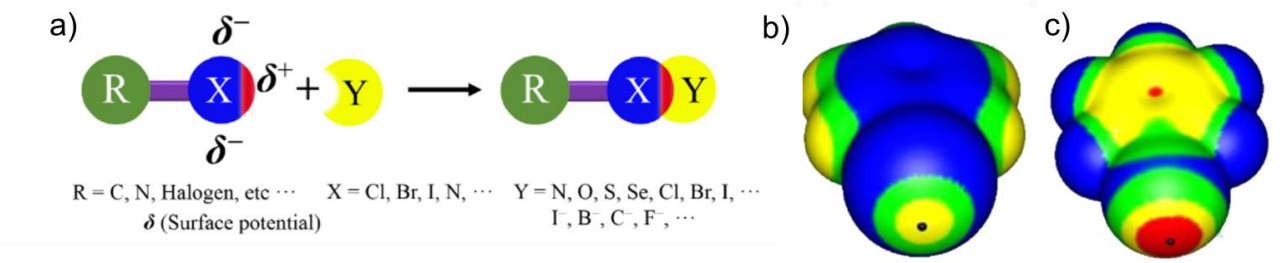

Figure 3.2 *a) Structural scheme of halogen bond (XB).*[243] *b-c) Computed electrostatic potentials on 0.001 au molecular surfaces of iodobenzene (b) and pentafluoroiodobenzene (c). Colour range (kcal/mol): red, greater than 20; yellow, between 20 and 10; green, between 10 and 0; blue, negative. Black hemispheres denote the positions of the halogen* $V_{S,max}$[242].

Such electrostatic configuration justifies the main features of XB: i) directionality, which originates from the localization of the σ-hole along the covalent bond R-X, giving rise to linear R-X···Y interactions (160° - 180°). ii) Strength tunability is then possible by changing the halogen atom involved, with XB donor ability increasing in the order F < Cl < Br < I, in accordance with increasing polarizability and lower electronegativity. Thus, XB strength can span from few kJ/mol to more than 100 kJ/mol. [244] Literature presents different cases in which halogenation, with halogens different from fluorine, can prompt dramatic changes in a functionalized amino acid system, suggesting that halogenation is a minimal, but relevant, local modification for a molecular structure.[222,235,245] Thus, the effect of further halogenation of Phe(F_5) is a fascinating topic. Iodine-substitution in *para* position of the perfluoro-aromatic side chain of this amino acid led to the new *N*-Fmoc-L-tetrafluoro-iodo-phenylalanine - Phe(F_4I) (**Figure 3.1**). The introduction of this different halogen atom gave place to the typical positive *σ*-hole on iodine, whose positive character is then increased by the surrounding C-F on the phenyl ring, as indicated by the electrostatic potential maps shown in **Figure 3.2b-c**.[242] As a consequence, fluorination should improve the strength of any possible XB, and its influence was studied both in the solid and gel state in the second part of this chapter. Another strategy was implemented to crystallize compound Phe(F_5) and Phe(F_4I), exploiting the coordination efficacy of their acidic group -COOH.[246,247] In particular, metal cations like Na^+ and K^+ were chosen because of their common presence in the physiological media. Structural information about the packing showed how the *σ*-hole in Phe(F_4I) led to an alteration of aromatic interactions. Subsequently, the corresponding hydrogels were studied to check the correspondence with the evidences obtained from crystal packing, to validate our general approach.

Results and discussion

3.2 Acid···Amide heterosynthon design

3.2.1 Solid-state study: co-crystallization

Given the strong gelation tendency of Fmoc-amino acids, the formation of single crystals represents a highly challenging task. As an evidence, the only crystal structure of Phe(F_5) (**Figure 3.1**) deposited in the Cambridge Structural Database (CSD) was reconstructed from powder X-ray data.[248] For this reason, a crystal engineering approach based on the acid···amide supramolecular synthon between Phe(F_5) and benzamide BZ was hypothesised to induce its crystallization, allowing to gain a thorough understanding of the molecular assembly properties of Phe(F_5).

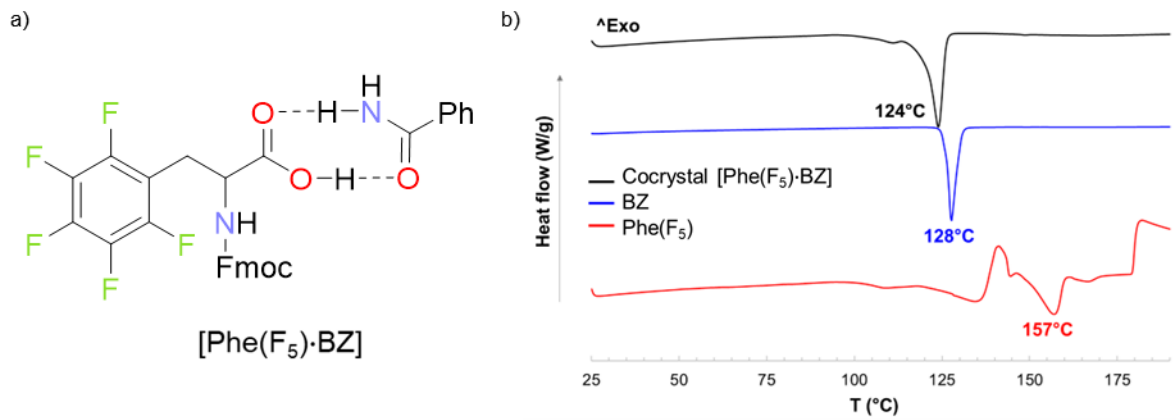

Figure 3.3 *a) Molecular structure of the supramolecular adduct [Phe(F_5)·BZ]. b) DSC thermograms of co-crystal [Ph(F_5)·BZ] and of the related starting building blocks (heating rate 10 °C/min).*

To test the possibility of a supramolecular adduct between Phe(F_5) and BZ, they were dissolved in acetonitrile and then the solution was evaporated to dryness. Complete evaporation of a Phe(F_5)+BZ equimolar solution afforded a crystalline powder. Differential scanning calorimetry (DSC) analysis performed on such solid residue showed a unique and sharp endothermic peak of melting at 124 °C (**Figure 3.3b**), different from the melting points of the starting monomers (157 °C for (Phe(F_5) and 128 °C for BZ), suggesting the formation of a new crystalline species (adduct [Phe(F_5)·BZ], **Figure 3.3a**). Fourier-Transform infrared (FT-IR) spectroscopic analysis of the powder provided a preliminary indication of the presence of the acid···amide heterodimer, as shown by the marked blueshifts of the characteristic N-H stretching bands of benzamide (3361 and 3161 cm^{-1}) (**Figure 3.4**).[237] In the formed adduct these two marker peaks moved to 3470 and 3216 cm^{-1}, with a frequency change of +107 and +55 cm^{-1} respectively. A similar, although less pronounced, blueshift (+8 cm^{-1})

was observed also for the amide I band, moving from 1623 to 1631 cm^{-1} in the adduct. At the same time, the O-H stretching band of the carboxylic moiety, at around 2800 cm^{-1}, was redshifted upon HB formation, and resulted in two broad peaks at about 2400 and 1900 cm^{-1}.

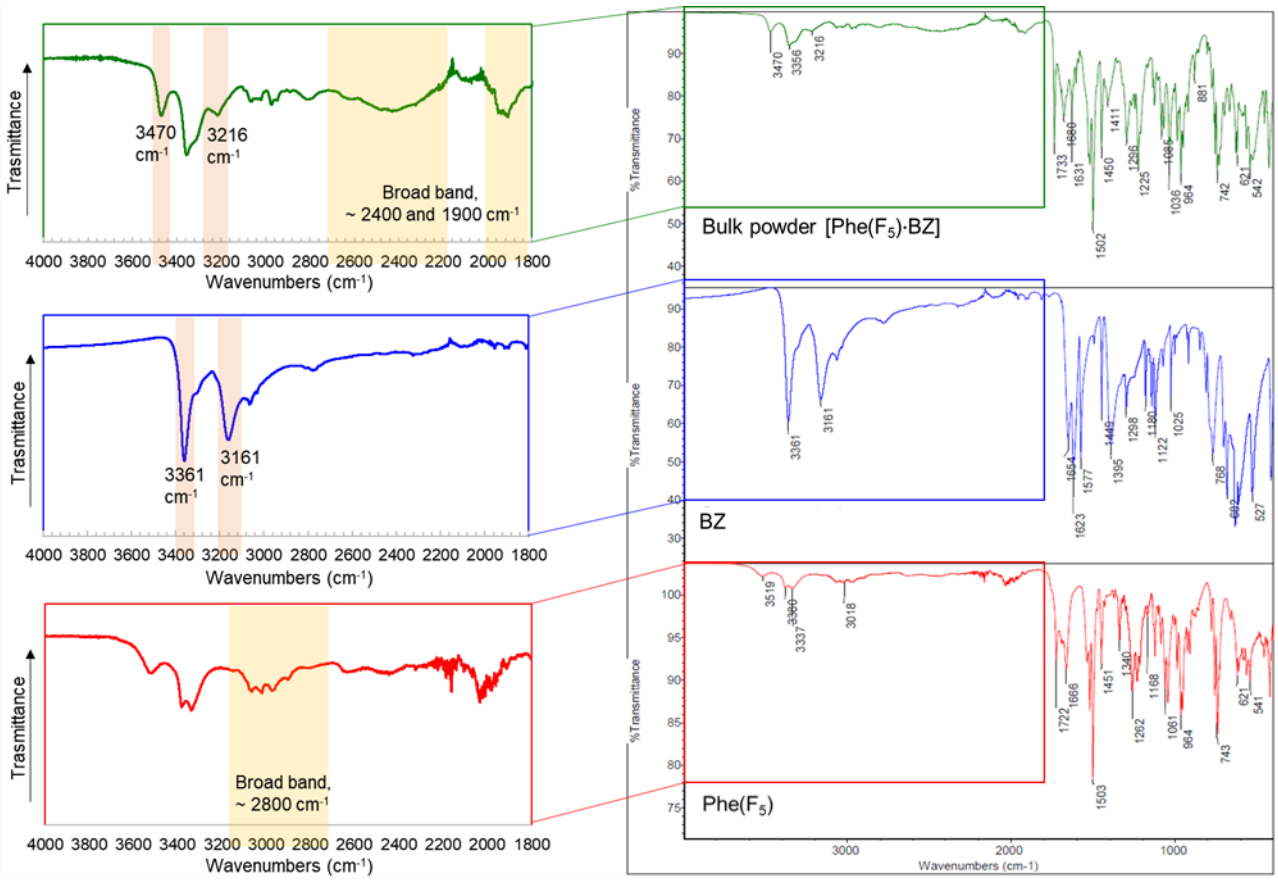

Figure 3.4 *FT-IR spectra of bulk powder of adduct [Phe(F_5)·BZ] and of its starting building blocks, highlighting the shifts due to the presence of an acid···amide HB synthon.*

Furthermore, spectroscopic studies in organic solution by NMR of the equimolar mix Phe(F_5)+BZ suggested the same dimeric interaction. In particular, ^{13}C-NMR spectra showed a slight shift to the downfield of the C=O signal of Phe(F_5), which can be attributed to HB with the amide moiety (**Figure 3.5a**).[248]

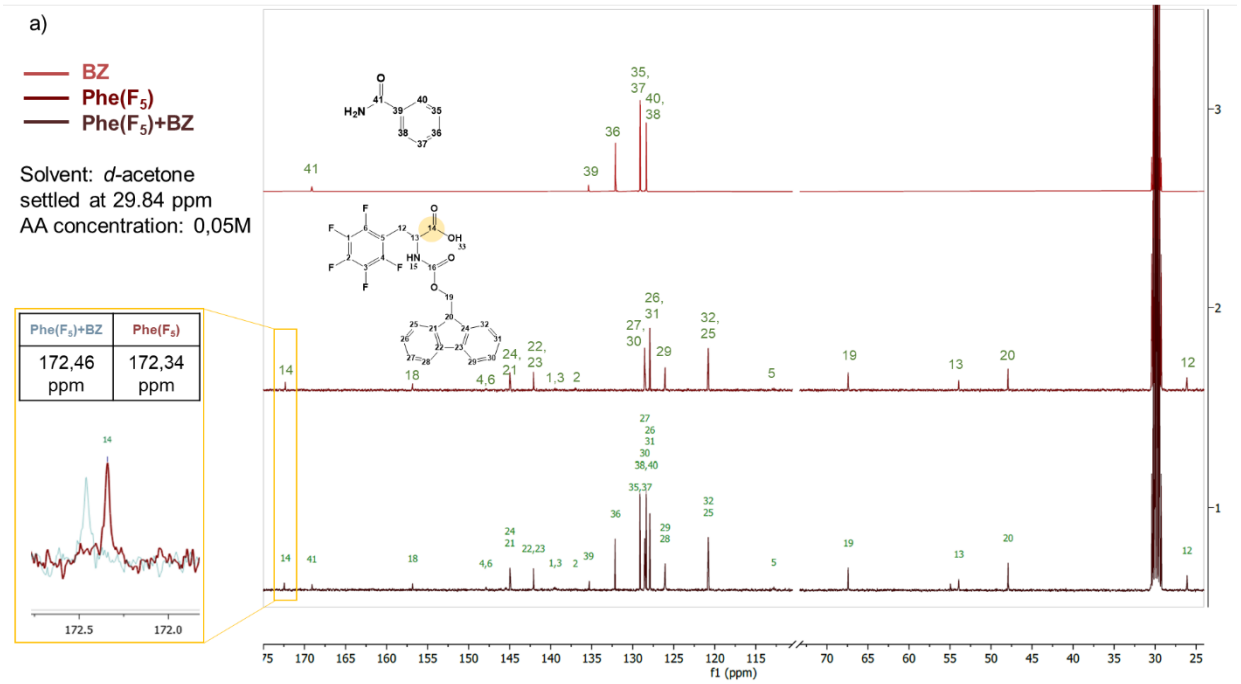

Figure 3.5 a) *^{13}C-NMR spectra (acetone-d_6) of BZ (50 mM), Phe(F_5) (50 mM), and their equimolar mixture. The zoom shows a downfield shift of the C=O signal of Phe(F_5).*

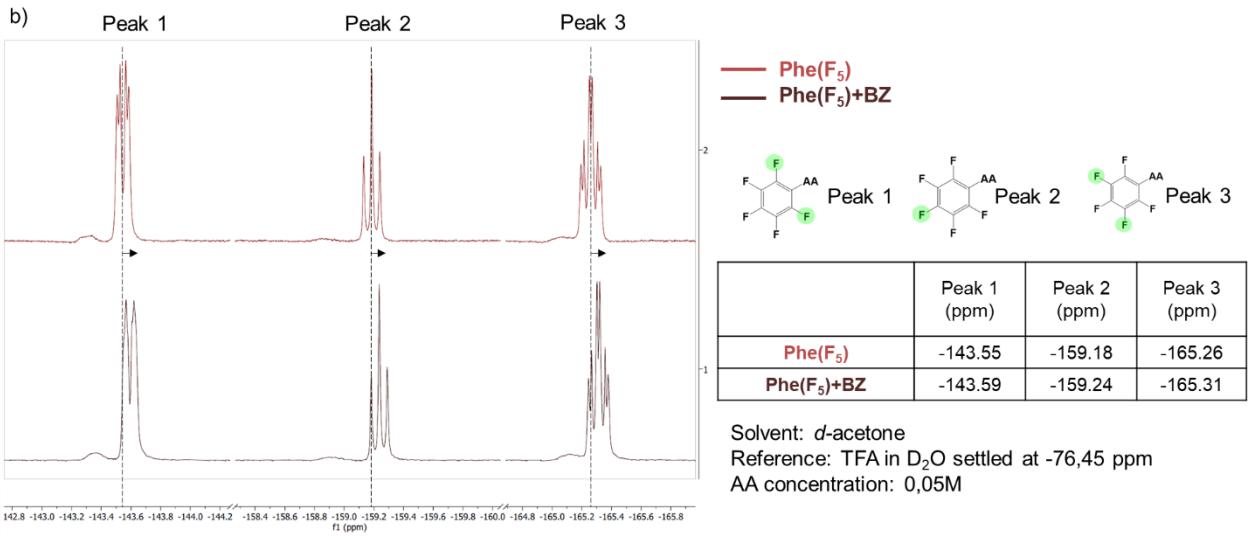

	Peak 1 (ppm)	Peak 2 (ppm)	Peak 3 (ppm)
Phe(F_5)	-143.55	-159.18	-165.26
Phe(F_5)+BZ	-143.59	-159.24	-165.31

Figure 3.5 b) *^{19}F-NMR spectra (acetone-d6) of Phe(F_5) (50 mM), and of its equimolar mixture with BZ.*

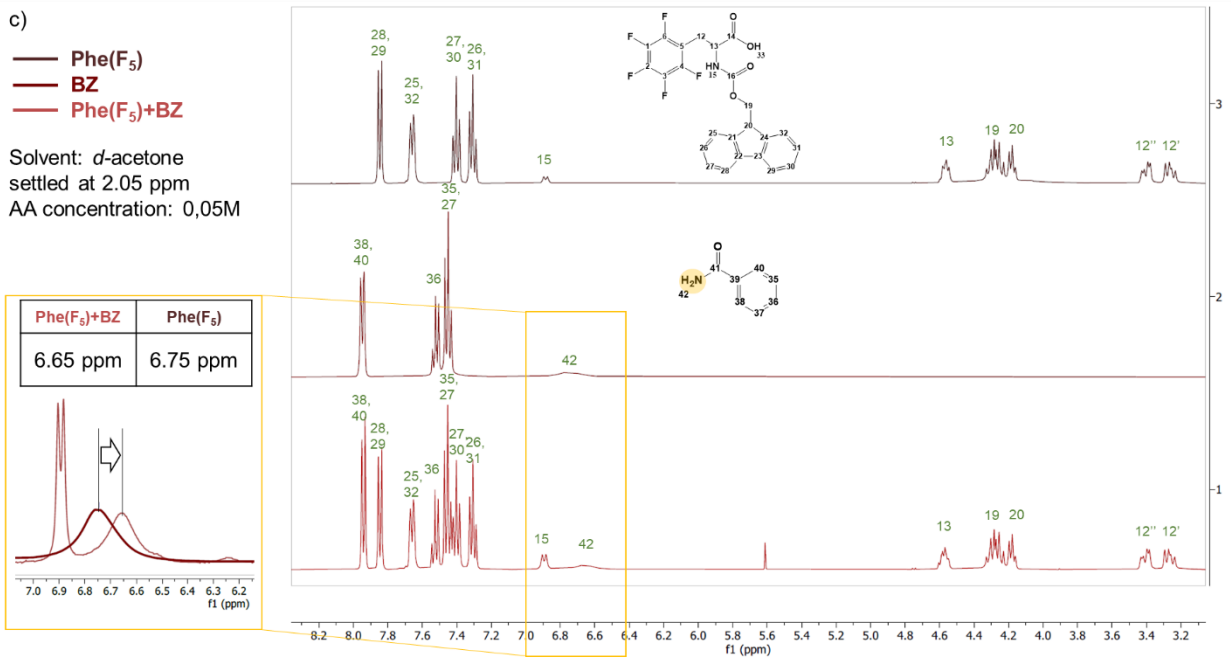

Figure 3.5 c) *^{1}H-NMR spectra (acetone-d6) of Phe(F_5) (50 mM), BZ (50 mM), and their equimolar mixture. The zoom shows an upfield shift of the NH_2 signal of BZ.*

In case of ^{19}F-NMR spectra, an upfield shift of all the signals of the amino acid fluorine atoms was observable in the 1:1 mixture due to the electron shielding effect of benzamide complexation (**Figure 3.5b**). Additionally, the upfield shift of the NH_2 signal of BZ detected by ^{1}H-NMR spectra might be attributed again to the complex formation (**Figure 3.5c**).

Inspired by these first results, we proceeded to slowly evaporate the 1:1 solution of Phe(F_5) and BZ in acetonitrile at room temperature, in order to grow single crystals suitable for crystallographic structural characterization. Within two days we obtained good-quality crystals of adduct [Phe(F_5)·BZ], which crystallized in the orthorhombic space group $P2_12_12_1$ with one molecule of each component in the asymmetric unit (**Figure 3.6a**). The driving acid⋯amide supramolecular synthon formation was confirmed by single-crystal X-ray structure analysis of [Phe(F_5)·BZ], with the following geometrical parameters: C=O⋯H–N (**HB1**) distance of 2.181 Å, and O–H⋯O=C (**HB2**) of 1.713 Å, respectively. The carboxylic C=O unit of the Fmoc-protected amino acid was also involved in the formation of further HB with N-H group of adjacent Phe(F_5) molecule (**HB3**, N–H⋯O distance 2.336 Å, **Figure 3.6b**). This two-fold HB-donor ability of the amino acid's carboxylic moiety created infinite chains of the dimers running along the crystallographic *a*-axis.

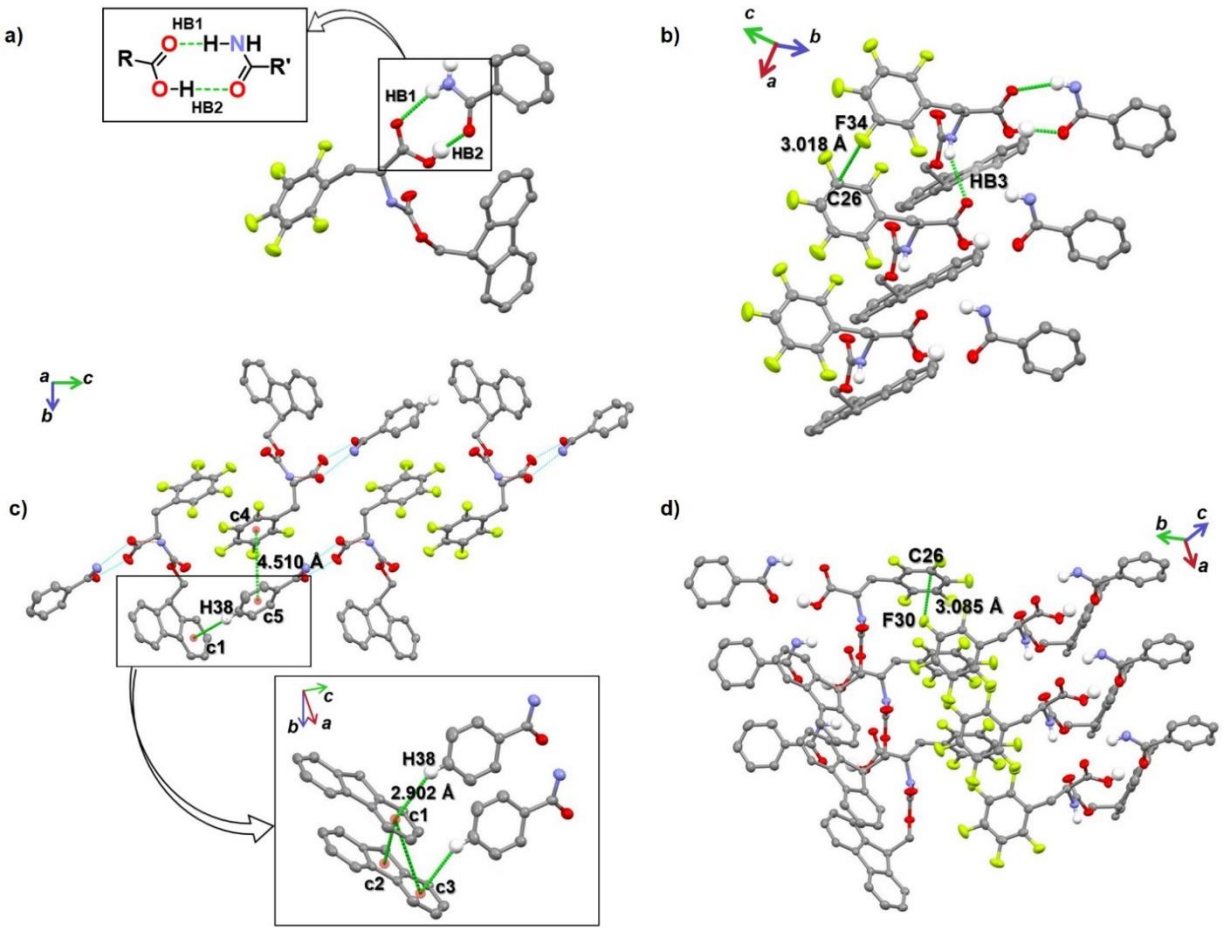

Figure 3.6 *Ball-and-stick crystallographic representations of: a) asymmetric unit of [Phe(F$_5$)·BZ] (zoom: acid···amide supramolecular synthon); b) packing of [Phe(F$_5$)·BZ] units in a chain, viewed along the crystallographic a-axis; c) packing of two adjacent chains of [Phe(F$_5$)·BZ] units (zoom: offset displacement of Fmoc groups); d) inter-chain interactions between fluorine moieties. Colour code: carbon, grey; oxygen, red; nitrogen, light blue; fluorine, yellow. HB contacts and other packing interactions are indicated by green dotted lines.*

Furthermore, π-π interactions between adjacent Fmoc units increased the stabilization of this hydrogen-bonded. The parallel lateral offset packing mode showed asymmetric distances between their centroids c1···c2 and c1···c3 (5.485 Å and 4.628 Å respectively, **Figure 3.6c**, zoom). The relative position of neighbouring pairs of molecules in the acid···amide supramolecular chain followed a specific tacticity, characterized by neat spatial separation among perfluorinated phenyl rings, Fmoc units, and phenyl rings of benzamide. Each different aromatic moiety formed stacked pillars, pointing towards different sides of the main backbone. Notably, a comparison of the Fmoc units arrangement in [Phe(F$_5$)·BZ] and Phe(F$_5$) showed that the distance between fluorenylmethyloxycarbonyl fragments was larger in the supramolecular dimer [Phe(F$_5$)·BZ] than in Phe(F$_5$) highlighting a minor overlap, and thus a minor stability, of the Fmoc groups in the benzamide adduct.[248] Furthermore,

adjacent acid···amide dimers belonging to different chains were stabilized by two additional types of interactions (**Figure 3.6c**).

Deepening the analysis, a complementary π-π stacking with lateral displacement involved pentafluorophenyl rings of Phe(F_5) and phenyl rings of BZ (c4···c5, **Figure 3.6c**), similar to the result previously reported for pentafluorobenzamide and benzamide 1:1 co-crystal.[249] T-shaped aromatic contacts between Fmoc and benzamide constituted the second major inter-chain interaction; their edge-to-face c1···H38 distance was even shorter than the intra-chain Fmoc-Fmoc spacing. Additionally, the overall crystal packing of [Phe(F_5)·BZ] was stabilized by weak F···C interactions among fluorinated rings (F34···C26, **Figure 3.6b** and F30···C26, **Figure 3.6d** respectively). Comparing crystal packing of Phe(F_5) alone and [Phe(F_5)·BZ], the latter is loosened by the presence of BZ, perturbing the Fmoc-Fmoc stacking and increasing the spacing among amino acid molecules. This ability of benzamide to interfere with the self-assembly of Phe(F_5) in the solid state might be used as a strategy to modulate the gelation process of Phe(F_5) creating a less tight hydrogel upon addition of BZ.

Table 3.1 *Crystallographic data and refinement details for co-crystal [F(F_5)·BZ].*

Chemical formula	$C_{24}H_{16}F_5NO_4 \cdot C_7H_7NO$
Mr	598.51
Crystal system	Orthorhombic
Space group	$P2_12_12_1$
Temperature (K)	173
a, b, c (Å)	5.4853 (2), 13.2333 (5), 36.8152 (12)
V (Å^3)	2672.34 (16)
Z	4
Radiation type	Cu Kα
μ (mm−1)	1.07
Crystal size (mm)	0.08 × 0.06 × 0.05
Absorption correction[a]	Multi-scan
Tmin, Tmax	0.232, 1.000
No. of measured, independent and observed [I > 2σ(I)] reflections	13918, 4753, 4008
Rint	0.055
(sin θ/λ)max (Å−1)	0.630
R[F^2 > 2σ(F^2)], wR(F^2), S	0.044, 0.105, 1.03
No. of reflections	4753
No. of parameters	390
H-atom treatment	H-atom parameters constrained
Δρmax, Δρmin (e Å−3)	0.25, −0.20
Absolute structure parameter[b]	0.03 (10)
CCDC number	2265129

[a]CrysAlis PRO 1.171.42.55a (Rigaku Oxford Diffraction, 2022) Empirical absorption correction using spherical harmonics, implemented in SCALE^3 ABSPACK scaling algorithm.
[b]Absolute structure: Flack x determined using 1292 quotients [(I+)-(I-)]/[(I+)+(I-)] (Parsons, Flack and Wagner, Acta Cryst. B69 (2013) 249-259).

3.2.2 Hydrogel state study

The hydrogelation features of 1:1 mixture of Phe(F_5) and BZ were then investigated. The possible correlation between the assembly in the gel phase and the crystal state was the next focus of this study. If the interactions observed in the solid state were preserved after the gelation, the increased distance among the Fmoc units should alter the hydrogel properties of Phe(F_5).

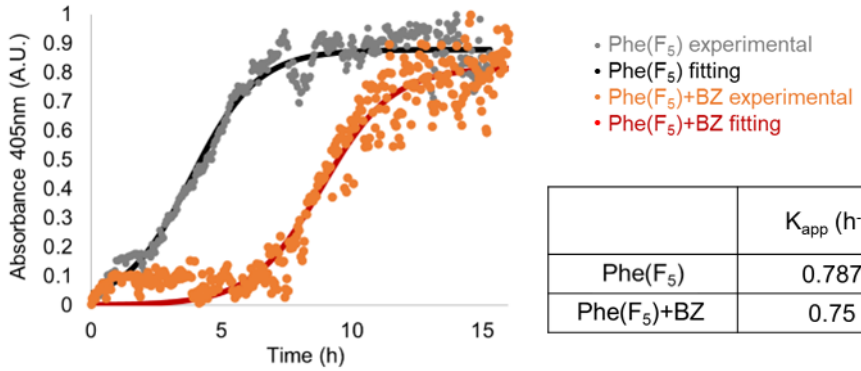

	K_{app} (h^{-1})	Delay time T (h)
Phe(F_5)	0.787	1.31
Phe(F_5)+BZ	0.75	6.18

Figure 3.7 *Fibrillation kinetics of 0.1 mM solutions of Phe(F_5) and Phe(F_5)+BZ. Fittings of experimental data are shown as solid lines.*

Fibrillation kinetics of Phe(F_5) – both with and without BZ – were monitored by recording the change over time of the UV-visible absorbance at 405 nm. The samples were prepared in dilute aqueous solutions (0.1 mM, 2 $\%_{v/v}$ DMSO in water) and incubated under controlled conditions of temperature and stirring (25 °C, 432 rpm). Plotting the results according to absorbance *versus* time a sigmoidal trend was observed, confirming the formation of fibrils in both cases (**Figure 3.7**) where the typical stages of amyloid fibrillation were discernible: initial lag phase, elongation step and final equilibrium steady state.[250] The fitting of the experimental data gave the possibility to define the two quantitative parameters, delay time (T) and apparent rate constant of fibril growth (K_{app}) which proved the much slower fibrillation kinetic in presence of BZ, due to its interaction with the amino acid in water. A 5-hour delay in the formation of light scattering fibrils was observed for Phe(F_5)+BZ mixture, with respect to a solution of pure Phe(F_5)**.** Given these encouraging fibrillation results, hydrogels were prepared through the solvent switch method previously reported by Nilsson and collaborators. [251]A stock solution of Phe(F_5) in DMSO (247 mM) was diluted with Milli-Q water up to a concentration of amino acid of either 5 mM (0.24 wt%) or 2.5 mM (0.12 wt%). Following the same protocol, from an equimolar DMSO stock solution of Phe(F_5) and BZ mixed hydrogels were prepared. In all cases, transparent gels were obtained within a few minutes. They were stable at room temperature and did not collapse upon vial inversion, until temperatures of 76 °C for Phe(F_5) and 68 °C for Phe(F_5)+BZ were reached. Rheological data for hydrogels of Phe(F_5) were in line with those reported in the

literature.[163,166] Hydrogel formation were confirmed by oscillatory rheological measurements (**Figure 3.8**), time sweep, and frequency sweep experiments (not shown), recorded after 24 hours from sample preparation.

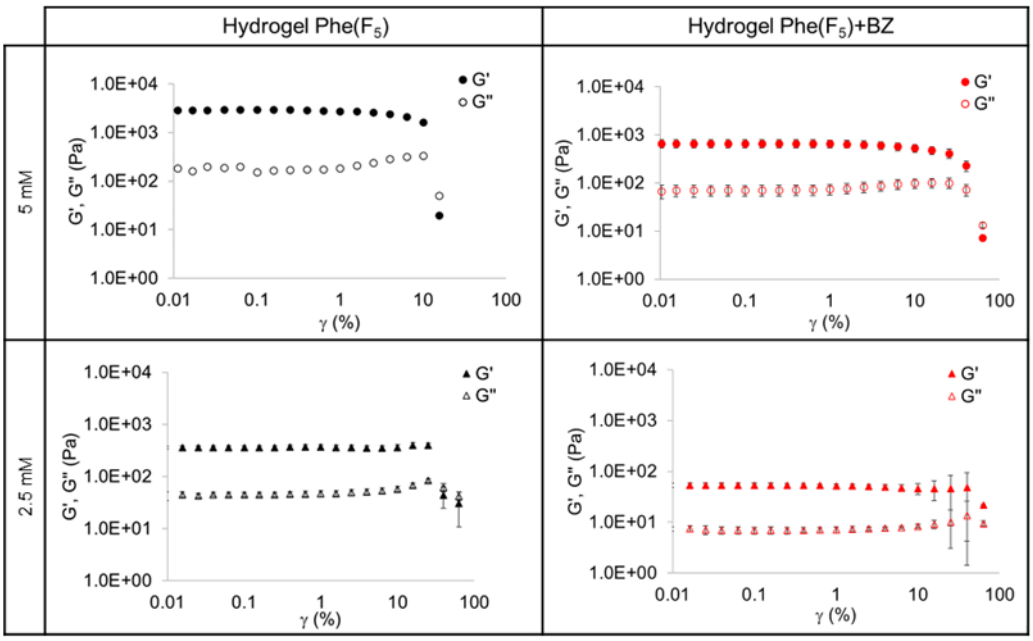

Figure 3.8 *Strain sweep experiment (Linear Viscoelastic Region) for Phe(F_5) (black) and Phe(F_5)+BZ (red) components, measured at different concentrations (5 mM and 2.5 mM). Oscillation amplitude table: frequency 0.95 Hz, 5 samples per decade.*

In particular, strain sweep experiments (**Figure 3.8**) revealed a typical gel-like behaviour for all 5 mM samples, within a similar linear viscoelastic region (G'>G"). Interestingly, the presence of benzamide did not prevent the hydrogel formation, but lowered its elastic modulus G' by 70 %, if compared to pure Phe(F_5) gel. The same trend was also observed when halving the concentration, with the stiffness of both mono and bicomponent gels decreasing of one order of magnitude. Transmission and scanning electronic microscopy analyses (TEM and SEM) were performed confirming the fibrillation nature of both hydrogels with average diameters of 11 ± 2 nm for Phe(F_5) and 8 ± 1 nm for Phe(F_5)+BZ (**Figure 3.9**).

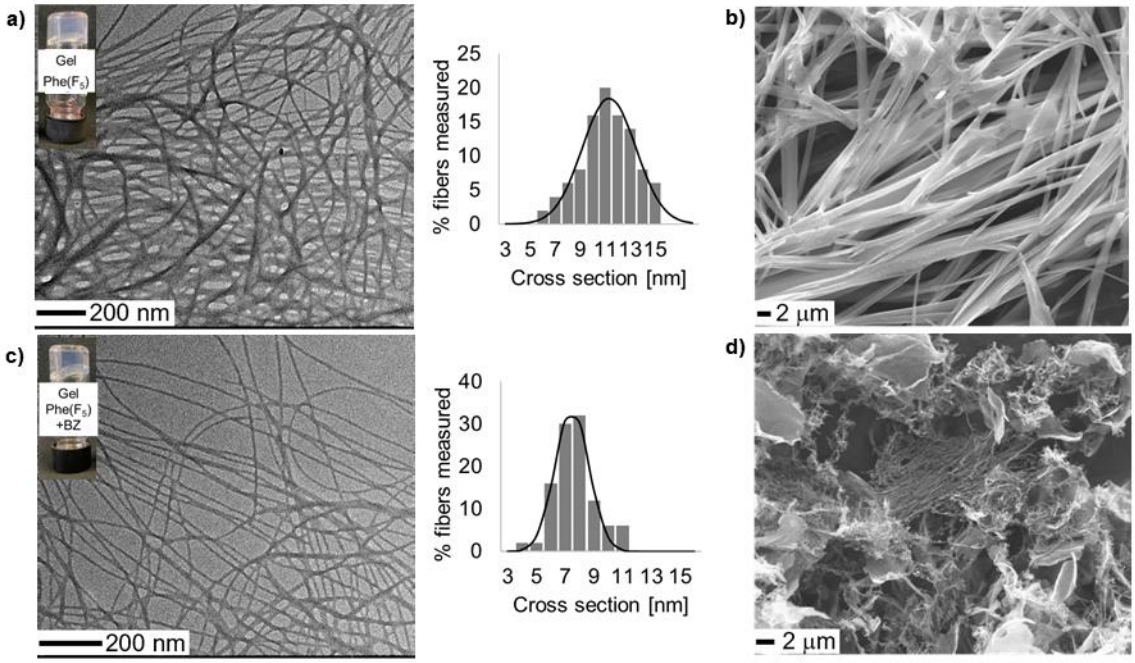

Figure 3.9 *a) TEM image and picture (insert) of Phe(F_5) hydrogel (2.5 mM) and its statistical analyses of the fibril cross sections, measured on 70 different fibrils. Gaussian fitting of data distributions are shown as solid black lines. b) SEM image of Phe(F_5) hydrogel (2.5 mM). c) TEM image and picture (insert) of Phe(F_5)+BZ hydrogel (2.5 mM) and its statistical analyses of the fibril cross sections, measured on 70 different fibrils. Gaussian fitting of data distributions are shown as solid black lines. d) SEM image of Phe(F_5)+BZ hydrogel (2.5 mM).*

The images show a tighter entanglement network for mono-component gel of Phe(F_5), in comparison to the fibrils of the mixed one, in accordance with the rheological data. Then, the 270-310 nm (π-π* transition) region analysis of circular dichroism (CD) spectra display similar signals for the two hydrogels, consistent with the π-π stacking of Fmoc groups and subsequent fibril formation (**Figure 3.10**). Moreover, the reduced stiffness of the hydrogel in presence of BZ is coherent with the observed redshift of n-π* transition from 219 nm to 223 nm for Phe(F_5) and Phe(F_5)+BZ respectively.[252,253]

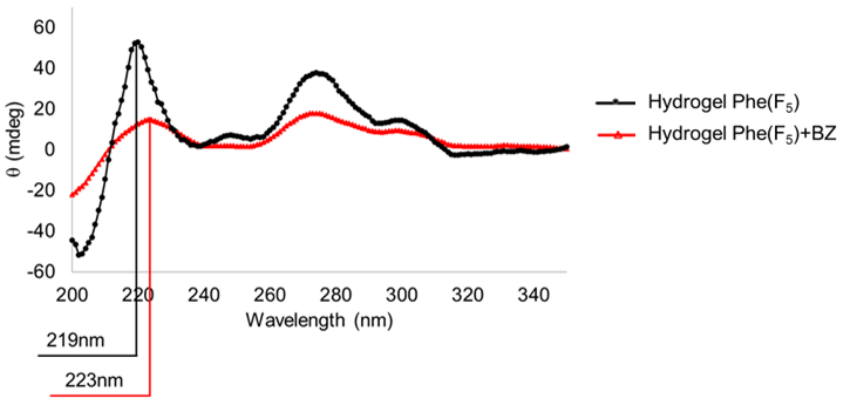

Figure 3.10 *CD spectra of hydrogel Phe(F_5) (black line) and hydrogel Phe(F_5)+BZ (red line). The 4 nm redshift of the band at 219 nm is compatible with a little change of conformation due the presence of compound BZ during hydrogelation.*

3.2.3 Approach validation

The preservation of the acid···amide dimeric synthon both in the solid state and in the hydrogel has been sharply demonstrated by the analysis of the lyophilised gel Phe(F_5)+BZ (5mM) compared with the single crystal and the bulk crystalline powder of [Phe(F_5)·BZ] precipitated from acetonitrile. The DSC thermogram of the mixed hydrogel residue exactly matched that of [Phe(F_5)·BZ], with no traces of uncomplexed starting compounds (**Figure 3.11a**). Furthermore, FT-IR spectra of the three samples are totally overlapping (**Figure 3.11c**).

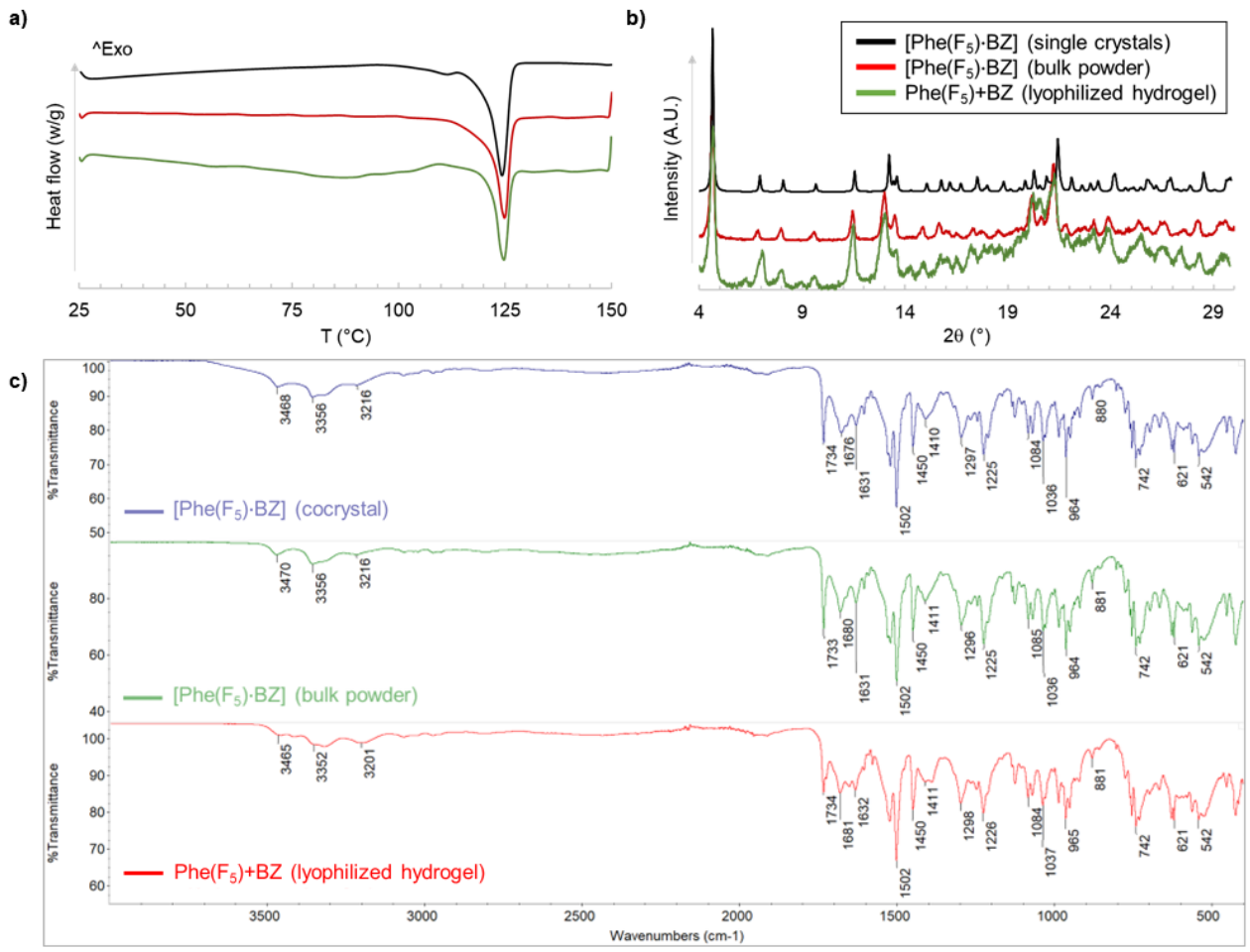

Figure 3.11 *a) DSC thermograms (first heating cycle at 10 °C/min heating rate) of: co-crystal [Phe(F_5)·BZ] (black), bulk co-crystal powder (red) and lyophilized Phe(F_5)+BZ hydrogel (green). b) PXRD patterns of: co-crystal [Phe(F_5)·BZ] (black, simulated from single crystal), bulk co-crystal powder (red, experimental) and lyophilized Phe(F_5)+BZ hydrogel (green, experimental). c) FT-IR spectra of co-crystal [Phe(F_5)·BZ] (blue), [Phe(F_5)·BZ] bulk co-crystal powder (green), and lyophilized Phe(F_5)+BZ hydrogel (red).*

Importantly, analyses using powder X-Ray diffraction (PXRD) offered the crucial proof that the same supramolecular interactions drove the self-assembly process in both the gel and crystalline phases. Indeed, the PXRD pattern of the Phe(F_5)+BZ dried hydrogel precisely matched the measurements

made on the co-crystal bulk powder and the simulated from [Phe(F_5)·BZ] single crystal structure (**Figure 3.11b**). Moreover, both solid mixtures were probed by ^{1}H-^{13}C cross-polarization magic angle spinning nuclear magnetic resonance (CP-MAS NMR) and yielded the same spectrum, which differed from that of lyophilized Phe(F_5) hydrogel in the COOH signal of the amino acid (**Figure 3.12**).

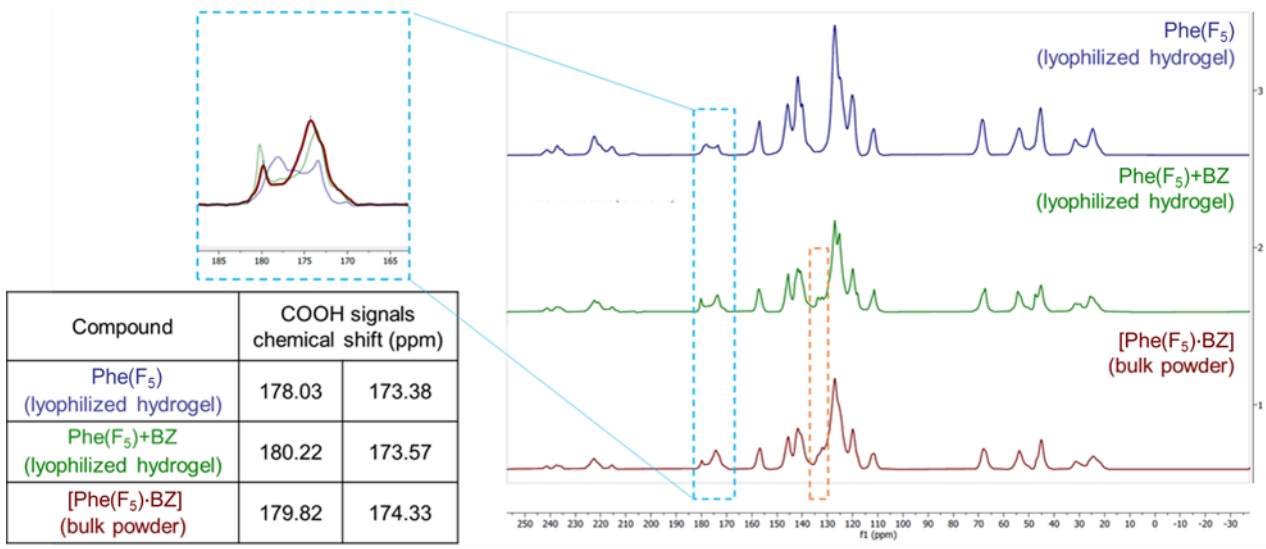

Compound	COOH signals chemical shift (ppm)	
Phe(F_5) (lyophilized hydrogel)	178.03	173.38
Phe(F_5)+BZ (lyophilized hydrogel)	180.22	173.57
[Phe(F_5)·BZ] (bulk powder)	179.82	174.33

Figure 3.12 *^{13}C CP-MAS NMR spectra of lyophilized Phe(F_5) hydrogel (blue), Phe(F_5)+BZ lyophilized hydrogel (green), and [Phe(F_5)·BZ] bulk powder (red). The presence of compound BZ in the last two samples is evidenced by the peak in the orange square. The blue square shows a zoom of the COOH signal of Phe(F_5). Phe(F_5)+BZ and [Phe(F_5)·BZ] COOH signals are similar in shape and chemical shift, but different from the signal of Phe(F_5) alone.*

Based on the collected data, it was evident that the supramolecular acid⋯amide heterosynthon was in charge of the self-assembly of Phe(F_5) and BZ in both the gel and crystal phases, which validated the preliminary hypothesis. These results validate the potential of strategies based on crystal engineering to design new hydrogels with tuned mechanical properties by carefully selecting appropriate gelling partners.

3.2.4 Tunable performance: delayed release of substances

On one side, modifying the initial building blocks' structures and supramolecular interaction patterns could open the possibility to enhance the rheological performance. On the other hand, in this study, the choice of strong HB-forming BZ co-former reduced density and stiffness of Phe(F_5) hydrogels. For biomedical applications, a less rigid hydrogel might be helpful, serving as a biocompatible carrier in the sustained release of bioactive molecules. With this in mind, the *in vitro* release profile of BZ from mixed Phe(F_5)+BZ hydrogel was performed in water.

When comparing the release profile to blank experiments conducted without the amino acid fibrillar network, it was evident from the plot of % release *vs* time that there was a significant delay (**Figure**

13a), and the diffusion coefficient (D) of BZ released from the mixed hydrogel was halved compared to the reference solution (**Figure 3.13b-c** and **Table 3.2**)

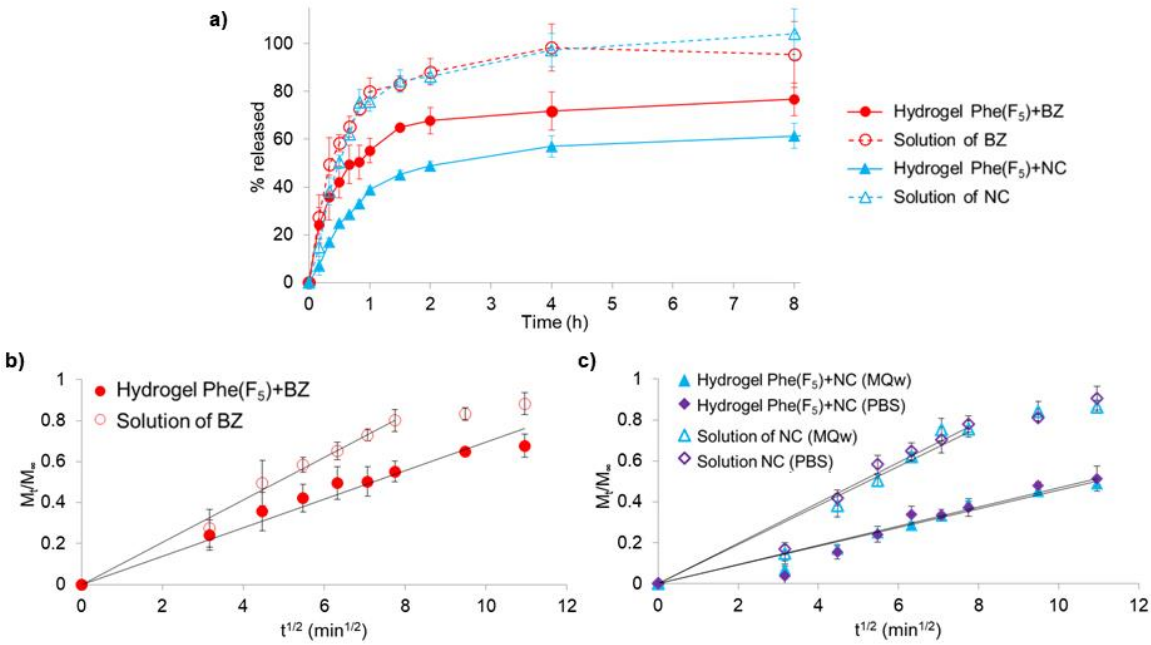

Figure 3.13 *a) Release profile in water of BZ (red) and NC (blue) from multicomponent hydrogels with Phe(F_5) (filled symbols), compared to their solutions (empty symbols). Released % of both compounds were quantified by HPLC calibration curves. b) Diffusion plots of BZ from Phe(F_5)+BZ hydrogel (filled symbols) and from solution (empty symbols). c) Diffusion plots of NC from Phe(F_5)+NC hydrogel (filled symbols) and from solution (empty symbols), in water (light blue) and in PBS buffer (pH=7.4, purple) respectively.*

Table 3.2 *Diffusion coefficients of BZ and NC calculated from the release tests.*

Compound Name	Diffusion coefficient [m^2 min^{-1}]
Hydrogel Phe(F_5)+BZ	5.24×10^{-7}
Solution of BZ	1.17×10^{-6}
Hydrogel Phe(F_5)+NC (MQw)	2.25×10^{-7}
Solution of NC (MQw)	9.48×10^{-7}
Hydrogel Phe(F_5)+NC (PBS)	2.39×10^{-7}
Solution of NC (PBS)	1.05×10^{-6}

In order to assess the overall effectiveness of this method, compound BZ was substituted with vitamin B_3 (**3, Figure 3.1**), a bioactive substance with a molecular structure resembling benzamide. Once again, under the same circumstances, a stable, transparent hydrogel was produced. The D coefficient of NC from Phe(F_5)+NC hydrogel was more than four times lower compared to the corresponding blank solution (**Figure 3.13c** and **Table 3.2**). Finally, trying to mimic a physiological environment, the release performance of Phe(F_5)+NC mixed gel was tested also in PBS buffer (pH 7.4), and the

results were in perfect agreement with those obtained in water (**Figure 3.13c**). Although some examples of Fmoc-modified oligopeptides have been previously reported for this purpose, the development of self-standing hydrogels of a single amino acid with a bioactive non-gelator partner,[254,255] characterized by the ability of extended release of the latter, would be extremely advantageous and cost-effective.

3.3 Halogen bond-based design

3.3.1 Crystallization trials

Given the promising results obtained from the supramolecular acid···amide dimeric synthon and considering the biomedical interest and cost-effectiveness of these supramolecular hydrogels, the same crystallographic approach was adopted for investigating another supramolecular interaction. In particular, halogen bonding was already demonstrated to participate in the hydrogelation process of *N*-Fmoc-amino acids,[235] and there is a connection between the positivity of the σ-hole and the strength of the resulting hydrogel. Among all halogens, iodine atom seemed to be the best candidate to enhance hydrogelation.[235] For this reason, *N*-Fmoc-2,3,5,6-tetrafluoro-4-iodophenylalanine (Phe(F_4I), **Figure 3.1**) was synthesised starting from *N*-Boc-pentafluorophenylalanine according to a published procedure, with some steps' optimization (**Section 3.3**).[256] The influence of such a strong XB donor on the crystal packing and the relative consequences during fibrillation were studied and compared with the already known fully fluorinated system Phe(F_5).

Aiming to have an insight into the molecular interactions involved in any possible self-assembly, the initial point for the analysis of this new system was the characterization of its solid-state behaviour. While the crystal structure of gelator Phe(F_5) in its acidic monomeric form was already know,[248] extrapolated from PXRD pattern, the crystal structure of compound Phe(F_4I) was completely unexplored. One of the first crucial issue about this new molecule was its not optimal solubility in most organic solvents. This feature was attributed to the significant size of the iodine atom itself, which favoured the precipitation of the amorphous compound when suspended in most common solvents (**Table 3.3**).

Table 3.3 *Solubility of compound Phe(F_4I) in most common organic solvent*

Solvent	**Solubility**	
	mg/mL	mM
Chloroform	3.25	5.5
Dichloromethane	2.35	4.0
Ethanol	13.0	22.0
Methanol	11.4	20.0
Acetone	40.0	68.0
Acetonitrile	4.75	8.1
Hexane	-	-
Toluene	-	-
Diethyl ether	-	-

The known difficulty in crystallising Fmoc-amino acids might be attributed to their high fibrillation tendency, and hampered also the crystallization of Phe(F_4I). In various crystallization attempts, the amorphous nature of Phe(F_4I) was proven by the poor crystallinity of the compound when analysed thought powder X-ray diffraction (**Figure 3.14**).

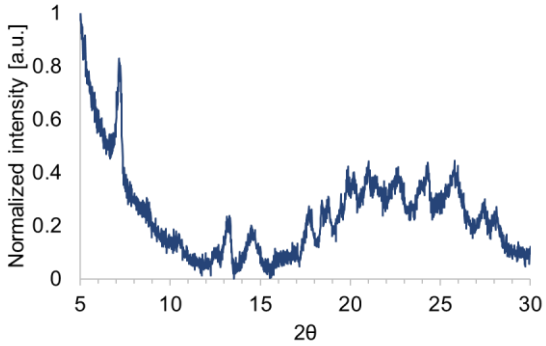

Figure 3.14 *Powder X-ray diffraction pattern of Phe(F_4I) from slow evaporation from acetonitrile.*

Taking inspiration from the case study of acid⋯amide with compound Phe(F_5), a similar strategy was adopted. In fact, engaging the -COOH functional group in special interactions could impart higher order over the molecular packing and favour crystallization. Moreover, single crystal X-ray structure of *N*-Fmoc-*p*-I-phenylalanine was already reported in the CCDC,[235] and showed the remarkable affinity of its *C*-terminus in coordinating water molecules to reach the crystal order. This fact supported the hypothesis and pushed the focus on the -COOH possible interactions. In particular, a good coordination system could be offered by $COO^-\cdots M^+$, where M^+ is a metal cation. Additionally, metal cations were already used as hydrogelation enhancers.[246,247] Consequently, the study of metal salts of Phe(F_4I) and Phe(F_5) could be a good compromise to compare the two systems and gain insights into the molecular effects due the introduction of an XB donor. The choice of metal cations was done preferring those commonly present in the biological environment, with the purpose to maintain biocompatibility for future applications. With these basics, amino acids' potassium and/or sodium salts were identified as the best candidates.

Mechanochemical synthesis was fine tuned for both amino acids Phe(F_5) and Phe(F_4I). Thus, powder of Phe(F_5) and Phe(F_4I) were mixed with an equimolar amount of solid NaOH or KOH, and grinded through ball milling. The powders of the salified salts of Phe(F_5) and Phe(F_4I) were obtained from such grinding. Interestingly, crystallization attempts led to two different salts, respectively the sodium salt of Phe(F_5) (named crystal [Phe(F_5)·Na]) and the potassium salt of Phe(F_4I) (named crystal [Phe(F_4I)·K]) (**Figure 3.15**). Both single crystals were obtained through slow evaporation from acetone. [Phe(F_5)·Na] crystallized in the triclinic space group *P1* with two molecules in the

asymmetric unit, both coordinating the same Na^+ cation. Differently, [Phe(F_4I)·K] crystallized in the monoclinic space group $P2_1$, and two molecules were displayed in the asymmetric unit, coordinating one K^+ cation. The change of geometrical disposition in the 3D space due the introduction of the iodine atom was immediately clear (**Figure 3.15**). The two perfluorophenyl groups of [Phe(F_5)·Na] laid on two parallel planes while the tetrafluoro-iodophenyl rings in [Phe(F_4I)·K] did not. Focusing of the metal coordination mode of [Phe(F_5)·Na], sodium cation was involved in two coordination bonds with the *C*-termini (CO-O7···Na1, CO-O4···Na1) of two opposite amino acid units and two acetone molecules (**Figure 3.15**, left). For crystal [Phe(F_4I)·K] the metal site was bonded to one carboxylate unit (CO22···K1, CO-O1···K1) and one carboxylic acid (CO12···K1), revealing a partial salification of Phe(F_4I). The potassium unit also interacted with one molecule of water (**Figure 3.15**, right).

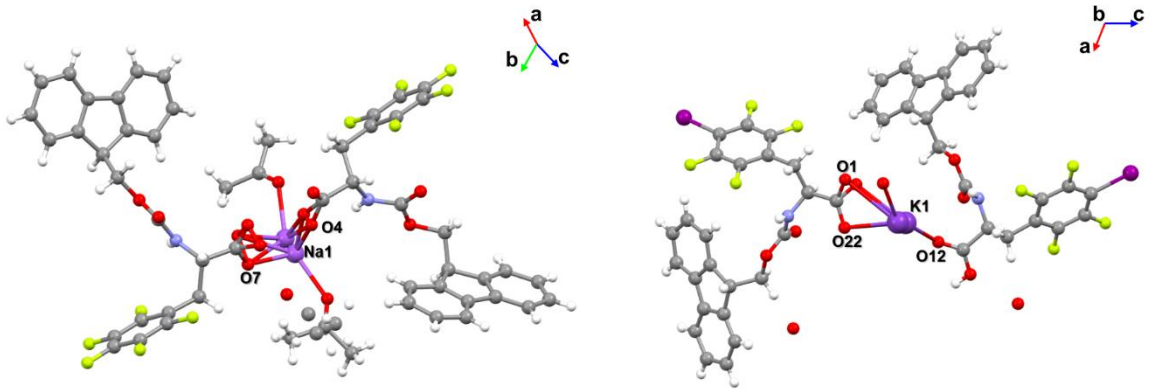

Figure 3.15 *Ball-and-stick crystallographic representations of: left) asymmetric unit of [Phe(F_5)·Na]; right) asymmetric unit of [Phe(F_4I)·K]. Colour code: carbon, grey; oxygen, red; nitrogen, light blue; fluorine, yellow; iodine, pink; sodium, light purple; potassium, purple. Cation and solvent residues of both crystals were treated as disordered.*

Concerning intra-chain interactions, in each crystal one metal cation coordinates two amino acid chains, and it was interesting to notice that the interactions which were involved were not the same. The typical hydrogen bonding between C=O unit of Fmoc-protected amino acid Phe(F_4I) with the NH group of an adjacent molecule was observed for both chains of crystal [Phe(F_4I)·K] as shown in **Figure 3.16** (right). The **HB3** and **HB4** (N–H···O, 2.20 Å and 2.02 Å respectively) contacts promoted the formation of infinite chains along crystallographic *b*-axis. Similarly supramolecular arrangement was detected in [Phe(F_5)·Na] (**Figure 3.16**, left). The chains were stabilized by two hydrogen bonds involving in this structure two different functionalities. In fact, **HB2** (N–H···O, 2.39 Å) resulted to be analogous to **HB3** and **HB4** while **HB1** (N–H···O-CO, 2.17 Å) was formed by the contact between N-H group and the COO^- terminus involved in the coordination of the sodium ion.

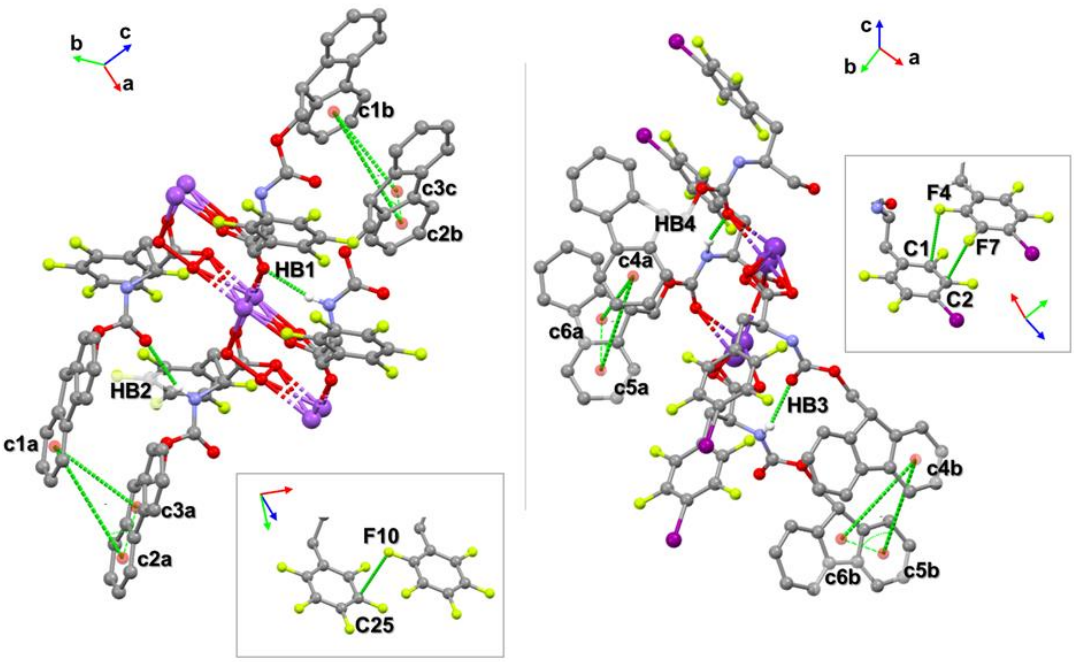

Figure 3.16 *left) packing of [Phe(F_5)·Na] units in a chain, viewed along the crystallographic a-axis (zoom: perfluoro-phenyl moieties packing along the same axis). Right) packing of [Phe(F_4I)·K] units in a chain, viewed along the crystallographic b-axis (zoom: tetrafluoroiodo-phenyl moieties packing along the same axis). HB contacts and other packing interactions are indicated by green dotted lines.*

The high importance of Fmoc-protective groups in the packing stabilization required to analyse the relative positions of these units (**Figure 3.16**). As previously observed for co-crystal [Phe(F_5)·BZ], a parallel lateral offset mode of packing was identified for both [Phe(F_5)·Na] and [Phe(F_4I)·K]. Intriguingly, considering the cation centre in crystal [Phe(F_5)·Na], both the Fmoc chains on the left and right side assumed a comb-like structure. Indeed, centroid distances c1a···c3a and c1b···c3b measured similarly (4.14 Å and 4.04 Å respectively) as the angle between centroids c1a···c2a···c3a and c1b···c2b···c3b (44.8° and 41.9°).

On the other side, in crystal [Phe(F_4I)·K] Fmoc-groups assumed a different comb-like structure. In fact, the distances c4a···c6a (3.95 Å) and c4b···c6b (4.82 Å) were very different one another, and in particular c4b···c6b was much higher than those observed so far. Furthermore, the angles counted 50.2° and 72.9° (respectively c4a···c5a···c6a and c4b···c5b···c6b), confirming the different off-set between Fmoc-chains.

In conclusion, additional stabilization was offered by fluorinated phenyl groups pairing. Thanks to quadrupolar inversion of the fluorinated ring, only one contact between C25···F10 (3.13 Å) could be observed in [Phe(F_5)·Na] crystal packing, while [Phe(F_4I)·K] displayed a total of two interactions of

the same type, C1···F4 (3.08 Å) and C2···F7 (3.12 Å). Furtherly, looking at [Phe(F_4I)·K], the same F4 was also involved in a week hydrogen bonding with the near Fmoc-group (**Figure 3.17**).

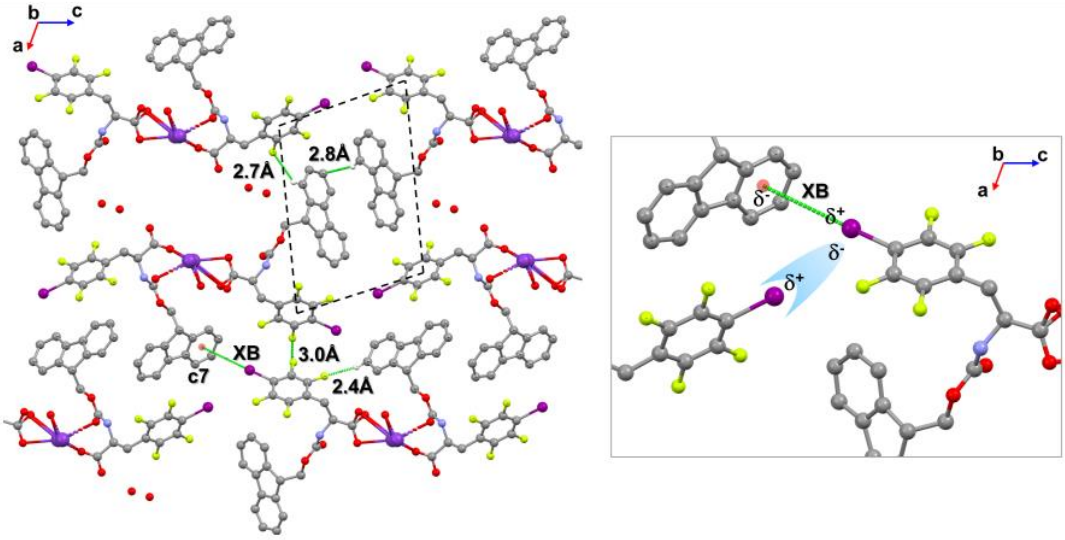

Figure 3.17 *Inter-chain interactions between two adjacent pair of chains of [Phe(F_4I)·K]. In the dotted square is indicated the geometrical disposition of the tetrafluoro-iodo phenyl lateral groups. The zoom represents the focus on the XB interaction and the destabilizing disposition of iodine δ^+ towards the belt δ^- of the nearby iodine.*

The presence of the iodine atom in crystal [Phe(F_4I)·K] played a crucial role in the overall inter-chain packing. In fact, the σ-hole on the iodine atom promoted the formation of a strong halogen bonding interaction. The Fmoc π-system functioned as electron rich moiety, namely the XB-acceptor unit, and interacted with iodine atom forming a short and directional contact, with a 3.88 Å distance between C-I···c7 (π-system) and a binding angle of 169° (**Figure 3.17**).

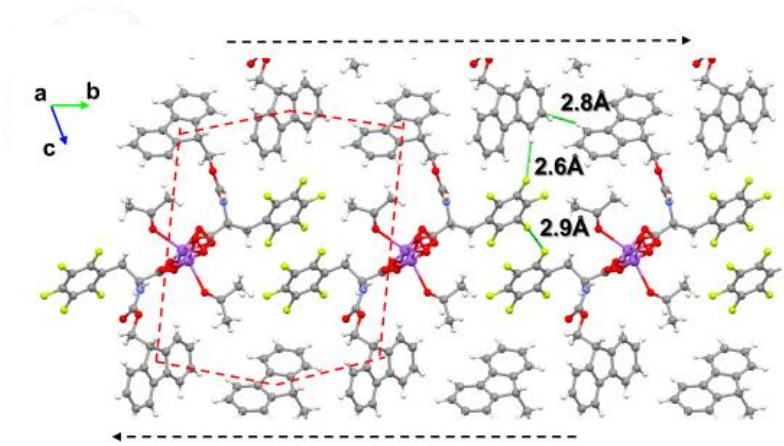

Figure 3.18 *Inter-chain interactions between two adjacent pair of chains of [Phe(F_5)·Na]. Dotted arrows indicate the Fmoc infinite chains along the crystallographic b-axis. Red dotted lines indicate the geometrical isolation of pefluorophenyl moieties.*

Notably, not all the iodine atoms present in the crystal packing were engaged in XB with the Fmoc group. This feature interested only one of the two amino acids of the asymmetric unit. The iodine atoms pointing away from the Fmoc units, instead formed XB contacts with adjacent iodine atoms of closed chain. Specifically the σ-hole of one iodine atom pointed towards the negative belt (δ^-) of iodine atom with I···I distance of 4.08 Å. (**Figure 3.17**, zoom).
As a consequence, the overall classical packing was altered by the presence of this iodine atom, and Fmoc moieties were isolated. With this disposition, a rhomboidal asset could be imagined, where four tetrafluoro-iodo phenyl groups determined the vertexes (**Figure 3.18**).

A different situation could be appreciated in case of [Phe(F_5)·Na], were Fmoc-chains interactions were uninterrupted along crystallographic *b*-axis. In fact, a special tacticity was created, separating Fmoc hydrogenated groups from fluorinated moieties. The latter ones resulted to be isolated and surrounded by Fmoc-chains (**Figure 3.18**).

From the comparison between the two crystals, two main considerations could be proposed:

1- as designed [Phe(F_4I)·K] showed a crystal packing enhanced by halogen bonding, and the comparison with [Phe(F_5)·Na] revealed that a higher number of noncovalent interactions stabilized its structure.
2- The presence of halogen bonding disrupted the infinite Fmoc pairing along the crystallographic *c*-axis of [Phe(F_4I)·K]**,** and this could determine a different hydrogelation tendency.

A slightly higher thermal stability of crystal [Phe(F_4I)·K] in comparison with [Phe(F_5)·Na] was shown by their melting points, which were observed through Polar Optical Microscope (POM) and are shown in **Figure 3.19**.

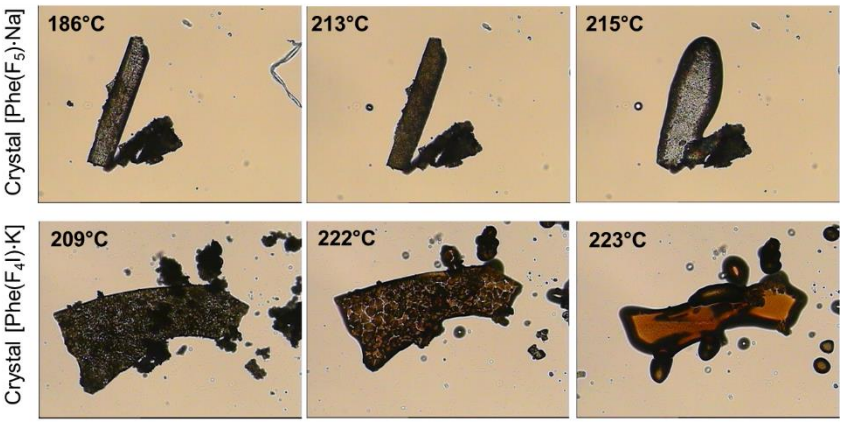

Figure 3.19 *Images acquired through POM, 10X camera magnification. Melting point of crystal [Phe(F_5)·Na] (top) and crystal [Phe(F_4I)·K] (bottom) were represented.*

As expected, the thermal resistance of crystal [Phe(F_4I)·K] was higher than that observed for crystal [Phe(F_5)·Na], showing a qualitative difference of ~8°C, confirming the first hypothesis.

Table 3.4 *Crystallographic data and refinement details for co-crystal [Phe(F_5)·Na].*

Chemical formula	$C_{54}H_{42}F_{10}N_2NaO_{10}$
Mr	1091.88
Crystal system	Triclinic
Space group	P1
Temperature (K)	173
a, b, c (Å)	5.3997 (2), 14.5936 (4), 17.7150 (5)
α, β, γ (°)	69.255 (2), 86.239 (2), 82.783 (2)
V (Å^3)	1294.78 (7)
Z	1
Radiation type	Cu Kα
μ (mm−1)	1.11
Crystal size (mm)	0.06 × 0.04 × 0.04
Absorption correction[a]	Multi-scan
Tmin, Tmax	0.860, 1.000
No. of measured, independent and observed [I > 2σ(I)] reflections	15411, 6486, 5500
Rint	0.047
(sin θ/λ)max (Å−1)	0.630
R[F^2 > 2σ(F^2)], wR(F^2), S	0.051, 0.145, 1.04
No. of reflections	6486
No. of parameters	778
No. of restraints	84
H-atom treatment	H-atom parameters constrained
Δρmax, Δρmin (e Å−3)	0.40, −0.26
Absolute structure parameter[b]	0.02 (12)
CCDC number	t.b.d.

Table 3.5 *Crystallographic data and refinement details for co-crystal [Phe(F_4I)·K].*

Chemical formula	$C_{48}H_{31}F_8I_2KN_2O_{11}$ + solvent[§]
Mr	1256.65
Crystal system	Monoclinic
Space group	$P2_1$
Temperature (K)	100
a, b, c (Å)	23.094 (5), 4.978 (1), 23.760 (5)
α, β, γ (°)	69.255 (2), 86.239 (2), 82.783 (2)
V (Å^3)	111.08 (3)
Z	4
Radiation type	0.7
μ (mm−1)	1.33
Crystal size (mm)	0.10 × 0.05 × 0.02
No. of measured, independent and observed [I > 2σ(I)] reflections	46730, 14616, 14023

Rint	0.038
(sin θ/λ)max (Å−1)	0.706
R[$F^2 > 2\sigma(F^2)$], wR(F^2), S	0.033, 0.100, 1.05
No. of reflections	14616
No. of parameters	676
No. of restraints	15
H-atom treatment	H-atom parameters constrained
Δρmax, Δρmin (e Å−3)	1.12, −1.14
Absolute structure parameter[b]	0.00 (12)
CCDC number	t.b.d.

*§ The electron densities corresponding to the disordered solvent molecules of **7** was flattened using 'SQUEEZE' option of PLATON (ref. A. L. Spek, PLATON99 A Multipurpose Crystallographic Tool, Utrecht University: Utrecht, 1999.)*
[a]CrysAlis PRO 1.171.42.55a (Rigaku Oxford Diffraction, 2022) Empirical absorption correction using spherical harmonics, implemented in SCALE[3] ABSPACK scaling algorithm.
[b]Absolute structure: Flack x determined using 1292 quotients [(I+)-(I-)]/[(I+)+(I-)] (Parsons, Flack and Wagner, Acta Cryst. B69 (2013) 249-259).

3.3.2 The influence of XB on hydrogelation

The behaviour of compound Phe(F_4I) in comparison with compound Phe(F_5) when exposed to water environment was analysed. Since their crystals were obtained as salts, the fibrillation tendency of the two compounds was tested in phosphate buffer saline (PBS, 0.01 M phosphate buffer, 0.0027 M potassium chloride and 0.137 M sodium chloride) to mimic the presence of the same metal cations. The kinetics of fibril formation was tested again by monitoring over time the change in the UV-visible absorbance at 405 nm (**Figure 3.20**).

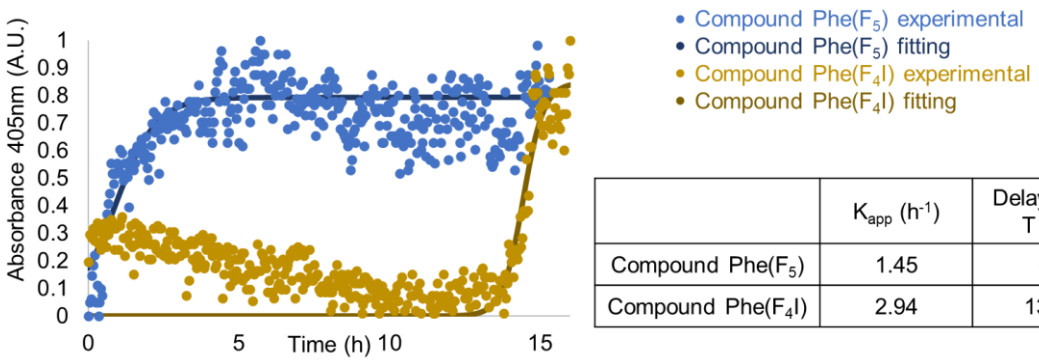

	K_{app} (h^{-1})	Delay time T (h)
Compound Phe(F_5)	1.45	0
Compound Phe(F_4I)	2.94	13.8

***Figure 3.20** Fibrillation kinetics of 0.1 mM solutions of Phe(F_5) and Phe(F_4I). Fittings of experimental data are shown as solid lines.*

Because of the poor solubility of compound Phe(F_4I), a higher amount of co-solvent was used. Indeed, samples were prepared in dilute buffered aqueous solution at pH 7.4 (0.1 mM, 5%$_{v/v}$ DMSO in PBS) and incubated under controlled conditions of temperature and stirring (25 °C, 432 rpm) for 16 hours. A similar sigmoidal trend was observed by plotting absorbance *vs* time. Despite the fibrillar tendency

of both component was confirmed, it was impressive the difference of initial lag time phase between the two curves. In fact, in case of Phe(F_5) there was no delay time before the fibrillation beginning (T = 0 h). On the contrary, compound Phe(F_4I) started to form fibrils only ~14 h after the initial dissolution. Interestingly, even if extremely delayed in time, the fibrils' growth rate of Phe(F_4I) (quantitively represented by K_{app}) was faster than Phe(F_5).

After the encouraging results on fibrillation, the corresponding hydrogels were prepared with the solvent switch method already described, with the addition of a heating step. A 100 mM stock solution in DMSO was prepared for both compounds, and diluted in PBS up to a final concentration of 2.5 mM (0.12 wt.% for gel Phe(F_5), and 0.15 wt.% for gel Phe(F_4I)). Before dilution, the solvent was heated up to 50°C, in order to obtain more homogeneous gels. Additionally, directly after dilution, a further heating at 100°C for 1 minute allowed the complete dissolution of the amino acids in the medium, and favoured a uniform fibrillation. More details are provided in the **Experimental section 3.3**.

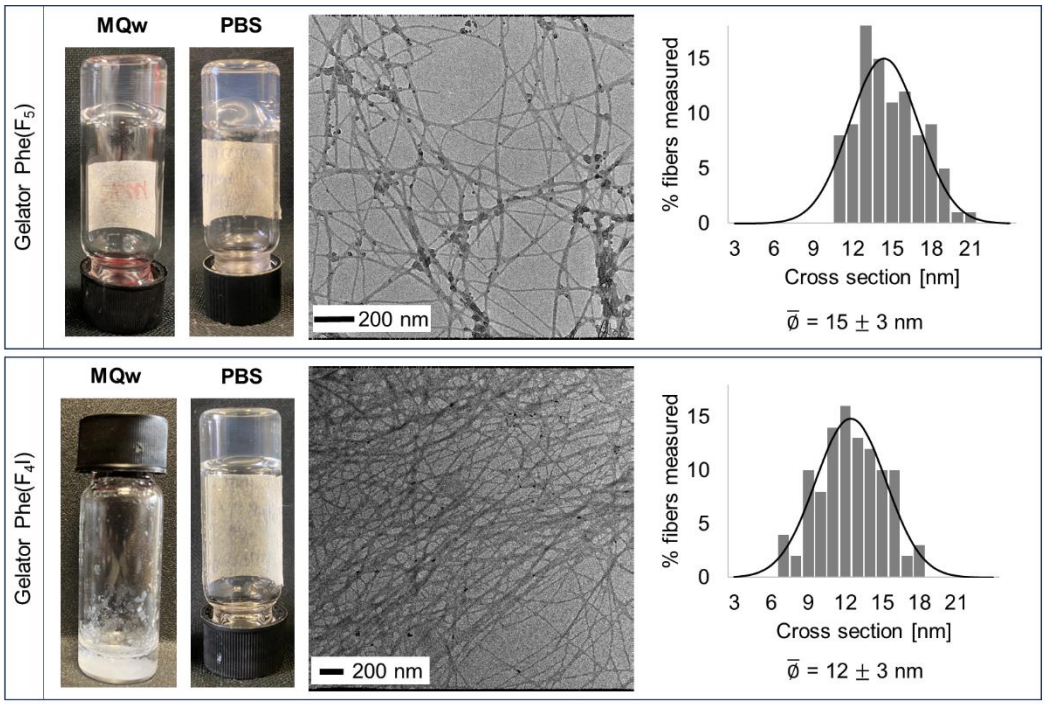

Figure 3.21 *Top) pictures of hydrogels of Phe(F_5) in MQw and PBS in comparison (2.5 mM). Then, TEM image of Phe(F_5) hydrogel in PBS (2.5 mM) and its statistical analyses of the fibril cross sections, measured on 70 different fibrils. Gaussian fitting of data distributions are shown as solid black lines. Bottom) pictures of hydrogels of Phe(F_4I) PBS (2.5 mM) in comparison with its precipitate in MQw. Then, TEM image of Phe(F_4I) hydrogel in PBS (2.5 mM) and its statistical analyses of the fibril cross sections, measured on 70 different fibrils. Gaussian fitting of data distributions are shown as solid black lines.*

Although this procedure was successful for the obtainment of both hydrogels Phe(F_5) and Phe(F_4I) in PBS buffer, hydrogel Phe(F_4I) was not stable in pure water (**Figure 3.21**). The homogeneous fibrillar

network of PBS hydrogels was confirmed by TEM analysis, which evidenced similar dimensions of the fibres' cross sections. Even if fibers' dimensions were comparable and both gels looked uniform and identical, their relative strength were very different when compared through rheological acquisitions. Indeed, 2.5 mM hydrogels were analysed for their linear viscoelastic region (strain sweep experiment, **Figure 3.22a**), followed by time sweep and frequency sweep experiments (not shown) after 24 hours from the preparation, to give both hydrogels the time to form and stabilise. Surprisingly, a dramatic decrease of hydrogel strength was recorded in the presence of iodine. Hydrogels of Phe(F_5) obtained from water and PBS were comparable (**Figure 3.8** and **Figure 3.22a**), whereas hydrogel Phe(F_4I) has a storage modulus G' one order of magnitude lower than Phe(F_5). This result was in accordance with what expected from the fibrillation kinetics and with the prediction from the crystal structure. In fact, the disruption of the Fmoc moieties interactions due to iodine justified both the fibrillation delay and the lower hydrogel stiffness.

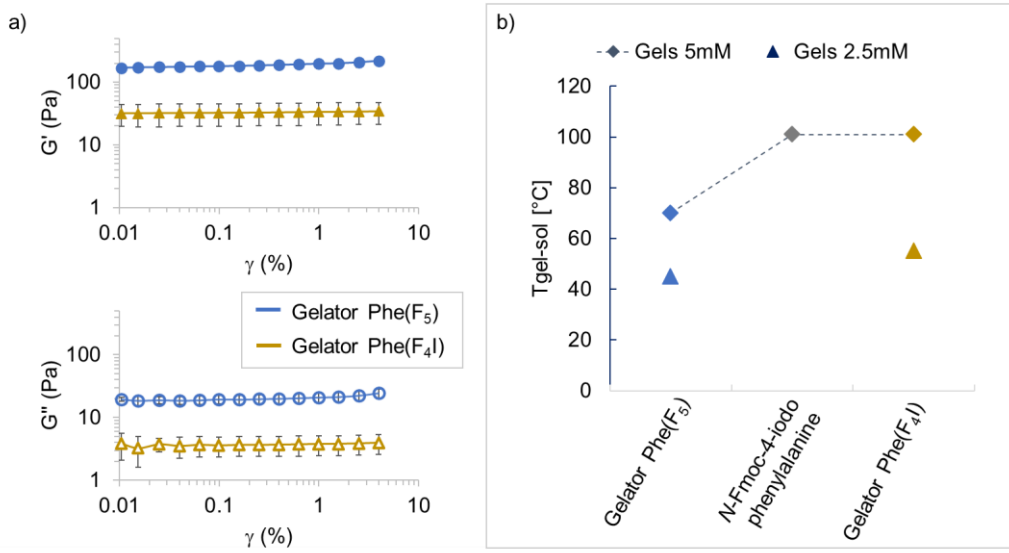

Figure 3.22 *a) Strain sweep experiment (Linear Viscoelastic Region) for Phe(F_5) (blue) and Phe(F_4I) (yellow) components, measured at 2.5 mM. Oscillation amplitude table: frequency 0.95 Hz, 5 samples per decade. b) Comparison among temperatures of transition gel-sol for Phe(F_5) and Phe(F_4I) at different concentrations: 2.5 mM (blue and yellow triangles respectively) and 5 mM (blue and yellow squares respectively). N-Fmoc-4-iodo-phenylalanine 5 mM was also represented (grey square).*

The higher thermal resistance observed comparing the melting points of crystalline [Phe(F_5)·Na] and [Phe(F_4I)·K] respectively, could be observed also in the case of their gel-sol transition temperature. In the latter experiment (**Figure 2.21b**), $T_{gel\text{-}sol}$ was assessed comparing Phe(F_5) and Phe(F_4I) hydrogels in two different concentrations, 2.5 mM and 5 mM. For the lower concentration a 10°C gap separated the transition of Phe(F_5) ($T_{gel\text{-}sol}$ = 45°C) from Phe(F_4I) ($T_{gel\text{-}sol}$ = 55°C). When comparing 5 mM hydrogels, the transition of Phe(F_4I) occurred only at the boiling point of the solvent

(101 °C), while 70°C was the gel's falling temperature for Phe(F_5). To attribute this behaviour to the beneficial presence of the iodine atom, the same experiment was performed formulating an hydrogel of *N*-Fmoc-4-iodo-phenylalanine (non-fluorinated counterpart of Phe(F_4I)). The latter showed the same temperature 101°C compared to Phe(F_4I), confirming the hypothesis.

The impossibility to obtain hydrogels of Phe(F_4I) in pure water might be related to the instability observed in the single crystal structure, due to the presence of unbound iodine atoms. The presence of PBS could favour the stabilization of these functionalities, thanks to the halogen bond accepting ability of chloride ions in the buffer. In fact, halides ions are strong XB acceptors.[242,257] In particular, an analytical investigation constituted by EDS (Energy Dispersive X-ray Spectroscopy) was performed in order to further characterise the fibers' composition from both Phe(F_5) and Phe(F_4I) hydrogels (**Figure 3.23**). Hydrogels 2.5 mM of Phe(F_5) and Phe(F_4I) were deposited over carbon tape and air-dried, then washed three times with MilliQ water in order to remove PBS salts. Dried samples were observed by SEM, coupled with EDS.

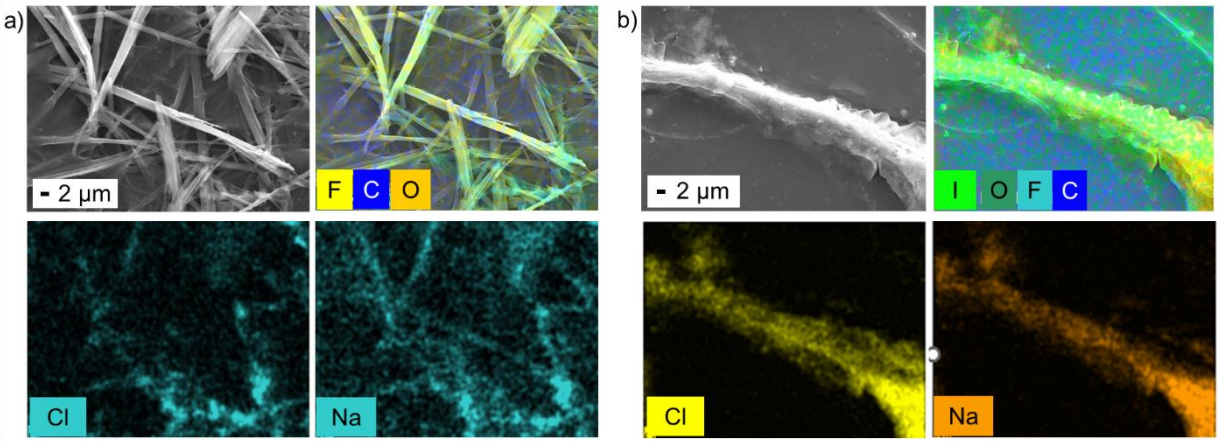

Figure 3.23 *a) Strain SEM and EDS of Phe(F_5) hydrogels after washes from PBS salts. Fluorine, chlorine and sodium channels are reported b) SEM and EDS of Phe(F_4I) hydrogels after washes from PBS salts. Iodine, chlorine and sodium channels are reported.*

It was immediately visible the difference between fibers originated from the two gelators. Indeed, Phe(F_5) displayed a rigid and entangled network of fibrils/rods, where a few chloride anions and mostly sodium cations were detectable (**Figure 3.23a**). This fact perfectly agreed with the coordination of Na^+ by the amino acid observed in the crystal structure [Phe(F_5)·Na]. On the other side, Phe(F_4I) showed less tight fibers, but bigger than Phe(F_5) (**Figure 3.23b**). EDS analysis demonstrated that a greater amount of sodium and chlorides ions covered the fiber, which was consistent with the hypothesis of halogen bonding between iodine and chloride, in addition to coordination of the metal cation. Thus, chlorides seemed to be necessary to stabilize the fibers, evidencing the influence of the iodine atom in the system.

3.3.3 Validation of the crystallographic approach

Despite the various analogies between solid state and hydrogels, the key demonstration of the maintenance of the same interactions between one form and the other was still missing. Again, spectroscopic and powder X-ray diffraction analyses were useful to validate the hypothesis.

In the case of Phe(F_5), the comparison between crystal [Phe(F_5)·Na], its bulk powder and Phe(F_5) lyophilized hydrogel from PBS (subtracting PBS background) gave overlapped results for both techniques (**Figure 3.25**). The impressive hydrogel crystallinity after freeze-drying proved the high stability and long-range order of the fibers, and it was clearly visible also after air-drying. In fact, microscope images exposed to white light displayed the presence of bundles of needles, which extinguished under polarized light (**Figure 3.25c-d**).

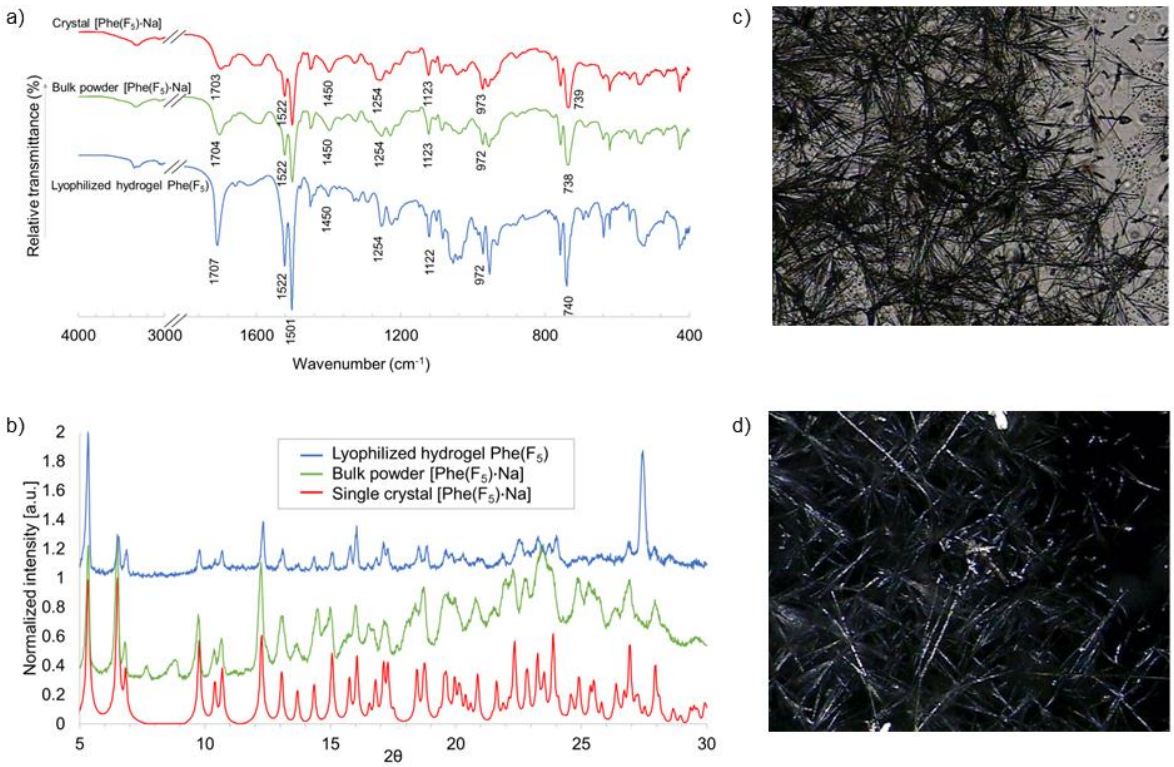

Figure 3.25 *a) FT-IR spectra of crystal [Phe(F_5)·Na] (red), [Phe(F_5)·Na] bulk co-crystal powder (green), and lyophilized Phe(F_5) hydrogel from PBS (blue) b) PXRD patterns of: crystal [Phe(F_5)·Na] (red, simulated from single crystal), bulk crystal powder (green, experimental) and lyophilized Phe(F_5) hydrogel (blue, experimental). c-d) POM images of air dried hydrogel Phe(F_5) exposed under white (c) and polarized (d) light. Magnification lens 5X.*

PXRD pattern of lyophilized gel Phe(F_5) was completely overlapped to that simulated from the single crystal [Phe(F_5)·Na], while the bulk powder's pattern showed two extra peaks in the 2θ region

between 7° and 9°. This fact might be explained by the presence of water or solvent impurities, which are not present after crystallization (**Figure 3.25b**).

FT-IR spectra of crystal [Phe(F_4I)·K], [Phe(F_4I)·K] bulk powder and lyophilized hydrogel Phe(F_4I) showed overlapped peaks as well (**Figure 3.26a**). The only exception concerned the C=O stretching relative to the *C*-terminus. A broad peak was recorded at 1698 cm^{-1}, blue shifted of 7 cm^{-1} in comparison with crystal **7** (1681 cm^{-1}), where the same C=O signal appeared as unique sharp peak. This difference could be clarified by the only presence of salified COO^- form in the hydrogel, while in the crystal both the COOH and COO^- forms coexisted. Differently from the case of Phe(F_5), PXRD analyses revealed a poor crystallinity of the freeze-dried hydrogel Phe(F_4I). Despite a few peaks were present in the same position of the two patterns, the overall amorphous feature of the lyophilized powder gave a further confirmation of the instability of fibers' packing. Indeed, POM images, acquired after hydrogel Phe(F_4I) air drying, explained exactly the situation. Only a few fibers survived solvent evaporation, while a big amount of amorphous material was clearly observed (**Figure3.26c-d**).

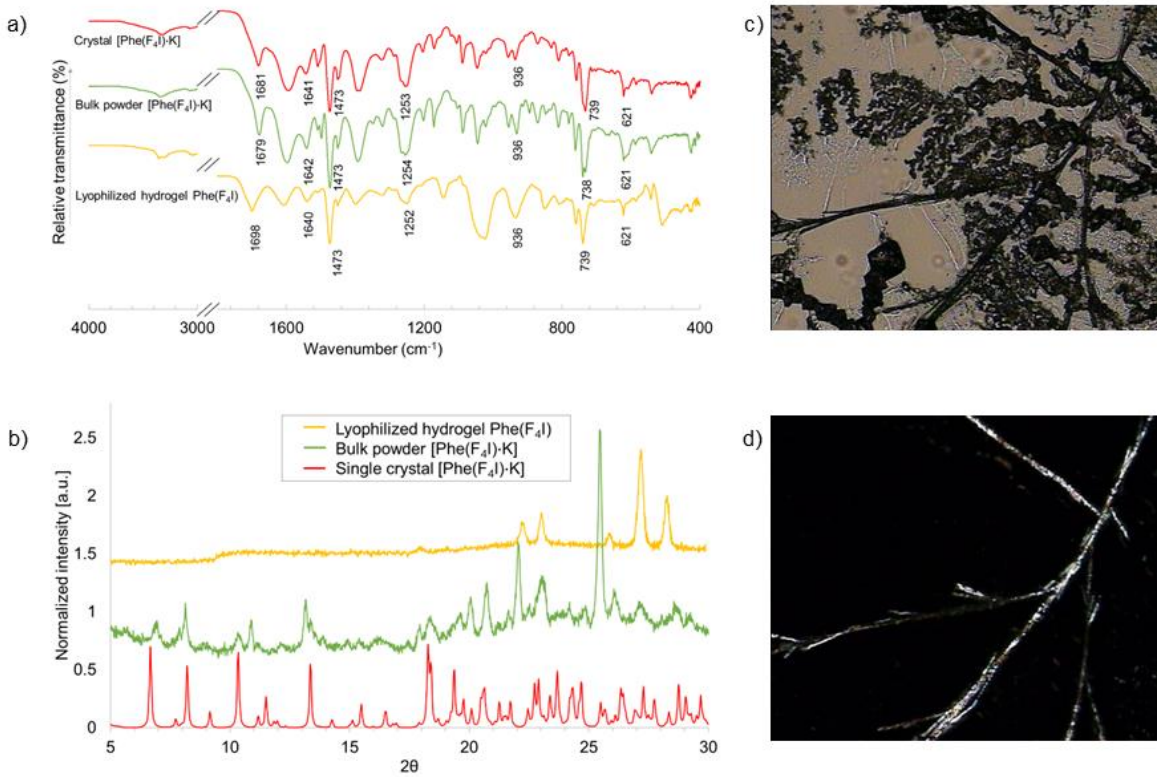

Figure 3.26 *a) FT-IR spectra of crystal [Phe(F_4I)·K] (red), [Phe(F_4I)·K] bulk co-crystal powder (green), and lyophilized Phe(F_4I) hydrogel from PBS (yellow) b) PXRD patterns of: crystal [Phe(F_4I)·K] (red, simulated from single crystal), bulk crystal powder (green, experimental) and lyophilized Phe(F_4I) hydrogel (yellow, experimental). c-d) POM images of air dried hydrogel Phe(F_4I) exposed under white (c) and polarized (d) light. Magnification lens 5X.*

In conclusion, the crystallographic approach resulted to be useful in the interpretation and prediction of the hydrogels behaviour. Furthermore, the presence of unbound iodine atoms unlocked the design of new hydrogels, exploiting the interaction of this XB-forming synthon with further possible partners.

3.3.4 Halogen bonding investigation

In order to investigate the possibility of improving the performance of hydrogel Phe(F_4I) thanks to its XB donor potential, a preliminary investigation was conducted, testing three different halogen bond acceptors. In a first instance, hydrogels were formulated in presence of a different XB-accepting halide ion, changing the type of salts contained in the PBS buffer. The buffer was prepared with the same concentration of phosphate buffer (0.01 M) and the same pH, but adding 0.0027 M potassium iodide and 0.137 M sodium iodide, instead of the chlorides used before. The second halogen bond acceptor was represented by *N*-Fmoc-4-pyridilalanine - Ala(py) (**Figure 3.27a**), which is a non-gelator amino acid. Finally, nicotinamide/vitamin B_3 (NC, **Figure 3.1**) was tested also in this study. Hydrogels containing these partners were formulated starting from a stock solution of gelator in DMSO (100 mM) with an equimolar amount of partner.

Mixed hydrogels were formulated in PBS, diluting the stock solution following the same protocol already described in **Section 3.2.6**, until a final concentration of 2.5 mM (for each component) in $5\%_{v/v}$ DMSO in PBS.

From the results, iodide salts slightly improved the storage modulus G' in the case of gelator Phe(F_5), while a significant increase was observed for gelator Phe(F_4I), demonstrating the hypothesis that halogen bonding with the halides present in the buffer contributed to the stabilization of the entire system. Furthermore, between iodide and chloride salts, the I^- anions seemed to be preferentially coordinated over Cl^-. This trend was already reported in the literature for halides in solution,[257–259] and might be the reason of the enhanced hydrogel obtained.

When a pyridyl group was introduced in the hydrogel, two opposite results were obtained according to the presence or not of the XB donor. In particular, an improvement of one order of magnitude (G') was recorded for gelator Phe(F_4I) in presence of both compounds Ala(py) and NC (**Figure 3.27c**). Additionally, the G' increase allowed to achieve hydrogels with a strength similar to monocomponent hydrogel Phe(F_5). On the other hand, gelator Phe(F_5) was not perturbed by the presence of XB acceptors, except for a marginal decrease in the storage moduli measured in its mixed hydrogels. This different behaviour of the two gelators, in connection with their possibility to engage in XB,

confirmed the initial design hypothesis and all the considerations deriving from the analysis of crystal structures.

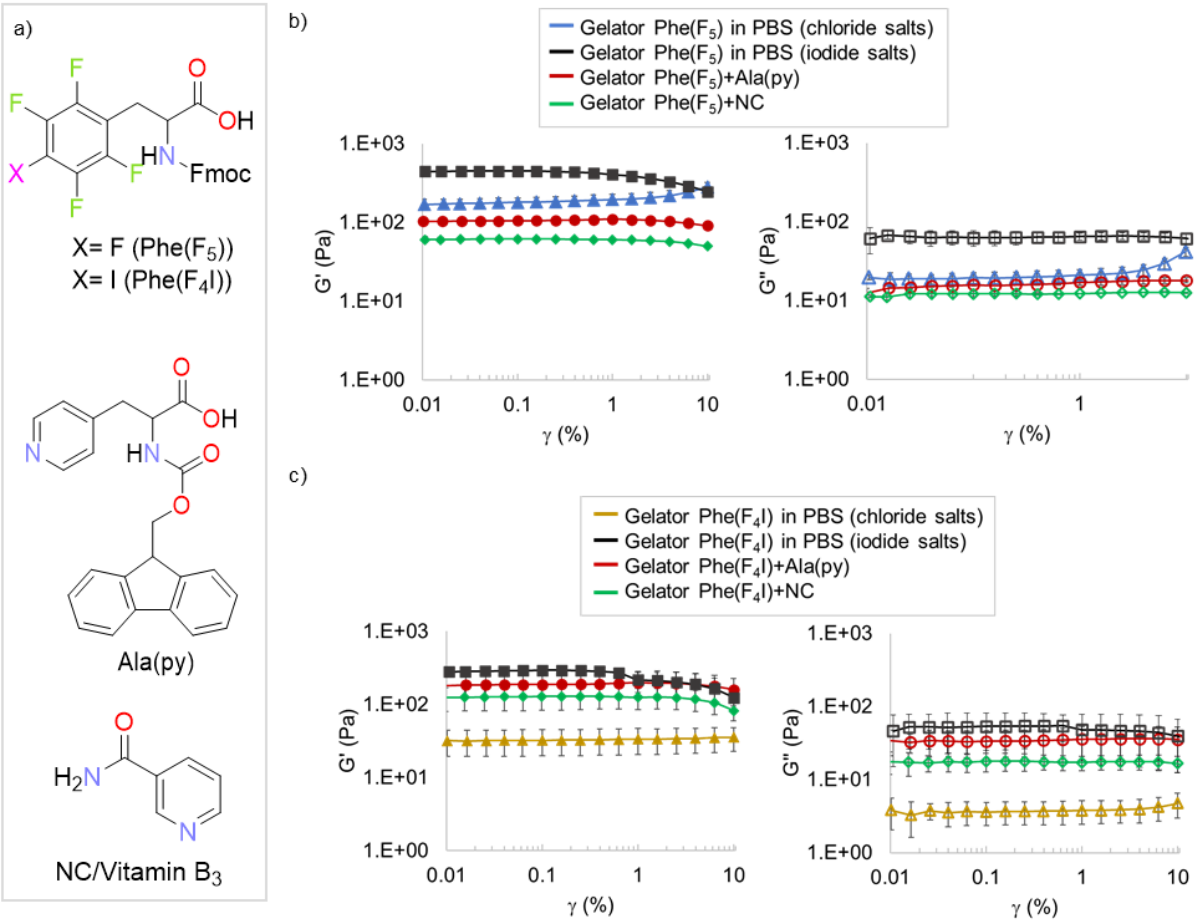

Figure 3.27 *a) Molecular structures of gelators Phe(F_5) and Phe(F_4I), N-Fmoc-4pyridilalanine (Ala(py)) and Vitamin B_3 (NC). b) Strain sweep experiment (Linear Viscoelastic Region) for Phe(F_5) formulated in common PBS (blue) and in PBS with iodide salts (black), Phe(F_5)+Ala(py) (red) components in PBS, Phe(F_5)+NC (green) component in PBS measured. All hydrogels components were measured in 2.5 mM condition. c) Strain sweep experiment (Linear Viscoelastic Region) for Phe(F_4I) formulated in common PBS (yellow) and in PBS with iodide salts (black), Phe(F_4I)+Ala(py) (red) components in PBS, Phe(F_4I)+NC (green) component in PBS measured. All hydrogels components were measured in 2.5 mM condition. Oscillation amplitude table: frequency 0.95 Hz, 5 samples per decade.*

Furthermore, considering the good performance obtained by bi-component hydrogel Phe(F_4I)+Ala(py), the same amino acids were used as scaffolds for the solid phase peptide synthesis of dipeptide Ala(py)Phe(F_4I) (**Figure 3.28a**). A solution of Ala(py)Phe(F_4I) (11 mg/mL) in DMSO was stored at +4°C for one month, leading to crystals suitable for SC-XRD analysis.

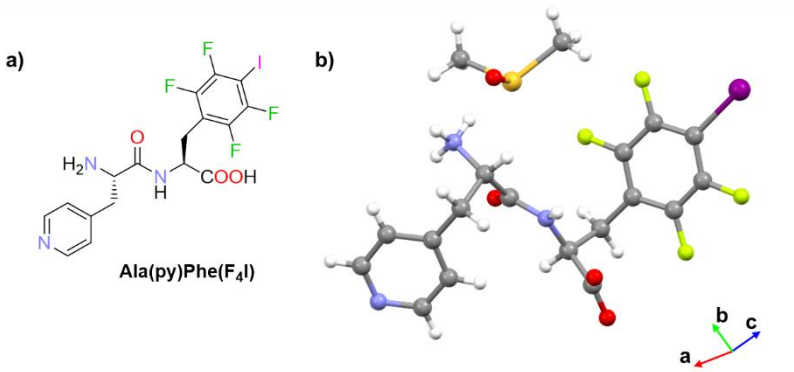

Figure 3.28 *Molecular structure of dipeptide Ala(py)Phe(F4I) (a) and its ball-and-stick crystallographic representations acquired by SC-XRD (b).*

[Ala(py)Phe(F_4I)] crystallized in monoclinic space group $P2_1$ displaying one molecule of dipeptide and one molecule of crystallization solvent in the asymmetric unit. The dipeptide formed an infinite chains along the crystallographic *a*-axis assembled by hydrogen bonding between peptide bonds (N1-H1⋯O3, 2.74 Å) (**Figure 3.29**).

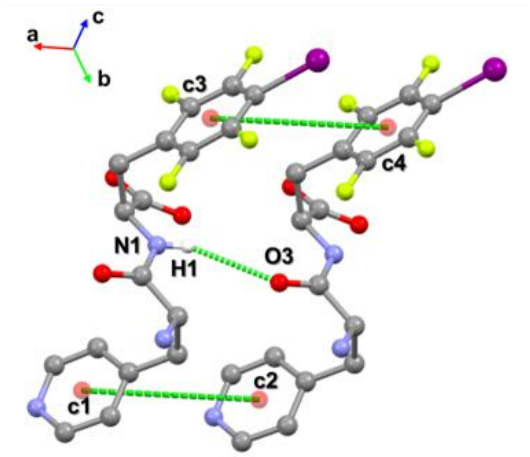

Figure 3.29 *Crystal packing of [Ala(py)Phe(F4I)] units in a chain, viewed along the crystallographic a-axis.*

The two aromatic side chains (pyridyl and tetrafluoro-iodophenyl groups) were held in position by CH⋯π contacts and the iodine-tetrafluorophenyl interaction which may weakly contribute to the stabilization of the supramolecular chain. Interesting is the latter interaction which involved the δ^- belt of the iodine atom and the electropositive area of the tetrafluorophenyl unit. Distances between

centroids c1⋯c2 and c3⋯c4 measured the same (5.23 Å), and they resulted to be longer than any other π-π distance analysed so far (**Figure 3.29b**).

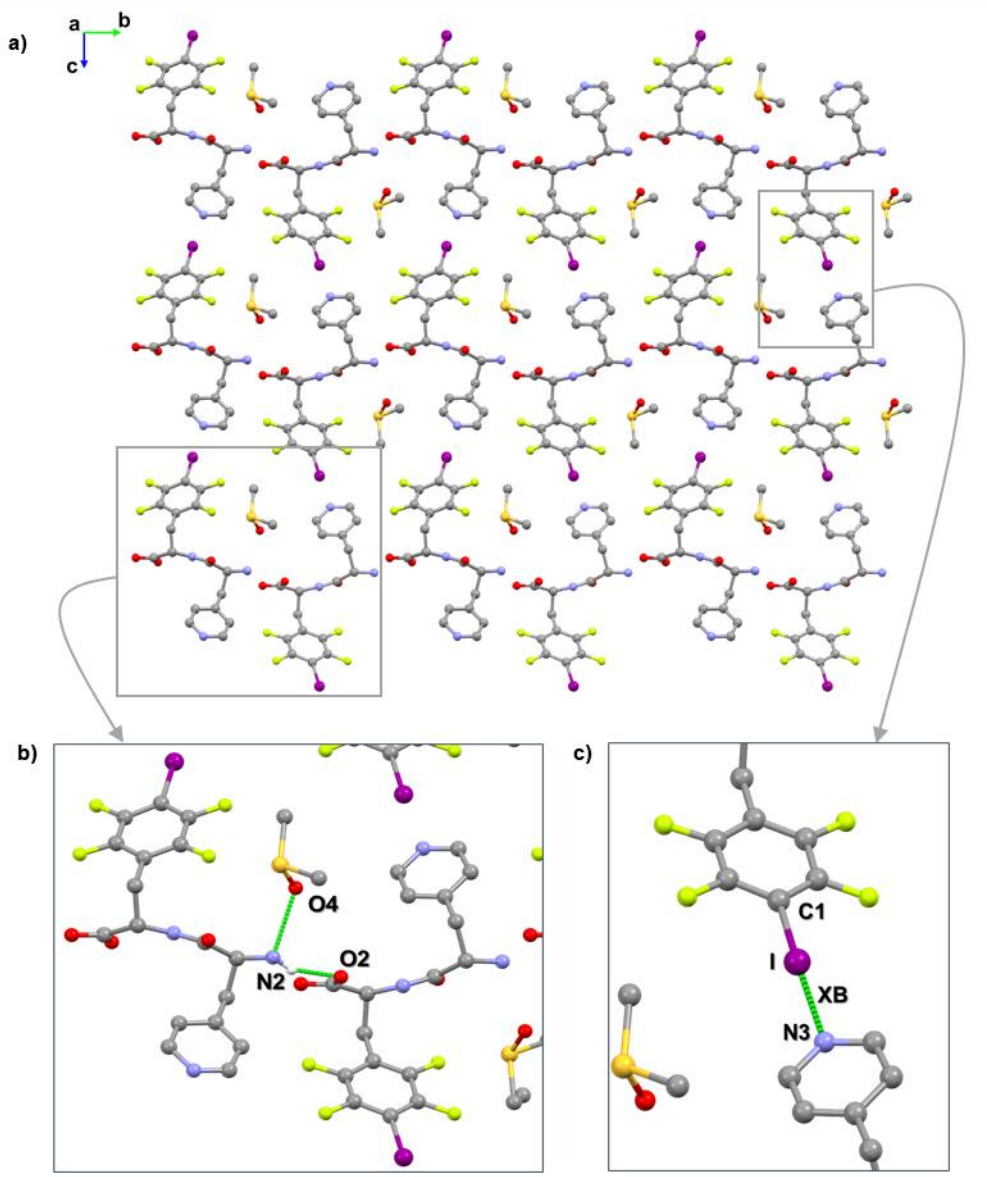

Figure 3.30 *Inter-chain interactions between adjacent chains of [Ala(py)Phe(F₄I)] (a). Zoom b represents the focus on the HB interactions between two dipeptide units along crystallographic b-axis. Zoom c displays the focus on halogen bonding occurring between pyridyl group and iodine atom along the crystallographic c-axis.*

The stabilization of the crystal packing was further promoted by a hydrogen bonding contact between *N*-terminus of one dipeptide unit and the *C*-terminus of the adjacent (N2H-H⋯O2-CO, 1.92 Å, **Figure 3.30**). This HB interaction defined infinite chains along the crystallographic *b*-axis. Thus, aromatic moieties were compartmentalized by dipeptide' backbones, originating a highly ordered structure (**Figure 3.30a**). The same -NH_2 group was engaged in a further hydrogen bond with the carbonyl group of the solvent residue (N2H-H⋯O4=S, 2,77 Å, **Figure 3.30b**). The iodine atom on the

tetrafluorophenyl unit functioned, as expected, as strong XB donor forming a short (thus strong) XB contact with the nitrogen atom of the pyridyl system with the following geometrical parameters N3···I distance 2.76 Å and N3···I-C1 angle of 178.5° (**Figure 3.30c**).[242] The XB contact linked adjacent hydrogen bonded chains creating a square framework which caged the DMSO molecule.

Considering the success of the crystallographic approach so far, the extremely ordered packing of this dipeptide might correlate with its hydrogelation tendency. Indeed, it would be reasonable that the organic solvent present in the structure could be replaced by water molecules, easily creating a porous soft materials suitable for biological purposes.

Table 3.6 *Crystallographic data and refinement details for co-crystal [Ala(py)Phe(F$_4$I)].*

Chemical formula	$C_{17}H_{14}F_4IN_3O_3 \cdot C_2H_5OS$
Mr	588.33
Crystal system	Monoclinic,
Space group	$P2_1$
Temperature (K)	173
a, b, c (Å)	5.2252 (2), 16.0413 (7), 13.5305 (4)
β (°)	99.876 (4)
V (Å^3)	1117.31 (8)
Z	2
Radiation type	Cu Kα
μ (mm−1)	12.73
Crystal size (mm)	0.06 × 0.02 × 0.02
Absorption correction[a]	Multi-scan
Tmin, Tmax	0.384, 1.000
No. of measured, independent and observed [I > 2σ(I)] reflections	5976, 3337, 3023
Rint	0.056
(sin θ/λ)max (Å−1)	0.631
R[F^2 > 2σ(F^2)], wR(F^2), S	0.047, 0.122, 1.02
No. of reflections	3337
No. of parameters	310
No. of restraints	25
H-atom treatment	H-atom parameters constrained
Δρmax, Δρmin (e Å−3)	0.88, −1.13
Absolute structure parameter[b]	-0.008 (8)
CCDC number	t.b.d.

[a]CrysAlis PRO 1.171.42.55a (Rigaku Oxford Diffraction, 2022) Empirical absorption correction using spherical harmonics, implemented in SCALE^3 ABSPACK scaling algorithm.
[b]Absolute structure: Flack x determined using 1292 quotients [(I+)-(I-)]/[(I+)+(I-)] (Parsons, Flack and Wagner, Acta Cryst. B69 (2013) 249-259).

3.4 Conclusion

The utilization of fluorine-driven intermolecular recognition facilitated the development of an amino acid-based hydrogel with customized properties. An innovative crystallographic approach was developed to gain insight into the molecular mechanisms governing hydrogel self-assembly, facilitating performance prediction. In particular, an acid⋯amide supramolecular heterodimer was exploited to achieve co-crystallization of Phe(F_5) in the presence of benzamide (BZ). Their 1:1 cocrystal [Phe(F_5)·BZ] enabled a detailed study of the interactions which govern the self-assembly. It was also confirmed that these forces are the same which drove the gelation, validating this crystal engineering-based strategy. The corresponding mixed hydrogel demonstrated to have a relevant role in the delayed release of gelation partner BZ. Moreover, replacing BZ with an API capable of engaging similar interactions, such as Vitamin B_3 (NC), maintained the same release profile.

The same crystallographic approach was utilized to compare the gelling performance of Phe(F_5) with *N*-Fmoc-2,3,5,6-tetrafluoro-4-iodophenylalanine (Phe(F_4I)), introducing the possibility of 'halogen bond' (XB) interactions due to the presence of an iodine atom in the side chain's para-position. This approach allowed the prediction of macroscopic behaviour of Phe(F_4I) hydrogels. In this case, the strength of the hydrogels were tailored by the proper choice of gelation partners containing XB acceptors. These findings offer a novel approach for fine-tuning hydrogel properties. As further step in the field, other partners could be studied, with particular care to the release performances of the mixed hydrogels obtained. Then, the investigation of the self-assembly potential of Ala(py)Phe(F_4I) dipeptide could be interesting because of the absence of the Fmoc-pairing typical of the other structures.

3.5 Materials and methods

N-Fmoc-L-pentafluorophenylalanine (Phe(F_5)) was purchased from abcr GmbH (Germany). Benzamide (BZ), nicotinamide/vitamin B_3 (NC) and organic solvents were purchased from Sigma-Aldrich. All chemicals were used without any further purification. Milli-Q water was obtained from a Simplicity® water purification system (MerckMillipore). Spectra/Por 6 Dialysis Tubes in Regenerated Cellulose (diameter 11.5 mm, MWCO 2 kDa) were used for release assays.

All reagents for *N*-Fmoc-L-2,3,5,6-tetrafluoro-4-iodo-phenylalanine (Phe(F4I)) were purchased from commercial suppliers (Alfa-Aesar, Sigma-Aldrich, Apollo, Fluorochem) and used without further purification.

Dipeptide Ala(py)Phe(F_4I)

Dipeptide Ala(py)Phe(F_4I) was provided, as a scientific collaboration, by Dr. Greta Bergamaschi (Consiglio Nazionale delle Ricerche – CNR). It was prepared through solid phase peptide synthesis and purified by LC-HPLC.

^{1}H NMR (400 MHz, D_2O): δ = 8.81 (m, 2H), 4.44 (m, 1H), 8.05 (m, 2H), 4.74 (m, 1H), 4.49 (td, J = 7.1, 1.4 Hz, 1H), 3.63 (dd, J = 14.0, 6.4 Hz, 1H), 3.54 (dd, J = 14.1, 8.2 Hz, 1H), 3.36 (m, 1H), 3.25 (dd, J = 14.4, 8.3 Hz, 1H) ppm. ^{19}F NMR (376 MHz, D_2O): δ = -121.83 (m, 2F), -141.70 (dd, 2F, J = 23.8, 10.9 Hz) ppm. IR (ATR): υ = 3067 (m), 1668 (s), 1639 (m), 1512 (s), 1479 (s), 1396 (s), 1256 (s), 1185 (m), 1237 (s), 1016 (s), 927 (s), 838 (s), 798 (s), 721 (s) cm^{-1}. MS (ESI+): m/z (%) = 512 (100) $[M+H]^+$.

X-ray crystallography

Single crystal X-ray diffraction data of crystal [Phe(F_5)·BZ], [Phe(F_5)·Na] and [Ala(py)Phe(F_4I)] were collected using a XtaLAB Synergy diffractometer equipped with a HyPix detector at 173 K (Oxford Cryosystems 800). Unit cell refinement and data reduction were performed with CrysAlisPro 1.171.41.98a.

Crystal [Phe(F_4I)·K] data collection was performed at the X-ray diffraction beamline (XRD1) of the Elettra Synchrotron, Trieste (Italy). Crystals were dipped in NHV oil and mounted on the goniometer head with kapton loops. Complete datasets were collected at 100 K (nitrogen stream supplied through an Oxford Cryostream 700) through the rotating crystal method. Data were acquired using a monochromatic wavelength of 0.7 Å, on a Pilatus 6M hybrid-pixel area detector. The diffraction data were indexed and integrated using XDS.

Powder X-ray diffraction (PXRD) measurements were run at r.t. on a Bruker D2-Phaser diffractometer equipped with Cu radiation (λ = 1.54184 Å), using Bragg−Brentano geometry.

Transmission electron microscopy (TEM)

For TEM analyses, 5 μL of hydrogel samples were deposited on a carbon-coated copper grid and air-dried overnight. Images were acquired with a Transmission Electron Microscope Philips CM 200 FEG (Field emission gun), 200 kV. For cross-section measurements, the cross sections of 50 different fibrils were measured with ImageJ software and data were fitted according to Gaussian function.

Scanning electron microscopy (SEM)

For SEM analyses, hydrogels were lyophilized and the solid residues were deposited on steel stubs coated by carbon tape. Samples were gilded and images were acquired with a scanning electron microscope Zeiss EVO 50 EP.

Energy Dispersive Spectroscopy analysis (EDS), for the qualitative characterization of amino acidic hydrogels, was performed with a Bruker XFlash 6l30 probe (resolution: 123 eV at Mn Kα, 45 eV at C Kα and 53 eV at F Kα).

Differential Scanning Calorimetry (DSC)

DSC analyses were performed with a Mettler Toledo DSC823e calorimeter, using aluminium crucibles. Mettler STARe software was used for data analysis. The heating step was recorded from 25 °C to 232 °C at a 10°C min^{-1} heating rate.

Polarized Light Optical Microscopy (POM)

POM images were registered with a Leica DM4500P POM system that was equipped with a Canon EOS 60D camera. Melting point of crystals [Phe(F_5)·Na] and [Phe(F_4I)·K] were determined using the optical microscope combined with a Linkam Scientific temperature-controlled stage. Heating rate, 10°C/min.

Attenuated Total Reflectance Fourier-Transform Infrared Spectroscopy (ATR FT-IR)

ATR FT-IR spectra were measured by using a Nicolet iS50 FTIR spectrometer equipped with an ATR device. Spectra were collected in the medium IR region (64 scans, 4000–400 cm^{-1}). All the spectra were measured with a resolution of ± 2 cm^{-1} and corrected for air background.

Nuclear Magnetic Resonance (NMR)

NMR spectra in solution were recorded on a Bruker Avance III 400 MHz spectrometer. Samples were dissolved in $(CD_3)_2CO$ (0.05 M referred to gelator Phe(F_5)). For ^{13}C-NMR experiments, chemical

shifts were reported in ppm downfield from the residual carbon solvent resonance as internal reference ($(CD_3)_2CO$: s = 206.26 ppm). For ^{19}F-NMR, experimental chemical shifts were reported in ppm from trifluoroacetic acid (-75.45 ppm), used as external standard.

Solid-state ^{13}C CP-MAS NMR spectra were collected at 125.77 MHz on a 500 MHz Spectrometer AvanceTM 500 operating at a static field of 11.7 Tesla (superconducting ultrashield magnet) and equipped with a 4 mm MAS probe. Samples were packed in zirconia rotors (80 µL internal volume), and spinned at 12 kHz at 298 K. Cross-polarization (CP) spectra, were recorded with a recycle delay d1 = 5 s; a contact time of 2.0 ms; 2560 scans for each experiment were acquired.

Fibrillation kinetics

Measurements were performed on a Tecan Infinite 200 PRO plate reader, employing a fully transparent 96 well-plate as sample holder. The instrument was set at 25 °C and orbital shaking was set at 432 revolutions per minute (rpm). Each well was filled with 150 µL of either Phe(F_5) (0.1 mM) or Phe(F_5)+BZ solution (1:1 molar ratio, both 0.1 mM) in 2 % DMSO in Milli-Q water. Each sample was measured in triplicate. Same conditions were used for the fibrillation kinetic of Phe(F_5) (0.1mM) and Phe(F_4I) (0.1mM) in 5 % DMSO in PBS, pH 7.4.

Method: (i) shake 30 s; (ii) wait 150 s; (iii) shake 2 s; (iv) measure absorption at 405 nm; (v) repeat stages ii-iv for 16 hours. Absorbance of neat solvent mixture was subtracted from each sample. Each measurement was fitted according to equation 3 (Verhulst logistic function):[250]

$$Y = y_i \frac{y_f}{1 + e^{-(t-t_0)/\tau}}$$

Eq. 3

Where: Y = absorbance, being y_i and y_f the initial and final absorbance values, respectively;

t_0 = time to 50% of maximal signal or the time of inflection point;

τ = time constant of fibril growth

From the fitting two parameters were extrapolated to figure out the fibril growth process:

$k_{app} = 1/\tau$ apparent growth rate of fibrils

$T = t_0 - 2\tau$ delay time

Rheology

All rheology tests were performed using a KINEXUS Pro+ rheometer (Malvern Panalytical, UK). Samples were pre-formed and directly transferred on the bottom rheometer plate, 24 hours after gelation. A 20-mm parallel plate geometry was used, with a gap distance of 0.5 mm. Temperature

was controlled with a Peltier device and maintained at 25 °C. All the oscillatory measurements were performed within the linear viscoelastic range. Each analysis was repeated at least 3 times, and representative measures are reported.

Time sweep experiments were performed at 25 °C for 12 minutes, at a frequency of 0.95 Hz (6 rad s^{-1}) and 0.2 % strain. Strain sweep experiments (Linear Viscoelastic Region) were performed at 0.01 % - 100 % strain with a constant frequency of 0.95 Hz (6 rad s-1). Frequency sweeps were performed over a range of frequencies from 0.01 - 16 Hz (0.06 - 100 rad s-1) with a constant shear stress chosen within the linear viscoelastic region.

Circular Dichroism (CD)

CD spectra were recorded in 2 % v/v MeOH/Milli-Q water (18.2 MΩ·cm) in a 0.1 mm quartz cuvette, using a JASCO J-815 CD spectrometer. Acquisitions were performed in the range 200−350 nm using 1.0 nm data pitch, 1.0 nm bandwidth, 100 nm/min scanning speed, and 1 s response time. All the spectra are an average of 3 scans.

Gel samples were prepared by adding 100 μL of 2.5 mM monomer in 2% MeOH/water, immediately after dissolution of the monomer in water and before gelation had completed.

Ball milling experiments

Mechanochemical syntheses were performed using a Retsch MM400 ball mill with 2.5 mL vessels, operating at 15 Hz.

Synthesis of co-crystal [Phe(F_5)·BZ]

In a glass vial, 10 mg of amino acid Phe(F_5) (0.02 mmol) and 2.54 mg of BZ (0.02 mmol) were dissolved in the minimum amount of acetonitrile. Slow evaporation at r.t. of the resulting solution afforded colourless single crystals of [Phe(F_5)·BZ] in 2 days. Bulk co-crystal powder was obtained with the same procedure, mixing a five-fold higher amount of both reactants and then evaporating the solvent.

[Phe(F_5)·BZ]: m.p. 124°C. FT-IR (selected bands, cm^{-1}): 3468, 3356, 2431, 1910, 1734, 1676, 1631, 1605, 1521, 1502, 1450, 1225, 964, 742, 628.

Synthesis of crystals [Phe(F_5)·Na]

For bulk synthesis of [Phe(F_5)·Na] liquid-assisted grinding (LAG) approach was performed: 50 mg of Phe(F_5) (0.105 mmol) and 4.2 mg of NaOH (0.105 mmol), added with 20 μL of acetone. Ball

milling was performed for 30 min. Crystal [Phe(F_5)·Na] were obtained through slow evaporation from acetone within one month.

[Phe(F_5)·Na]: m.p. 215°C. FT-IR (selected bands, cm^{-1}): 3323, 1680, 1599, 1520, 1500, 1397, 1264, 1123, 1044, 961, 734, 540.

Synthesis of crystals [Phe(F_4I)·K]

For bulk synthesis of [Phe(F_4I)·K] liquid-assisted grinding (LAG) approach was performed: 50 mg of Phe(F_4I) (0.085 mmol) and 4.8 mg of KOH (0.085 mmol), added with 150 µL of acetone and 5 µL of water. Ball milling was performed for 25 min. Crystal [Phe(F_4I)·K] were obtained through slow evaporation from acetone within eight month.

[Phe(F_4I)·K]: m.p. 223°C. FT-IR (selected bands, cm^{-1}): 3322, 1680, 1594, 1473, 1394, 1253, 1088, 1046, 732, 621, 540.

Synthesis of crystal [Ala(py)Phe(F_4I)]

Purified dipeptide [Ala(py)Phe(F_4I)] was dissolved in pure DMSO (11 mg/mL) and stored at + 4°C. After one month crystals suitable for SC-XRD were obtained.

Crystal [Ala(py)Phe(F_4I)]: m.p. 169°C. FT-IR (selected bands, cm^{-1}): 2924 (m), 2853 (m), 1742 (s), 1680 (s), 1640 (s), 1575 (s), 1463 (s), 1231 (s), 1181 (m), 1122 (s), 981 (s), 745 (s), 712 (m), 646 (m).

Preparation of hydrogels

Following the solvent switch method reported by Nilsson et al.,[251] gelator Phe(F_5) (247 mM) was dissolved in DMSO, and the resulting stock solution was diluted with Milli-Q water up to a concentration of amino acid of 5 mM (0.24 wt%) or 2.5 mM (0.12 wt%) respectively. Additional DMSO was eventually added as to have always 2 %v/v of organic solvent in the final mixture. Diluted samples were then vortexed for 3 seconds, and let to rest at room temperature until gelation occurred (within 5 min). Multicomponent hydrogels were obtained with the same procedure, diluting Phe(F_5)+BZ or Phe(F_5)+NC stock solutions (in 1:1 molar ratio).

For preparation of hydrogels in PBS, gelator Phe(F_5) and gelator Phe(F_4I) (100mM) were dissolved in DMSO respectively and the resulting stock solution was diluted with PBS (pH 7.4, 10mM) up to a concentration of amino acid of 2.5 mM (0.12 wt%) respectively. Diluted samples were vortexed for 3 seconds and heated at 50°C with a thermoblock. Directly after the dilution, hydrogels were heated at 100°C for one minute and replaced in the thermoblock at 50°C, then brought at room temperature 1°C/min, then stored overnight.

Release assays

Accurately weighed amounts of hydrogels (about 1.7 g) were transferred in a dialysis membrane (MWCO 2 kDa) and incubated in 40 mL of Milli-Q water or PBS at 37 °C. 1 mL aliquots were withdrawn from the release bath at different time intervals (10 min, 20 min, 30 min, 40 min, 50 min, 1 h, 1.5 h, 2 h, 4 h, and 8 h from immersion), and immediately replaced by the same volume of fresh solvent. Concentrations of released BZ or NC in each aliquot were determined by HPLC calibration curves (column: C18, 2.7 µm particle size, 150 mm×4.6 mm; eluent: acetonitrile/water gradient, acidified with 0.1 %v/v HCO_2H; flow rate: 0.5 mL/min; UV absorbance detection at 262 nm).

Blank tests were performed following the same procedure on aqueous solutions of BZ or NC alone instead of gels, in order to evaluate the intrinsic release delay due to the dialysis membrane.

Compound BZ peak was detected after 8 min from sample injection, whereas compound NC had a retention time of about 4 min.

Diffusion coefficients (D) were calculated from equation 4:[255,260]

$$\frac{M_t}{M_\infty} = 4\sqrt{\frac{Dt}{\pi\lambda^2}}$$

Eq. 4

Where: M_t/M_∞ = ratio between released moles of BZ (or NC) and total number of moles of BZ (or NC) in the system (unitless)

t = time (min)

λ = gel thickness (height, m)

D = diffusion constant ($m^2\ min^{-1}$)

For each time point, the concentration of BZ (or NC) obtained from HPLC calibration curves was used to calculate the total amount of BZ (or NC) present in the 40 mL of Milli-Q water (or PBS). Each Mt value was adjusted including also the amount of BZ (or NC) removed in the previous aliquots. All data were collected in triplicate, and plotted as M_t/M_∞ against time (min), with the error reported as standard deviation. A second plot was constructed by plotting M_t/M_∞ against $t^{1/2}$ ($min^{1/2}$) from the initial linear section of the first plot, comprising the first 120 minutes of the release study.

Equation 4 was rearranged to yield a linear relationship between M_t/M_∞ and $t^{1/2}$ ($min^{1/2}$), as follows:

$$\frac{M_t}{M_\infty} = 4\sqrt{\frac{D}{\pi\lambda^2}} \cdot \sqrt{t}$$

Thus, diffusion coefficients D (m^2 min^{-1}) were determined by measuring the slope of M_t/M_∞ against $t^{1/2}$ ($min^{1/2}$), and setting this value equal to the coefficient of $t^{1/2}$ ($min^{1/2}$) above in order to solve for the value of D (m^2 min^{-1}).

Synthesis of gelator Phe(F_4I)

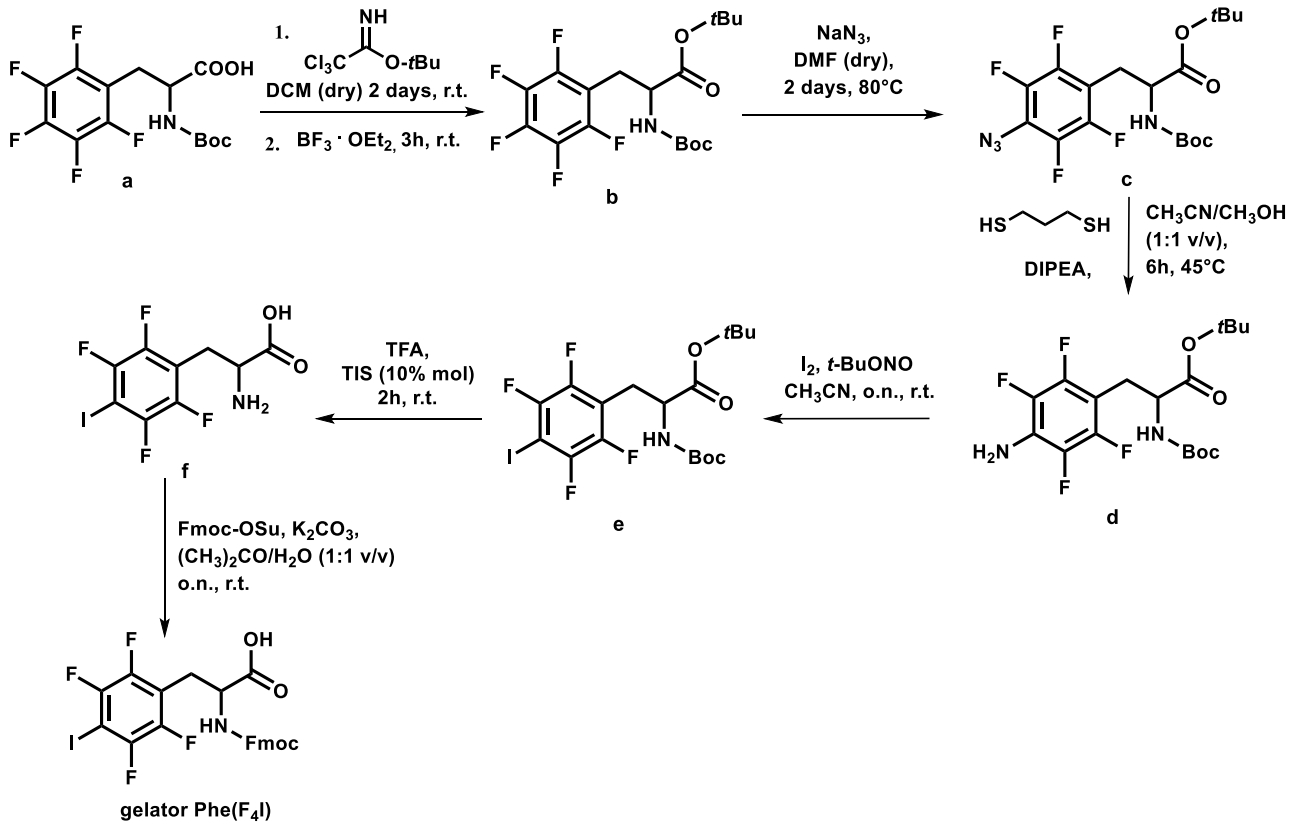

Synthetic procedure was taken from Bergamaschi *et al.*[256] and modified in some steps as optimization. Characterization of the intermediates is in accordance with the literature.

Synthesis of **compound b**

Commercially available N-Boc-pentafluoro-L-phenylalanine **a** (5g, 14.1 mmol, 1 equiv) was dissolved in dichloromethane (DCM, dry) to have a ≈ 0.1 M solution. To the solution tert-butyl 2,2,2-trichloroacetimidate (0.28 mmol, 5.03 mL, d=1.22 g/mL, 2 equiv) was slowly added. The mixture was stirred at r.t. for 2 days and monitored by TLC; the formation of a white solid occurred. Subsequently, $BF_3{\cdot}OEt_2$ was added (260 µL, d=1.15 g/mL, 0.15 equiv), and the mixture was stirred for further two hours. Then, the reaction was quenched by adding a $NaHCO_3$ saturated solution and the resulting mixture was extracted with DCM (3 x 50 mL). The combined organic layers were washed with brine, dried over Na_2SO_4, filtered and concentrated under vacuum. The crude product was purified by flash column chromatography (Hexane/AcOEt 10:1), yielding 4.2 g of desired

compound (72% yield) as a pale thick oil that solidifies to give a white solid (R_f = 0.3 in Hex/AcOEt 10:1, permanganate staining solution).

^{1}H NMR (400 MHz, $CDCl_3$): δ = 5.12 (m, 1H, N*H*), 4.44 (m, 1H, C*H*NH), 3.23 (dd, 1H, J = 4.0, 13.5 Hz, PhC*H*H), 3.04 (dd, J = 8.0, 13.2 Hz, 1H, PhCH*H*), 1.45 (s, 9H, COOCCH_3), 1.39 (s, 9H, NCOOCCH_3) ppm. ^{19}F NMR (376 MHz, $CDCl_3$): δ = -141.87 (dd, 2F, J = 22.5, 7.9 Hz, 2F), -156.11 (t, 1F, J = 20.8 Hz), -162.75 (td, 2F, *J* = 22.1, 23.0, 7.4 Hz) ppm.

Synthesis of **compound c**

In a dried round bottom flask, **compound b** (4.2 g, 10 mmol, 1 equiv) was dissolved in dry DMF in order to have a 0.7 M solution. After complete dissolution, NaN_3 (1.33 g, 20mmol, 2 equiv) was added at 0°C under nitrogen flux. The resulting solution was immerged in an 80 °C pre-heated bath and stirred at the same temperature for two days; slowly the mixture turns to a brownish colour. The reaction was then poured into cool water (200 mL). The product precipitates as brown solid which was washed with fresh water. The crude product was purified by flash column chromatography (Hexane/AcOEt 97:3), yielding 3 g of desired compound (R_f = 0.39, 69% yield) as a white powder. From the same column is possible to isolate also compound **d** as white solid (R_f 0.02 in Hexane/AcOEt 97:3, 3% yield).

^{1}H NMR (400 MHz, $CDCl_3$): δ = 5.11 (d, *J* = 8.0 Hz, 1H, N*H*), 4.44 (d, *J* = 6.6 Hz, 1H, C*H*NH), 3.22 (dd, *J* = 14.1, 5.8 Hz, 1H, PhC*H*H), 3.03 (dd, *J* = 14.0, 7.51 Hz, 1H, PhCH*H*), 1.45 (s, 9H, COOCCH_3), 1.40 (s, 9H, NCOOCH_3) ppm. ^{19}F NMR (376 MHz, $CDCl_3$): δ -142.11 (dd, 2F, J = 21.2, 10.1 Hz), -152.55 (dd, 2F, J = 21.2, 10.1 Hz).

Synthesis of **compound d**

Compound c (2.5 g, 5.74 mmol, 1 equiv) was dissolved in a 1:1 mixture of MeOH/CH3CN to have a ≈ 0.15 M solution. To the resulting mixture 1,3-propanedithiol (1.24 g g, 11.5 mmol, 1.15 mL, d = 1.076 g/mL, 2 equiv) and *N*,*N*diisopropylethylamine (1.48 g, 11.5 mmol, 2 mL, d = 0.742 g/mL, 2 equiv) were added. A slight effervescence was observed. The reaction was immerged in a 45 °C preheated bath and stirred for six hours. Then the mixture was concentrated, poured in 100 ml of saturated NH_4Cl solution and extracted with DCM (3 x 30 mL). The combined organic layers were then washed with brine and dried over Na_2SO_4, filtered and concentrated under vacuum. The resulting waxy brownish solid was purified by flash column chromatography, eluting with Hexane/AcOEt 8:2, to give the desired product as a white solid with a 77% yield (R_f = 0.43 in Hexane/AcOEt 8:2).

^{1}H NMR (400 MHz, $CDCl_3$): δ = 5.08 (d, *J* = 8.4 Hz, 1H, N*H*), 4.41 (q, *J* = 7.3 Hz, 1H, C*H*NH), 3.14 (dd, *J* = 14.4, 5.8 Hz, 1H, PhC*H*H), 2.97 (dd, *J* = 14.1, 7.3 Hz, 1H, PhCH*H*), 1.44 (s, 9H, COOCCH_3), 1.40 (s, 9H, NCOOCCH_3) ppm. ^{19}F NMR (376 MHz, $CDCl_3$): δ = -145.00 (dd, 2F, *J* = 20.9, 8.8 Hz), -162.41 (m, 2F) ppm.

Synthesis of **compound e**

To a 0 °C cooled solution of **compound d** (1.8 g, 4.46 mmol, 1 equiv) in freshly distilled CH_3CN (0.1 M in **d**) protected from light, iodine (2.26 g, 8.92 mmol, 2 eqv) was added. After 15 min, *t*-Butyl nitrite (0.69 g, 6.69 mmol, 780 µL, d= 0.867 g/mL, 1.5 equiv) was added dropwise over a period of 5 min, at 0°C. The resulting solution was allowed to return at r.t. and stirred further for 2 h. Then it was concentrated to reduced volume avoiding the use of heat and subsequently poured into 100 mL of a 2 M $NaHSO_3$ solution. The aqueous mixture was extracted with DCM (4 x 120 mL). The collected organic layers were then washed with brine, dried over Na_2SO_4 and concentrated. The crude was purified via flash column chromatography eluting with a polarity gradient starting with DCM/Hexane 1:1 to 100% DCM, to yield a white solid with a 52% yield (R_f = 0.21 in DCM/Hexane).

^{1}H NMR (400 MHz, $CDCl_3$): δ = 5.12 (d, *J* = 8.1 Hz, 1H, N*H*), 4.47 (m, 1H, C*H*NH), 3.25 (dd, 1H, J = 4.0, 12.0, PhC*H*H), 3.07 (ddt, 1H *J* = 13.7, 7.6, 1.6 Hz, PhCH*H*), 1.44 (s, 9H, COOCCH_3), 1.38 (s, 9H, NCOOCCH_3) ppm. ^{19}F NMR (376 MHz, $CDCl_3$): δ = -121.31 (dd, 2F *J* = 22.0, 9.9 Hz), -140.08 (m, 2F) ppm.

Synthesis of **compound f**

At 0 °C, **compound e** (0.42 g, 0.8 mmol, 1 equiv) TFA (3 mL, d= 1.49 g/mL, 49 equiv) was used added as solvent of reaction. To the stirring solution TIPS (0.0126 g, 0.08 mmol, 17 µL, d= 0.773 g/mL, 10 mol%) was added. The resulting solution was allowed to return at r.t. and stirred further for 2 hours. Then the mixture was added with toluene (5 mL) and reduced to dryness. The resulting crude was washed with Et_2O/Hexane (1:1 v/v) (6 x 5 mL). The yellowish oil obtained was added with fresh Et_2O obtainin the precipitation of a solid which was separated through centrifugation (6000 rpm, 5 min). The white solid was washed again with Et_2O (3 x 10 mL) obtaining a white solid (Yield 100%) directly used for the next reaction. (R_f = 0.16 in $CHCl_3$/AcOEt 2:1 +0.5 % v/v CH_3COOH, permanganate staining solution, strongly fluorescent at 365 nm).

^{1}H NMR (400 MHz, methanol-d_4): δ = 3.75 (dd, 1H, *J* = 7.9, 6.8 Hz, C*H*NH), 3.42 (m, 1H, PhC*H*H), 3.19 (m, 1H, PhCH*H*) ppm. ^{19}F NMR (376 MHz, methanol-d_4): δ = -123.79 (m, 2F), -141.91 (m, 2F) ppm.

Synthesis of **gelator Phe(F_4I)**

K_2CO_3 (0.38 g, 7.7 mmol, 5 equiv) was dissolved in a 1:1 acetone/water mixture and was used to dissolve **Compound f** (crude, 0.2 g, 0.55 mmol, 1 equiv, 0.03 M in starting material). The mixture was cooled at 0°C and added with and FmocOSu (0.222 g, 0.66 mmol, 1.2 equiv), then stirred at r.t. overnight protecting it from light. The reaction mixture was concentrated, and added with HCl 6M (3 mL). The precipitate was separated through centrifugation (7000 rpm, 7 min) and washed with hexane (10 x 10mL) to get the final product as white solid (81% yield). (R_f = 0.15 in Hexane/AcOEt 1:1 v/v + 1% CH_3COOH).

^{1}H NMR (400 MHz, Acetone-*d*): δ = 7.85 (d, 2H, *J* = 7.6 Hz, C*H*), 7.65 (d, 2H, *J* = 7.5 Hz, C*H*), 7.41 (m, 2H, C*H*), 7.31 (m, 2H, C*H*), 6.95 (d, 1H, *J* = 8.9 Hz, COO*H*), 4.62 (m, 1H C*H*NH), 4.25 (m, 3H, CH_2, OCH$_2$C*H*), 3.43 (dd, 1H, *J* = 14.2, 5.7 Hz, PhC*H*H), 3.32 (dd, 1H, *J* = 14.1, 8.8 Hz, PhCH*H*) ppm. ^{19}F NMR (376 MHz, Acetone-*d*): δ = -125.23 (m, 2F), -143.53 (m, 2F) ppm. ^{13}C NMR (101 MHz, Acetone-*d*): δ = 171.94 (s, 1C, *C*OOH), 156.80 (s, 1C, NH*C*OOFmoc), 144.95 (d, 2C, *J* = 1.7 Hz), 142.09 (d, 2C, *J* = 2.9 Hz), 128.54 (s, 2C), 127.94 (s, 2C), 126.09 (d, 2C, *J* = 5.6 Hz), 120.79 (d, 2C, *J* = 2.1 Hz), 118.39 (s, 1C, *C*CH2), 67.45 (s, 1C, O*C*H$_2$), 53.60 (s, 1C, *C*HNH), 47.93 (s, 1C, OCH$_2$*C*H), 26.68 (s, 1C, *C*H$_2$), 26.09 (s, *C*I). IR (ATR): υ = 3345 (m), 2923 (m), 1731 (s), 1698 (s), 1533 (m), 1477 (m), 1266 (m), 1250 (m), 1230 (m), 1086 (m), 1049 (m), 949 (m), 871 (s), 802 (s), 757 (s), 738 (s), 621 (s) cm^{-1}. MS (ESI+): m/z (%) = 608 (100) [M+Na]$^+$. MS (ESI-): m/z (%) = 584 (100) [M]$^-$.

Conclusions

The present thesis was centred upon the potential of the fluorine atom as driver of intermolecular recognition in three different systems: dendrimeric vectors, proteins and hydrogels. The first one is set in the frame of ^{19}F-magnetic resonance, an innovative and powerful technique for *in vivo* imaging that requires the development of suitable probes. Recently reported ^{19}F-MRI contrast agent PERFECTA seemed to satisfy most of the requirements, but has a main drawback in its complete insolubility in biological environments. Thanks to F-F interactions, fluorinated dendrimers demonstrated to be promising carriers for solubilising PERFECTA, while maintaining its good magnetic properties (**Chapter 2.2**). Two dendrimers – BFTG2-OH and BFTG2-S – were investigated. The latter ones belong to the family of the Janus dendrimers, bearing a branched fluorinated (BF) hydrophobic part, a triazole core (T) and a second-generation oligoglycerol dendron (G2) as hydrophilic portion. The different nature of their eight end-groups – hydroxyl (OH) or sulphate (S) units – determined different behaviour in the aqueous environment, defining vesicles and micelles respectively. They were both effective in solubilising the probe thanks to a formulation *via* nanoprecipitation, achieving good colloidal properties and reproducibility. Both dendrimers were suitable for MRI, affording a bright signal when subjected to a 7T magnetic field. Furthermore, both gave a high cell viability towards two different cell lines. Preliminary data about cellular uptake defined BFTG2-S as the best candidate for further optimization and future *in vivo* studies. Indeed, according to the initial dendrimer design, its sulphate end-groups were demonstrated to selectively target inflammatory cells. This achievement is highly desirable in the administration of any pharmaceutical agent. In fact, considering the high concentration of inflammatory cells in the peripherical areas of many diseases, the possibility to obtain good images of these specific zones could be very interesting for the scientific research in the field.

The same contrast agent was then formulated with two different proteins: Lysozyme (LYS) and Bovine serum albumin (BSA) (**Chapter 2.3**). In this case, the unique properties of PERFECTA determined interesting structural changes in both proteins. Although the grade of protein structure modification was much more pronounced for LYS than BSA, both systems could serve as model of biological transport for fluorinated pharmaceuticals and pollutants. Additionally, the impressive structural transition obtained for LYS is particularly valuable in the field of protein manipulation.

Although amyloid fibrillation of LYS was not a novelty, the β-transition obtained after addition of PERFECTA was particularly controlled. Indeed, the reproducible oligomerization did not end up in complete amyloid deposition of the protein. The fascinating unicity of this mechanism will be further characterized with the help of computational tools in order to point out the interaction mechanism between C-F units and proteins which constitutes a quite unexplored issue.

Another intermolecular recognition driven by fluorine allowed to obtain an amino acid-based hydrogel with tuned properties. *N*-Fmoc-amino acids are known to organise into anisotropic structures, such as fibers. This tendency often led to the formation of supramolecular hydrogels with a high water content, and mechanical properties similar to those of biological tissues. The biocompatibility of such soft materials defined an increasing interest, and fluorination of these gelators was proposed as an efficient strategy to tune their behaviour. Indeed, the increased hydrogel strength of *N*-Fmoc-pentafluoro-phenylalanine - Phe(F_5), in comparison with unsubstituted phenylalanine, was exploited to obtain the delayed release of APIs (**Chapter 3.2**). An innovative crystallographic approach was developed to have an insight into the molecular mechanisms which govern the self-assembly of the hydrogel, in order to predict its performance. In particular, an acid⋯amide supramolecular heterodimer was exploited to achieve co-crystallization of Phe(F_5) in the presence of benzamide (BZ). Their 1:1 cocrystal [Phe(F_5)·BZ] allowed a useful in-depth study of the interactions involved in the self-assembly process and proved that they were also the driving forces of gelation. Indeed, the synthon exploited for crystallization was preserved even after hydrogelation. Furtherly, the overlapping behaviour of 1:1 complex in the solid and semisolid states validated this crystal engineering-based strategy. The corresponding mixed hydrogel demonstrated to have a relevant role in the delayed release of gelation partner BZ. Moreover, the replacement of compound BZ with an API able to engage the same interactions, *e.g.* Vitamin B_3 (NC), maintained the same release profile.

The same crystallographic approach was then exploited to compare the gelling performance of Phe(F_5) with *N*-Fmoc-2,3,5,6-tetrafluoro-4-iodophenylalanine - Phe(F_4I) (**Chapter 3.3**). The presence of an iodine atom in the side chain's *para*-position added a new type of possible interactions: the 'halogen bond' (XB). The previously described supramolecular strategy was validated again, making possible to predict the macroscopic behaviour of the respective hydrogels. In addition, the XB donor attitude of Phe(F_4I) was explored with the contemporary presence of hydrogelation partners bearing a XB acceptor. The latter ones made possible to furtherly tailor the strength of Phe(F_4I) hydrogels. These results opened up a new scenario for a proper fine-tuning depending on the gelation partner and performance desired.

Appendix – Advanced Characterization Techniques

Small angle X-ray scattering – SAXS

Small-angle-X-ray scattering (SAXS) is a powerful technique used for the analysis of macromolecules in solution, obtaining information about size and shape.[218] The basic principles of this biophysical technique are close to those of light scattering, which is commonly used for the estimation of particles size in the submicron domain.[261] When comparing SAXS analysis to other structural methods like X-ray crystallography and NMR, there are a number of benefits:[218]

- Materials can be studied in their native state in solution since the presence of few limitations on buffer composition, salts, or pH.
- There is no size limit for analyzing structures using Small-Angle X-ray Scattering (SAXS). Large molecules or particles, such as proteins and viruses (~500 Å in diameter), which fall beyond the range of NMR and X-ray crystallography, can be effectively studied through SAXS. Moreover, structures that may not be visible in electron microscopy due to their small size can be analysed using SAXS.
- Relatively small amount of sample is required.

In a SAXS experiment, a solution containing the particle in object is exposed to X-rays. The resulting scattered radiation, specifically the diffuse scattering at very small angles from the incident beam, is recorded on a 2D area detector. This area captures structural information at a low resolution, comprehending data that would normally be halted by the beam stop in experiments utilizing X-ray crystallography. SAXS operates within a high-resolution limit typically ranging between 10 and 20 Å. Consequently, the analysis conducted using SAXS predominantly offers insights into the overall molecular shape of the investigated object.[218]

The SAXS data allows to determine various parameters related to the objects size, including molecular mass, radius of gyration, hydrated volume, and the maximum diameter of the molecule. **Figure 4.1a** shows the typical scattering geometry of a conventional SAXS experimental setup. SAXS data collection requires a monochromatic X-ray source and a compatible two-dimensional detector system which collects the scattered intensities from the sample. The primary beam that passes through the sample is entirely absorbed by a beamstop positioned in front of the detector. The flight path both before and after the sample is usually in a vacuum to prevent absorption and scattering by air. Following this, the two-dimensional scattering pattern undergoes radial integration to generate the one-dimensional scattering function, I(q), where q represents the length of the scattering vector

(i.e., the momentum transfer). The formula for q is defined as $q = \frac{4\pi \sin(\theta/2)}{\lambda}$, where λ denotes the incident wavelength (typically around ~1 Å), and θ is the scattering angle.[261]

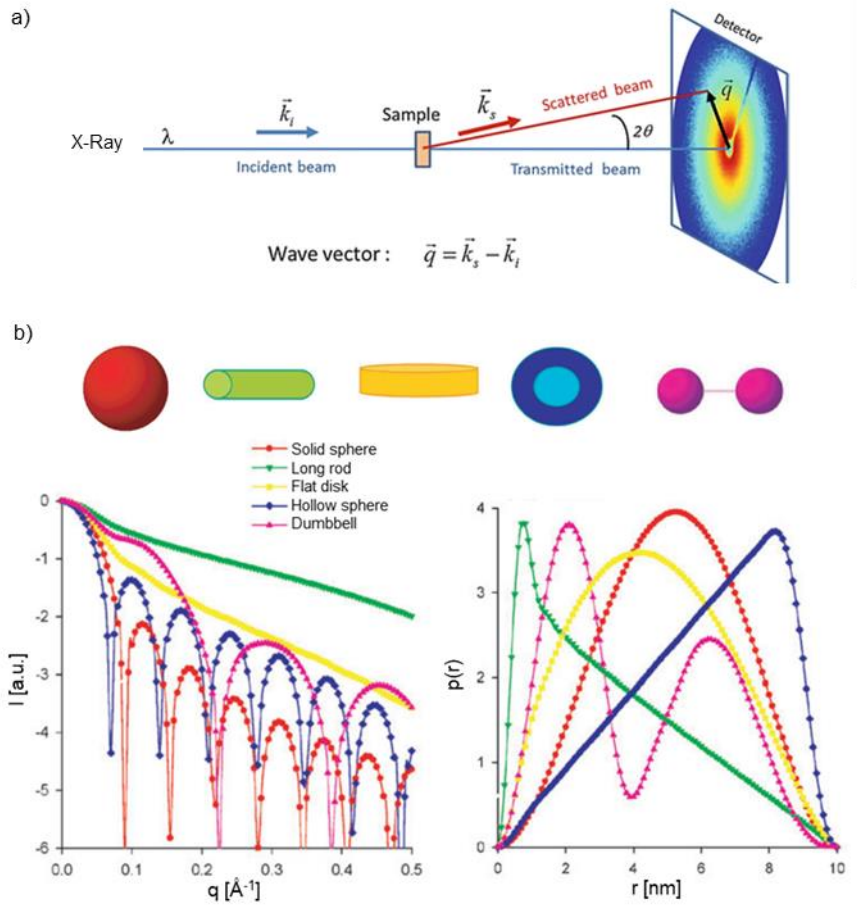

Figure 4.1 *a) Layout of a conventional small angle X-ray or neutron scattering setup. b) Scattering intensities and distance distribution functions of geometrical bodies.*[262]

The SAXS profile exhibits three discernible regions, namely Guinier, Fourier, and Porod (**Figure 4.2**). In the Guinier region, the experimental radius of gyration (R_g) can be estimated by fitting the natural logarithm of the intensity (I(q)) plotted against the square of the scattering vector q^2. It is important to note that the accuracy of the radius of gyration is susceptible to factors such as particle aggregation, polydispersity, and the correct subtraction of background or buffer effects.

In the Fourier region, the determination of the pair distribution function involves an indirect Fourier transformation of the experimental form factor. The pair distribution function concerns the distribution of electrons averaged over a radius *r*. The curves derived from this function are employed to determine the overall particle shape, assuming uniformity in shape among all particles in the sample.

The Porod region allows the extraction of surface-related information, such as the surface-to-volume ratio and specific surface estimation, particularly applicable to compact particles. It's worth noting that the logarithm of the form factor is proportional to q^4 for particles with uniform density in this context.

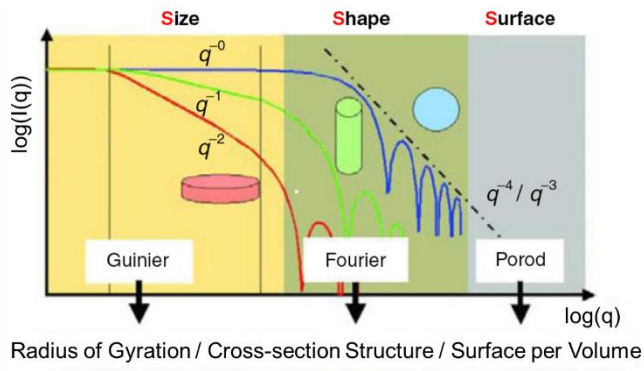

Figure 4.2 *Regions of SAXS profile and data that may be extracted from each.*

Dynamic Light Scattering – DLS

Dynamic Light Scattering (DLS), also known as Photon correlation spectroscopy (PCS), is a technique for investigating solution dynamics and particles sizes. It is based on the scattering of light due to interaction with particles in solution. DLS exploits temporal fluctuations in scattered light to provide insights into the diffusion coefficient of particles, which is indirectly associated with their size.[263]

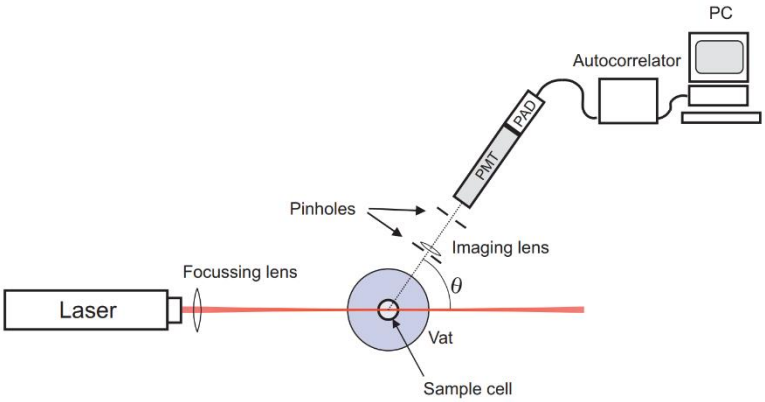

Figure 4.3 *Dynamic Light Scattering setup.*[263]

The instrument setup (**Figure 4.3**) is basically composed by a monochromatic laser light (typically 633 nm). A collimation system to focus the beam on the sample. A photodetector/photomultiplier tube (PMT) which detects and records the intensity fluctuation of the scattered light over time. A correlator which processes the intensity fluctuation recorded by the detector and analyses the temporal

autocorrelation function of the scattered light. Then, a data analysis system to extract information about the particle size distribution.

The intensity autocorrelation function, $g(\tau)$, is a key parameter in dynamic light scattering. It is related to the time-dependent fluctuations in scattered light intensity. The correlation function is typically described by the following equation:

$$g(\tau) = \frac{\langle \Delta I(t) \Delta(I(t+\tau)) \rangle}{\langle I(t) \rangle^2} \qquad \text{Eq. 5}$$

Where $\Delta I(t)$ is the fluctuation in intensity at time t; τ it the time delay between intensity measurements and $\langle \cdot \rangle$ denotes an average over time. The correlation function is then analysed using the autocorrelation function to obtain information about the particles' size and diffusion coefficient. The analysis is typically performed using the Stokes-Einstein equation:

$$D = \frac{k_B T}{3\pi\eta R_H} \qquad \text{Eq. 6}$$

where D represents the diffusion coefficient, T is the absolute temperature, η is the viscosity of the medium, k_B is Boltzmann's constant and R_H is the hydrodynamic radius of the particles.

To obtain accurate and meaningful results with dynamic light scattering, certain conditions need to be considered. (i) Dilute Samples: the sample should be sufficiently dilute to avoid multiple scattering events, which can complicate the analysis. (ii) Monodisperse Samples: ideally, the sample should consist of particles that are similar in size. What has been described so far is the so called cumulant fitting method, which holds true if the autocorrelation function is measured on a monodisperse system. For polydisperse populations, the determination of the distribution of diffusion coefficient is mathematically equivalent of doing an inverse Laplace transformation of the field autocorrelation function. This can be done in several ways through computer algorithms and the data analysis method chosen in this thesis project is called CONTIN. (iii) Stable Conditions: the sample should be stable over the measurement period to ensure consistent and reliable results. (iv) Appropriate scattering angle: the scattering angle is a critical parameter. The choice of angle depends on the characteristics of the sample and the instrument being used.

Dynamic light scattering is widely used in various fields, including colloid and polymer science, biochemistry, and pharmaceutical research, providing valuable information about particle size distribution and dynamics in solution.

Cryogenic Transmission Electron Microscopy – CryoTEM

Electron microscopy (EM) is based on the wave nature of electrons, which have much shorter wavelengths than photons (light). This property enables electron microscopes to achieve much higher resolution than traditional light microscopes, making it possible to visualize structures at the nanoscale.[264] Electron microscopes utilize electron sources, such as tungsten filaments or field-emission guns, to generate high-energy electron beams. Then, electromagnetic lenses focus and shape the electron beam, crucial for achieving high resolution and magnification. When the focused beam hit the sample, a signal is derived from both deflected and undeflected electrons that traverse the thickness of the specimen. The key advantages compared to traditional microscopy methods include superior resolution (approximately 0.2 nm in high-voltage Transmission-EM) and the capability to furnish both imaging and diffraction details from a sample. Since scattering is influenced by the target element, elements with higher atomic numbers (Z) exhibit better electron scattering compared to those with lower Z. This phenomenon is evident in various image contrasts, where regions with high Z appear darker and vice versa.[264]

Among the advanced techniques available with the advent of EM, there are Energy-Dispersive X-ray Spectroscopy (EDS) and Cryogenic Transmission Electron Microscopy (cryoTEM).

EDS is a powerful analytical technique commonly used in conjunction with scanning electron microscopy (SEM) or transmission electron microscopy (TEM). EDS provides information about the elemental composition of a sample through the discernment of characteristic X-rays emitted upon exposure to a focused electron beam. Indeed, when a high-energy electron beam interacts with the sample, it can displace inner-shell electrons from atoms in the sample. Electrons from outer shells then fall into the vacancies created in the inner shells, emitting X-rays in the process. Each element has distinct X-ray energies associated with transitions between specific electron shells, allowing identification and quantification of the elements present in the sample.

CryoTEM is a specialized technique that involves imaging samples at extremely low temperatures, typically close to or below the temperature of liquid nitrogen (-196°C or 77 K). This method is particularly valuable for studying biological specimens, soft materials, and other samples that are sensitive to electron beam radiation or prone to artifacts at room temperature. The primary principle of cryoTEM involves imaging samples at cryogenic temperatures. By rapidly freezing the sample in its native state, water molecules are vitrified, forming an amorphous, glass-like ice matrix that preserves the structural integrity of biological specimens and other delicate materials. Additionally, cryoTEM minimizes radiation damage caused by the electron beam, allowing for the

imaging of biological samples without the need for chemical fixation, dehydration, or heavy metal staining, which can introduce artifacts.[265]

Particularly delicate is the sample preparation for cryoTEM: firstly, a thin film of the sample is applied to a TEM grid. For biological samples, this may involve applying a suspension of the specimen on a thin carbon film or a lacey carbon support grid. Excess liquid is blotted away using filter paper, leaving a thin layer of sample. The grid is then rapidly plunged into a cryogen (usually liquid ethane or propane), instantly freezing the sample and creating a vitreous ice layer.

CryoTEM offers distinct advantages over alternative morphological analysis techniques. It guarantees the preservation of the native structure of the sample (in its hydrated state, especially for biological specimens and soft materials). The minimization of the artifacts (it avoids heavy metal staining or chemical fixation reducing the risk of introducing artifacts). The vitreous ice matrix provides high contrast, enabling the visualization of detailed structures and the low temperature conditions reduce the radiation damage, allowing longer exposure times and improving image quality without compromising the sample integrity.

List of abbreviations

AcOEt Ethyl acetate

[Ala(py)Phe(F_4I)] Crystal of the dipeptide Ala(py)Phe(F_4I)

Ala(py) *N*-Fmoc-3-(4-pyridyl)-L-alanine

AMPs Antimicrobial peptides

APIs Active Pharmaceutical Ingredients

BHTG2-OH Branched Hydrogenated dendrimer with Triazole core and oligoglycerol dendron of Generation 2 ending with eight -OH groups

BFTG2-OH Branched Fluorinated dendrimer with Triazole core and oligoglycerol dendron of Generation 2 ending with eight -OH groups

BFTG2-S Branched Fluorinated dendrimer with Triazole core and oligoglycerol dendron of Generation 2 ending with eight $-OSO_3^-$ groups

BSA Bovine serum albumin

BZ Benzamide

ATR-FTIR Attenuated total reflectance-Fourier transformed infrared spectroscopy

CA Contrast agent

CD Circular dichroism

CMC Critical micelle concentration

CP-MAS NMR Cross-polarization magic angle spinning nuclear magnetic resonance

CPP molecular packing parameter

cryoTEM Cryo-transmission electron microscopy

DLS Dynamic light scattering

EDS Energy Dispersive Spectroscopy

FAAs Fluorinated amino acids

Fmoc Fluorenylmethyloxycarbonyl

HB Hydrogen bond

HLB Hydrophilic-lipophilic balance

HSA Human serum albumin

LMWHs Low molecular weight hydrogelators

LYS Lysozyme

MRI Magnetic resonance imaging

NC Nicotinamide/Vitamin B_3

NMR Nuclear magnetic resonance

P PERFECTA

PERFECTA	suPERFluorinatEd ContrasT Agent
P@BSA	Complex between PERFECTA and bovine serum albumin
P@LYS	Complex between PERFECTA and lysozyme
PET	Positron emission tomography
Phe	Phenylalanine
Phe(F_5)	*N*-Fmoc-pentafluorophenylalanine
Phe(F_4I)	*N*-Fmoc-2,3,5,6-tetrafluoro-4-Iodo-phenylalanine
[Phe(F_5)·BZ]	Cocrystal 1:1 of Phe(F_5) and benzamide
[Phe(F_5)·Na]	Cocrystal of Phe(F_5) and sodium
[Phe(F_4I)·K]	Cocrystal of Phe(F_4I) and potassium
PFC	Perfluorocarbon
PFCE	perfluoro-*n*-crown-*n*-ether
POM	Polar optical microscopy
PXRD	Powder X-ray diffraction
SC-XRD	Single crystal X-ray diffraction
SEM	Scanning electron microscopy
SNR	Signal to noise ratio
T_1	Spin-lattice relaxation time
T_2	Spin-spin relaxation time
TEM	Transmission electron microscopy
RF	Radiofrequency
UV-vis	Ultraviolet-visible
XB	Halogen bond

Bibliography

1. O'Hagan, D. Understanding organofluorine chemistry. An introduction to the C–F bond. *Chem Soc Rev* **37**, 308–319 (2008).

2. Wade, A. D., Rizzi, A., Wang, Y. & Huggins, D. J. Computational Fluorine Scanning Using Free-Energy Perturbation. *J Chem Inf Model* **59**, 2776–2784 (2019).

3. Wermuth, C. G. *The Practice of Medicinal Chemistry*. (Academic Press, 2011).

4. Thiehoff, C., Rey, Y. P. & Gilmour, R. The Fluorine *Gauche* Effect: A Brief History. *Isr J Chem* **57**, 92–100 (2017).

5. Wolfe, S. Gauche effect. Stereochemical consequences of adjacent electron pairs and polar bonds. *Acc Chem Res* **5**, 102–111 (1972).

6. Aufiero, M. & Gilmour, R. Informing Molecular Design by Stereoelectronic Theory: The Fluorine Gauche Effect in Catalysis. *Acc Chem Res* **51**, 1701–1710 (2018).

7. Zimmer, L. E., Sparr, C. & Gilmour, R. Fluorine Conformational Effects in Organocatalysis: An Emerging Strategy for Molecular Design. *Angewandte Chemie International Edition* **50**, 11860–11871 (2011).

8. Cheerlavancha, R., Lawer, A., Cagnes, M., Bhadbhade, M. & Hunter, L. Sequential deoxyfluorination approach for the synthesis of protected α,β,γ-trifluoro-δ-amino acids. *Org Lett* **15**, 5562–5565 (2013).

9. Yamamoto, I. *et al.* The enantiomers of syn-2,3-difluoro-4-aminobutyric acid elicit opposite responses at the GABAC receptor. *Chemical Communications* **48**, 829–831 (2012).

10. Deniau, G. *et al.* Synthesis, conformation and biological evaluation of the enantiomers of 3-fluoro-γ-aminobutyric acid ((R)- and (S)-3F-GABA): An analogue of the neurotransmittter GABA. *ChemBioChem* **8**, 2265–2274 (2007).

11. Mathad, R. I., Gessier, F., Seebach, D. & Jaun, B. The effect of backbone-heteroatom substitution on the folding of peptides - A single fluorine substituent prevents a β-heptapeptide from folding into a 3 14-helix (NMR analysis). *Helv Chim Acta* **88**, 266–280 (2005).

12. Hunter, L. & O'Hagan, D. Multi-vicinal fluoroalkanes: a new class of organofluorine compounds. *Org Biomol Chem* **6**, 2843 (2008).

13. Hunter, L., Kirsch, P., Slawin, A. M. Z. & O'Hagan, D. Synthesis and Structure of Stereoisomeric Multivicinal Hexafluoroalkanes. *Angewandte Chemie* **121**, 5565–5568 (2009).

14. Czajka, A., Hazell, G. & Eastoe, J. Surfactants at the Design Limit. *Langmuir* **31**, 8205–17 (2015).

15. Hussain, S. M. S. *et al.* Fluorinated surfactants: A review on recent progress on synthesis and oilfield applications. *Adv Colloid Interface Sci* **303**, 102634 (2022).

16. Henaut, I., Pasquier, D., Rovinetti, S. & Espagne, B. HP-HT Drilling Mud Based on Environmently-Friendly Fluorinated Chemicals. *Oil and Gas Science and Technology* **70**, 917–930 (2015).

17. Renner, R. The long and the short of perfluorinated replacements. *Environ Sci Technol* **40**, 12–13 (2006).

18. Castelvetro, V., Francini, G., Ciardelli, G. & Ceccato, M. Evaluating Fluorinated Acrylic Latices as Textile Water and Oil Repellent Finishes. *Textile Research Journal* **71**, 399–406 (2001).

19. Satoh, K., Nakazumi, H. & Morita, M. *Surface Modification of Fabrics Using a One-Atmosphere Glow Discharge Plasma to Improve Fabric Wettability*. *Surgery, Gynecol. Obstet* vol. 79 (2004).

20. Zenasni, O., Jamison, A. C. & Lee, T. R. The impact of fluorination on the structure and properties of self-assembled monolayer films. *Soft Matter* **9**, 6356 (2013).

21. Patois, T. *et al.* Microtribological and corrosion behaviors of 1H,1H,2H,2H-perfluorodecanethiol self-assembled films on copper surfaces. *Surf Coat Technol* **205**, 2511–2517 (2010).

22. Wang, M., Liu, H., Li, L. & Cheng, Y. A fluorinated dendrimer achieves excellent gene transfection efficacy at extremely low nitrogen to phosphorus ratios. *Nat Commun* **5**, 1–8 (2014).

23. Cametti, M., Crousse, B., Metrangolo, P., Milani, R. & Resnati, G. The fluorous effect in biomolecular applications. *Chem Soc Rev* **41**, 31–42 (2012).

24. Zhao, Z., Li, P., Li, Y. & Wang, S. Durable thermal fluid super-repellency of elastic fluorine-modified SiO2@sponge composite aerogel. *Chemical Engineering Journal* **454**, (2023).

25. Krafft, M. P. & Riess, J. G. Per- and polyfluorinated substances (PFASs): Environmental challenges. *Curr Opin Colloid Interface Sci* **20**, 192–212 (2015).

26. Alves, A. V., Tsianou, M. & Alexandridis, P. Fluorinated Surfactant Adsorption on Mineral Surfaces: Implications for PFAS Fate and Transport in the Environment. *Surfaces* **3**, 516–566 (2020).

27. Dichiarante, V., Milani, R. & Metrangolo, P. Natural surfactants towards a more sustainable fluorine chemistry. *Green Chemistry* **20**, 13–27 (2018).

28. Fried, J. & Sabo, E. F. 9α-FLUORO DERIVATIVES OF CORTISONE AND HYDROCORTISONE. *J Am Chem Soc* **76**, 1455–1456 (1954).

29. Maienfisch, P., Hall, R. G. & Maienfisch, P. The Importance of Fluorine in the Life Science Industry. *Chimia (Aarau)* **58**, 93–99 (2004).

30. Hodgetts, K. J., Combs, K. J., Elder, A. M. & Harriman, G. C. The Role of Fluorine in the Discovery and Optimization of CNS Agents. in *Annual Reports in Medicinal Chemistry* vol. 45 429–448 (2010).

31. Park, B. K. & Kitteringham, N. R. Effects of Fluorine Substitution on Drug Metabolism: Pharmacological and Toxicological Implications. *Drug Metab Rev* **26**, 605–643 (1994).

32. Shah, P. & Westwell, A. D. The role of fluorine in medicinal chemistry. *J Enzyme Inhib Med Chem* **22**, 527–540 (2007).

33. Gillis, E. P., Eastman, K. J., Hill, M. D., Donnelly, D. J. & Meanwell, N. A. Applications of Fluorine in Medicinal Chemistry. *J Med Chem* **58**, 8315–8359 (2015).

34. Inoue, M., Sumii, Y. & Shibata, N. Contribution of Organofluorine Compounds to Pharmaceuticals. *ACS Omega* **5**, 10633–10640 (2020).

35. Sheikhi, N., Bahraminejad, M., Saeedi, M. & Mirfazli, S. S. A review: FDA-approved fluorine-containing small molecules from 2015 to 2022. *Eur J Med Chem* **260**, 115758 (2023).

36. Monkovic, J. M., Gibson, H., Sun, J. W. & Montclare, J. K. Fluorinated Protein and Peptide Materials for Biomedical Applications. *Pharmaceuticals* **15**, 1201 (2022).

37. Vicente, A. M., Ballensiefen, W. & Jönsson, J. I. How personalised medicine will transform healthcare by 2030: The ICPerMed vision. *J Transl Med* **18**, (2020).

38. Campbell, E., Jordan, C. & Gilmour, R. Fluorinated carbohydrates for ^{18}F-positron emission tomography (PET). *Chem Soc Rev* **52**, 3599–3626 (2023).

39. Herholz, K. & Heiss, W. D. Positron emission tomography in clinical neurology. *Mol Imaging Biol* **6**, 239–269 (2004).

40. Cho, M. H. *et al.* Targeted, Stimuli-Responsive, and Theranostic 19F Magnetic Resonance Imaging Probes. *Bioconjug Chem* **30**, 2502–2518 (2019).

41. Li, Y. *et al.* ^{19}F MRI Nanotheranostics for Cancer Management: Progress and Prospects. *ChemMedChem* **17**, (2022).

42. Lohrke, J. *et al.* 25 Years of Contrast-Enhanced MRI: Developments, Current Challenges and Future Perspectives. *Adv Ther* **33**, 1–28 (2016).

43. Alzola-Aldamizetxebarria, S., Fernández-Méndez, L., Padro, D., Ruíz-Cabello, J. & Ramos-Cabrer, P. A Comprehensive Introduction to Magnetic Resonance Imaging Relaxometry and Contrast Agents. *ACS Omega* **7**, 36905–36917 (2022).

44. Attari, H., Cao, Y., Elmholdt, T. R., Zhao, Y. & Prince, M. R. A Systematic Review of 639 Patients with Biopsy-confirmed Nephrogenic Systemic Fibrosis. *Radiology* **292**, 376–386 (2019).

45. Yim, H., Seo, S. & Na, K. MRI Contrast Agent-Based Multifunctional Materials: Diagnosis and Therapy. *J Nanomater* **2011**, 1–11 (2011).

46. Tirotta, I. *et al.* ^{19}F Magnetic Resonance Imaging (MRI): From Design of Materials to Clinical Applications. *Chem Rev* **115**, 1106–1129 (2015).

47. Ruiz-Cabello, J., Barnett, B. P., Bottomley, P. A. & Bulte, J. W. M. Fluorine (^{19}F) MRS and MRI in biomedicine. *NMR Biomed* **24**, 114–129 (2011).

48. Holland, G. N., Bottomley, P. A. & Hinshaw, W. S. 19F magnetic resonance imaging. *Journal of Magnetic Resonance (1969)* **28**, 133–136 (1977).

49. Weibel, S. *et al.* Imaging of Intratumoral Inflammation during Oncolytic Virotherapy of Tumors by 19F-Magnetic Resonance Imaging (MRI). *PLoS One* **8**, (2013).

50. Bidhult, S. *et al.* Validation of T1 and T2 algorithms for quantitative MRI: Performance by a vendor-independent software. *BMC Med Imaging* **16**, (2016).

51. Ashur, I., Allouche-Arnon, H. & Bar-Shir, A. Calcium Fluoride Nanocrystals: Tracers for In Vivo 19 F Magnetic Resonance Imaging . *Angewandte Chemie* **130**, 7600–7604 (2018).

52. Chalmers, K. H. *et al.* Design principles and theory of paramagnetic fluorine-labelled lanthanide complexes as probes for19F magnetic resonance: a proof-of-concept study. *Chemistry - A European Journal* **16**, 134–148 (2010).

53. Chalmers, K. H., Kenwright, A. M., Parker, D. & Blamire, A. M. 19F-lanthanide complexes with increased sensitivity for 19F-MRI: Optimization of the MR acquisition. *Magn Reson Med* **66**, 931–936 (2011).

54. Kotková, Z. *et al.* Copper(ii) complexes of cyclams with N-(2,2,2-trifluoroethyl)-aminoalkyl pendant arms as potential probes for 19F magnetic resonance imaging. *Dalton Transactions* **52**, 1861–1875 (2022).

55. Zhang, C. *et al.* Biological Utility of Fluorinated Compounds: from Materials Design to Molecular Imaging, Therapeutics and Environmental Remediation. *Chem Rev* **122**, 167–208 (2022).

56. Mattrey, R. F. *et al.* Perflubron as an oral contrast agent for MR imaging: results of a phase III clinical trial. *Radiology* **191**, 841–848 (1994).

57. Chirizzi, C. *et al.* Multispectral MRI with dual fluorinated probes to track mononuclear cell activity in mice. *Radiology* **291**, 351–357 (2019).

58. Janjic, J. M., Srinivas, M., Kadayakkara, D. K. K. & Ahrens, E. T. Self-delivering nanoemulsions for dual fluorine-19 MRI and fluorescence detection. *J Am Chem Soc* **130**, 2832–2841 (2008).

59. Krafft, M. P. & Riess, J. G. Perfluorocarbons: Life sciences and biomedical uses dedicated to the memory of Professor Guy Ourisson, a true RENAISSANCE man. *J Polym Sci A Polym Chem* **45**, 1185–1198 (2007).

60. Fernando Bonetto *et al.* A novel 19F agent for detection and quantification of human dendritic cells using magnetic resonance imaging. *Int J Cancer* **129**, 365–373 (2011).

61. Ahrens, E. T., Flores, R., Xu, H. & Morel, P. A. In vivo imaging platform for tracking immunotherapeutic cells. *Nat Biotechnol* **23**, 983–987 (2005).

62. Tirotta, I. *et al.* A Superfluorinated Molecular Probe for Highly Sensitive *in Vivo* ^{19} F-MRI. *J Am Chem Soc* **136**, 8524–8527 (2014).

63. Yue, X., Taraban, M. B., Hyland, L. L. & Yu, Y. B. Avoiding steric congestion in dendrimer growth through proportionate branching: A twist on da Vincis rule of tree branching. *Journal of Organic Chemistry* **77**, 8879–8887 (2012).

64. Krafft, M. P. & Riess, J. G. Selected physicochemical aspects of poly- and perfluoroalkylated substances relevant to performance, environment and sustainability-Part one. *Chemosphere* **129**, 4–19 (2015).

65. Chirizzi, C. *et al.* A bioorthogonal probe for multiscale imaging by 19F-MRI and Raman Microscopy: From whole body to single cells. *J Am Chem Soc* **143**, (2021).

66. Krafft, C. *et al.* Label-Free Molecular Imaging of Biological Cells and Tissues by Linear and Nonlinear Raman Spectroscopic Approaches. *Angewandte Chemie International Edition* **56**, 4392–4430 (2017).

67. Yamakoshi, H. *et al.* Alkyne-tag Raman imaging for visualization of mobile small molecules in live cells. *J Am Chem Soc* **134**, 20681–20689 (2012).

68. Vanna, R. *et al.* Raman spectroscopy reveals that biochemical composition of breast microcalcifications correlates with histopathologic features. *Cancer Res* **80**, 1762–1772 (2020).

69. Zhao, Z. *et al.* Ultra-bright Raman dots for multiplexed optical imaging. *Nat Commun* **12**, (2021).

70. Egli, M. The steric hypothesis for DNA replication and fluorine hydrogen bonding revisited in light of structural data. *Acc Chem Res* **45**, 1237–1246 (2012).

71. Linclau, B. *et al.* Fluorinated carbohydrates as chemical probes for molecular recognition studies. Current status and perspectives. *Chem Soc Rev* **49**, 3863–3888 (2020).

72. Bucher, C. & Gilmour, R. A Modular Synthesis of Fluorinated, Chiral Polar Lipids. *Synthesis (Stuttg)* **2011**, 549–552 (2011).

73. Preslar, A. T. *et al.* Calcium-Induced Morphological Transitions in Peptide Amphiphiles Detected by ^{19} F-Magnetic Resonance Imaging. *ACS Appl Mater Interfaces* **9**, 39890–39894 (2017).

74. Hingorani, D. V. *et al.* Cell penetrating peptide functionalized perfluorocarbon nanoemulsions for targeted cell labeling and enhanced fluorine-19 MRI detection. *Magn Reson Med* **83**, 974–987 (2020).

75. Giroud, M. *et al.* Fluorine Scan of Inhibitors of the Cysteine Protease Human Cathepsin L: Dipolar and Quadrupolar Effects in the π-Stacking of Fluorinated Phenyl Rings on Peptide Amide Bonds. *ChemMedChem* **11**, 1042–1047 (2016).

76. Burade, S. S. *et al.* Self-Assembly of Fluorinated Sugar Amino Acid Derived α,γ-Cyclic Peptides into Transmembrane Anion Transport. *Org Lett* **19**, 5948–5951 (2017).

77. Miles, S. A., Nillama, J. A. & Hunter, L. Tinker, Tailor, Soldier, Spy: The Diverse Roles That Fluorine Can Play within Amino Acid Side Chains. *Molecules* **28**, 6192 (2023).

78. Berger, A. A., Völler, J. S., Budisa, N. & Koksch, B. Deciphering the Fluorine Code - The Many Hats Fluorine Wears in a Protein Environment. *Acc Chem Res* **50**, 2093–2103 (2017).

79. Sloand, J. N., Miller, M. A. & Medina, S. H. Fluorinated peptide biomaterials. *Peptide Science* **113**, (2021).

80. Botz, A. *et al.* (R)-a-Trifluoromethylalanine Containing Short Peptide in the Inhibition of Amyloid Peptide Fibrillation. *Biopolymers* **104**, 601–610 (2015).

81. Zhou, M., Feng, Z. & Zhang, X. Recent advances in the synthesis of fluorinated amino acids and peptides. *Chemical Communications* **59**, 1434–1448 (2023).

82. Moschner, J. *et al.* Approaches to Obtaining Fluorinated α-Amino Acids. *Chem Rev* **119**, 10718–10801 (2019).

83. March, T. L., Johnston, M. R., Duggan, P. J. & Gardiner, J. Synthesis, Structure, and Biological Applications of α -Fluorinated β -Amino Acids and Derivatives. *Chem Biodivers* **9**, 2410–2441 (2012).

84. Luis Acena, J., Simon-Fuentes, A. & Fustero, S. Recent Developments in the Synthesis of Fluorinated Amino Acids. *Curr Org Chem* **14**, 928–949 (2010).

85. Larsson, R., Dhar, S., Ehrsson, H., Nygren, P. & Lewensohn, R. Comparison of the cytotoxic activity of melphalan with L-prolyl-m-L-sarcolysyl-L-p-fluorophenylalanine in human tumour cell lines and primary cultures of tumour cells from patients. *Br J Cancer* **78**, 328–335 (1998).

86. Dhillon, S. Melphalan Flufenamide (Melflufen): First Approval. *Drugs* **81**, 963–969 (2021).

87. Vine, W. H., Hsieh, K.-H. & Marshall, G. R. Synthesis of fluorine-containing peptides. Analogs of angiotensin II containing hexafluorovaline. *J Med Chem* **24**, 1043–1047 (1981).

88. Huhmann, S. & Koksch, B. Fine-Tuning the Proteolytic Stability of Peptides with Fluorinated Amino Acids. *European J Org Chem* **2018**, 3667–3679 (2018).

89. Deniau, G. *et al.* Synthesis, Conformation and Biological Evaluation of the Enantiomers of 3-Fluoro-γ-Aminobutyric Acid ((*R*)- and (*S*)-3F-GABA): An Analogue of the Neurotransmitter GABA. *ChemBioChem* **8**, 2265–2274 (2007).

90. Chia, P. W. *et al.* 3-Fluoro-N-methyl-D-aspartic acid (3F-NMDA) stereoisomers as conformational probes for exploring agonist binding at NMDA receptors. *Chemistry - A European Journal* **18**, 8813–8819 (2012).

91. Müller, K., Faeh, C. & Diederich, F. Fluorine in Pharmaceuticals: Looking Beyond Intuition. *Science (1979)* **317**, 1881–1886 (2007).

92. He, T. *et al.* Fluorinated aromatic amino acids distinguish cation-π interactions from membrane insertion. *Journal of Biological Chemistry* **290**, 19334–19342 (2015).

93. Jin, C. *et al.* Interaction of Halogenated Tyrosine/Phenylalanine Derivatives with Organic Anion Transporter 1 in the Renal Handling of Tumor Imaging Probes. *Journal of Pharmacology and Experimental Therapeutics* **375**, 451–462 (2020).

94. Giménez, D. *et al.* The introduction of fluorine atoms or trifluoromethyl groups in short cationic peptides enhances their antimicrobial activity. *Bioorg Med Chem* **14**, 6971–6978 (2006).

95. Setty, S. C., Horam, S., Pasupuleti, M. & Haq, W. Modulating the Antimicrobial Activity of Temporin L Through Introduction of Fluorinated Phenylalanine. *Int J Pept Res Ther* **23**, 213–225 (2017).

96. Rajbhandary, A., Raymond, D. M. & Nilsson, B. L. Self-Assembly, Hydrogelation, and Nanotube Formation by Cation-Modified Phenylalanine Derivatives. *Langmuir* **33**, 5803–5813 (2017).

97. Ryan, D. M., Doran, T. M., Anderson, S. B. & Nilsson, B. L. Effect of C-terminal modification on the self-assembly and hydrogelation of fluorinated Fmoc-Phe derivatives. *Langmuir* **27**, 4029–4039 (2011).

98. Raymond, D. M. *et al.* Low-Molecular-Weight Supramolecular Hydrogels for Sustained and Localized in Vivo Drug Delivery. *ACS Appl Bio Mater* **2**, 2116–2124 (2019).

99. Liyanage, W., Vats, K., Rajbhandary, A., Benoit, D. S. W. & Nilsson, B. L. Multicomponent dipeptide hydrogels as extracellular matrix-mimetic scaffolds for cell culture applications. *Chemical Communications* **51**, 11260–11263 (2015).

100. Schnaider, L. *et al.* Enhanced Nanoassembly-Incorporated Antibacterial Composite Materials. *ACS Appl Mater Interfaces* **11**, 21334–21342 (2019).

101. Yuran, S., Dolid, A. & Reches, M. Resisting Bacteria and Attracting Cells: Spontaneous Formation of a Bifunctional Peptide-Based Coating by On-Surface Assembly Approach. *ACS Biomater Sci Eng* **4**, 4051–4061 (2018).

102. Langen, K.-J. *et al.* O-(2-[18F]fluoroethyl)-l-tyrosine: uptake mechanisms and clinical applications. *Nucl Med Biol* **33**, 287–294 (2006).

103. Wei, X., Wang, Q. & Liu, C. Nanopore sensing of γ-cyclodextrin induced host-guest interaction to reverse the binding of perfluorooctanoic acid to human serum albumin. *Proteomics* **22**, (2022).

104. Verreault, J. *et al.* Perfluorinated alkyl substances in plasma, liver, brain, and eggs of glaucous gulls (Larus hyperboreus) from the Norwegian Arctic. *Environ Sci Technol* **39**, 7439–7445 (2005).

105. Di Giosia, M., Zerbetto, F. & Calvaresi, M. Incorporation of Molecular Nanoparticles Inside Proteins: The Trojan Horse Approach in Theranostics. *Acc Mater Res* **2**, 594–605 (2021).

106. Di Giosia, M. *et al.* Proteins as supramolecular hosts for C60: A true solution of C60 in water. *Nanoscale* **10**, 9908–9916 (2018).

107. Lu, R. C., Cao, A. N., Lai, L. H. & Xiao, J. X. Protein-surfactant interaction: Differences between fluorinated and hydrogenated surfactants. *Colloids Surf B Biointerfaces* **64**, 98–103 (2008).

108. Gao, S., Cao, Z., Niu, Q., Zong, W. & Liu, R. Probing the toxicity of long-chain fluorinated surfactants: Interaction mechanism between perfluorodecanoic acid and lysozyme. *J Mol Liq* **285**, 607–615 (2019).

109. Ciurleo, A. *et al.* Some properties of lysozyme - Lithium perfluorononanoate complexes. *Biomacromolecules* **8**, 399–405 (2007).

110. Scanavachi, G. *et al.* Aggregation features of partially unfolded bovine serum albumin modulated by hydrogenated and fluorinated surfactants: Molecular dynamics insights and experimental approaches. *J Colloid Interface Sci* **572**, 9–21 (2020).

111. Gazzera, L. *et al.* Design of Highly Stable Echogenic Microbubbles through Controlled Assembly of Their Hydrophobin Shell. *Angewandte Chemie - International Edition* **55**, 10263–10267 (2016).

112. Ayaz, N. *et al.* Hydrophobin-Coated Solid Fluorinated Nanoparticles for 19F-MRI. *Adv Mater Interfaces* **9**, (2022).

113. Zhang, S. Emerging biological materials through molecular self-assembly. *Biotechnol Adv* **20**, 321–339 (2002).

114. Biswas, A. *et al.* Advances in top-down and bottom-up surface nanofabrication: Techniques, applications & future prospects. *Advances in Colloid and Interface Science* vol. 170 2–27 Preprint at https://doi.org/10.1016/j.cis.2011.11.001 (2012).

115. Huie, J. C. Guided molecular self-assembly: a review of recent efforts. *Smart Mater Struct* **12**, 264–271 (2003).

116. Ramanathan, M. *et al.* Amphiphile nanoarchitectonics: from basic physical chemistry to advanced applications. *Physical Chemistry Chemical Physics* **15**, 10580 (2013).

117. Kumar, A. *et al.* Self-Assembly and Transport Behaviour of Non-ionic Fluorinated and Alkylated Amphiphiles for Drug Delivery. *ChemistrySelect* **7**, (2022).

118. Ghosh, S., Ray, A. & Pramanik, N. Self-assembly of surfactants: An overview on general aspects of amphiphiles. *Biophys Chem* **265**, 106429 (2020).

119. Sun, Q. The physical origin of hydrophobic effects. *Chem Phys Lett* **672**, 21–25 (2017).

120. Lombardo, D., Kiselev, M. A., Magazù, S. & Calandra, P. Amphiphiles Self-Assembly: Basic Concepts and Future Perspectives of Supramolecular Approaches. *Advances in Condensed Matter Physics* **2015**, 1–22 (2015).

121. Nagarajan, R. & Ruckenstein, E. Theory of surfactant self-assembly: a predictive molecular thermodynamic approach. *Langmuir* **7**, 2934–2969 (1991).

122. Nagarajan, R. Molecular packing parameter and surfactant self-assembly: The neglected role of the surfactant tail. *Langmuir* **18**, 31–38 (2002).

123. Ricardo C. Pasquali, Natalia Sacco & Carlos Bregni. The Studies on Hydrophilic-Lipophilic Balance (HLB): Sixty Years after William C. Griffin's Pioneer Work (1949-2009). *Lat. Am. J. Pharm* **28**, 313–317 (2009).

124. Griffin, W. C. Calculation of HLB Values of Non-Ionic Surfactants. *J Soc Cosmet Chem* **5**, 235–249 (1954).

125. Salim, M., Minamikawa, H., Sugimura, A. & Hashim, R. Amphiphilic designer nano-carriers for controlled release: from drug delivery to diagnostics. *Med. Chem. Commun.* **5**, 1602–1618 (2014).

126. Kanicky, J., Lopez-Montilla, J.-C., Pandey, S. & Shah, D. Surface Chemistry in the Petroleum Industry. in *Handbook of Applied Surface and Colloid Chemistry* (2001).

127. Sevink, G. J. A. & Zvelindovsky, A. V. Self-assembly of complex vesicles. *Macromolecules* **38**, 7502–7513 (2005).

128. Tomalia, D. A. Dendritic effects: dependency of dendritic nano-periodic property patterns on critical nanoscale design parameters (CNDPs). *New J. Chem.* **36**, 264–281 (2012).

129. Lee, C. C., MacKay, J. A., Fréchet, J. M. J. & Szoka, F. C. Designing dendrimers for biological applications. *Nat Biotechnol* **23**, 1517–1526 (2005).

130. Patel, V., Patel, P., Patel, J. V. & Patel, P. M. Dendrimer as a versatile platform for biomedical application: A review. *Journal of the Indian Chemical Society* **99**, 100516 (2022).

131. Rosen, B. M. *et al.* Dendron-mediated self-assembly, disassembly, and self-organization of complex systems. *Chem Rev* **109**, 6275–6540 (2009).

132. Thota, B. N. S., Urner, L. H. & Haag, R. Supramolecular Architectures of Dendritic Amphiphiles in Water. *Chem Rev* **116**, 2079–2102 (2016).

133. Percec, V. *et al.* Self-Assembly of Janus Dendrimers into Uniform Dendrimersomes and Other Complex Architectures. *Science (1979)* **328**, 1009–1014 (2010).

134. Filippi, M. *et al.* First in vivo MRI study on theranostic dendrimersomes. *Journal of Controlled Release* **248**, 45–52 (2017).

135. Filippi, M. *et al.* Novel stable dendrimersome formulation for safe bioimaging applications. *Nanoscale* **7**, 12943–12954 (2015).

136. Krafft, M. P. & Riess, J. G. Highly fluorinated amphiphiles and colloidal systems, and their applications in the biomedical field. A contribution. *Biochimie* **80**, 489–514 (1998).

137. Dichiarante, V. *et al.* Superfluorinated and NIR-luminescent gold nanoclusters. *Chemical Communications* **53**, 621–624 (2017).

138. Rosati, M. *et al.* Janus-Type Dendrimers Based on Highly Branched Fluorinated Chains with Tunable Self-Assembly and 19F Nuclear Magnetic Resonance Properties. *Macromolecules* **55**, 2486–2496 (2022).

139. Krafft`institut, M. P. Fluorocarbons and fluorinated amphiphiles in drug delivery and biomedical research. *Adv Drug Deliv Rev* **47**, 209–228 (2001).

140. Caminade, A.-M., Turrin, C.-O., Sutra, P. & Majoral, J.-P. Fluorinated dendrimers. *Curr Opin Colloid Interface Sci* **8**, 282–295 (2003).

141. Khayet, M., García-Payo, C. & Matsuura, T. Superhydrophobic nanofibers electrospun by surface segregating fluorinated amphiphilic additive for membrane distillation. *J Memb Sci* **588**, (2019).

142. Wang, M., Xue, H., Gao, M., Wang, Q. & Yang, H. Synthetic fluorinated polyamides as efficient gene vectors. *J Biomed Mater Res B Appl Biomater* **107**, 2132–2139 (2019).

143. McMahon, M. T. & Bulte, J. W. M. Two decades of dendrimers as versatile MRI agents: a tale with and without metals. *Wiley Interdiscip Rev Nanomed Nanobiotechnol* **10**, (2018).

144. Wang, M. & Cheng, Y. The effect of fluorination on the transfection efficacy of surface-engineered dendrimers. *Biomaterials* **35**, 6603–6613 (2014).

145. Wang, H., Hu, J., Cai, X., Xiao, J. & Cheng, Y. Self-assembled fluorodendrimers in the co-delivery of fluorinated drugs and therapeutic genes. *Polym Chem* **7**, 2319–2322 (2016).

146. Percec, V., Glodde, M., Johansson, G., Balagurusamy, V. S. K. & Heinev, P. A. Transformation of a spherical supramolecular dendrimer into a pyramidal columnar supramolecular dendrimer mediated by the fluorophobic effect. *Angewandte Chemie - International Edition* **42**, 4338–4342 (2003).

147. Tomalia, D. A. Fluorine makes a difference. *Nat Mater* **2**, 711–712 (2003).

148. Percec, V. *et al.* Self-organization of supramolecular helical dendrimers into complex electronic materials. *Nature* **417**, 384–387 (2002).

149. Omar, J., Ponsford, D., Dreiss, C. A., Lee, T. & Loh, X. J. Supramolecular Hydrogels: Design Strategies and Contemporary Biomedical Applications. *Chem Asian J* **17**, (2022).

150. Draper, E. R. & Adams, D. J. Low-Molecular-Weight Gels: The State of the Art. *Chem* **3**, 390–410 (2017).

151. Wang, C., Luo, Y., Cao, X., Li, B. & Luo, Z. Supramolecular polyurea hydrogels with anti-swelling capacity, reversible thermochromic properties, and tunable water content and mechanical performance. *Polymer (Guildf)* **233**, (2021).

152. Draper, E. R. *et al.* Hydrogels formed from Fmoc amino acids. *CrystEngComm* **17**, 8047–8057 (2015).

153. Dawn, A. Supramolecular Gel as the Template for Catalysis, Inorganic Superstructure, and Pharmaceutical Crystallization. *Int J Mol Sci* **20**, 781 (2019).

154. Tao, K., Levin, A., Adler-Abramovich, L. & Gazit, E. Fmoc-modified amino acids and short peptides: simple bio-inspired building blocks for the fabrication of functional materials. *Chem Soc Rev* **45**, 3935–3953 (2016).

155. de Loos, M., Feringa, B. L. & van Esch, J. H. Design and Application of Self-Assembled Low Molecular Weight Hydrogels. *European J Org Chem* **2005**, 3615–3631 (2005).

156. Johnson, E. K., Adams, D. J. & Cameron, P. J. Peptide based low molecular weight gelators. *J Mater Chem* **21**, 2024–2027 (2011).

157. Demirel, G., Malvadkar, N. & Demirel, M. C. Control of protein adsorption onto core-shell tubular and vesicular structures of diphenylalanine/parylene. *Langmuir* **26**, 1460–1463 (2010).

158. Reches, M. & Gazit, E. Controlled patterning of aligned self-assembled peptide nanotubes. *Nat Nanotechnol* **1**, 195–200 (2006).

159. Smith, A. M. *et al.* Fmoc-diphenylalanine self assembles to a hydrogel via a novel architecture based on π-π interlocked β-sheets. *Advanced Materials* **20**, 37–41 (2008).

160. Mahler, A., Reches, M., Rechter, M., Cohen, S. & Gazit, E. Rigid, self-assembled hydrogel composed of a modified aromatic dipeptide. *Advanced Materials* **18**, 1365–1370 (2006).

161. Orbach, R. *et al.* The rheological and structural properties of Fmoc-peptide-based hydrogels: The effect of aromatic molecular architecture on self-assembly and physical characteristics. *Langmuir* **28**, 2015–2022 (2012).

162. Singh, V., Snigdha, K., Singh, C., Sinha, N. & Thakur, A. K. Understanding the self-assembly of Fmoc-phenylalanine to hydrogel formation. *Soft Matter* **11**, 5353–5364 (2015).

163. Ryan, D. M., Anderson, S. B., Senguen, F. T., Youngman, R. E. & Nilsson, B. L. Self-assembly and hydrogelation promoted by F5-phenylalanine. *Soft Matter* **6**, 475–479 (2010).

164. Ryan, D. M., Anderson, S. B. & Nilsson, B. L. The influence of side-chain halogenation on the self-assembly and hydrogelation of Fmoc-phenylalanine derivatives. *Soft Matter* **6**, 3220–3231 (2010).

165. Ji, W. *et al.* Coassembly-Induced Transformation of Dipeptide Amyloid-Like Structures into Stimuli-Responsive Supramolecular Materials. *ACS Nano* **14**, 7181–7190 (2020).

166. Ryan, D. M., Doran, T. M. & Nilsson, B. L. Stabilizing self-assembled Fmoc-F5-Phe hydrogels by co-assembly with PEG-functionalized monomers. *Chemical Communications* **47**, 475–477 (2011).

167. Abraham, B. L., Agredo, P., Mensah, S. G. & Nilsson, B. L. Anion Effects on the Supramolecular Self-Assembly of Cationic Phenylalanine Derivatives. *Langmuir* **38**, 15494–15505 (2022).

168. Lu, H. *et al.* Fluorine Substitution Tunes the Nanofiber Chirality of Supramolecular Hydrogels to Promote Cell Adhesion and Proliferation. *Advanced Fiber Materials* **5**, 377–387 (2023).

169. Aviv, M. *et al.* Modification of a single atom affects the physical properties of double fluorinated fmoc-phe derivatives. *Int J Mol Sci* **22**, (2021).

170. Pace, C. J. & Gao, J. Exploring and Exploiting Polar−π Interactions with Fluorinated Aromatic Amino Acids. *Acc Chem Res* **46**, 907–915 (2013).

171. Wheeler, S. E. & Houk, K. N. Through-Space Effects of Substituents Dominate Molecular Electrostatic Potentials of Substituted Arenes. *J Chem Theory Comput* **5**, 2301–2312 (2009).

172. Raymond, D. M. & Nilsson, B. L. Multicomponent peptide assemblies. *Chem Soc Rev* **47**, 3659–3720 (2018).

173. Zhang, H., Lou, S. & Yu, Z. Polar-π Interactions Promote Self-assembly of Dipeptides into Laminated Nanofibers. *Langmuir* **35**, 4710–4717 (2019).

174. Halperin-Sternfeld, M., Ghosh, M., Sevostianov, R., Grigoriants, I. & Adler-Abramovich, L. Molecular co-assembly as a strategy for synergistic improvement of the mechanical properties of hydrogels. *Chemical Communications* **53**, 9586–9589 (2017).

175. Berlepsch, H. V. *et al.* Controlled self-assembly of stomatosomes by use of single-component fluorinated dendritic amphiphiles. *Soft Matter* **14**, 5256–5269 (2018).

176. Rashmi, R. *et al.* Supramolecular Engineering of Alkylated, Fluorinated, and Mixed Amphiphiles. *Macromol Rapid Commun* **43**, (2022).

177. Guitton-Spassky, T. *et al.* Fluorinated dendritic amphiphiles, their stomatosome aggregates and application in enzyme encapsulation. *Nanoscale* **15**, 7781–7791 (2023).

178. Zieringer, M. *et al.* Size-tunable micron-bubbles based on fluorous-fluorous interactions of perfluorinated dendritic polyglycerols. *ChemPhysChem* **11**, 2617–2622 (2010).

179. Garcia-Bernabé, A., Tzschucke, C. C., Bannwarth, W. & Haag, R. Supramolecular immobilization of a perfluoro-tagged Pd-catalyst with dendritic architectures and application in Suzuki reactions. *Adv Synth Catal* **347**, 1389–1394 (2005).

180. Dichiarante, V. *et al.* A Short-Chain Multibranched Perfluoroalkyl Thiol for More Sustainable Hydrophobic Coatings. *ACS Sustain Chem Eng* **6**, 9734–9743 (2018).

181. Singh, A. K. *et al.* Synthesis and Linker-Controlled Self-Assembly of Dendritic Amphiphiles with Branched Fluorinated Tails. *Macromol Biosci* **22**, (2022).

182. Paulus, F. *et al.* The effect of polyglycerol sulfate branching on inflammatory processes. *Macromol Biosci* **14**, 643–654 (2014).

183. Cherri, M. *et al.* Biodegradable Dendritic Polyglycerol Sulfate for the Delivery and Tumor Accumulation of Cytostatic Anticancer Drugs. *ACS Biomater Sci Eng* **7**, 2569–2579 (2021).

184. Silberreis, K., Niesler, N., Rades, N., Haag, R. & Dernedde, J. Sulfated Dendritic Polyglycerol Is a Potent Complement Inhibitor. *Biomacromolecules* **20**, 3809–3818 (2019).

185. Ferraro, M. *et al.* Biodegradable Polyglycerol Sulfates Exhibit Promising Features for Anti-inflammatory Applications. *Biomacromolecules* **19**, 4524–4533 (2018).

186. Rades, N., Licha, K. & Haag, R. Dendritic Polyglycerol Sulfate for Therapy and Diagnostics. *Polymers (Basel)* **10**, 595 (2018).

187. Türk, H., Haag, R. & Alban, S. Dendritic Polyglycerol Sulfates as New Heparin Analogues and Potent Inhibitors of the Complement System. *Bioconjug Chem* **15**, 162–167 (2004).

188. Licha, K. *et al.* Fluorescence Imaging with Multifunctional Polyglycerol Sulfates: Novel Polymeric near-IR Probes Targeting Inflammation. *Bioconjug Chem* **22**, 2453–2460 (2011).

189. Bujacz, A. Structures of bovine, equine and leporine serum albumin. *Acta Crystallogr D Biol Crystallogr* **68**, 1278–1289 (2012).

190. Xu, X. *et al.* Applications of human and bovine serum albumins in biomedical engineering: A review. *Int J Biol Macromol* **253**, 126914 (2023).

191. Peters, T. *All About Albumin: Biochemistry, Genetics, and Medical Applications*. (Elsevier Science, 1995).

192. Swaminathan, R., Ravi, V. K., Kumar, S., Kumar, M. V. S. & Chandra, N. Lysozyme: A Model Protein for Amyloid Research. in *Advances in Protein Chemistry and Structural Biology* vol. 84 63–111 (Academic Press Inc., 2011).

193. Di Giosia, M. *et al.* A Bio-Conjugated Fullerene as a Subcellular-Targeted and Multifaceted Phototheranostic Agent. *Adv Funct Mater* **31**, (2021).

194. Spector, A. A., John, K. & Fletcher, J. E. Binding of long-chain fatty acids to bovine serum albumin. *J Lipid Res* **10**, 56–67 (1969).

195. Chirizzi, C. *et al.* Optimization of superfluorinated PLGA nanoparticles for enhanced cell labelling and detection by 19F-MRI. *Colloids Surf B Biointerfaces* **220**, (2022).

196. Fleige, E., Ziem, B., Grabolle, M., Haag, R. & Resch-Genger, U. Aggregation Phenomena of Host and Guest upon the Loading of Dendritic Core-Multishell Nanoparticles with Solvatochromic Dyes. *Macromolecules* **45**, 9452–9459 (2012).

197. Petit, F., Iliopoulos, I. & Audebert, R. Aggregation of associating polymers studied by 19F n.m.r. *Polymer (Guildf)* **39**, 751–753 (1998).

198. Wang, X. *et al.* Monitoring the different micelle species and the slow kinetics of tetraethylammonium perfluorooctane-sulfonate by 19F NMR spectroscopy. *Adv Colloid Interface Sci* **246**, 153–164 (2017).

199. Iliopoulos, I. & Furó, I. NMR Study of the Association of Anionic Surfactants with an Anionic Polyelectrolyte Hydrophobically Modified with Perfluorinated Side Chains. *Langmuir* **17**, 8049–8054 (2001).

200. Huc, I. & Oda, R. Gemini surfactants: studying micellisation by 1H and 19F NMR spectroscopy. *Chemical Communications* 2025–2026 (1999) doi:10.1039/a906141j.

201. Ayaz, N. *et al.* Hydrophobin-Coated Solid Fluorinated Nanoparticles for 19F-MRI. *Adv Mater Interfaces* **9**, (2022).

202. Wright, A. K. & Thompson, M. R. Hydrodynamic structure of bovine serum albumin determined by transient electric birefringence. *Biophys J* **15**, 137–141 (1975).

203. Cegielska-Radziejewska, R., Leśnierowski, G. & Kijowski, J. Properties and Applicagtion of Egg White Lysozyme and its Modified Preparations – A Review. *Pol J Food Nutr Sci* **58**, 5–10 (2008).

204. Güler, G., Vorob'ev, M. M., Vogel, V. & Mäntele, W. Proteolytically-induced changes of secondary structural protein conformation of bovine serum albumin monitored by Fourier transform infrared (FT-IR) and UV-circular dichroism spectroscopy. *Spectrochim Acta A Mol Biomol Spectrosc* **161**, 8–18 (2016).

205. Tokunaga, Y., Sakakibara, Y., Kamada, Y., Watanabe, K. & Sugimoto, Y. Analysis of Core Region from Egg White Lysozyme Forming Amyloid Fibrils. *Int J Biol Sci* **9**, 219–227 (2013).

206. Cao, A. Formation of amyloid fibrils from fully reduced hen egg white lysozyme. *Protein Science* **13**, 319–324 (2004).

207. Mitra, A., Mitra, A. & Sarkar, N. Differential effects of DTT on HEWL amyloid fibrillation and fibril morphology at different pH. *Biophys Chem* **294**, (2023).

208. Natalello, A. & Doglia, S. M. Insoluble Protein Assemblies Characterized by Fourier Transform Infrared Spectroscopy. in *Methods in Molecular Biology* vol. 1258 347–369 (Humana Press Inc., 2015).

209. Pakdel, M., Moosavi-Nejad, Z., Kermanshahi, R. K. & Hosano, H. Self-assembled uniform keratin nanoparticles as building blocks for nanofibrils and nanolayers derived from industrial feather waste. *J Clean Prod* **335**, (2022).

210. Mikalauskaite, K., Ziaunys, M. & Smirnovas, V. Lysozyme Amyloid Fibril Structural Variability Dependence on Initial Protein Folding State. *Int J Mol Sci* **23**, 5421 (2022).

211. Ochbaum, G. & Bitton, R. Using small-angle X-ray scattering (SAXS) to study the structure of self-assembling biomaterials. in *Self-assembling Biomaterials* 291–304 (Elsevier, 2018). doi:10.1016/B978-0-08-102015-9.00015-0.

212. Pai, S. S. *et al.* The conformation of the poly(ethylene glycol) chain in mono-PEGylated Lysozyme and mono-PEGylated human growth hormone. *Bioconjug Chem* **22**, 2317–2323 (2011).

213. Guilbaud, J. B. & Saiani, A. Using small angle scattering (SAS) to structurally characterise peptide and protein self-assembled materials. *Chem Soc Rev* **40**, 1200–1210 (2011).

214. https://www.sasview.org/. http://www.sasview.org/.

215. Lu, J. R., Su, T. J., Thomas, R. K., Penfoldc, J. & Websterc, J. *Structural Conformation of Lysozyme Layers at the Air/Water Interface Studied by Neutron ReÑection*.

216. Holtzer, A. Interpretation of the angular distribution of the light scattered by a polydisperse system of rods. *Journal of Polymer Science* **17**, 432–434 (1955).

217. Lin, T. Lang., Chen, S. Hsin., Gabriel, N. Elise. & Roberts, M. F. Small-angle neutron scattering techniques applied to the study of polydisperse rodlike diheptanoylphosphatidylcholine micelles. *J Phys Chem* **91**, 406–413 (1987).

218. Choi, K. H. & Morais, M. Use of small-angle X-ray scattering to investigate the structure and function of dengue virus NS3 and ns5. *Methods in Molecular Biology* **1138**, 241–252 (2014).

219. Altwaijry, N., Almutairi, G. S., Khan, M. S., Shaik, G. M. & Alokail, M. S. Effect of Antihypertensive Drug (Chlorothiazide) on Fibrillation of Lysozyme: A Combined Spectroscopy, Microscopy, and Computational Study. *Int J Mol Sci* **24**, 3112 (2023).

220. Schroer, M. A. *et al.* Dependence of the Nanoscale Composite Morphology of Fe3O4 Nanoparticle-Infused Lysozyme Amyloid Fibrils on Timing of Infusion: A Combined SAXS and AFM Study. *Molecules* **26**, (2021).

221. James, S. L., Lloyd, G. O. & Zhang, J. Supramolecular gels in crystal engineering. *CrystEngComm* **17**, 7976–7977 (2015).

222. Marchetti, A. *et al.* Fibril Structure Demonstrates the Role of Iodine Labelling on a Pentapeptide Self-Assembly. *Chemistry – A European Journal* **28**, (2022).

223. Sandhu, B., McLean, A., Sinha, A. S., Desper, J. & Aakeröy, C. B. Assessment of Computational Tools for Predicting Supramolecular Synthons. *Chemistry (Easton)* **3**, 612–629 (2021).

224. Adams, D. J. Personal Perspective on Understanding Low Molecular Weight Gels. *J Am Chem Soc* **144**, 11047–11053 (2022).

225. Dastidar, P., Roy, R., Parveen, R. & Sarkar, K. Supramolecular Synthon Approach in Designing Molecular Gels for Advanced Therapeutics. *Adv Ther (Weinh)* **2**, (2019).

226. Ghosh, D., Farahani, A. D., Martin, A. D., Thordarson, P. & Damodaran, K. K. Unraveling the Self-Assembly Modes in Multicomponent Supramolecular Gels Using Single-Crystal X-ray Diffraction. *Chemistry of Materials* **32**, 3517–3527 (2020).

227. Ghosh, D., Bjornsson, R. & Damodaran, K. K. Role of N–Oxide Moieties in Tuning Supramolecular Gel-State Properties. *Gels* **6**, 41 (2020).

228. Manna, U., Roy, R., Datta, H. K. & Dastidar, P. Supramolecular Gels from Bis-amides of *L* -Phenylalanine: Synthesis, Structure and Material Applications. *Chem Asian J* **17**, (2022).

229. Parveen, R., Jayamma, B. & Dastidar, P. Supramolecular Gels Derived from Simple Organic Salts of Flufenamic Acid: Design, Synthesis, Structures, and Plausible Biomedical Application. *ACS Biomater Sci Eng* **5**, 2180–2189 (2019).

230. Chakraborty, P. & Dastidar, P. An easy access to topical gels of an anti-cancer prodrug (5-fluorouracil acetic acid) for self-drug-delivery applications. *Chemical Communications* **55**, 7683–7686 (2019).

231. Chakraborty, P., Datta, H. K., Biswas, P. & Dastidar, P. Supramolecular Synthon Approach in Designing Organic Sulfonates as Supramolecular Gelators: An Easily Accessible Topical Gel with Antibacterial Properties. *Chemistry of Materials* **33**, 2274–2288 (2021).

232. Roy, R., Majumder, J., Datta, H. K., Parveen, R. & Dastidar, P. Supramolecular Hydrogels Developed from Mafenide and Indomethacin as a Plausible Multidrug Self-Delivery System as Antibacterial and Anti-inflammatory Topical Gels. *ACS Appl Bio Mater* **5**, 610–621 (2022).

233. Biswas, P., Dutta, A. & Dastidar, P. Design, Synthesis, and Structural Insights of a Series of Zn(II)–NSAID Based Coordination Complex Derived Metallogels and Their Plausible Applications in Self Drug Delivery. *Cryst Growth Des* **23**, 342–353 (2023).

234. Biswas, P., Datta, H. K. & Dastidar, P. Multi-NSAID-based Zn(II) coordination complex-derived metallogelators/metallogels as plausible multi-drug self-delivery systems. *Chem Commun (Camb)* **58**, 969–972 (2022).

235. Pizzi, A. *et al.* Halogen bonding modulates hydrogel formation from Fmoc amino acids. *CrystEngComm* **19**, 1870–1874 (2017).

236. Chakraborty, P., Aviv, M., Netti, F., Cohen-Gerassi, D. & Adler-Abramovich, L. Molecular Co-Assembly of Two Building Blocks Harnesses Both their Attributes into a Functional Supramolecular Hydrogel. *Macromol Biosci* **22**, (2022).

237. Saha, S. & Desiraju, G. R. Acid⋯Amide Supramolecular Synthon in Cocrystals: From Spectroscopic Detection to Property Engineering. *J Am Chem Soc* **140**, 6361–6373 (2018).

238. Torres-Moya, I. *et al.* Highly Thermally Resistant Bisamide Gelators as Pharmaceutical Crystallization Media. *Gels* **9**, 26 (2022).

239. Metrangolo, P. IUPAC definition of the halogen bond. *Acta Crystallogr A Found Adv* **73**, C309–C309 (2017).

240. Desiraju, G. R. *et al.* Definition of the halogen bond (IUPAC recommendations 2013). *Pure and Applied Chemistry* **85**, 1711–1713 (2013).

241. Clark, T., Hennemann, M., Murray, J. S. & Politzer, P. Halogen bonding: the σ-hole. *J Mol Model* **13**, 291–296 (2007).

242. Cavallo, G. *et al.* The Halogen Bond. *Chem Rev* **116**, 2478–2601 (2016).

243. Wang, Y., Miao, X. & Deng, W. Halogen Bonds Fabricate 2D Molecular Self-Assembled Nanostructures by Scanning Tunneling Microscopy. *Crystals (Basel)* **10**, 1057 (2020).

244. Kolář, M., Hostaš, J. & Hobza, P. The strength and directionality of a halogen bond are co-determined by the magnitude and size of the σ-hole. *Physical Chemistry Chemical Physics* **16**, 9987–9996 (2014).

245. Pizzi, A. *et al.* Halogen bonding as a key interaction in the self-assembly of iodinated diphenylalanine peptides. *Peptide Science* **112**, (2020).

246. Ma, M. *et al.* A Stable Green Amino Acid Hydrogel. *ChemistrySelect* **8**, (2023).

247. Ma, M. *et al.* A novel green amino acid derivative hydrogel with multi-stimulus responsiveness. *Colloid Polym Sci* **301**, 569–576 (2023).

248. Cohen-Gerassi, D. *et al.* Phase Transition and Crystallization Kinetics of a Supramolecular System in a Microfluidic Platform. *Chemistry of Materials* **32**, 8342–8349 (2020).

249. Reddy, L. S., Nangia, A. & Lynch, V. M. Phenyl-Perfluorophenyl Synthon Mediated Cocrystallization of Carboxylic Acids and Amides. *Cryst Growth Des* **4**, 89–94 (2004).

250. Lee, C. C., Nayak, A., Sethuraman, A., Belfort, G. & McRae, G. J. A three-stage kinetic model of amyloid fibrillation. *Biophys J* **92**, 3448–3458 (2007).

251. Ryan, D. M., Doran, T. M. & Nilsson, B. L. Complementary π-π Interactions induce multicomponent coassembly into functional fibrils. *Langmuir* **27**, 11145–11156 (2011).

252. Yang, Z., Gu, H., Zhang, Y., Wang, L. & Xu, B. Small molecule hydrogels based on a class of antiinflammatory agents. *Chemical Communications* **4**, 208–209 (2004).

253. Ma, M. *et al.* Aromatic-aromatic interactions induce the self-assembly of pentapeptidic derivatives in water to form nanofibers and supramolecular hydrogels. *J Am Chem Soc* **132**, 2719–2728 (2010).

254. Jayawarna, V. *et al.* Nanostructured hydrogels for three-dimensional cell culture through self-assembly of fluorenylmethoxycarbonyl-dipeptides. *Advanced Materials* **18**, 611–614 (2006).

255. Nagai, Y., Unsworth, L. D., Koutsopoulos, S. & Zhang, S. Slow release of molecules in self-assembling peptide nanofiber scaffold. *Journal of Controlled Release* **115**, 18–25 (2006).

256. Bergamaschi, G. *et al.* A halogen bond-donor amino acid for organocatalysis in water. *Chemical Communications* **54**, 10718–10721 (2018).

257. Erdélyi, M. Halogen bonding in solution. *Chem Soc Rev* **41**, 3547 (2012).

258. Kilah, N. L. *et al.* Enhancement of Anion Recognition Exhibited by a Halogen-Bonding Rotaxane Host System. *J Am Chem Soc* **132**, 11893–11895 (2010).

259. Mele, A., Metrangolo, P., Neukirch, H., Pilati, T. & Resnati, G. A Halogen-Bonding-Based Heteroditopic Receptor for Alkali Metal Halides. *J Am Chem Soc* **127**, 14972–14973 (2005).

260. Panda, J. J., Mishra, A., Basu, A. & Chauhan, V. S. Stimuli responsive self-assembled hydrogel of a low Molecular weight free dipeptide with potential for tunable drug delivery. *Biomacromolecules* **9**, 2244–2250 (2008).

261. Di Cola, E., Grillo, I. & Ristori, S. Small Angle X-ray and Neutron Scattering: Powerful Tools for Studying the Structure of Drug-Loaded Liposomes. *Pharmaceutics* **8**, 10 (2016).

262. Svergun, D. I. & Koch, M. H. J. Small-angle scattering studies of biological macromolecules in solution. *Reports on Progress in Physics* **66**, 1735–1782 (2003).

263. Øgendal, L. H. Light Scattering Demystified Theory and Practice. *University of Copenhagen* vol. 125 Preprint at (2017).

264. C. R. Brundle, C. A. Evans & S. Wilson. *Encyclopedia of Materials Characterization: Surfaces, Interfaces, Thin Films*. (Butxetworch-Heinemann, 1992).

265. Kuntsche, J., Horst, J. C. & Bunjes, H. Cryogenic transmission electron microscopy (cryo-TEM) for studying the morphology of colloidal drug delivery systems. *Int J Pharm* **417**, 120–137 (2011).

List of publications

Peer-reviewed journals

Acid⋯Amide Supramolecular Synthon for Tuning Amino Acid-Based Hydrogels' Properties
Veronese E., Pigliacelli C., Bergamaschi G., Terraneo G., Dichiarante V., Metrangolo P. *Chem. Eur. J.*, **2023**, e202301743

- Front cover: https://doi.org/10.1002/chem.202302836
- Cover profile: https://doi.org/10.1002/chem.202302838

Engineering Amino Acid and Peptide Supramolecular Architectures through Fluorination
Veronese E., Metrangolo P., Dichiarante V. *Chem. Eur. J.*, **2024**. Submitted

Posters and presentations

Effect of fluorination on the thermal stability of azide-tagged amino acids, poster at XXVII CONGRESSO NAZIONALE DELLA SOCIETÀ CHIMICA ITALIANA (SCI2021). 14th-23rd September 2021.

Synthesis and applications of superfluorinated thiol-derivatives, oral presentation at Workshop NiFty – "New-Generation Nanostructured Fluorinated Materials for ^{19}F-MRI and their Biophysicochemical Interactions" organized by Università di Modena. 24th September 2021 in Modena.

Effects of Poly-Halogenation on Fmoc-Phenylalanine Hydrogels, poster at the PhD school "1ST school of supramolecular and bio- nanomaterials, lake Como school of advanced studies" organized by Politecnico di Milano & Lake Como School of Advanced Studies. 13th-17th June 2022.

- Best group project award for the project entitled "Artificial photosynthesis: Eco3Cat"

Co-Crystal Strategy for Tuning Fmoc-Amino Acidic Hydrogels, poster and flash presentation at PhD day organized by the Department of Chemistry, Materials and Chemical Engineering of Politecnico di Milano. 26th January 2023.

Proteins as supramolecular hosts for PERFECTA, oral presentation at Workshop NiFty – "New-Generation Nanostructured Fluorinated Materials for ^{19}F-MRI and their Biophysicochemical Interactions" organized by Università degli studi di Trieste. 30th-31st March 2023.

Co-crystal strategy for tuning the properties of amino acid-based hydrogels, poster (not presenting) at XIII National Congress AICIng, organized by Politecnico di Milano. 25th-28th June 2023.